ORNL/TM-7201

ornl

OAK RIDGE NATIONAL LABORATORY

UNION CARBIDE

Expected Environments in High-Level Nuclear Waste and Spent Fuel Repositories in Salt

H. C. Claiborne
L. D. Rickertsen
R. F. Graham

OPERATED BY
UNION CARBIDE CORPORATION
FOR THE UNITED STATES
DEPARTMENT OF ENERGY

Printed in the United States of America. Available from
National Technical Information Service
U.S. Department of Commerce
5285 Port Royal Road, Springfield, Virginia 22161
NTIS price codes—Printed Copy: A10 Microfiche A01

DISCLAIMER

ORNL/TM-7201
Dist. Category UC-70

Contract No. W-7405-eng-26

CHEMICAL TECHNOLOGY DIVISION

NUCLEAR WASTE PROGRAMS

Program Coordination and Special Problems
(Activity No. AP 05 15 15; 189 No. ONW-2801)

EXPECTED ENVIRONMENTS IN HIGH-LEVEL NUCLEAR WASTE AND SPENT FUEL REPOSITORIES IN SALT

H. C. Claiborne, L. D. Rickertsen,* and R. F. Graham*

*Science Applications, Inc., Oak Ridge, Tennessee 37830.

Date Published: August 1980

This report was prepared by Oak Ridge National Laboratory under Contract No. W-7405-eng-26 with the U.S. Department of Energy. The project was administered by the Office of Nuclear Waste Isolation, Battelle Memorial Institute.

OAK RIDGE NATIONAL LABORATORY
Oak Ridge, Tennessee 37830
operated by
UNION CARBIDE CORPORATION
for the
U.S. DEPARTMENT OF ENERGY

CONTENTS

LIST OF FIGURES

LIST OF TABLES

EXPECTED ENVIRONMENTS IN HIGH-LEVEL NUCLEAR WASTE AND SPENT FUEL REPOSITORIES IN SALT

H. C. Claiborne, L. D. Rickertsen, and R. F. Graham

EXECUTIVE SUMMARY

The uncertainties that exist in the identification of rock formations for sites of nuclear waste repositories and their design are gradually being reduced. At this time, design parameters for a high-level waste (HLW) or spent fuel (SF) repository in salt are sufficiently well defined that it is possible to predict, with some confidence, many of the conditions that will be encountered in the vicinity of the waste canisters in the repository. These conditions, along with the range of uncertainty in the variables describing these conditions, can serve as a framework:

1. to scientists conducting material performance tests,
2. to engineers preparing repository designs,
3. for license application information,
4. to those developing waste forms,
5. for studies needing reference conditions,
6. to identify areas requiring further investigation.

The purpose of this report is to describe the expected environments associated with HLW and SF repositories in salt formations. These environments include the thermal, fluid, pressure, brine chemistry, and radiation fields predicted for repository conceptual designs.

In this study, it is assumed that the repository will be a room and pillar mine in a rock-salt formation with the disposal horizon located ∿2000 ft (610 m) below the surface of the earth. Canistered waste packages containing HLW in a solid matrix or SF elements are emplaced in vertical holes in the floor of the room. The emplacement holes are backfilled with crushed salt or other material, and the storage room is backfilled and sealed at some later time.

In determining the expected environments associated with HLW and SF repositories in salt formations, the baseline repository was considered to have single rows of canisters in a room with an initial local areal thermal loading (includes distribution over room and pillar areas) of 150 kW/acre (37.1 W/m^2) for HLW and 60 kW/acre (14.8 W/m^2) based on HLW or SF that has aged 10 yr. Lower initial thermal loadings of 100 kW/acre (24.7 W/m^2) for HLW and 40 kW/acre (9.88 W/m^2) for SF were also considered, as well as a two-row configuration for SF that is based on a Conceptual Reference Repository Design (CRRD) being prepared for inclusion in a Preliminary Information Report (PIR) that will become part of the licensing effort.

The maximum temperatures and the time of their occurrence for the salt, the canister surface, and the centerline (or central fuel pin) are shown in Table S-1 for these areal thermal loadings. It was assumed that the thermal load was 2.16 kW/canister for SF. The change in areal thermal loading was achieved by varying the pitch along an emplacement row.

The corresponding maximum temperatures and times of their occurrence for the two-row configuration are shown in Table S-2. The local areal loadings of 83 kW/acre (20.5 W/m^2) for the boiling-water-reactor (BWR) elements and 130 kW/acre (32.1 W/m^2) for the pressurized-water reactors (PWR) were derived on the basis of putting either PWR or BWR canisters in the array of emplacement holes specified in the CRRD design. Mixing of the two types (ratio as yet undetermined) will be a more likely condition. Consequently, the results for these areal loads represent upper and lower limits. Sensitivity studies are presented to show the effect of changing the areal heat load, the canister heat load, the barrier material and thickness, delaying the backfilling of the canister hole, and ventilation of a storage room prior to backfilling.

The effect of decreasing either the areal heat load or the canister heat load reduces the canister surface temperature. For decreasing areal heat load, the effect becomes more pronounced as the years after emplacement increase; however, the effect for a decreasing canister heat load is most dramatic during the early years after emplacement. The

Table S-1. Maximum temperatures[a] in the salt rock formation, canister surface, and waste centerline

	Salt			Canister surface			Waste centerline (or center pin)		
	Maximum temperature		Years after emplacement	Maximum temperature		Years after emplacement	Maximum temperature		Years after emplacement
	°F	°C		°F	°C		°F	°C	
HLW, 150 kW/acre (37.1 W/m^2)	412	211	15	587	308	10	670	354	3
HLW, 100 kW/acre (24.7 W/m^2)	312	156	15	508	264	3	603	317	1.5
HLW, 50 kW/acre (12.4 kW/m^2)	228	109	5	459	237	0.67	580	304	0.5
SF, 60 kW/acre (14.8 W/m^2)	211	99	50	237	113	25	280	138	∿5
SF, 40 kW/acre (9.88 W/m^2)	171	77	50	202	94	15	270	132	∿3

[a]Assumes the waste is 10 yr old on emplacement. The HLW decay rates were based on fuel that is a 3:1 mix of fresh UO_2 and MOX fuels. The HLW canister thermal loading was 2.16 kW, and the SF was 0.55 kW (one PWR fuel element).

Table S-2. Maximum temperatures[a] of the rock salt, canister surface, and fuel pin and times of occurrence for the two-row configuration

	Pressurized water reactor, 130 kW/acre (32.1 W/m^2)			Boiling-water reactor, 83 kW/acre (20.5 W/m^2)		
	Maximum temperature		Time	Maximum temperature		Time
	°F	°C	(yr)	°F	°C	(yr)
Rock salt	351	177	60	248	120	50
Canister surface	358	181	50	253	123	55
Fuel pin	403	206	30	311	155	15

[a]Age at emplacement, 10 yr. The PWR canister loading is 0.525 kW (one fuel element), and the BWR canister loading is 0.324 kW (two fuel elements). Ambient rock salt temperature, 93°F (34°C).

effect of a change in the barrier on the canister surface temperature is presented in the form of graphs with backfill materials and barrier thicknesses as parameters. The importance of the thermal resistance of the barrier is demonstrated, and from these graphs, the designer can select the barrier material and thickness based on the design temperature limitation of the canister surface.

A delay in backfilling around the canister has virtually no effect on the surface and centerline temperature histories after backfilling is effected. The temperature history is quickly reestablished to that which would occur at this latter time had backfilling been initiated earlier. However, this delay does serve to reduce the maximum temperatures during the retrieval period. In the case of HLW, for an areal thermal loading of 150 kW/acre (37.1 W/m^2), a reduction of ∿300°F (167°C) at the waste centerline occurs for a delay of 25 yr.

Ventilation of a storage room during a long retrieval phase after backfilling the canister can lower the maximum temperatures significantly in the near field.

The HLW salt temperatures for an areal loading of 150 kW/acre (37.1 W/m^2) is reduced by 120°F (67°C) when ventilated for times beyond the time of peak temperature, whereas temperatures for SF at 60 kW/acre (14.8 W/m^2) were lowered by nearly 62°F (34°C). The effect on the canister surface temperatures is not as dramatic but is still substantial. Temperatures for the HLW canister surfaces are reduced by 57°F (32°C), while for SF, the reduction is 34°F (19°C) to 202°F (94°C). Waste centerline (or SF pin) temperatures would be reduced by ∿40°F (22°C) for HLW and by ∿10°F (6°C) for SF. Generally, within a few years after sealing, the formation attains the temperature distribution it would have reached had the rooms been sealed from the beginning.

The calculated temperature histories are inputs to the brine migration calculations that utilized an empirical equation relating the speed of migration of brine inclusions up a thermal gradient to the temperature and temperature gradient. It is assumed that the brine inclusions are not trapped on the grain boundaries (although evidence indicates that this will happen); consequently, the amount of brine entering the emplacement hole should be an overestimate. The brine inclusions can be

considered in terms of particle density that obeys the continuity equation. A computer code (MIGRAIN) was developed for this model. The predicted results of the Salt Block II experiment at Sandia Laboratories by this code compared reasonably well with the reported experimental results.

The total brine inflow calculated for HLW at an areal loading of 150 kW/acre (37.1 W/m^2) was $\sim$6 ℓ. Ventilation of storage rooms for a few years caused a significant decrease in the total brine inflow.

The pressures exerted by vapors and gases in a sealed repository will gradually increase until the entire repository is essentially at the lithostatic pressure. Until mine closure is large, no significant pressure rises can be expected. However, in the unlikely event that an emplacement hole develops a good seal, significant pressures could develop. In order to estimate the possible pressure histories, the vapor pressure in the emplacement hole was calculated for three different scenarios (i.e., no hole closure—no backfill, no hole closure—backfill, and hole closure—no backfill). The calculations are made using the thermal and moisture environments that were previously calculated. It was assumed that the gas in the system consisted of air and water vapor. A computer code (REPRESS) was developed assuming that these changes occurred slowly (equilibrium conditions for brine and vapor). For scenario case 1, the vapor-space pressure for HLW peaks at 700 psi (4.8 MPa) and SF vapor space pressure does not reach saturation. Scenario case 2 shows a peak pressure of 1000 psi (6.9 MPa) for HLW and 18 psi (0.12 MPa) for SF. When hole closure is assumed (scenario case 3), the pressure shows a decrease of only 100 psi (0.69 MPa) from the no-hole-closure case for HLW. The pressure increases to 50 psi (0.34 MPa) 50 yr after emplacement for SF.

The brine chemical environment is briefly discussed in terms of brine chemistry, corrosion, and compositions. An important chemical consideration is the corrosion of the canister during the period that retrievability is required. It was concluded that four areas of additional experimental information would be useful. Estimates of the corrosion rates that might occur around a reference SF canister emplaced in a salt repository indicate that a steel canister could remain essentially

intact for hundreds of years. Three types of brine compositions are considered; namely, brine inclusions, reacted brine in the emplacement hole, and brine resulting from dissolution of the salt formation. The compositions of the first and third types can be described as containing very little potassium, some magnesium, and calcium in the anhydrite form. If brine inclusions enter the emplacement hole, water is lost by reaction with the iron canister, radiolytic decomposition, or evaporation.

The nuclear radiation environment is divided into the following three categories:

1. exposure to operating personnel,
2. radiation chemistry, and
3. stored energy in the waste forms and rock salt.

The category emphasized in this report is the stored energy that can be released as a result of radiation damage or crystal dislocations within crystal lattices by gamma radiation. The phenomenon of thermal annealing can take place at elevated temperatures and release this stored energy. The stored energy has an effect (but not large) on the radiation chemistry involved, but it has been shown previously that the sudden release of stored energy is not a credible event. Even if it were suddenly released, the consequences would not be severe. The maximum absorbed dose rate at the inner edge of the crushed salt backfill at emplacement was calculated to be 1.0×10^5 and 4.1×10^3 rads/h for HLW and SF, respectively. The absorbed dose integrated over 10,000 yr was estimated to be 1.6×10^{10} and 9.6×10^8 rads for HLW and SF, respectively.

EXPECTED ENVIRONMENT IN HIGH-LEVEL NUCLEAR WASTE AND SPENT FUEL REPOSITORIES IN SALT

H. C. Claiborne, L. D. Rickertsen,* and R. F. Graham*

ABSTRACT

The purpose of this report is to describe the expected environments associated with high-level waste (HLW) and spent fuel (SF) repositories in salt formations. These environments include the thermal, fluid, pressure, brine chemistry, and radiation fields predicted for the repository conceptual designs.

In this study, it is assumed that the repository will be a room and pillar mine in a rock-salt formation, with the disposal horizon located ∿2000 ft (610 m) below the surface of the earth. Canistered waste packages containing HLW in a solid matrix or SF elements are emplaced in vertical holes in the floor of the rooms. The emplacement holes are backfilled with crushed salt or other material and sealed at some later time.

Initial thermal loadings, distributed over the room and pillar areas, are assumed to be 2.16 kW/canister and 150 kW/acre (37.1 W/m^2) for HLW and 0.55 kW/canister and 60 kW/acre (14.8 W/m^2) for SF in a baseline repository. Thermal environments are calculated in terms of near-field and far-field models. The salt temperature for HLW peaks at 412°F (211°C) ∿15 yr after emplacement of 10-yr-old waste. The peak for SF is broader, occurring ∿50 yr after emplacement at a temperature of 211°F (99.4°C). At the canister surface, with a 4-in. (10.2-cm) barrier [2 in. (1 cm) of crushed salt and a 2-in. (5.1-cm) air gap], the maximum HLW temperature is 587°F (308°C) and peaks ∿10 yr after emplacement. For SF, the maximum canister temperature is 237°F (114°C) and occurs ∿25 yr after emplacement. The maximum HLW waste centerline temperature of 670°F (354°C) is reached ∿3 yr after emplacement. The maximum temperature of the SF pin assembly is 280°F (138°C), occurring ∿5 yr after emplacement.

Sensitivity studies are presented to show the effect of changing the areal heat load, the canister heat load, the barrier material and thickness, ventilation of the storage room, and adding a second row to the emplacement configuration. Decreasing either the areal heat load or the canister heat load reduces the canister surface temperature. For decreasing areal heat load, the effect becomes more pronounced as the years after emplacement increase; however, the effect for a decreasing canister heat load is most dramatic during the early years after emplacement. The effect on canister surface temperature of a change in the barrier is presented in the form of graphs which will permit the designer

*Science Applications, Inc., Oak Ridge, Tennessee 37830.

to select the barrier material and thickness based on the design limitation of canister surface or centerline temperature. The effect of ventilating the storage room is to lower the maximum salt temperature of the HLW by 120°F (67°C) and the maximum salt temperature of the SF by 62°F (34°C). Canister SF assembly temperatures are reduced by 10°F (5.6°C).

The calculated thermal environment is used as input for brine migration calculations. The brine inclusions can be considered in terms of a particle density that obeys the time-dependent continuity equation. A computer code (MIGRAIN) was developed, and predictions compared favorably with experimental data of the Waste Isolation Pilot Plant (WIPP) Salt Block II. The total flow for HLW is ∿12 ℓ after 1500 yr, and the corresponding flow for SF is 6 ℓ.

The vapor and gas pressure will gradually attain the lithostatic pressure in a sealed repository. In the unlikely event that an emplacement hole will become sealed in relatively early years, the vapor space pressure was calculated for three scenarios (i.e., no hole closure—no backfill, no hole closure—backfill, and hole closure—no backfill). It was assumed that the gas in the system consisted of air and water vapor in equilibrium with brine. A computer code (REPRESS) was developed assuming that these changes occur slowly (equilibrium conditions). For scenario 1, the HLW vapor space pressure peaks at 700 psi (4.8 MPa), and SF vapor space pressure does not reach saturation. Scenario 2 shows a peak pressure of 1000 psi (6.9 MPa) for HLW and 18 psi (0.12 MPa) for SF. When hole closure is assumed (scenario 3), the pressure shows a decrease of only 100 psi (0.70 MPa) from the no-hole-closure case for HLW. The pressure increases to 50 psi (0.34 MPa) 50 yr after emplacement for SF.

The brine chemical environment is outlined in terms of brine chemistry, corrosion, and compositions. Three types of brine compositions are considered, namely, brine inclusions, reacted brine in the emplacement hole, and brine resulting from dissolution of the salt formation. The compositions of the first and third types can be described as containing very little potassium, some magnesium, and calcium is in the anhydrite form. If brine inclusions enter the emplacement hole, water is lost by reaction with the iron canister, radiolytic decomposition, or evaporation.

The nuclear radiation environment emphasized in this report is the stored energy that can be released as a result of radiation damage or crystal dislocations within crystal lattices. The maximum absorbed dose rates to the crushed salt at emplacement are 1.0×10^5 and 4.1×10^3 rads/h for HLW and SF, respectively. The absorbed dose integrated over 10,000 yr was estimated to be 1.6×10^{10} and 9.6×10^8 rads for HLW and SF, respectively.

1. INTRODUCTION

Among the most challenging problems facing the nation today is the question of geologic isolation of radioactive wastes. Large uncertainties have existed concerning the identification of an appropriate rock formation for waste emplacement and the future successful isolation of the waste in this formation for possibly many thousands of years. As waste repository concepts have evolved, however, considerable progress has been made in reducing these uncertainties. At this time, design parameters for a high-level-waste (HLW) or spent fuel (SF) repository in salt are sufficiently well defined that it is possible to predict, with some confidence, many of the conditions that will be encountered in the vicinity of the waste canisters in the repository. As these and other conditions are established, along with the range of uncertainty in the variables describing these conditions, they can serve as a framework:

1. to scientists conducting material performance tests,
2. to engineers preparing repository designs,
3. for license application information,
4. to those developing waste forms,
5. for studies needing reference conditions,
6. to identify areas requiring further investigation.

The purpose of this report is to describe the expected environments associated with HLW and SF repositories in salt formations. These environments include the thermal, fluid, pressure, brine chemistry, and radiation fields predicted for the repository conceptual designs.

In present repository conceptual designs, storage rooms are mined in the salt ∿2000 ft (610 m) below the surface of the earth, and canistered waste packages containing HLW in a solid matrix or SF elements are emplaced in vertical holes in the floor of the storage rooms. The emplacement holes are backfilled with such material as crushed salt or other material, and the storage room is backfilled and sealed at some later time. Heat generated by the waste flows from the waste, through

the waste package and backfill, through the surrounding rock, into the geologic formation, and up to the surface of the earth until it is convected or radiated away to the atmosphere. The increased temperatures associated with this heat flow has an important influence on the repository in that the temperature is the driving force for many phenomena. Naturally occurring moisture in the salt will migrate due to the induced temperature gradients and rock stresses. Creep rates will be altered by the increased temperatures, and chemical reaction rates will be enhanced.

The assessment of the conditions encountered due to the emplacement of the waste requires a design basis. Although a number of conceptual designs now exist, such as the *Generic Environmental Impact Statement (GEIS) for the Management of Commercially Generated Radioactive Waste* (ref. 1), *The National Waste Terminal Storage (NWTS) Repository for Storing Reprocessing Wastes in a Domed Salt Formation* (ref. 2), and *The NWTS Conceptual Reference Repository Description (CRRD)* (ref. 3), the baseline design of this report differs in some aspects from each of these. The waste is 10 yr old at emplacement, at which time the HLW is generating 2.16 kW per canister and the SF is generating 0.55 kW per canister. The waste canister is assumed to be readily retrievable for at least 5 yr after emplacement, at which time the storage rooms are backfilled with crushed salt. The HLW matrix fills 80% of the canister volume and a single spent pressurized water reactor (PWR) assembly is included in the SF canister. A realistic canister design for boiling-water reactor (BWR) SF assemblies would generate no more heat than that for one PWR assembly. Consequently, if BWR assemblies were used, the analysis would be conservative (i.e., the temperatures would be less). The waste canister is emplaced in a 10-in. (25.4-cm)-diam hole with an overpack or protective sleeve located at an outside radius of 8 in. (20.3 cm). The emplacement hole is then backfilled so that the volume between the overpack and the hole wall is filled with some material. The gap between the canister and the overpack is assumed to be filled with air. The air gap width and the backfill material are part of the engineered barrier design. The canister and engineered barrier design will be presented in greater detail in Sect. 2.

For the baseline repositories, it was assumed that the average amount of waste emplaced per unit storage area of the repository (local areal heat load) is 150 kW/acre (37.1 W/m^2) for HLW and 60 kW/acre (14.8 W/m^2) for SF. The thermal environment is predicted for these baseline repositories, with some sensitivity studies carried out for variations in the repository design such as for lower thermal loadings. The results from the thermal analysis are used to obtain the brine migration and the vapor space pressures. Finally, some comments are presented on the expected brine chemical environment and the expected nuclear radiation environment.

In addition, the expected environments for the CRRD design utilizing two rows of SF canisters in a disposal room were also determined as part of a special study.

2. THERMAL ENVIRONMENT

Previous analyses of the repository thermal environments have been made in terms of near-field and far-field models. The near-field model takes into consideration details of the waste package design and analyses of conditions in the vicinity of the waste and the emplacement hole during the first several years after emplacement.

The thermal environments depend on the layout of the repository, particularly the canister spacing. When these details are taken into account, temperatures in the vicinity of a waste package can be adequately determined if the effect of other canisters through the use of unit cells or some other technique is considered.

The far field includes a region at a sufficient distance from the source that details of the near field do not have a significant bearing. The distances concerned are on the order of tens of meters from the repository, and the time periods are hundreds of years or longer. The most important factors for the far-field response are the average waste emplacement density, the average formation thermal properties, and the long-term time dependence of the waste-heat generation rate. In addition, heat removal by ventilation of the repository during the operational phase, by water flow in aquifers, and at the surface of the earth can be important. Far-field models provide temperature fields that are useful in understanding the long-term thermal and mechanical response of the repository host formation and its surrounding strata. These models, however, cannot be expected to provide an accurate representation of the temperatures within the repository itself.

The thermal environment discussed in this section is predicted using both the near-field model and the far-field model. A sensitivity analysis is performed using the near-field model to show the effect of varying such parameters as the canister and areal heat load, the backfill thermal conductivity, the barrier thickness, and the time after emplacement that the canisters are backfilled. Special studies are also performed for ventilation of the storage room and for a two-row waste configuration.[3]

The far-field analysis includes temperature predictions for both the dome and bedded salt stratigraphics. All thermal calculations were performed using the HEATING5 computer code.[4] This code has been widely used in the thermal analyses of repositories, but additional numerical sensitivity studies were carried out as a part of this effort (Appendix H) to estimate the effects of mesh spacing, boundary conditions, and time steps in order to validate the approach for this study.

2.1 The Near-Field Analysis

The near-field analysis is based on the repository characteristics given in Table 1. As shown in Table 1, two waste types have been calculated under different thermal loading conditions and slight variations in the room and emplacement holes. All waste was assumed to be 10 yr old at emplacement, and all calculations were made for dome salt with no effect of interbedded layers included in these calculations. The heat-generation decay rates were different for the two baseline waste types, and these decay rates are shown in Table 2. The baseline thermal properties of materials are given in Table 3, with the temperature-dependent thermal conductivity properties of salt presented in Table 4. The near-field analysis assumed the same ambient formation temperatures for both waste types, and this is presented in Table 5.

2.1.1 The near-field model

The unit-cell concept was used in modeling the near-field domain since the canisters located away from boundaries of the repository may be considered part of any infinite array. Two different unit cells were used in the calculations; one for the surrounding salt and the other for the waste package.

In the calculations for the thermal histories in the salt surrounding the emplacement hole, a three-dimensional (3-D) cartesian coordinate model was used, and a schematic representation is shown in Fig. 1. The areal limits of the unit cell are defined by the adiabatic boundaries that are vertical planes along the centerlines of the room and pillars and a vertical plane that is normal to the pillars and located midway

Table 1. Baseline repository characteristics

Characteristics	High-level waste	Spent fuel
Thermal loading		
Areal thermal loading, kW/acre (kW/m^2)	150 (37.1)	60 (14.8)
Canister thermal power, kW	2.16	0.55
Age of waste, yr	10	10
Room dimensions		
Room length, ft (m)	Several hundred feet	
Room width, ft (m)	18 (5.5)	18 (5.5)
Room height, ft (m)	18 (5.5)	25 (7.6)
Pillar thickness, ft (m)	60 (18.3)	60 (18.3)
Canister burial holes		
Drill hole diameter, in. (cm)	20 (6.1)	20 (6.1)
Drill hole depth, ft (m)	18 (5.5)	25 (7.6)
Pitch (single row), ft (m)	8.04 (2.45)	5.12 (1.56)

Table 2. Relative heat-generation decay properties[a]

Year after emplacement[b]	High-level waste	Spent fuel
0	1.0	1.0
1	0.95	0.956
2	0.907	0.919
3	0.871	0.889
4	0.851	0.861
5	0.810	0.838
6	0.783	0.819
7	0.769	0.799
8	0.734	0.782
9	0.714	0.763
10	0.692	0.750
15	0.600	0.681
20	0.529	0.622
25		0.571
30	0.402	0.525
40	0.313	
50		0.397
70	0.157	0.301
100	0.0864	0.239
190	0.0296	0.137
290	0.0215	0.108
400	0.0167	0.0910
590	0.0127	0.0711
690	0.0113	
790		0.0569
890	0.0081	0.0514
990	0.0081	
1,990	0.00404	0.0247
3,300		0.0125
10,000		0.0114
40,000		0.0027
100,000		0.00081
500,000		0.00004

[a]See Nuclear Waste Projections and Source Term Data for FY 1977, Y/OWI/TM-34. The HLW decay rates correspond to waste arising from fuel, which is a 3:1 mix of fresh UO_2 and MOX fuels.

[b]Waste is assumed to be 10 yr old at emplacement.

Table 3. Baseline thermal properties of materials

Material	Density		Heat capacity		Conductivity	
	lb/ft^3	kg/m^3	Btu/lb·°F	J/g·K	Btu/hr·ft·°F	W/m·K
Vitrified high-level waste	187	3000	0.20	0.84	0.70	1.2
Spent fuel	187	3000	0.20	0.84	0.70	1.2
Salt	135	2170	0.20	0.84	See Table 4	

Table 4. Assumed thermal conductivities for salt[a]

Temperature °F	Temperature °C	Thermal conductivity Btu/hr·ft·°F	Thermal conductivity W/m·K
32	0	3.53	6.11
122	50	2.90	5.02
212	100	2.43	4.20
302	150	2.08	3.60
392	200	1.80	3.11
482	250	1.60	2.77
572	300	1.44	2.49
662	350	1.33	2.30

[a]For more information, consult Baseline Rock Properties, ORNL/TM-3614-7.

Table 5. Assumed ambient formation temperatures[a]

Depth below earth's surface		Temperature	
ft	m	°F	°C
0	0	59.0	15.0
400	120	63.0	17.2
750	230	72.5	22.5
1100	335	74.0	23.3
3500	1070	124	51.1
4000	1220	135	57.2
8000	2440	212	100

[a]See R. L. Bradshaw and W. C. McClain, Project Salt Vault: A Demonstration of the Disposal of High-Activity Solidified Wastes in Underground Salt Mines, ORNL-4555 (1971).

ORNL DWG 80-216

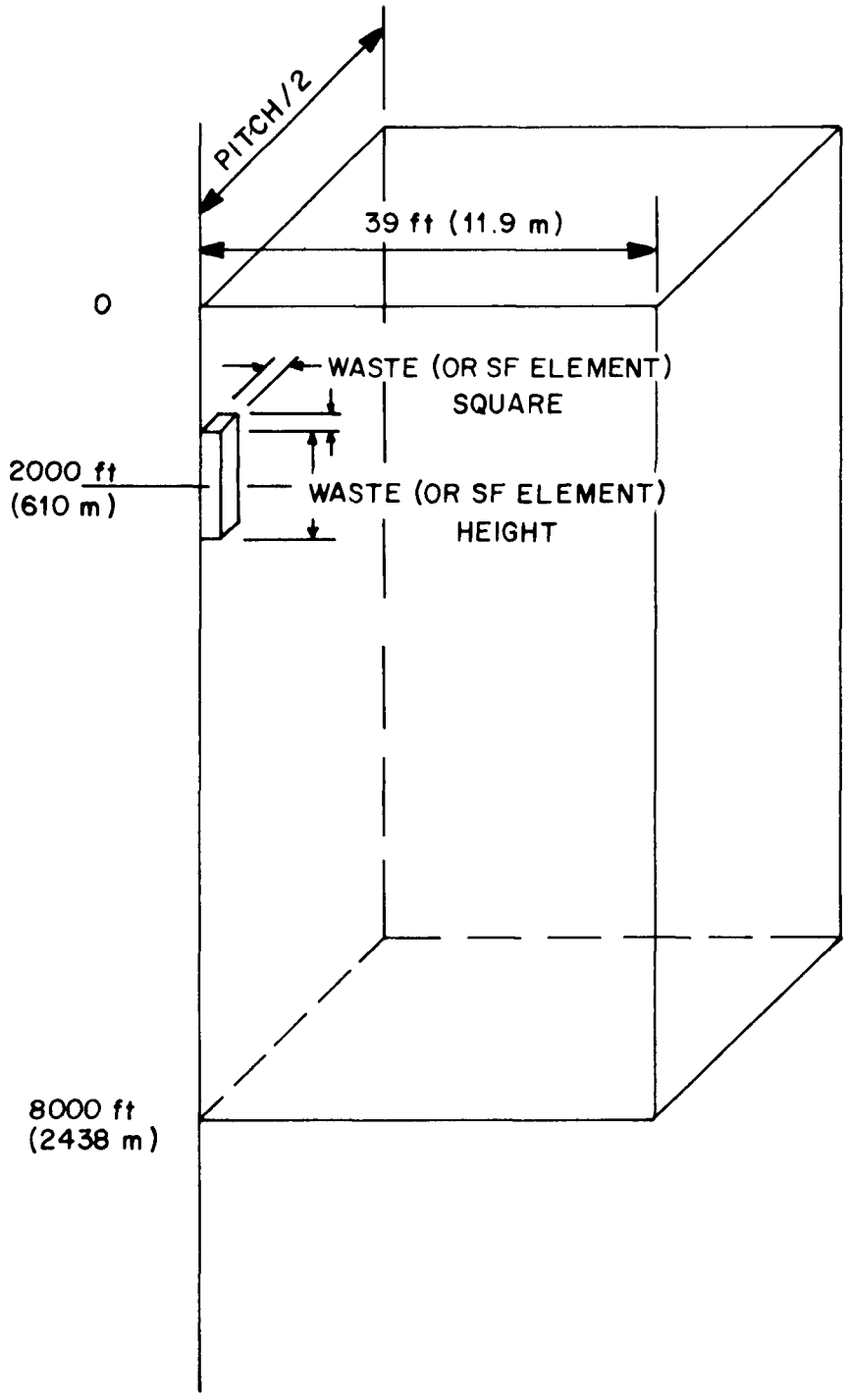

Fig. 1. The three-dimensional unit-cell near-field model.

between the row of canisters. Because of axial symmetry in the plane of the room floor, only one-quarter of the cell is required in the calculation. The vertical limits are isothermal boundaries at the surface of the earth and at a depth sufficiently far from the disposal horizon so as to have no significant effect on the near-field temperatures. Because the region boundaries must lie along coordinate surfaces in finite-difference calculations, the emplacement hole was modeled as a right parallelepiped whose cross-sectional area is equal to that of the circular emplacement hole. The heat source was considered to be uniformly distributed throughout the volume of the parallelepiped. Errors in the temperature of in the salt introduced by these approximations are not significant.

The temperatures in the waste-package emplacement hole will not be correctly predicted with the model; consequently, a second axisymmetric model (2-D, R-Z geometry) was used (see Fig. 2). Details of the waste package dimensions used in the calculations for both HLW and SF are shown in Figs. 3 and 4, respectively, and in Table 6. This model is used to calculate the maximum temperature increases from the rock to the canister for HLW and SF and from the canister to the centerline for HLW. The centerline temperature calculations for SF required a special technique involving radiative, convective, and conductive heat transfer among pins of a SF assembly. This is described in Appendix B. An adiabatic boundary condition was applied at the outer radius of the unit cell to account for the influence of the other canisters of the array. The value of outer radius was selected based on producing a unit cell equal in cross-sectional area to the 3-D unit cell of Fig. 1.

The results of the calculations for axisymmetric and 3-D unit cells can be combined to obtain the expected near-field temperature environment. Since the axisymmetric unit cell contains the temperature differentials that occur from the waste centerline to the canister surface and from the canister surface across the engineered barrier, these temperature differentials can be added to the salt temperatures obtained from the 3-D unit cell to obtain the expected thermal environment. Since the axisymmetric unit cell is a cylindrical geometry and the 3-D unit cell is a Cartesian geometry, special care must be taken to match the temperatures at the interface of the two unit cells.

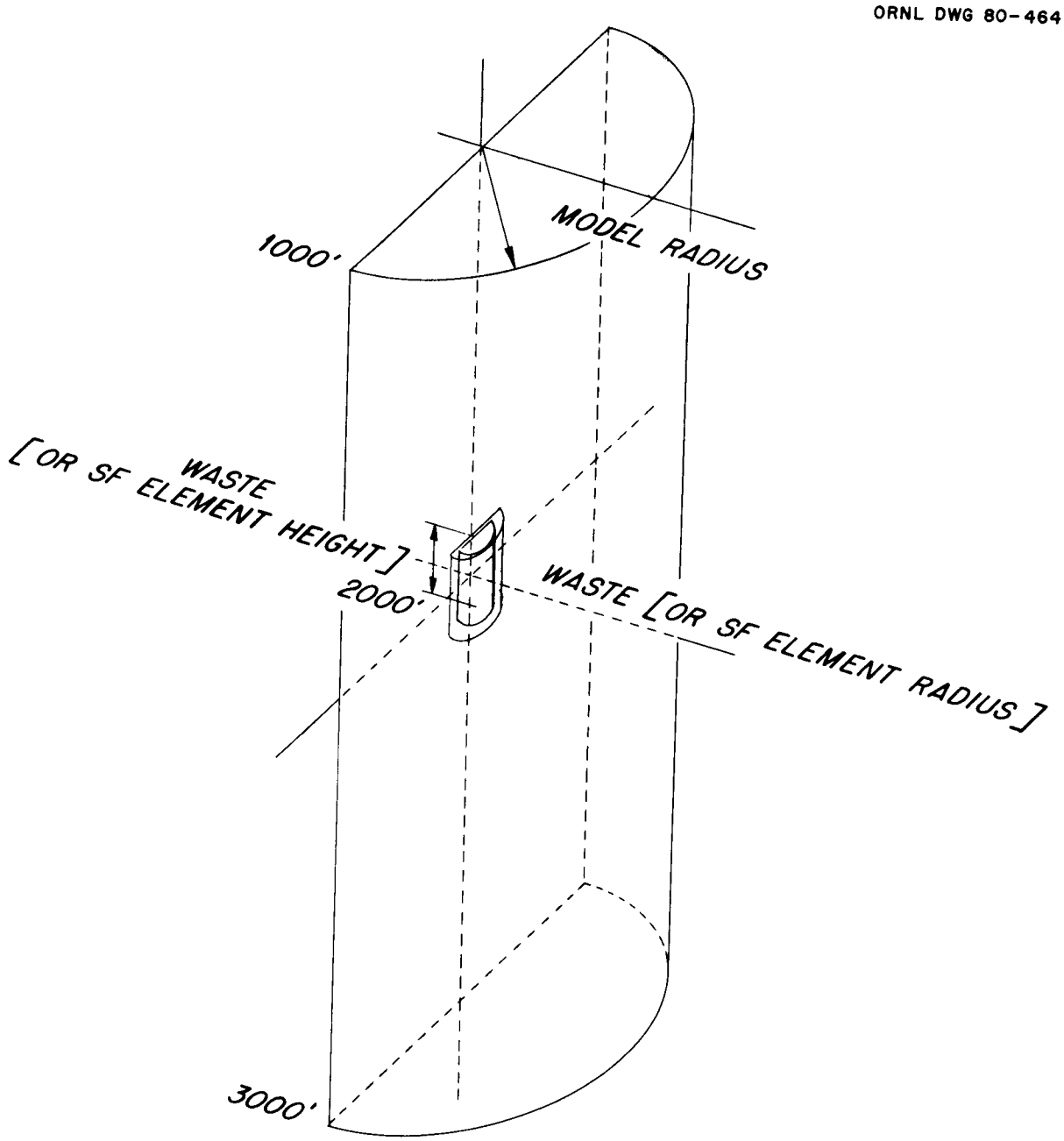

Fig. 2. The axisymmetric unit-cell near-field model.

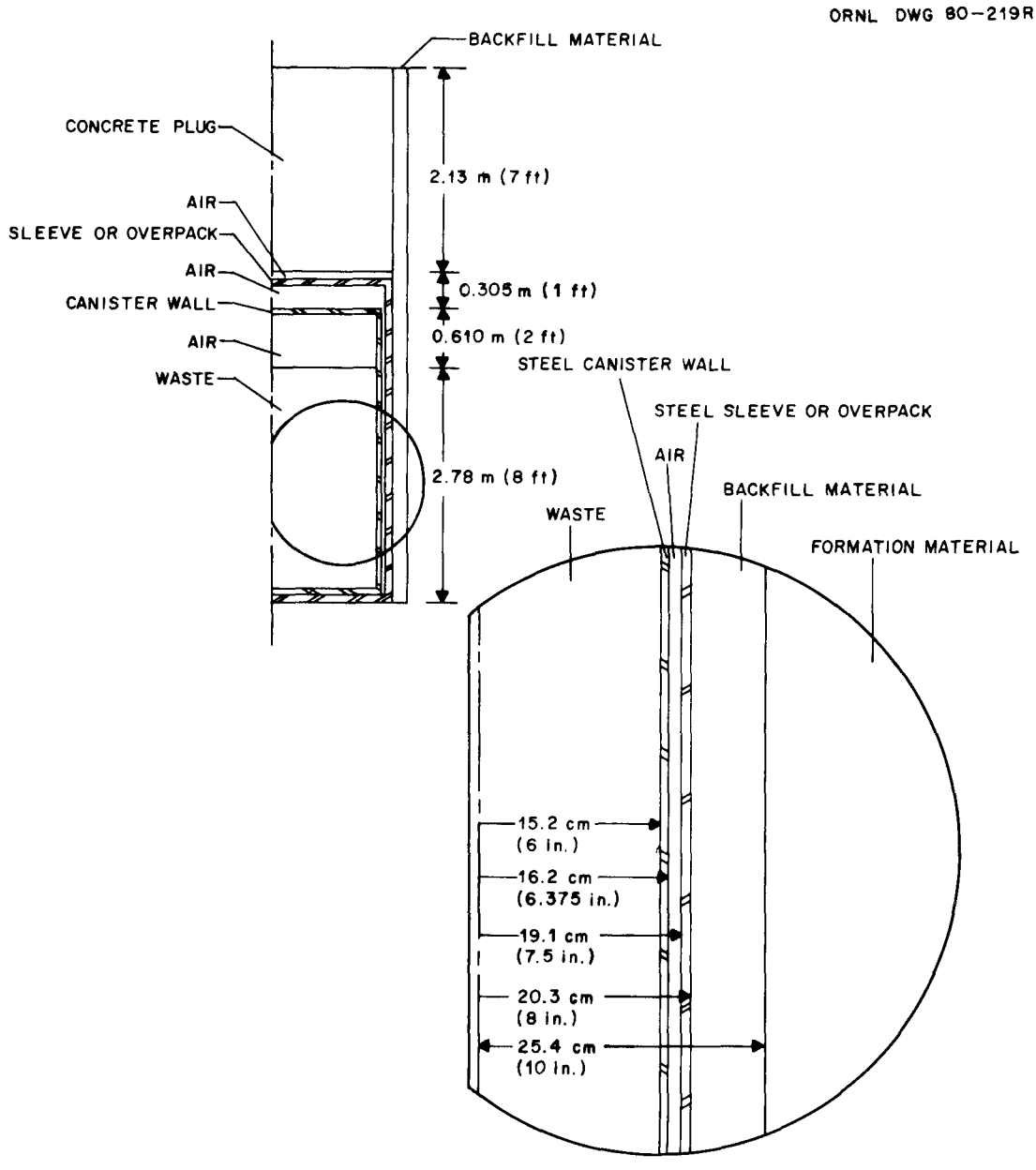

Fig. 3. Details of a waste package for high-level waste.

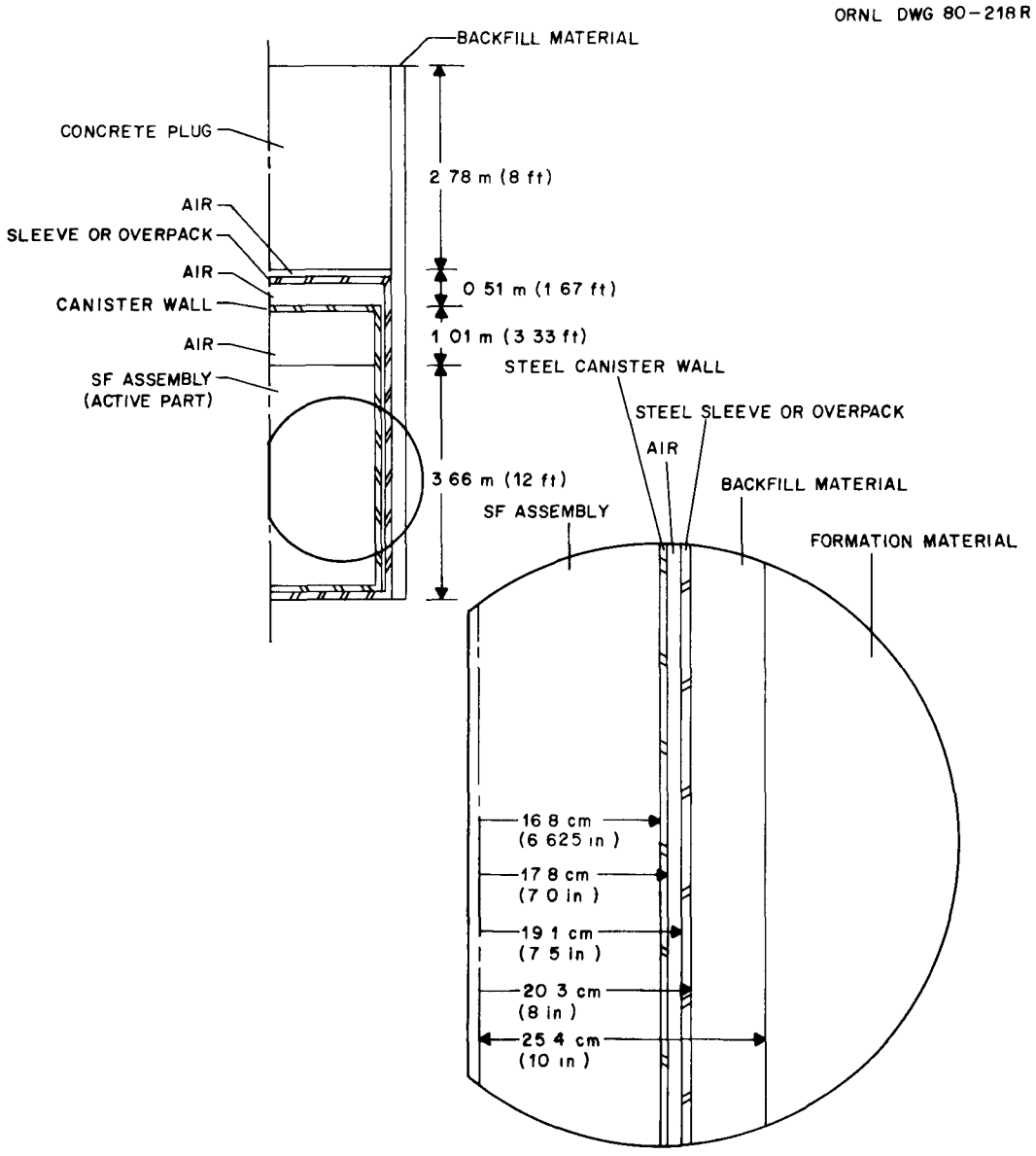

Fig. 4. Details of a waste package for spent fuel.

Table 6. Canister and overpack characteristics

Characteristics	High-level waste	Spent fuel
Canister dimensions		
Outer diameter, in. (cm)	12.7 (32.4)[a]	14.0 (35.6)[b]
Inner diameter, in. (cm)	12 (30.5)	13.25 (33.7)
Wall thickness, in. (cm)	0.375 (0.953)	0.375 (0.953)
Overall length, ft (m)	10 (3.05)	15.33 (4.67)
Active length, ft (m)	8 (2.44)	12 (3.66)
Active volume of waste, ft^3 (m^3)	6.28 (0.160)	
Filler in canister	Air	Air
Canister protective sleeve (or overpack) dimensions		
Outer diameter, in. (cm)	16 (40.6)[c]	16 (40.6)[c]
Inner diameter, in. (cm)	15 (38.1)	15 (38.1)
Wall thickness, in. (cm)	0.5 (1.27)	0.5 (1.27)
Overall length, ft (m)	11 (3.35)	16.5 (5.03)
Materials		
Canister	304L stainless steel	Carbon steel
Overpack	Carbon steel	Carbon steel
Backfill between sleeve and salt	Crushed salt	Crushed salt
Plug in top of drill hole	Concrete	Concrete

[a]Standard 12-in.-diam schedule 40 pipe.

[b]Standard 14-in.-diam schedule 30 pipe.

[c]Standard 16-in.-diam schedule 40 pipe.

2.1.2 Expected maximum salt, canister, and waste temperatures

The expected maximum salt temperatures calculated for the HLW and SF baseline repositories are shown in Fig. 5 as temperature histories. The salt temperature for HLW peaks at 412°F (211°C) ∿15 yr after emplacement, and the SF salt temperature peak occurs ∿50 yr after emplacement at 211°F (99°C). The dependence on the loading density or the separation between canisters is also shown in Fig. 5. If the HLW loading density is decreased to 100 kW/acre (24.7 W/m^2), the maximum salt temperatures decrease by 100°F (42°C), and an additional loading density decrease to 50 kW/acre (12.4 W/m^2) causes another 75°F (42°C) decrease in the maximum salt temperature. The maximum salt temperature and the years after emplacement where the peak temperature occurs are shown in tabular form in Table 7.

A second important quantity is the maximum temperature of the canister wall itself. It is desirable that the canister remain intact throughout the retrievability period, and, for this purpose, it is of interest to know the temperatures and pressures encountered in the barrier region. Temperature histories of the canister wall at the midplane level (which is essentially the maximum) are shown in Fig. 6. Temperatures are elevated above those of the surrounding rock because of the insulating effect of any low-conductivity backfill material and because of the gap between the canister and protective sleeve or overpack. For the design considered, canister, overpack, and crushed salt backfill with a conductivity equal to 10% of the salt conductivity is designated as the engineered barrier. The backfill is taken to be 2 in. (5.08 cm) thick. For this case, the maximum HLW canister temperature is 587°F (308°C) and occurs ∿10 yr after emplacement; the peak is broad, however, with sustained temperatures for 5 yr or more. For SF, the maximum canister temperature is 237°F (114°C) and occurs ∿25 yr after emplacement, with the broad peak characteristic of the SF. If the HLW loading is decreased by 33% to 100 kW/acre (24.7 W/m^2), the temperature is decreased by nearly 80°F (44°C) and occurs ∿3 yr after emplacement. A further decrease of the HLW loading to 50 kW/acre (12.4 W/m^2) causes the temperatures to decrease by 50°F (28°C) <1 yr after emplacement. This indicates

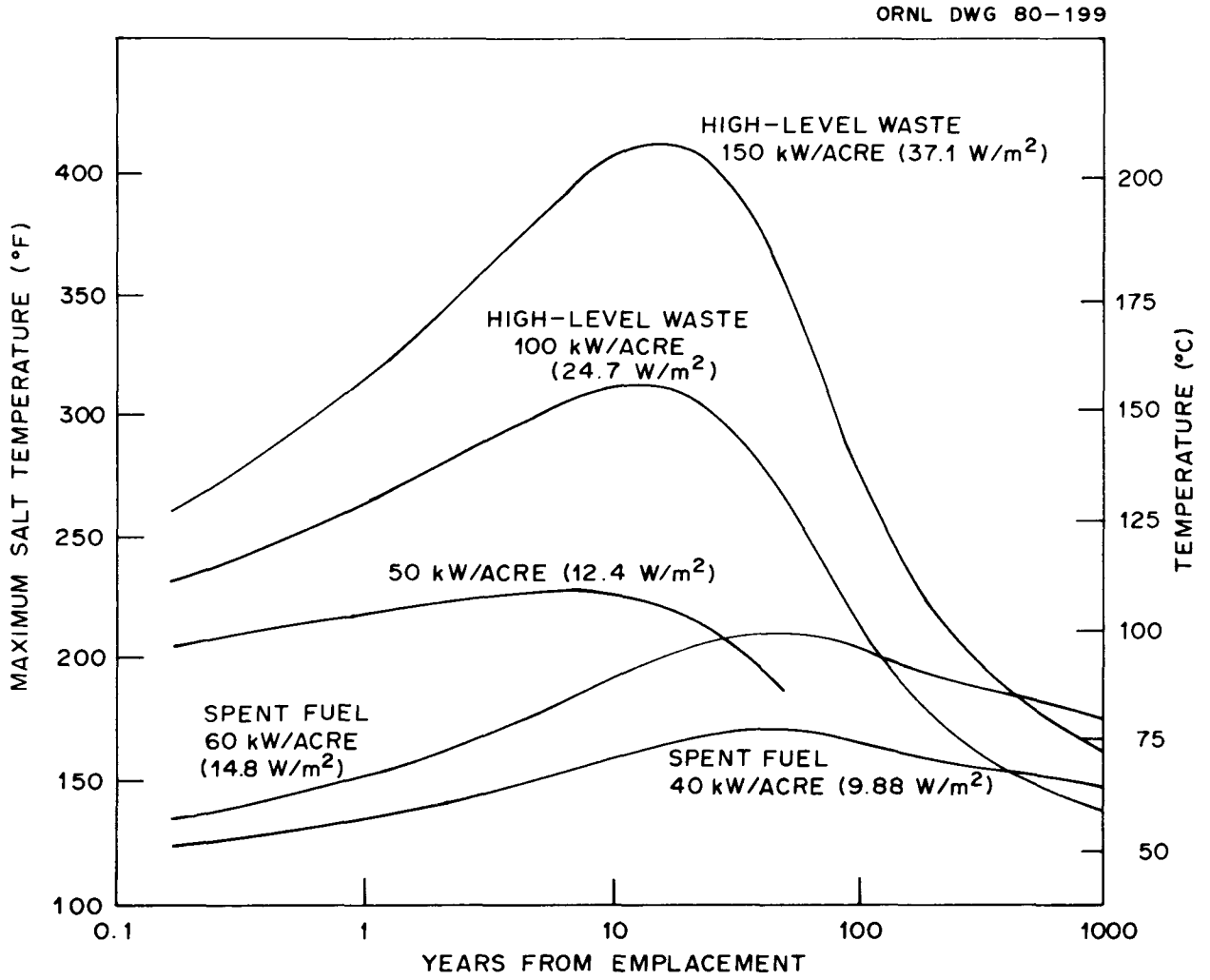

Fig. 5. Maximum salt temperature histories.

Table 7. Maximum temperatures in the salt rock formation, canister surface, and waste centerline[a]

	Salt			Canister surface			Waste centerline (or center pin)		
	Maximum temperature		Years after emplacement	Maximum temperature		Years after emplacement	Maximum temperature		Years after emplacement
	°F	°C		°F	°C		°F	°C	
HLW, 150 kW/acre (37.1 W/m^2)	412	211	15	587	308	10	670	354	3
HLW, 100 kW/acre (24.7 W/m^2)	312	156	15	508	264	3	603	317	1.5
HLW, 50 kW/acre (12.4 kW/m^2)	228	109	5	459	237	0.67	580	304	0.5
SF, 60 kW/acre (14.8 W/m^2)	211	99	50	237	113	25	280	138	~5
SF, 40 kW/acre (9.88 W/m^2)	171	77	50	202	94	15	270	132	~3

[a]Assumes that waste is 10 yr old on emplacement. The HLW decay rates were based on fuel that is a 3:1 mix of fresh UO_2 and MOX fuels. The HLW canister thermal loading was 2.16 kW, and the SF was 0.55 kW (one PWR fuel element).

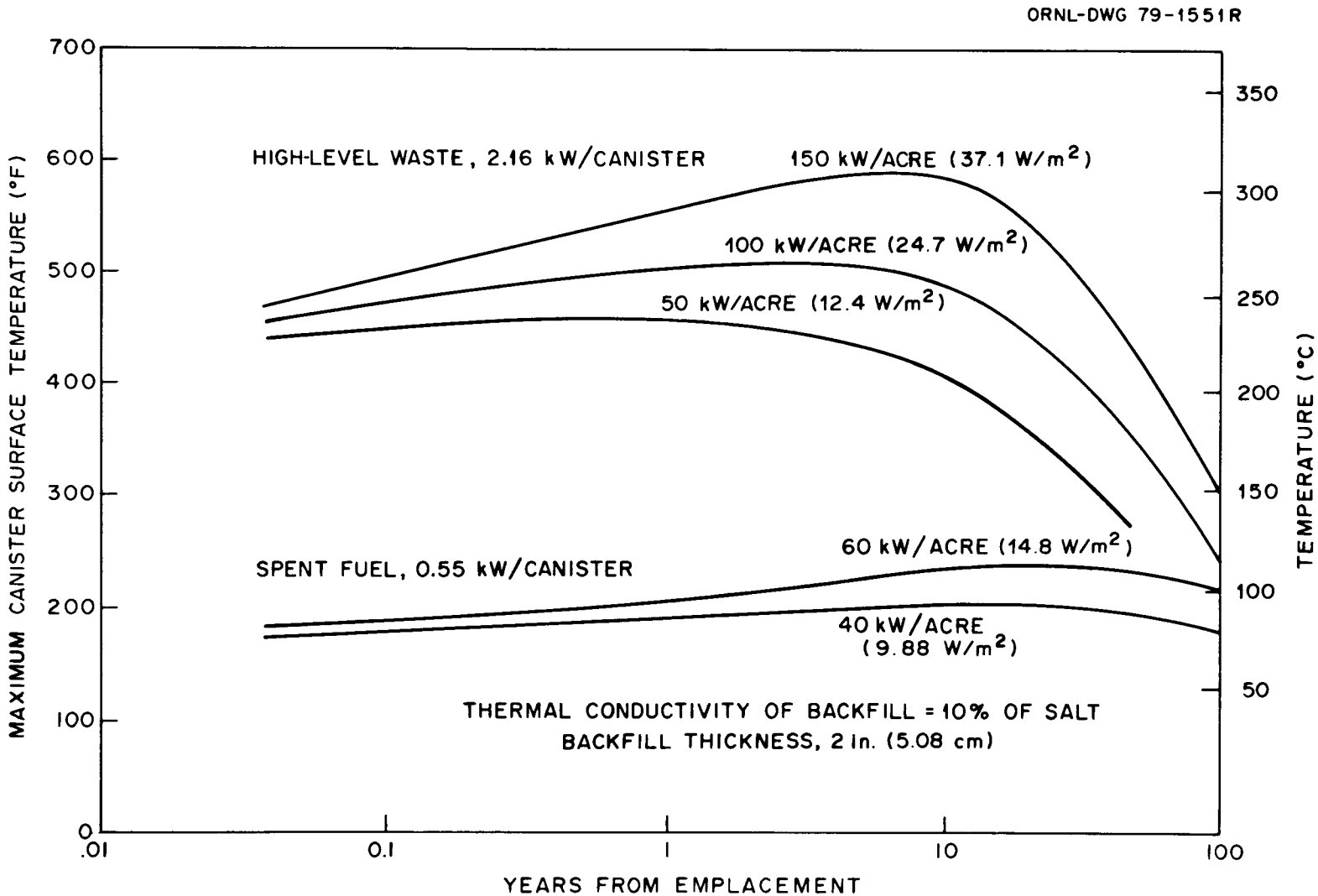

Fig. 6. Maximum temperature histories for the canister surface.

a slightly smaller dependency on the areal heat load for the canister surface temperatures than for the maximum salt temperatures. If the SF loading is reduced to 40 kW/acre (9.88 W/m^2), the canister surface temperature is decreased by >30°F (17°C), and this peak temperature occurs ∿15 yr after emplacement. The canister surface temperatures and the years after emplacement where the peak temperature occurs are shown in Table 7.

Maximum temperature criteria may also be applied to temperatures in the waste or SF assemblies. In addition, it is of interest to know these variables in order to estimate the performance of the waste matrix or SF cladding and pellets. Figure 7 gives the histories for the maximum HLW temperatures and for the center pin in the SF assembly. For HLW, the maximum calculated waste temperature is 670°F (354°C), occurring at ∿3 yr after emplacement. This is reduced by nearly 75°F (42°C) when the areal loading is decreased to 100 kW/acre (24.7 W/m^2), with the peak temperature now occurring at 1.5 yr. A further reduction to 50 kW/acre (12.4 W/m^2) decreases the waste centerline temperature by 40°F (22°C), with the peak temperature now occurring after 0.5 yr. For SF, the cladding of the center pin has a maximum temperature of 280°F (138°C), which is reduced by 10°F (6°C) when the areal loading is reduced to 40 kW/acre (9.88 W/m^2). In these calculations, the gas filler in the canister is assumed to be air (modeled as nitrogen), and free convection is allowed to take place. The internal convective cooling is relatively important and reduces the temperature from canister to center pin by >50%. The waste centerline temperature and the years after emplacement where the peak occurs are shown in Table 7.

2.2 Sensitivity Studies

The thermal parameters used for the baseline repositories are based somewhat on previous concepts. Such design parameters as the areal heat load, the canister heat load, the backfill material, the barrier thickness, and the time of canister backfill may vary as the design of a repository progresses. It is therefore desirable to determine the effect of a change in the above parameters from the values used in the previous section.

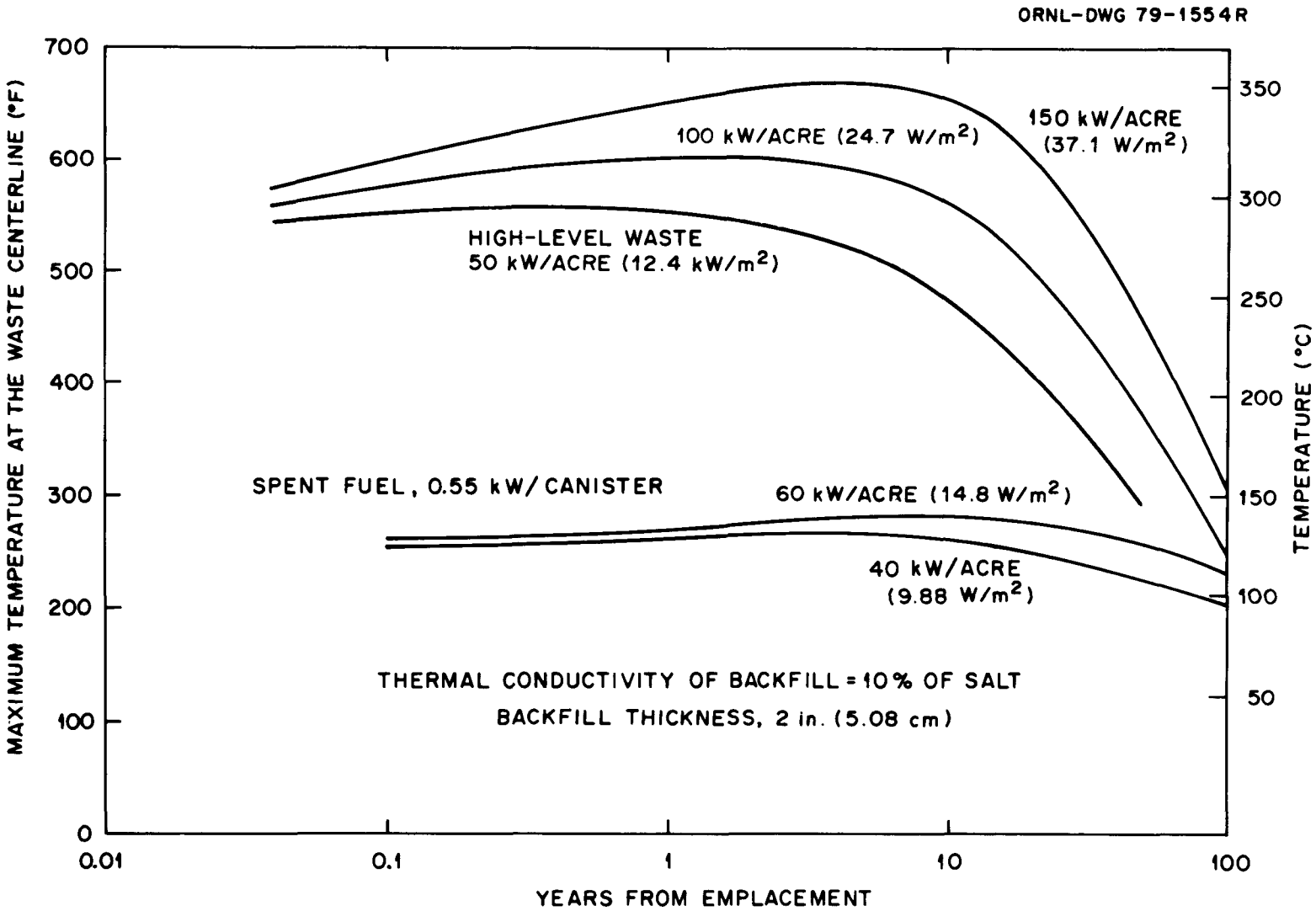

Fig. 7. Maximum temperature histories for waste centerline and spent fuel assembly.

2.2.1 Canister and areal heat load

Two important parameters in the design of a repository are the canister and areal heat loads. In the previous section, the canister heat loads for HLW was specified as 2.16 kW/canister. Different packing densities could result in a different canister heat load. Figures 8, 9, and 10 show the variation of the maximum temperatures for the salt, waste centerline, and canister surface, respectively, as a function of the canister heat load for the HLW with an areal heat load of 150 kW/acre (37.1 W/m^2). Figures 11 and 12 show the effect of the variation of the canister heat load for SF on the maximum salt and canister temperatures, respectively, for an areal heat load of 60 kW/acre (14.8 W/m^2). As expected, the effect of a decreasing canister heat load is to reduce the maximum temperatures. This decrease is much more dramatic during the early years after emplacement, particularly for the HLW.

The variation of the maximum salt, canister surface, and the waste centerline (or center pin) temperatures vs areal heat load for HLW at 2.16 kW/canister and SF at 0.55 kW/canister is shown in Figs. 13 through 18. The trend of decreasing temperature with decreasing areal heat load in the temperature is the same as that shown for canister heat load, but the effect becomes more pronounced in the case of canister surface temperature and center pin temperatures for SF (Figs. 17 and 18) as the years after emplacement increase.

2.2.2 Backfill thermal conductivity and barrier thickness

All of the previous analyses have been made for a single design concept for the structure surrounding the canister; that is, an overpack around the canister is backfilled with crushed salt which is assumed to have a thermal conductivity equal to 10% of the original salt. Other design concepts are of interest, and these alternatives may have different heat transfer properties. For example, engineered barriers that prevent water intrusion into the canister hole or delay nuclide migration from the emplacement hole may be used. The thermal environment within the interior of the barrier is very sensitive to the barrier material properties. This fact is illustrated in Fig. 19, where temperature profiles are shown for four distinct barrier designs. The case shown is

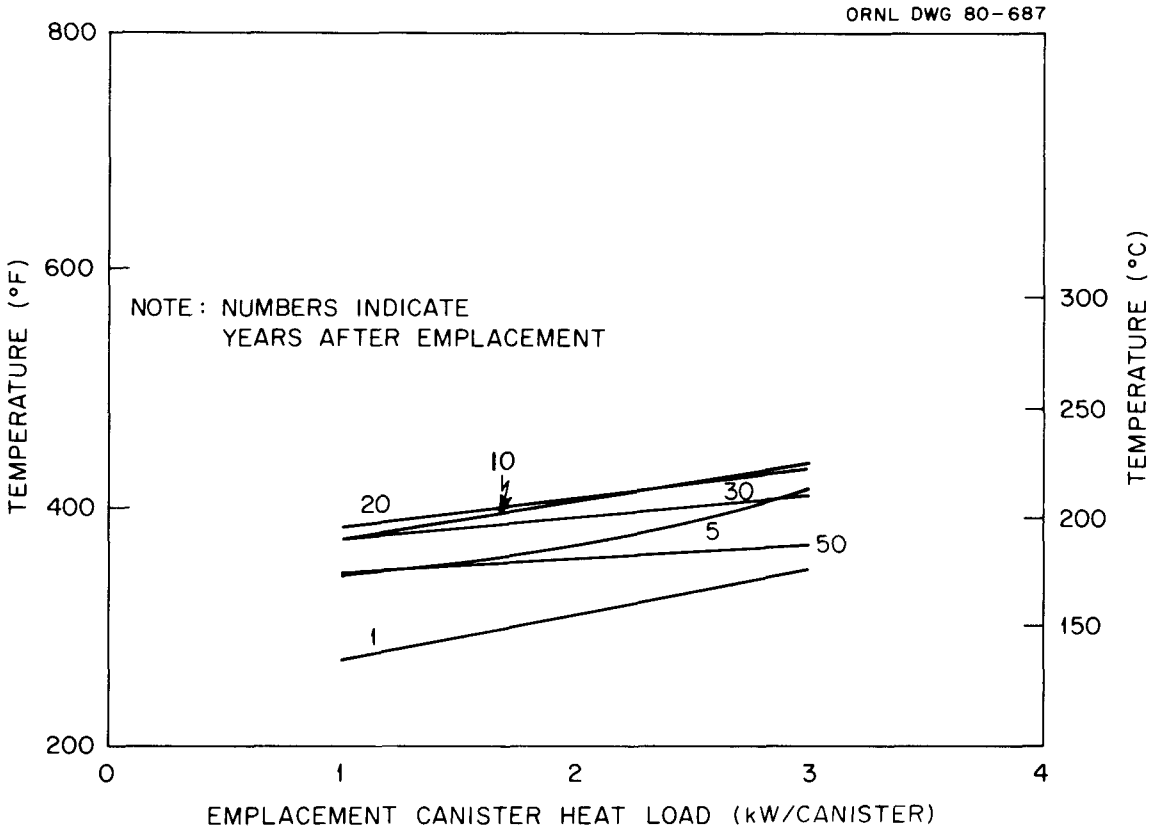

Fig. 8. Maximum salt temperature vs canister heat load for high-level waste for an areal heat load of 150 kW/acre (37.1 W/m^2).

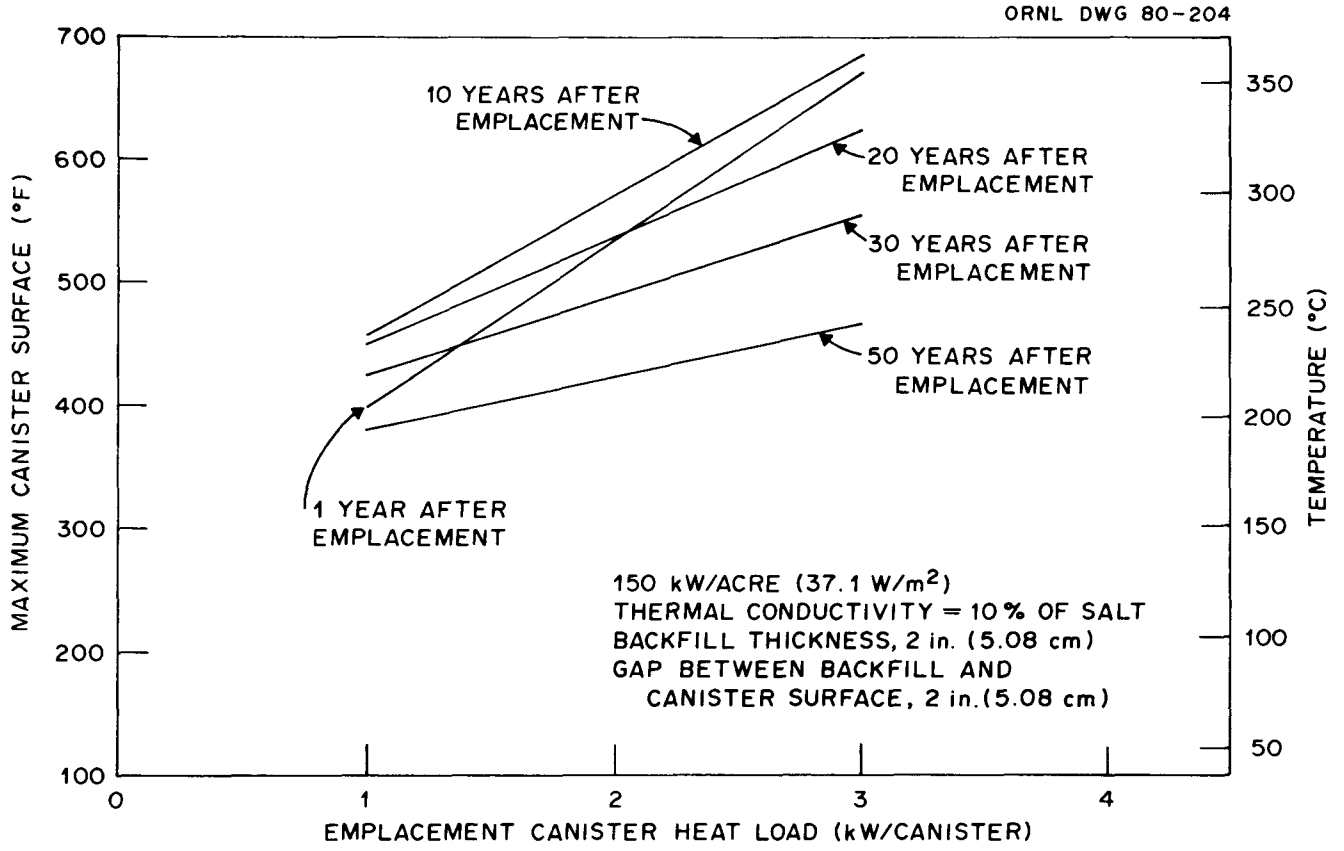

Fig. 9. Maximum canister surface temperature vs canister heat load for high-level waste for an areal heat load of 150 kW/acre (37.1 W/m^2).

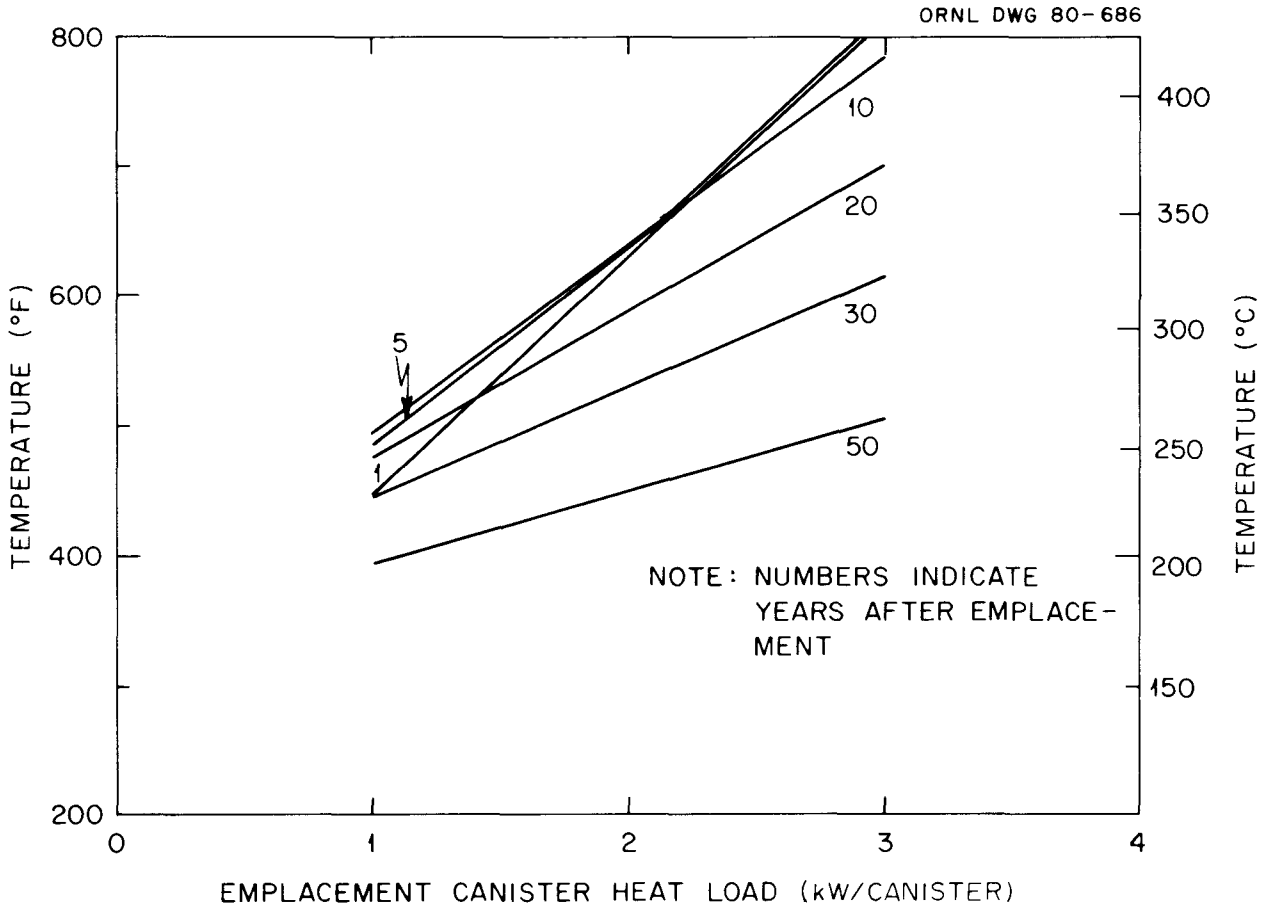

Fig. 10. Maximum waste centerline temperature vs canister heat load for high-level waste for an areal heat load of 150 kW/acre (37.1 W/m^2).

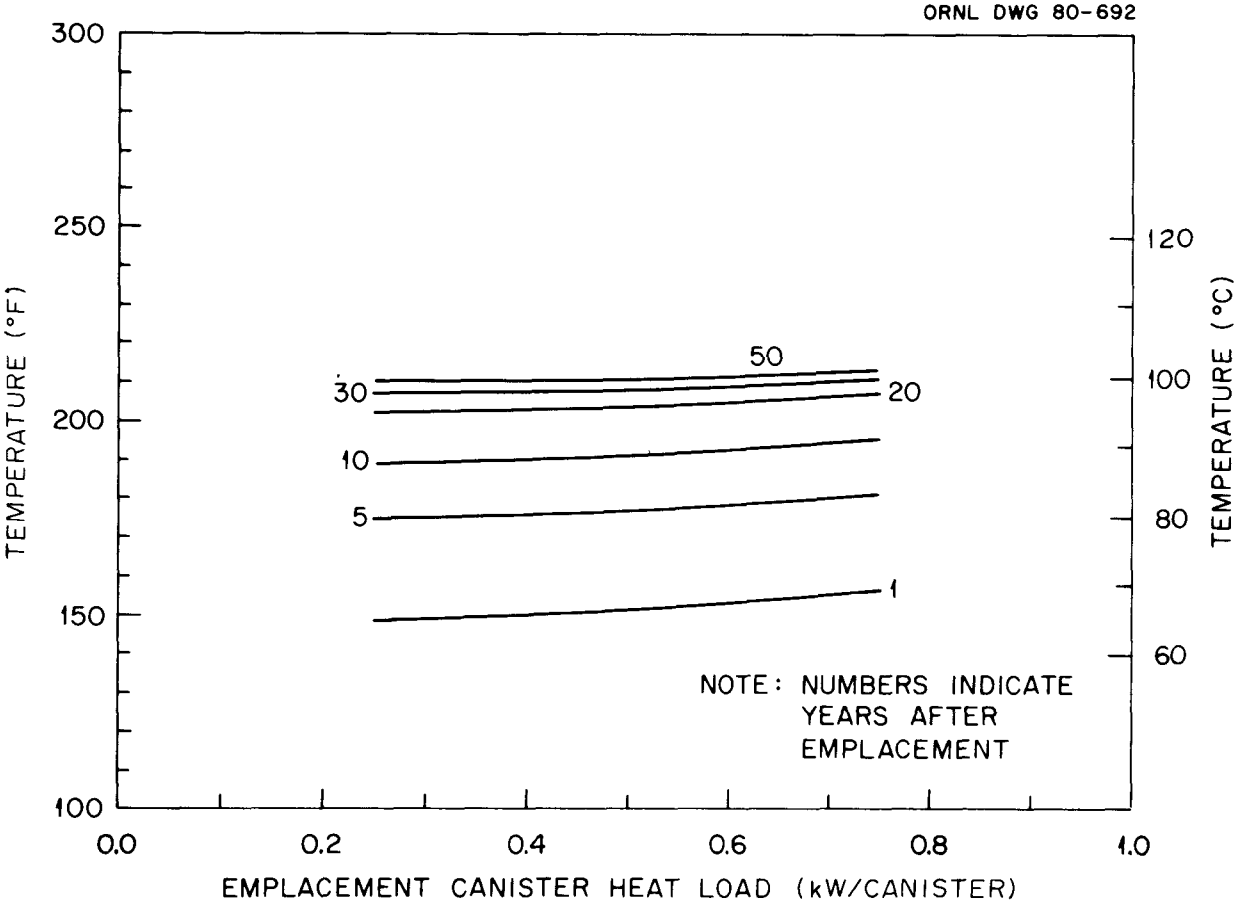

Fig. 11. Maximum salt temperature vs canister heat load for spent fuel for an areal heat load of 60 kW/acre (14.8 kW/m^2).

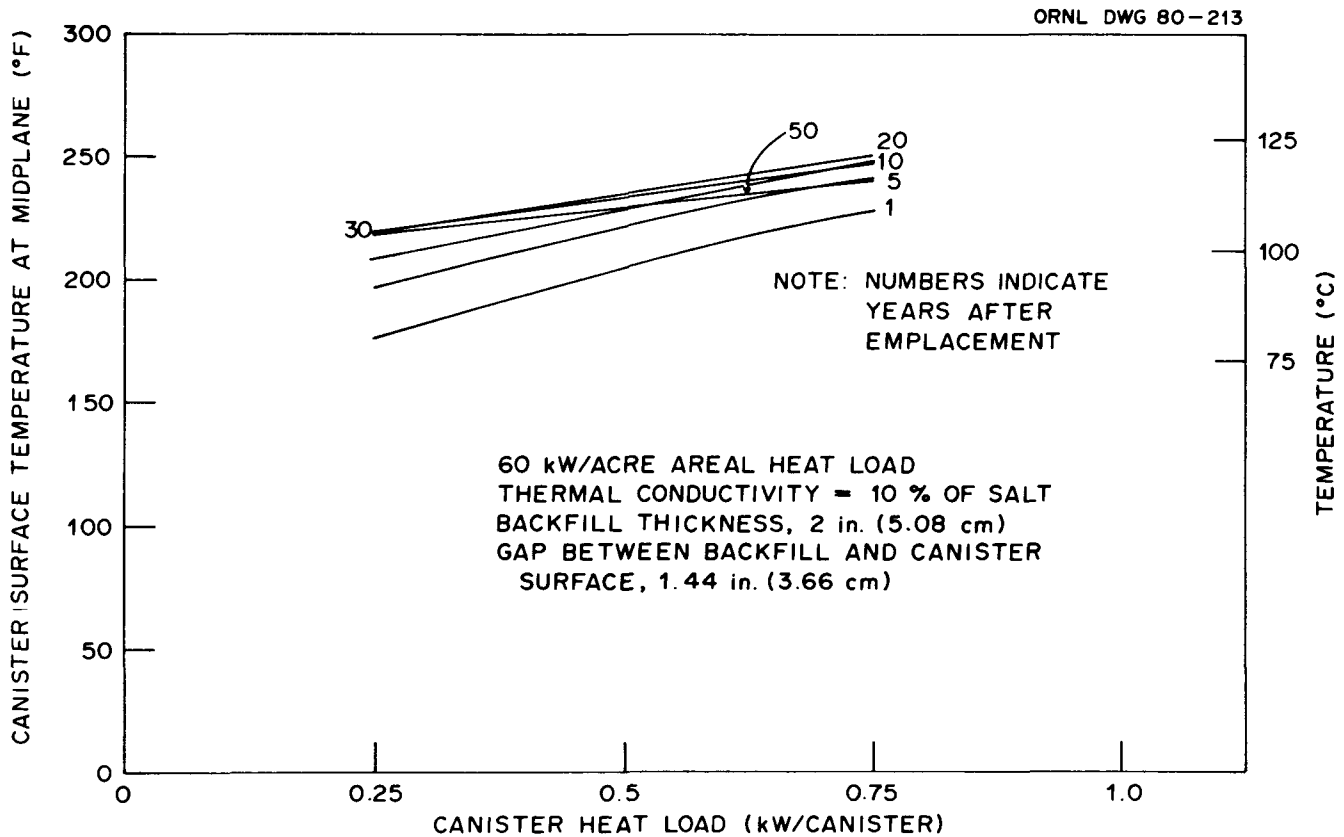

Fig. 12. Maximum canister surface temperature vs canister heat load for spent fuel for an areal heat load of 60 kW/acre (14.8 W/m^2).

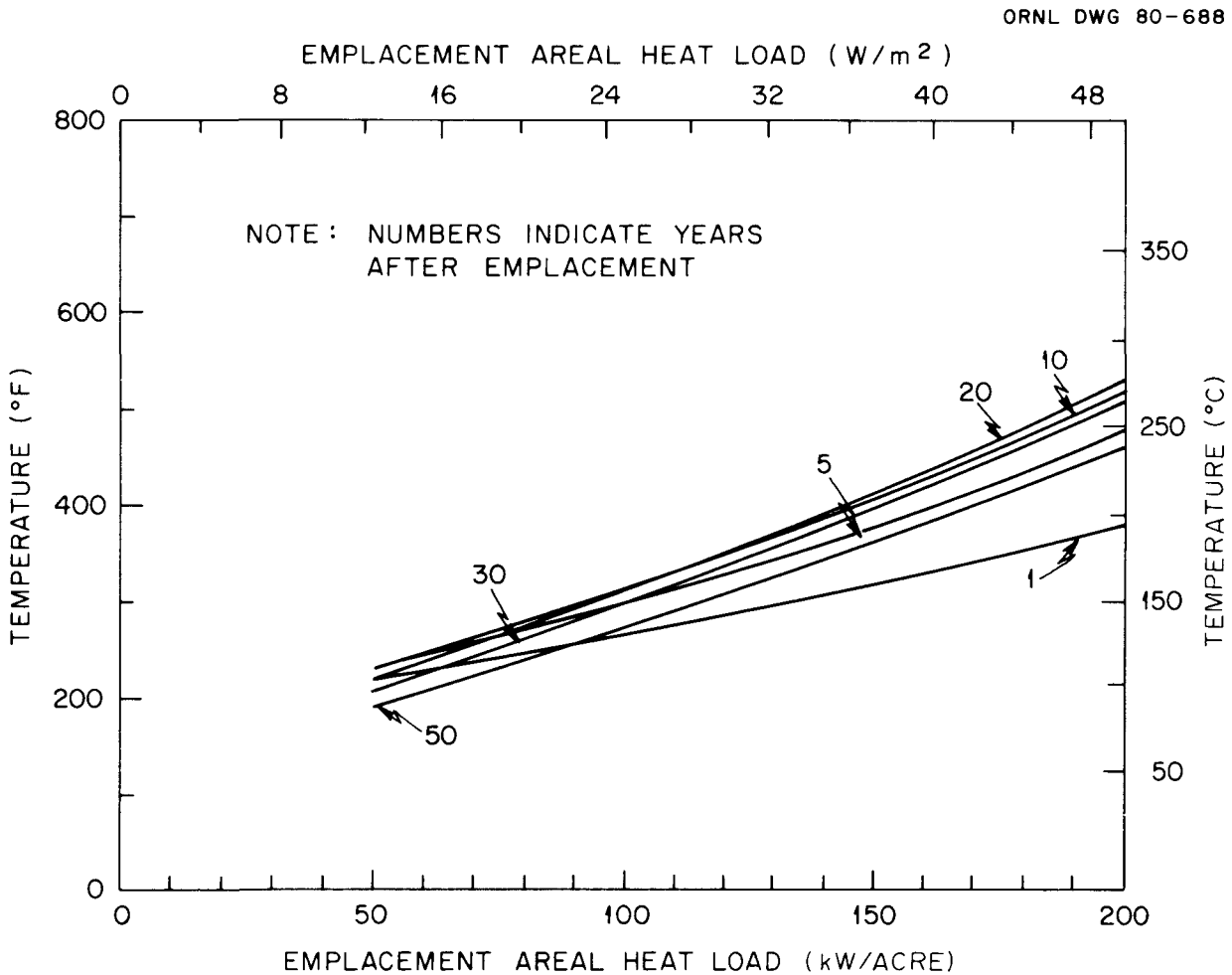

Fig. 13. Maximum salt temperature vs areal heat load for high-level waste (2.16 kW/canister).

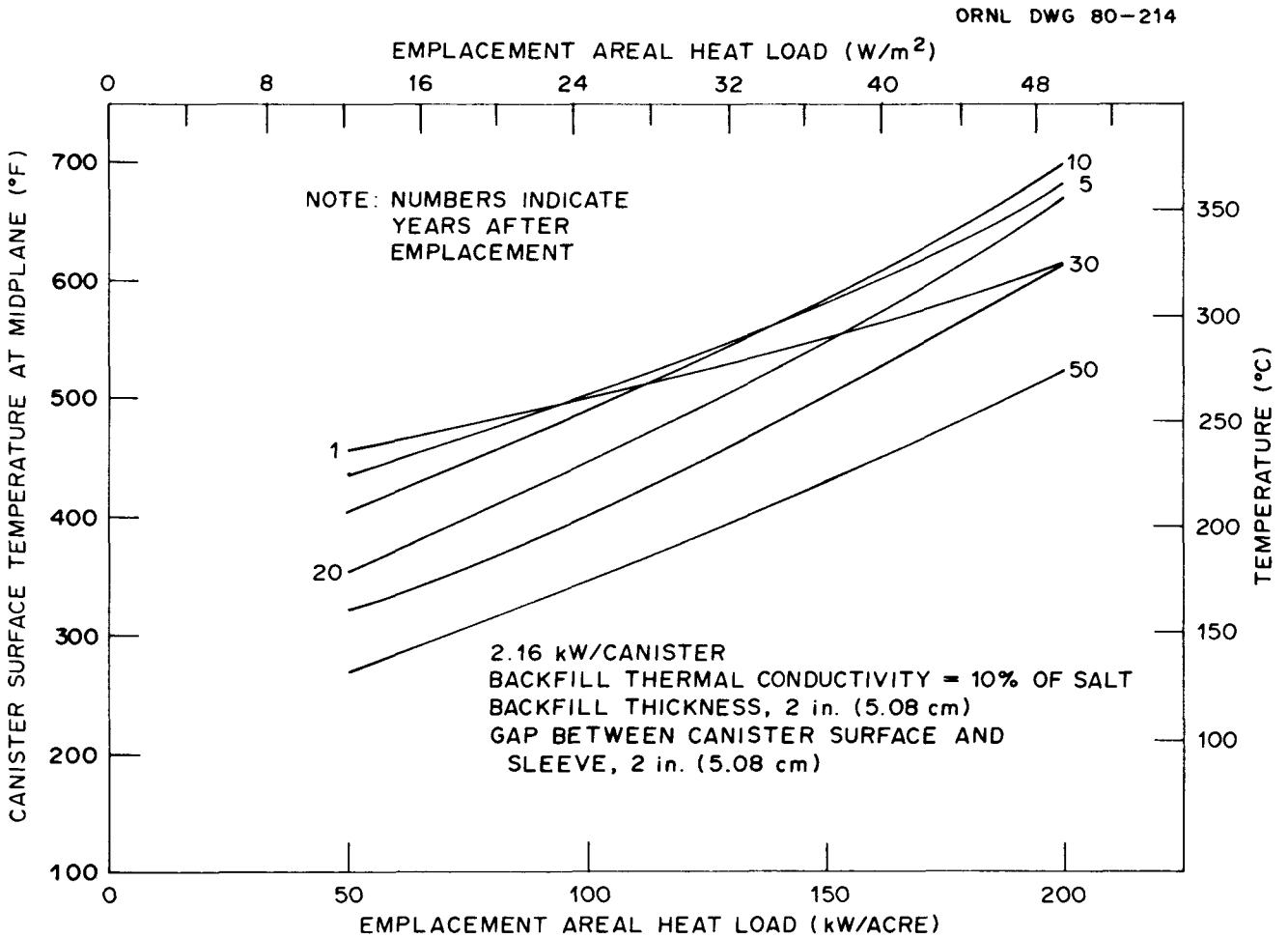

Fig. 14. Maximum canister surface temperature vs areal heat load for high-level waste (2.16 kW/canister).

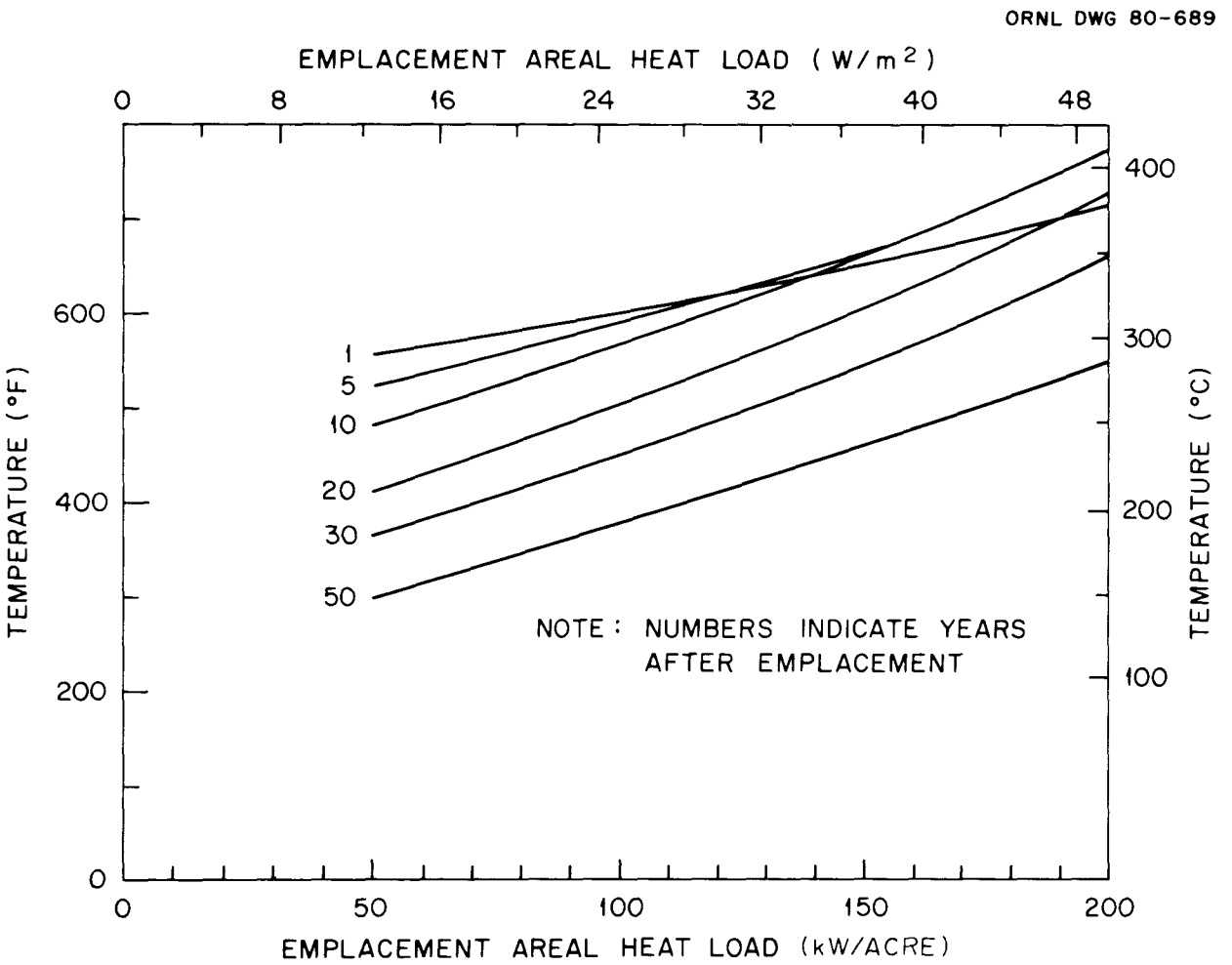

Fig. 15. Maximum waste centerline temperatures vs areal heat load for high-level waste (2.16 kW/canister).

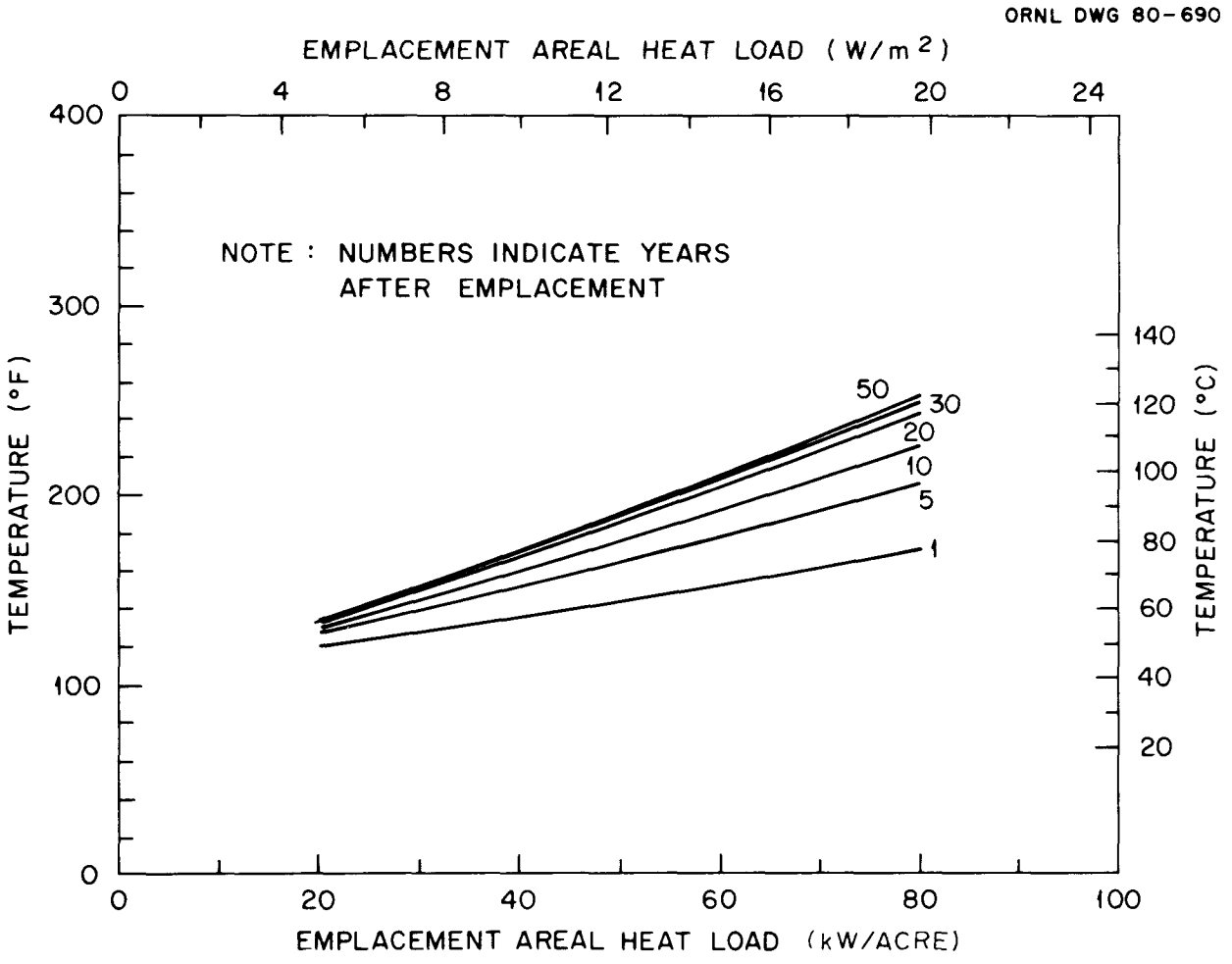

Fig. 16. Maximum salt temperatures vs areal heat load for spent fuel (0.55 kW/canister).

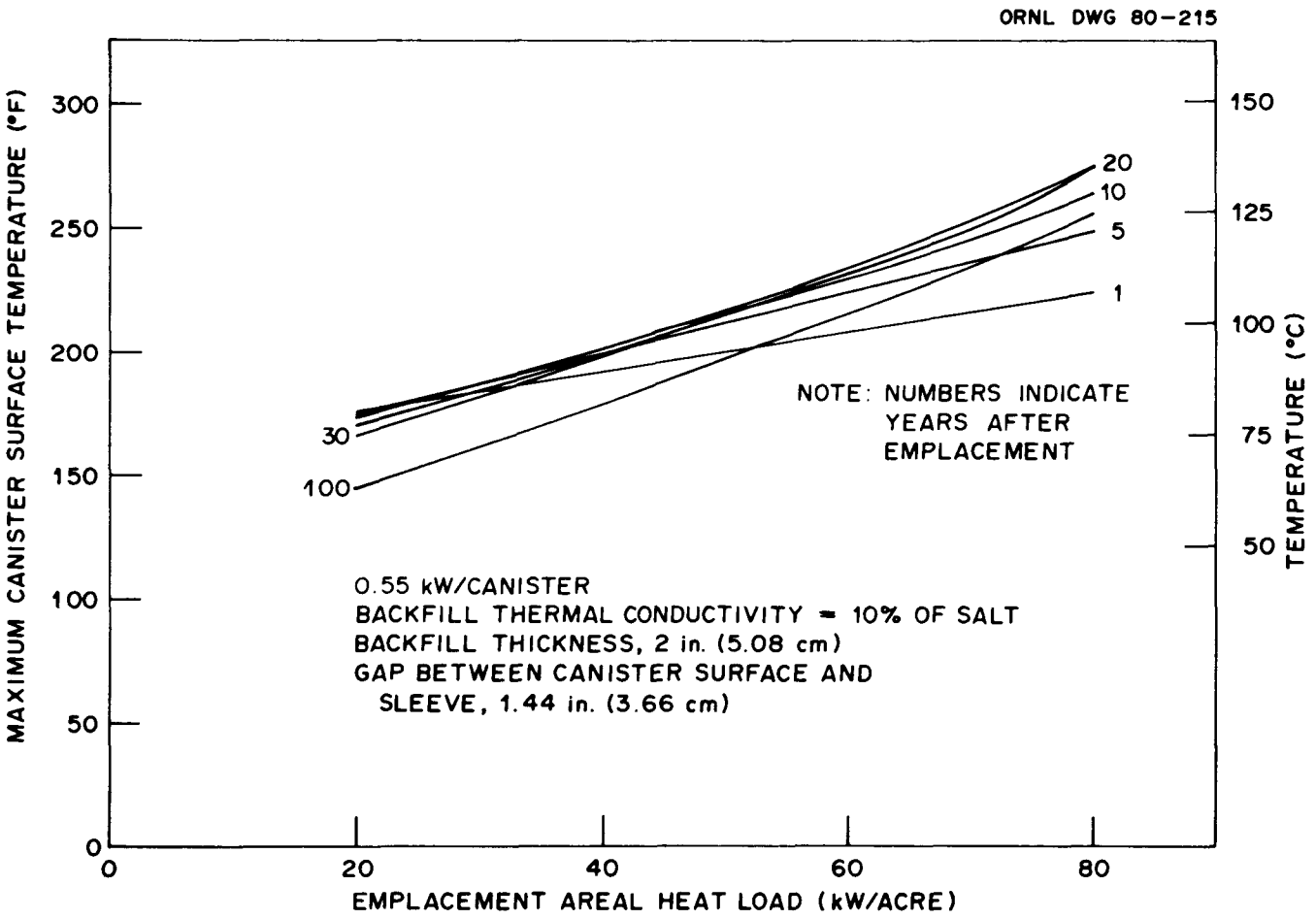

Fig. 17. Maximum canister surface temperature vs areal heat load for spent fuel (0.55 kW/canister).

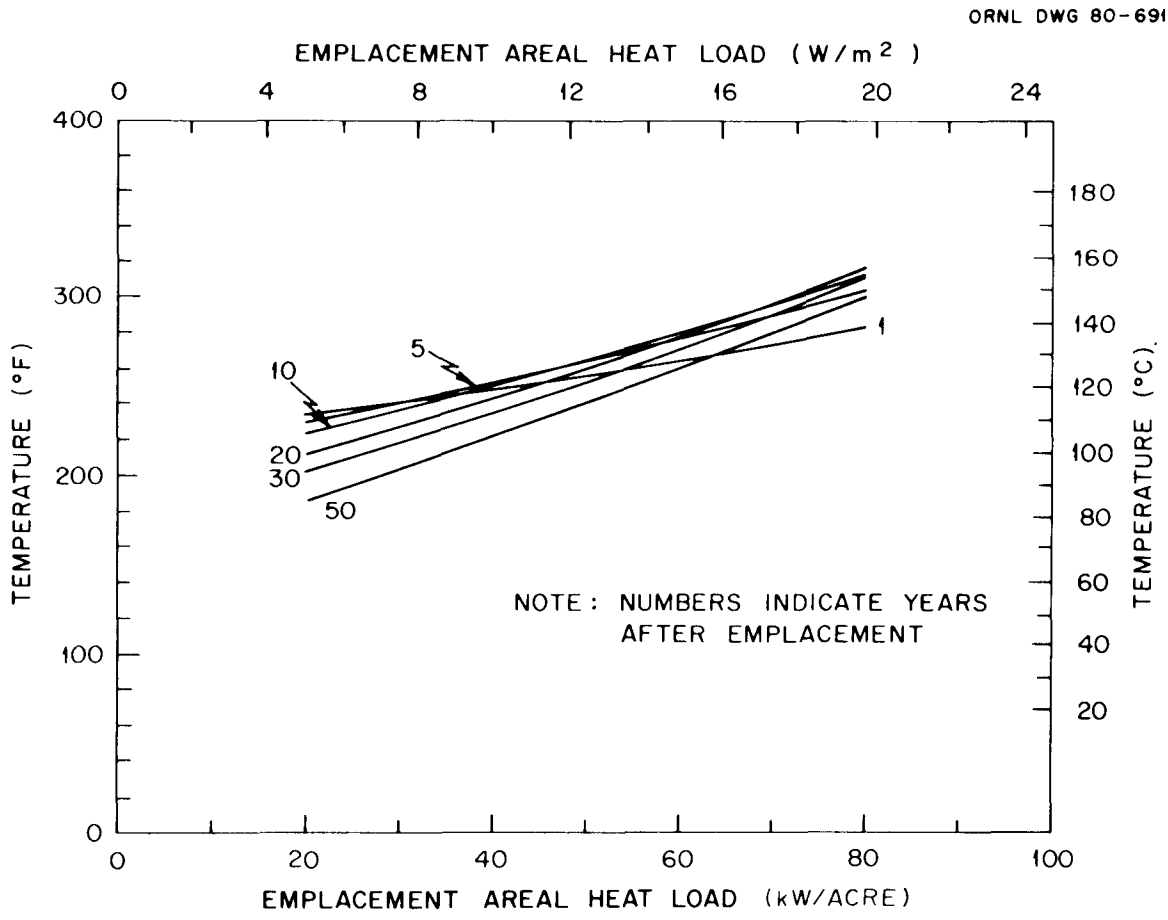

Fig. 18. Maximum temperatures vs areal heat load for spent fuel (0.55 kW/canister).

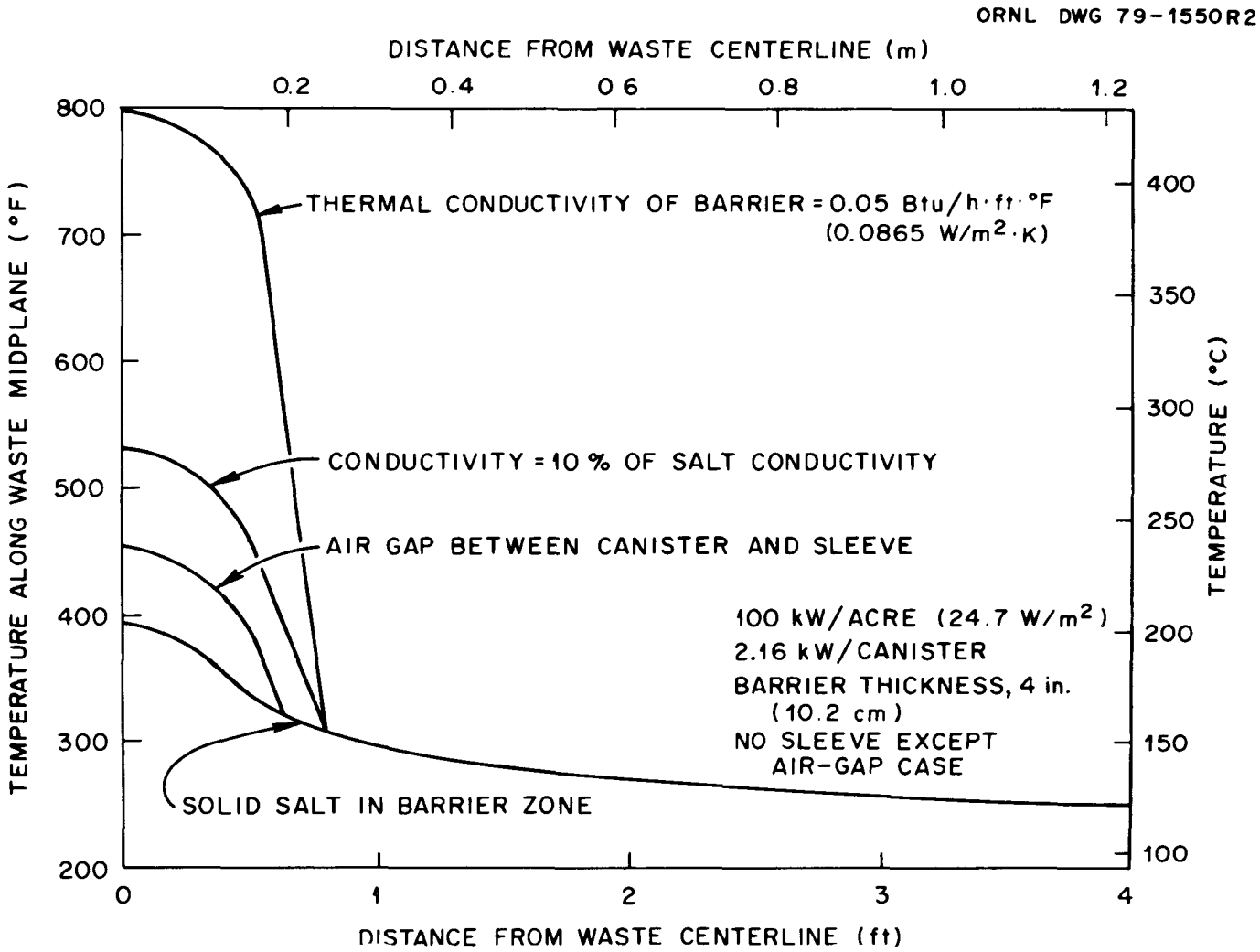

Fig. 19. Temperature vs distance from the waste centerline for high-level waste 15 yr after emplacement.

for HLW emplaced at 2.16 kW/canister and 100 kW/acre (24.7 W/m^2). This waste had been out of the reactor 10 yr and had been emplaced for 15 yr. The lowest curve gives the profile for a barrier material filling the emplacement hole between the canister and the emplacement hole wall. The canister is not overpacked. The conductivity is the same as that for the premined salt, as would occur for crushed salt which has reconsolidated to solid salt. The second curve corresponds to the result that is obtained due to a 2-in. (5.08-cm) annular gap of air in the region between the canister surface and the overpack with the backfill being solid salt. This gap causes an increase of 60°F (33°C) in the canister surface temperature. The third curve shows the effect of a barrier material that has a thermal conductivity equal to 10% of the salt conductivity and is placed in the 4-in. (10.2-cm) annulus between the canister and the emplacement hole wall; that is, there is no overpack, and the canister is backfilled with crushed salt. Note that the baseline case described earlier has a 2-in. (5.08-cm)-thick annulus and therefore differs from this case. This material results in a temperature increase of nearly 140°F (78°C) over the case with reconsolidated salt in the barrier zone. Finally, the figure shows the result of a barrier material in this region having a conductivity of 0.05 Btu/hr·°F·ft (0.0865 W/m·K). In this case, the temperature increases by >400°F (220°C). Careful consideration of these conditions needs to be made as design concepts are selected and modified.

The temperature variations caused by changes in the effective thermal conductivity are shown as a function of the reciprocal of thermal conductivity in Figs. 20 and 21. In Fig. 20, the results are shown for a 2-in. (5.08-cm)-thick backfill with an air gap between the canister surface and the backfill. The solid portions of the curves show the results of calculations, while the dashed portions give extrapolations of these curves. Approximate conductivities for prospective backfill materials such as sand, crushed salt, and bentonite are indicated in Fig. 20. Figure 21 introduces the concept of effective conductivity. In this case, the engineered barrier is not divided into an air gap and a backfill material. It is considered to be an effective barrier and

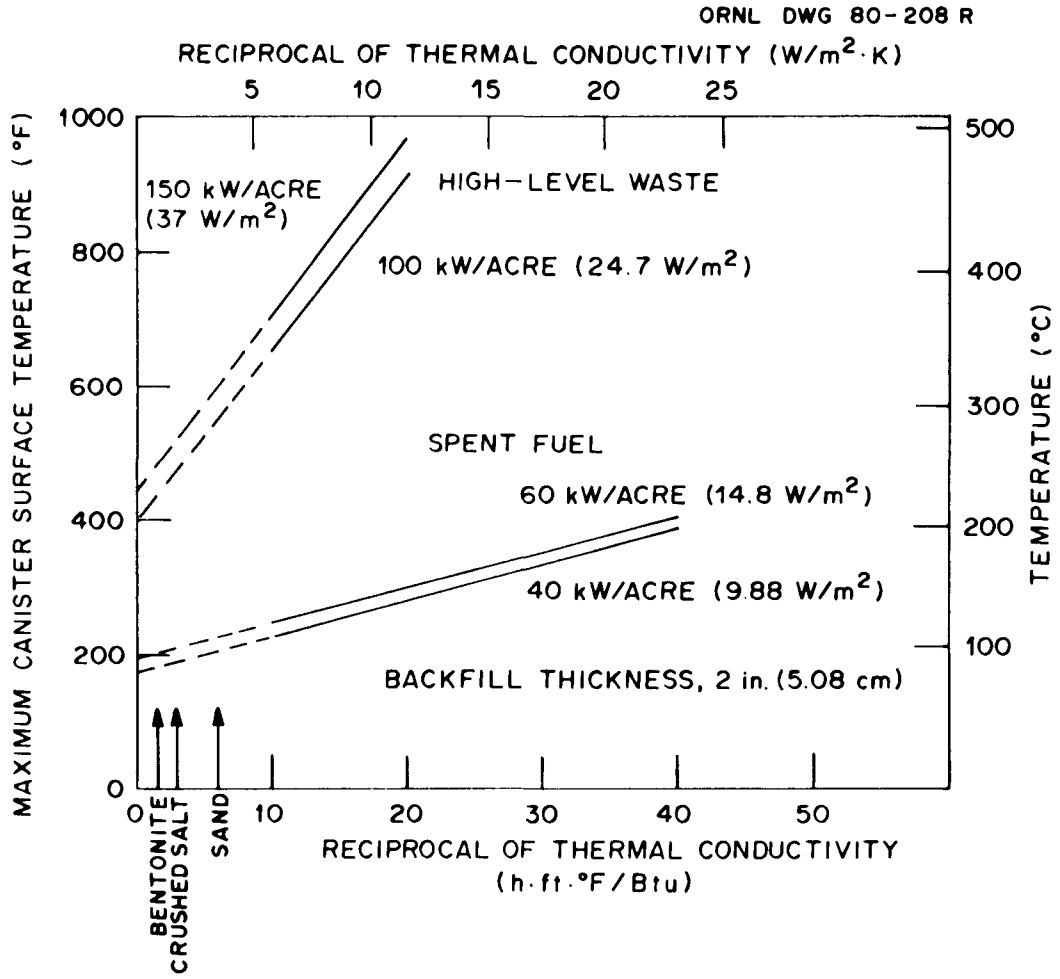

Fig. 20. Maximum canister surface temperature as a function of thermal conductivity for 2-in. (5.08-cm)-thick backfill with an air gap between the canister surface and the backfill.

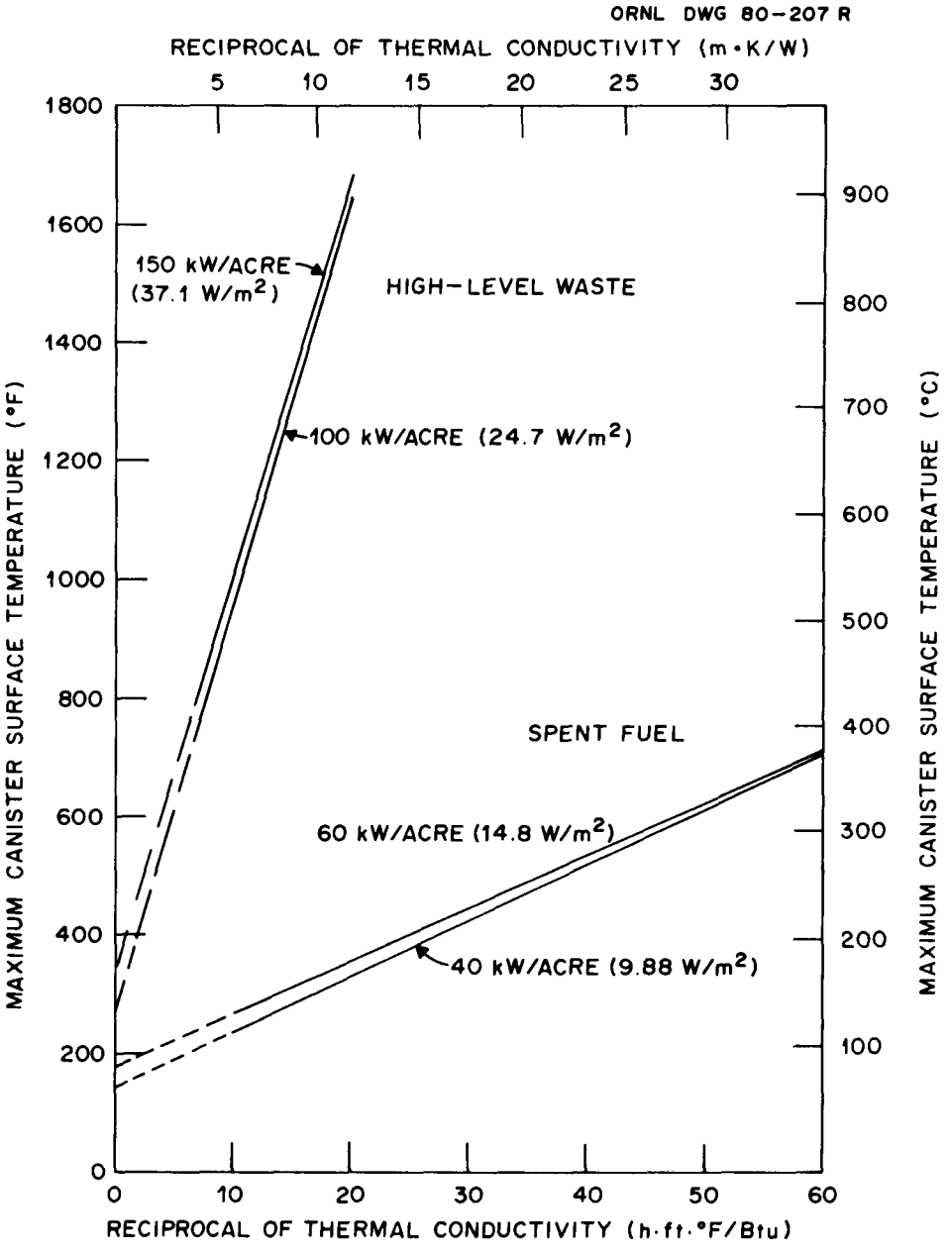

Fig. 21. Maximum canister surface temperature vs the inverse thermal conductivity for backfill with no air gap.

could be any combination of an air gap and/or backfill materials which when added together produce the effective conductivity. Hence, Fig. 21 has a much more general application than Fig. 20. One special application of Fig. 21 would be in the case of wet backfill where the conductivity of this backfill could be incorporated into the effective conductivity, depending on the geometry of the engineered barrier.

The effect of barrier thickness on canister surface temperature is shown in Figs. 22 to 25 for HLW at 150 and 100 kW/acre (37.1 and 24.7 W/m^2) and SF at 60 and 40 kW/acre (14.8 and 9.88 W/m^2), respectively. The results are correlated in terms of the logarithm of the ratio of outer barrier radius and the inner barrier radius. All results are presented for an effective barrier thermal conductivity of 0.1 Btu/hr·°F·ft (0.17 W/m·K), and the backfill material is assumed to fill the region between the canister surface and the salt formation. It can be seen that the barrier thickness will have to be limited because of the strong dependence of the canister and waste temperatures on this parameter.

Additional details on the effect of backfill thermal conductivity and barrier thickness are given in Appendix C. In particular, temperature histories are shown for various backfill thermal conductivity values, and the effect of barrier thickness at the waste centerline (or SF assembly pin) is presented.

2.2.3 Delay of canister backfill

Because a small conductance can markedly increase canister and waste temperatures, and because prospective backfill materials may have small conductivities, it is of interest to determine the result of delaying the canister backfill operation until some point after emplacement (e.g., at the end of the retrievability period). The general results of this procedure are illustrated in Fig. 26. In this case, the emplacement cavity is not backfilled immediately after emplacement. Closure of the hole with a barrier material having a conductivity of 0.1 Btu/hr·°F·ft (0.17 W/m·K) takes place 5 or 25 yr after emplacement. Although the hole is unfilled, the canister waste centerline temperatures are 550°F (288°C) or less. Virtually no difference in temperature can

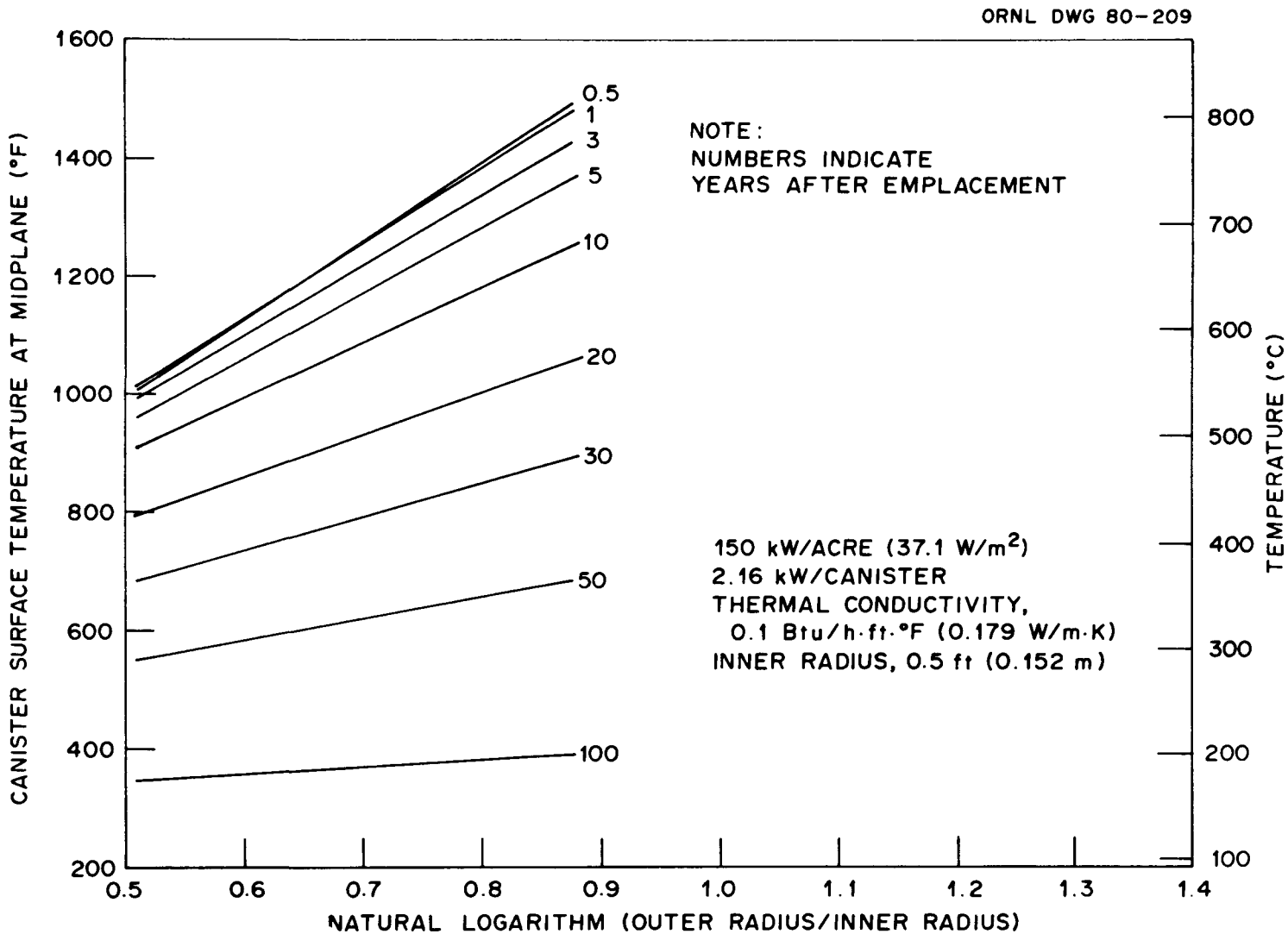

Fig. 22. Maximum canister surface temperatures vs the natural logarithm of the ratio of barrier radii for 150-kW/acre (37.1-W/m^2) high-level waste.

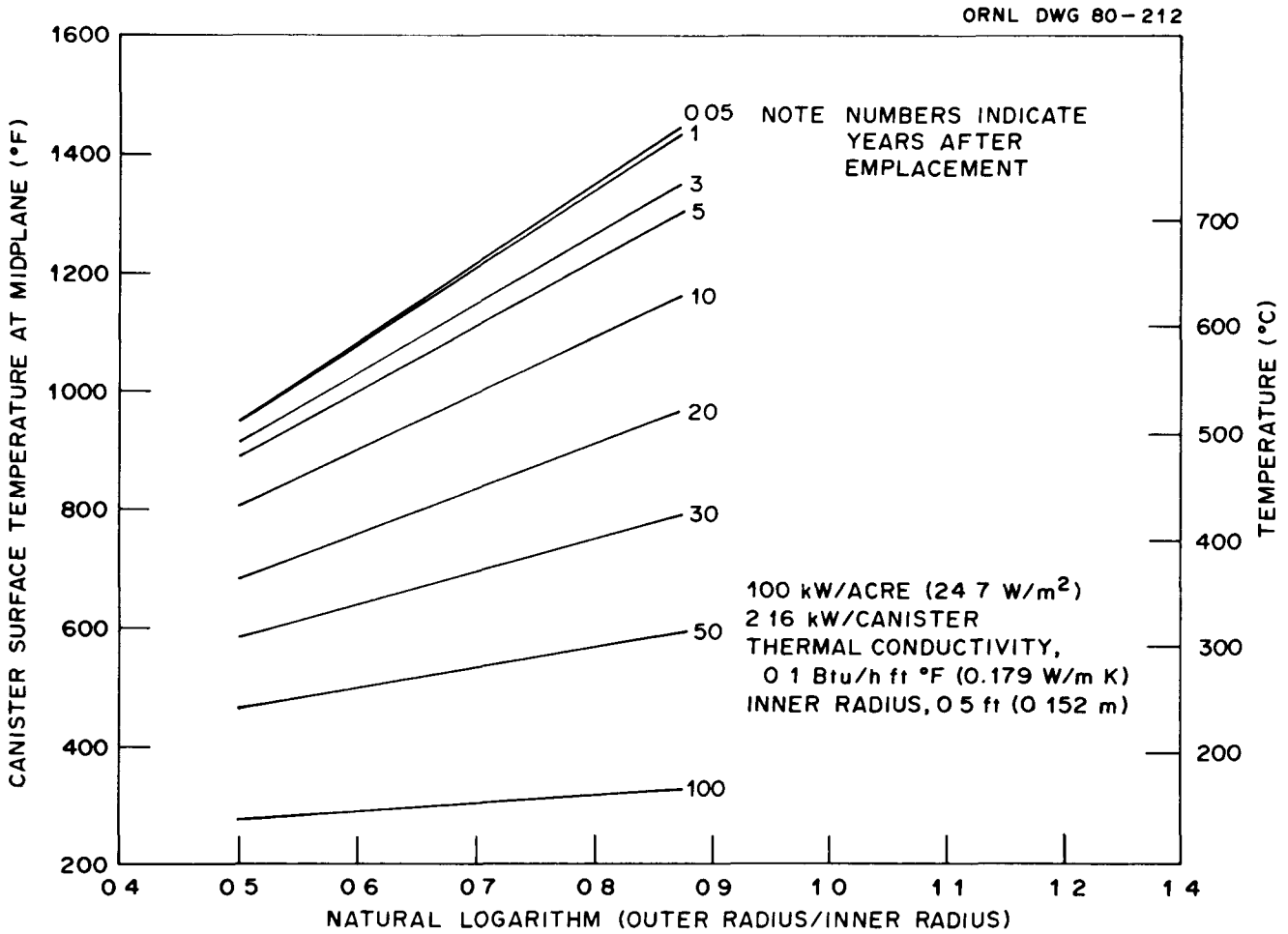

Fig. 23. Maximum canister surface temperatures vs the natural logarithm of the ratio of barrier radii for 100-kW/acre (24.7-W/m^2) high-level waste.

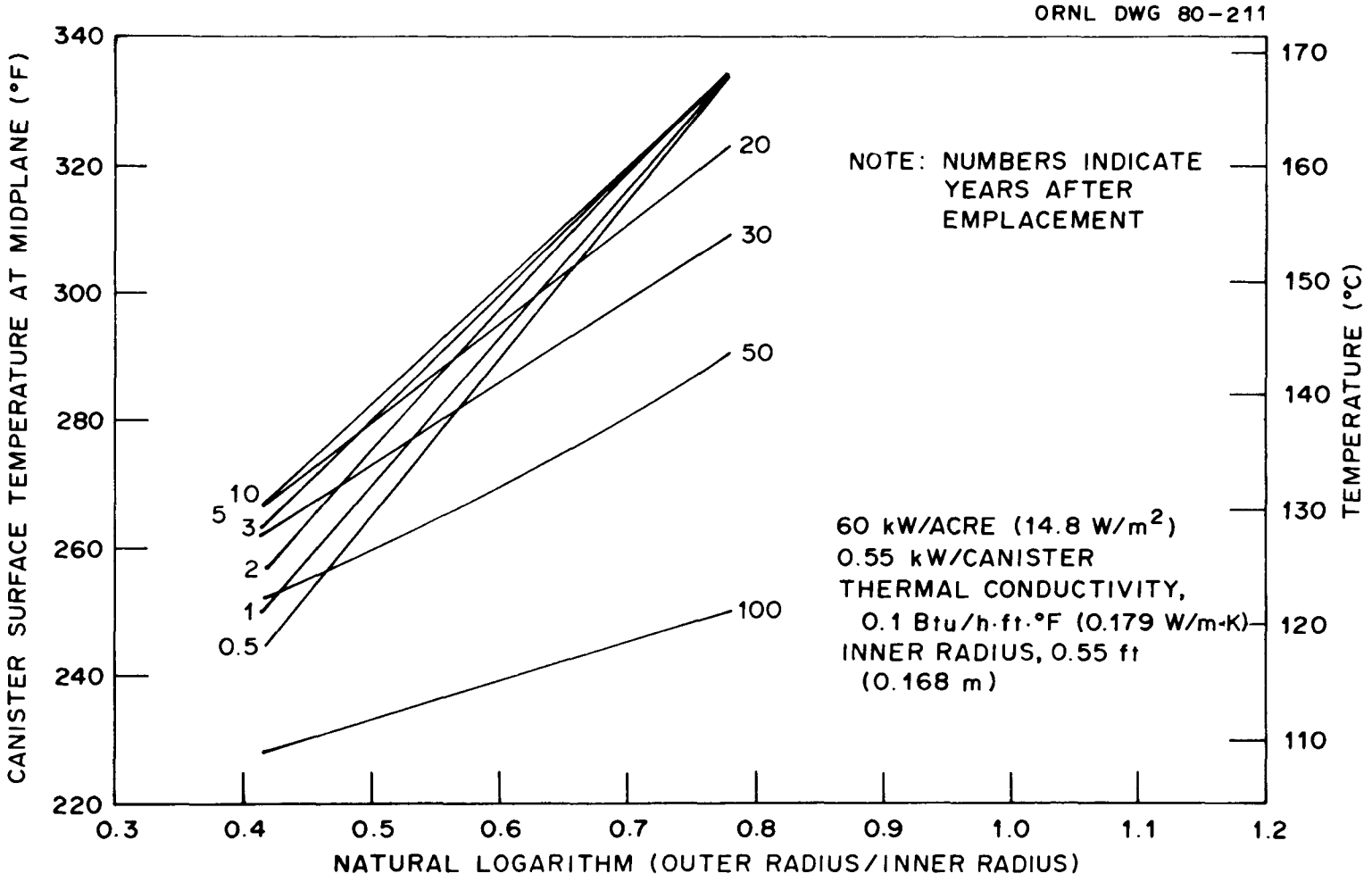

Fig. 24. Maximum canister surface temperatures vs the natural logarithm of the ratio of barrier radii for 60-kW/acre (14.8-W/m^2) spent fuel.

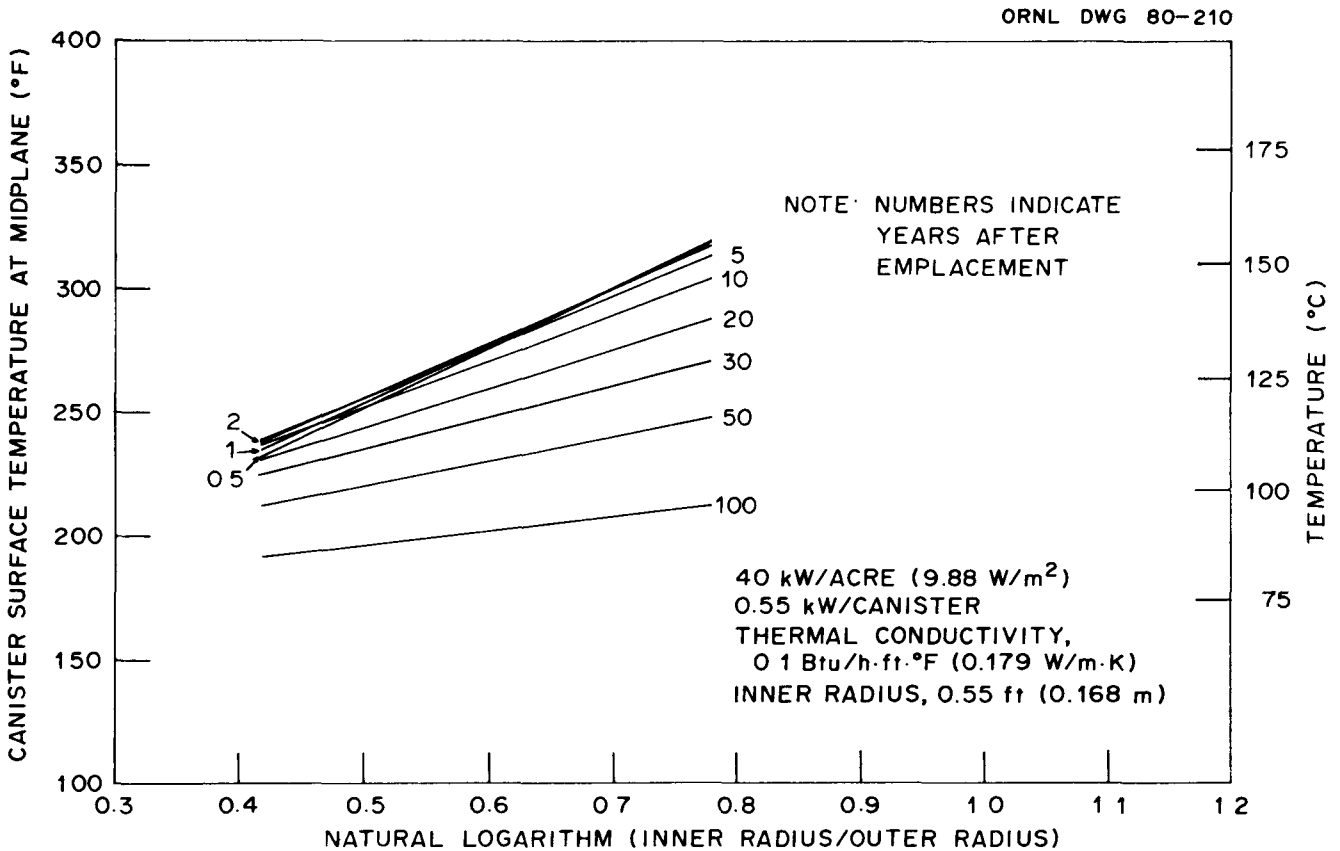

Fig. 25. Maximum canister surface temperature vs the natural logarithm of the ratio of barrier radii for 40-kW/acre (9.88-W/m^2) spent fuel.

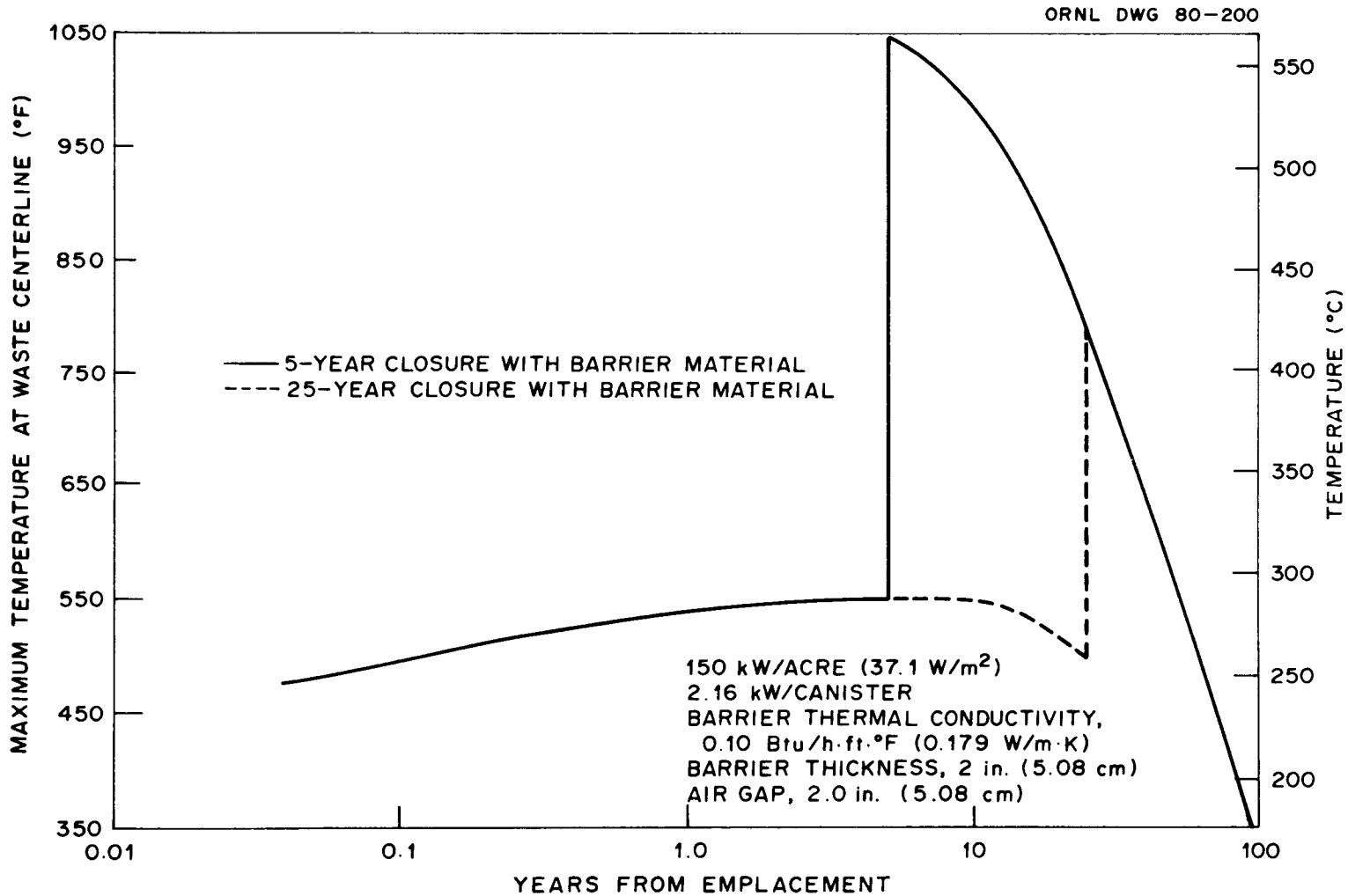

Fig. 26. Waste centerline temperature histories for 5- and 25-yr retrievability of high-level waste.

be observed after backfilling, regardless of whether this operation takes place 5 or 25 yr after emplacement. Such delays can reduce the time the canister is subjected to high temperatures. In addition, if delays are sufficiently long that temperatures start to decrease (e.g., 25 yr for HLW), maximum canister temperatures may be reduced.

The results for HLW for an areal heat load of 150 kW/acre (37.1 W/m^2) are shown in Fig. 26. Other areal heat loads and SF results are shown in Appendix C. Other studies have been previously reported for backfill of the room,[5] but the results presented herein are applicable to canister backfill only.

2.3 Special Studies

Two variations of the thermal environment have been analyzed as special cases of the results presented in Sect. 2.1. These are ventilation of the storage room and multiple rows of canisters down the storage room.

2.3.1 Ventilation of the storage room

During the time the storage room remains open for mining or waste emplacement operations or during the retrievability period, the free circulation of air or forced ventilation of the storage room offers a way to remove a substantial portion of the heat generated in the formation in addition to permitting personnel access. Depending on the temperature of the ventilating air and the heat transfer from the rock to this cooling air, gradients will be set up in the salt to induce conduction of energy away from the vicinity of the waste canisters. This effect may significantly lower temperatures in the very near field. The results of calculations to investigate this effect are shown in Figs. 27 to 29. For these calculations, 100°F (38°C) air is assumed to ventilate the room, and a heat transfer coefficient of 1.0 $Btu/hr \cdot °F \cdot ft^2$ (5.7 $W/m^2 \cdot K$) is assumed to transfer the energy between the ventilating air and the floor and walls of the storage room. Although ventilating air is likely to enter the storage room at a lower temperature, it will heat up as it moves down the room. The choice of 100°F (38°C) is a

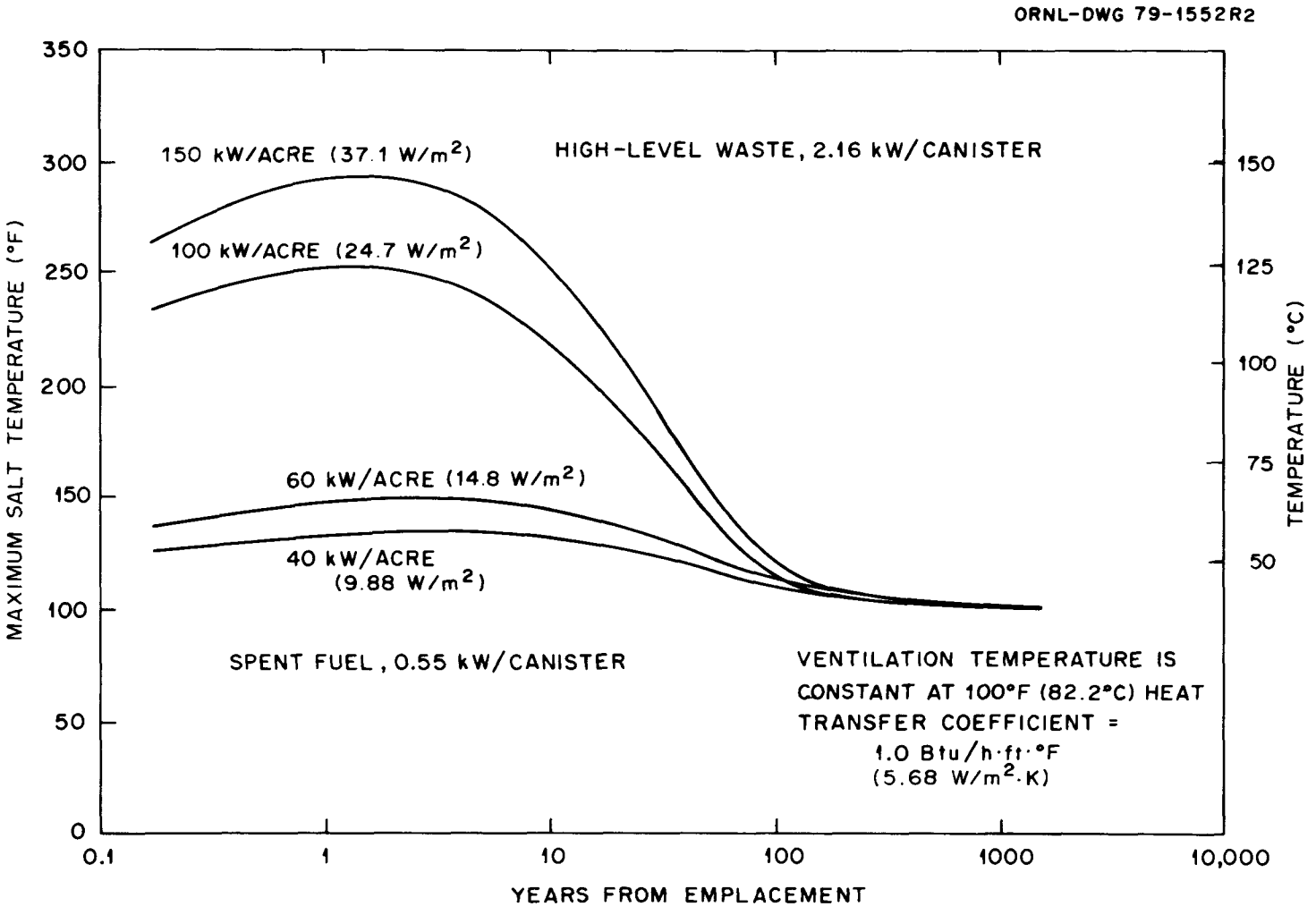

Fig. 27. Maximum salt temperature histories for a ventilated repository.

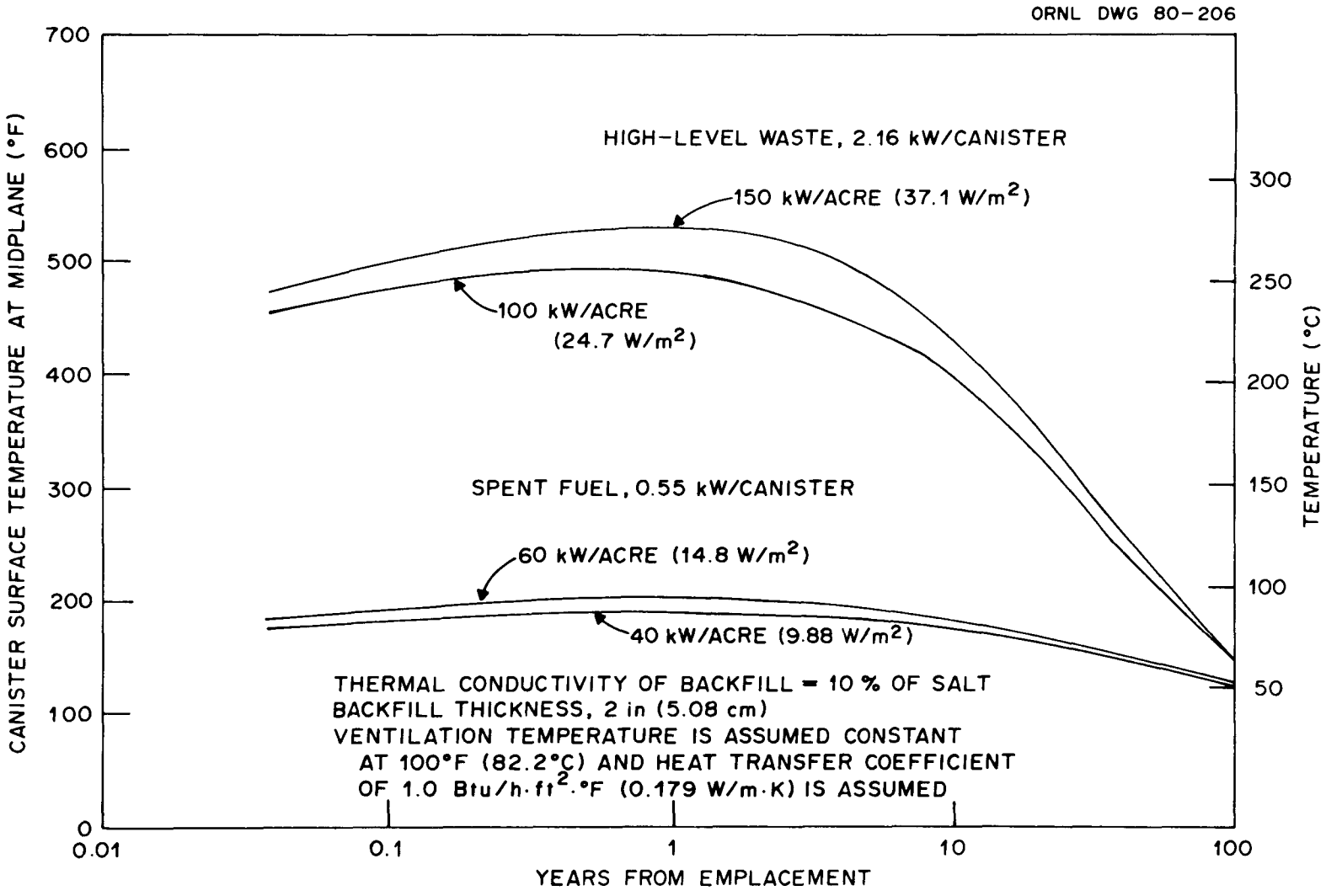

Fig. 28. Maximum canister-surface temperature histories for a ventilated repository.

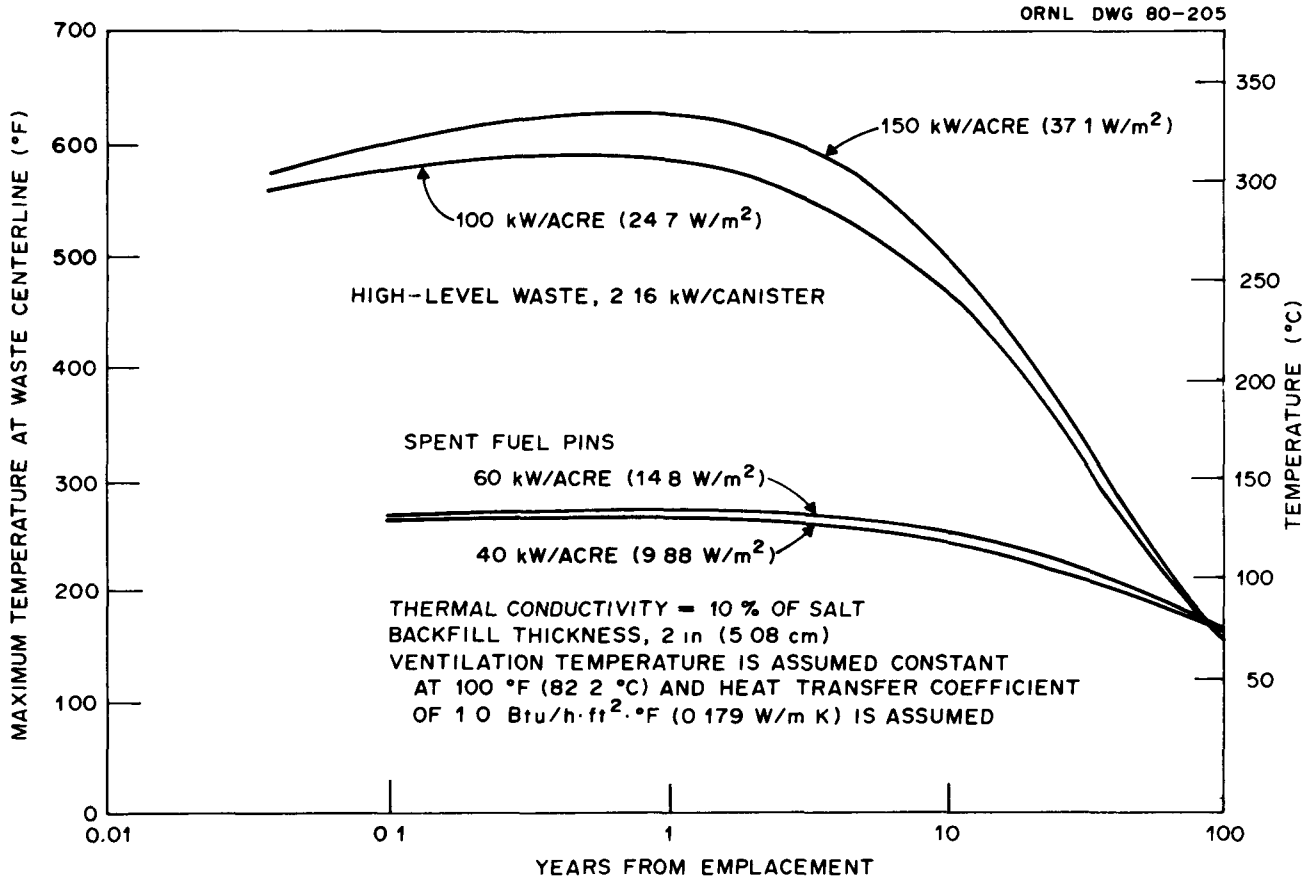

Fig. 29. Temperature histories of waste centerline and spent fuel assembly for a ventilated repository.

somewhat conservative value for the average air temperature of the room. For example, some results of convective heat removal from a storage room have been presented in the *Technical Support for GEIS: Radioactive Waste Isolation in Geologic Transformations* (ref. 6). For an inlet air temperature of 80°F (27°C) and an exhaust air temperature of 127°F (53°C), a flow rate of 16000 cfm (7.6 m^3/s) removes 78% of the heat generated. Therefore, these results correspond to a canister located approximately midway down such a storage room. The heat transfer coefficient is representative of those estimated for rooms of the given dimension, geometry, and surface roughness and for the flow rates appropriate for repository ventilation.

Figure 27 gives the resulting maximum salt temperatures. Comparison with Fig. 5 shows that the HLW salt temperatures [150 kW/acre (37.1 W/m^2)] have been reduced by 120°F (67°C) to 293°F (145°C), whereas temperatures for SF [60 kW/acre (14.8 W/m^2)] have been lowered by nearly 62°F (34°C) to 149°F (65°C). The effect on the canister surface temperatures is not as dramatic but is still substantial. As can be seen by comparing Figs. 6 and 28, temperatures for the HLW canister surfaces are reduced by 57°F (32°C) to ∿530°F (277°C), whereas for SF, the reduction is 34°F (19°C) to 202°F (94°C). Waste centerline (or SF center pin) temperatures, shown by a comparison of Figs. 7 and 29, would be reduced by ∿40°F (22°C) to 630°F (332°C) for HLW and by ∿10°F (6°C) to 270°F (132°C) for SF. These reductions would be lost soon after the storage room is sealed. Generally, within a few years after sealing, the formation attains the temperature distribution it would have reached had the rooms been sealed from the beginning (see ref. 5 for an example).

Details of the model used to obtain results for a ventilated storage room are included in Appendix D.

2.3.2 Two-row configuration

Although a specific repository design has been chosen for the baseline calculations discussed in Sect. 2.1, the impact of alternative designs is important. An alternative repository design of particular interest includes different extraction ratios or multiple rows of

canisters in the storage room. These alternatives may serve the purpose of decreasing the construction costs or modifying the thermal environment. The conceptual reference repository design (CRRD)[3] configuration used for two-row SF isolation in this section is an example which incorporates both of these modifications. The design parameters (Appendix D) include a 4-ft (1.2-m) canister pitch and a 70-ft (21-m) pillar thickness [18-ft (5.5-m) room width]. The canister heat load is 0.525 kW per assembly for pressurized water reactors (PWR) and 0.167 kW per assembly for boiling-water reactors (BWR). The areal heat load for a configuration of PWR and BWR canisters is 130 kW/acre (32.2 kW/m^2) and 83 kW/acre (20.5 kW/m^2), respectively. The actual design would contain a mixture of these two canister types; therefore, the above two areal loads were calculated as an upper and lower limit.

The near-field model as described in Sect. 2.1 was used to calculate the expected temperatures. Details of the model are included in Appendix D. The temperature histories of the two cases are shown in Fig. 30 for the maximum salt, canister surface, and maximum SF pin temperatures. A direct comparison with the PWR-SF results from Sect. 1 is difficult due to the higher areal heat load, but extrapolation of the base-case canister surface temperatures (Fig. 17) yields ∿375°F (191°C) for 130 kW/acre (32.2 W/m^2), which corresponds to nearly 370°F (188°C) for the two-row configuration. This suggests that there is little discernible difference between the salt temperature environments for the two configurations as long as thermal loading densities are the same. Additional data for other areal heat loads for the two-row configuration are included in Appendix D.

2.4 The Far-Field Analysis

The design of an underground repository must be concerned with the thermal environment far removed from the source (e.g., the temperature rise at the surface of the earth and where an aquifier may exist). The unit-cell concept as described in the near-field analysis is not appropriate in the far-field analysis because of the boundary conditions that have been imposed. In the far-field model used, the details of the

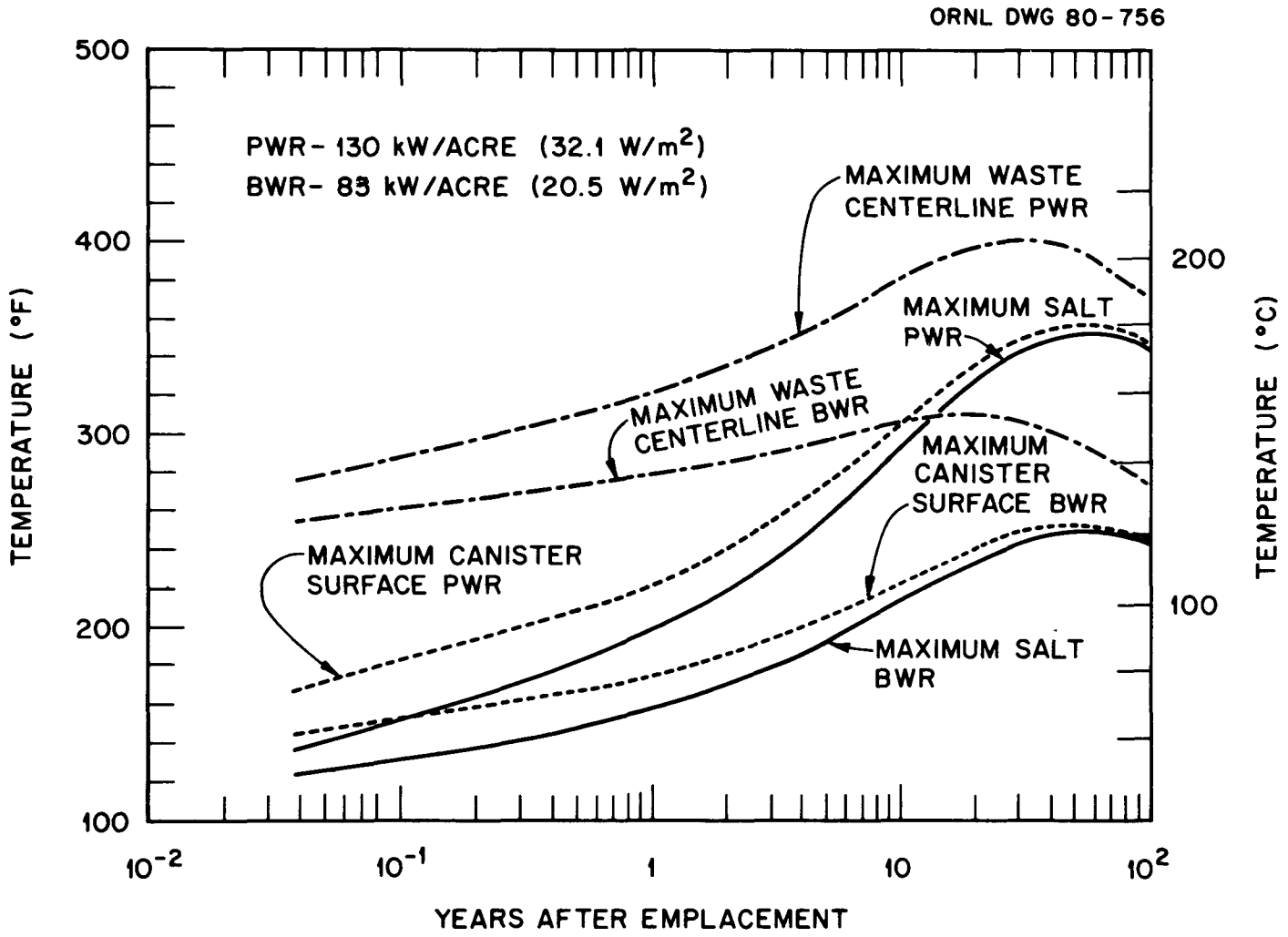

Fig. 30. Temperature histories for the spent-fuel two-row configuration.

waste packages and distribution are not considered; the waste (or SF) is assumed to be spread uniformly over the repository area. Thus, it will provide sufficiently accurate results that are removed from the vicinity of the repository. The far-field model is a cylindrical geometry shown in Fig. 31. The repository is modeled as a 50-ft (15.2-m)-thick (t) by 5282-ft (1610-m)-radius (a) heat source. The repository is located 1975 ft (602 m) below the surface of the earth (d), and the outer model radius boundary is insulated but is located 15,000 ft (4570 m) from the center of the repository. An initial temperature gradient is assumed to be 0.019°F/ft (3.2×10^{-3} °C/m), with an isothermal boundary located at a depth of 15,000 ft (4570 m). It is assumed that the solar flux is equal to 73 Btu/hr·ft^2·°F (230 W/m^2) and that the radiation occurs at a sky temperature of 45°F (25°C). Convection is also assumed to take place at the surface with an assumed air temperature of 65°F (36°C) and a convective heat-transfer coefficient of 5.0 Btu/hr·ft^2·°F (28 W/m^2·K). Llewellyn[7] has shown that the selection of the convective heat-transfer coefficient does not have a strong effect on the far-field results. Input decay rates for all far-field analyses are given in Appendix E.

The following sections describe the dome salt and the bedded salt models with the expected salt temperatures that result from these model calculations.

2.4.1 The dome salt model

All the analyses of the previous sections have assumed that the waste canister is emplaced in a solid salt formation (i.e., the medium has thermal properties of rock salt only). This condition would be met for the most part in a repository constructed in a salt dome. The analyses for a far-field model can also be calculated in this case. The salt and waste properties are the same as those used in Sect. 2.1. Details of the model are included in Appendix E.

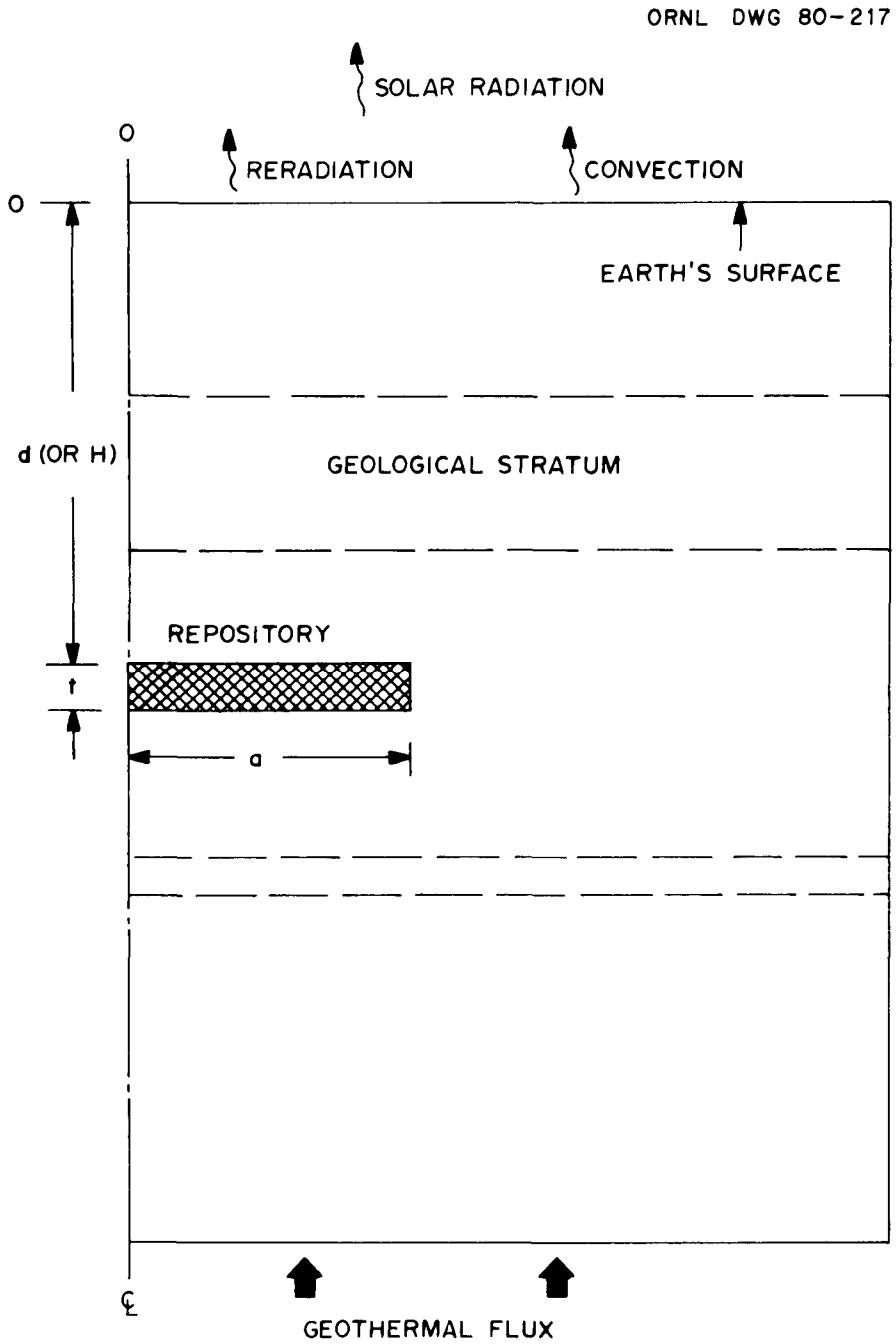

Fig. 31. Baseline model for the far-field calculations.

2.4.2 The bedded salt model

A model that takes into account a stratigraphy associated with a bedded salt formation can also be calculated. In this case, layers of material having conductivities different from salt are included and can modify the far-field results. A generic bedded salt stratigraphy has been defined in *Technical Support for GEIS: Radioactive Waste Isolation in Geologic Formations*[6] and is used here. The description of this formation is given in Table 8. The waste and salt properties are the same as those of the dome salt model. All specific heat values were held constant at 0.20 Btu/lb·°F (0.84 J/g·K). Details of the model are included in Appendix E.

2.4.3 Expected salt temperatures

The results of the far-field analyses are presented in Figs. 32 to 35. Figures 32 and 33 show temperatures for selected times and depths, respectively, for the HLW repository. The thermal loading in this case is 150 kW/acre (37.1 W/m^2). Figures 34 and 35 show similar results for a SF repository loaded to 60 kW/acre (14.7 W/m^2). [Analogous results for HLW at 100 kW/acre (24.7 W/m^2) and SF at 40 kW/acre (9.88 W/m^2) are shown in Appendix E.] It is noted that, although some differences exist, the actual temperature rises are not significantly different for the two stratigraphies in spite of the widely differing thermal properties of nonsalt layers. The calculated surface temperature rises were <0.1°C. It is also noted that the temperature rises occur for long periods after repository closure, in fact, long after the heat operation rate has decayed to negligible values. Nevertheless, these increases are probably not significant when compared to ambient formation temperatures, except within the immediate vicinity of the repository itself.

Table 8. Salt stratigraphy

Depth		Rock	Thermal conductivity		Density	
ft	m		Btu/hr·ft°F	W/m·K	lb/ft^3	kg/m^3
0-50	0-15	Unconsolidated material	0.48	0.86	119	1910
50-250	15-76	Unconsolidated material	1.69	3.03	150	2400
250-380	76-116	Sandstone	3.37	6.04	147	2360
380-500	116-152	Dolomite	2.41	4.32	174	2790
500-800	152-244	Shale	1.69	3.03	150	2400
800-1050	244-320	Limestone	2.17	3.89	170	2720
1050-1200	320-366	Salt				
1200-1400	366-427	Dolomite	2.41	4.32	174	2790
1400-1500	427-457	Salt				
1500-1700	457-518	Dolomite/shale	1.69	3.03	150	2400
1700-1900	518-579	Salt				
1900-1950	579-594	Shale	0.96	1.7	141	2260
1950-2000	594-610	Salt				
2000-2100	610-640	Dolomite	2.4	4.32	174	2790
2100-2200	640-671	Salt				
2200-2250	671-686	Shale	0.96	1.7	141	2260
2250-2550	686-777	Dolomite	2.41	4.32	174	2790
2550-3200	777-975	Shale	1.21	2.17	166	2660
3200-3400	975-1036	Limestone	1.21	2.17	166	2660
3400-3750	1036-1143	Dolomite	1.93	3.46	169	2710
3750-3900	1143-1189	Dolomite	2.41	4.32	174	2790
3900-4000	1189-1219	Dolomite	2.89	5.18	172	2760
4000-4500	1220-1372	Consolidated material	2.00	3.58	170	2720

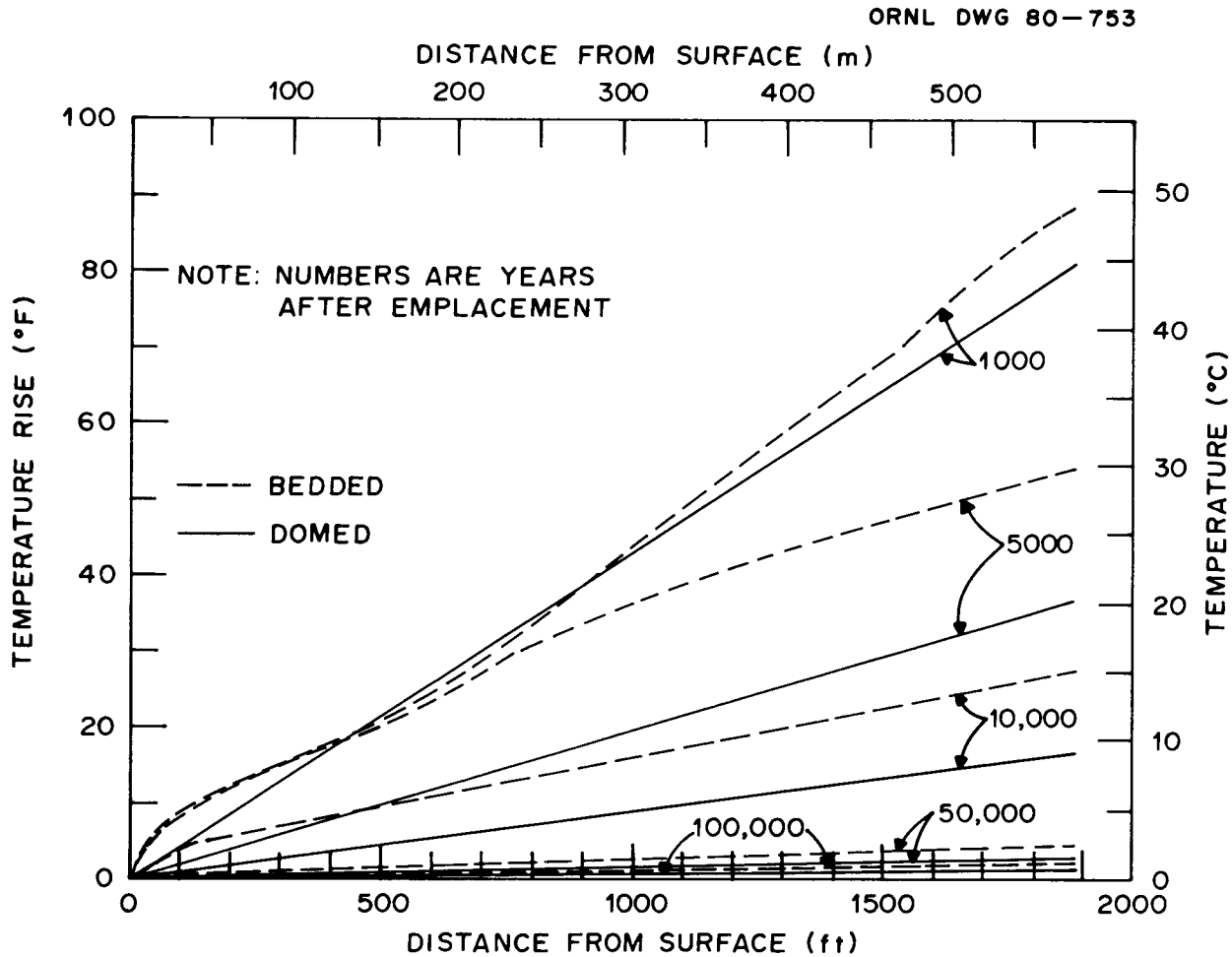

Fig. 32. Temperature rise vs the distance from the surface of the earth for high-level waste for an areal heat load of 150 kW/acre (37.1 W/m^2).

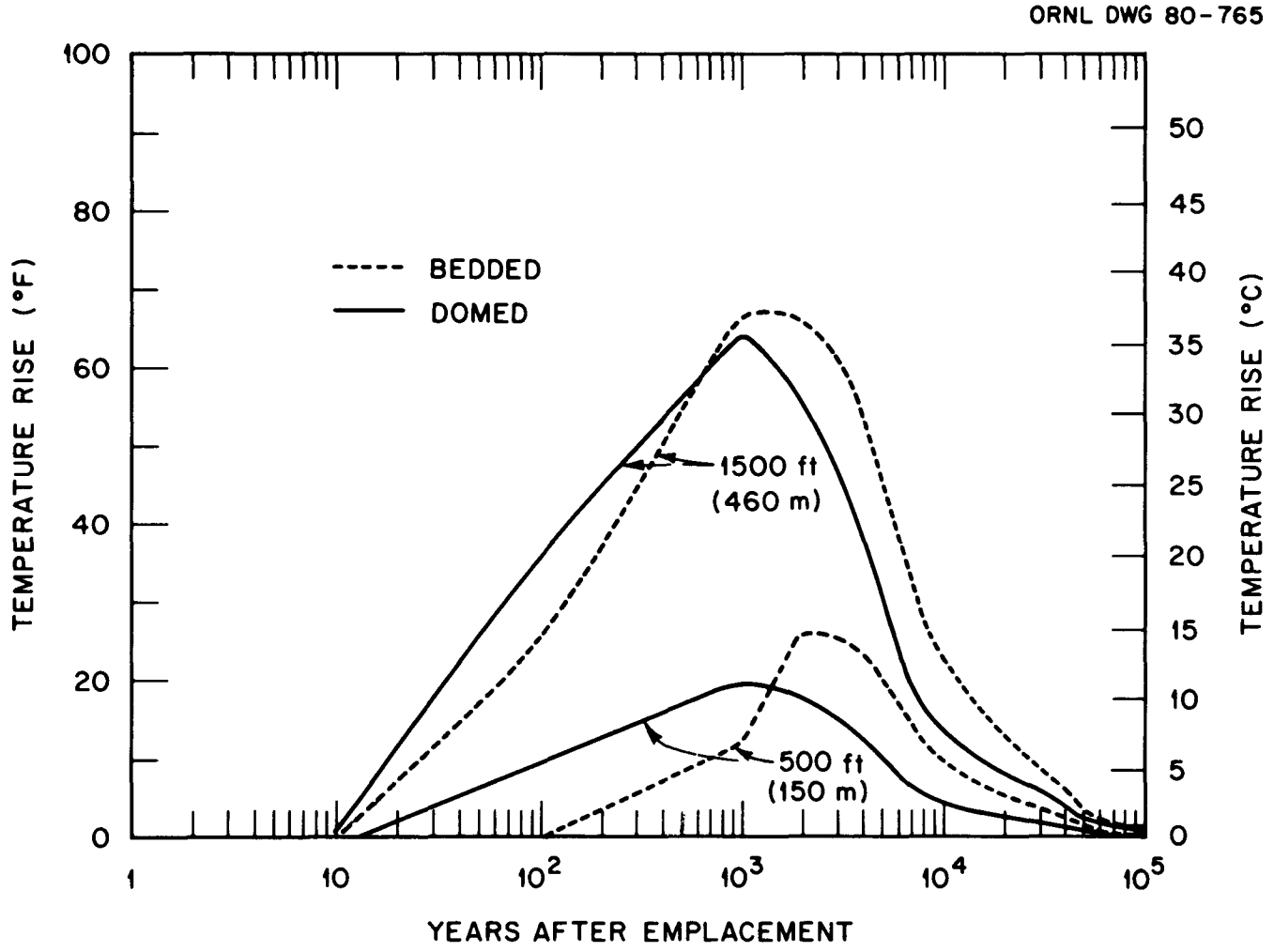

Fig. 33. Temperature histories for 150-kW/acre (37.1-W/m^2) high-level waste at 500 and 1500 ft (150 and 460 m) below the surface of the earth.

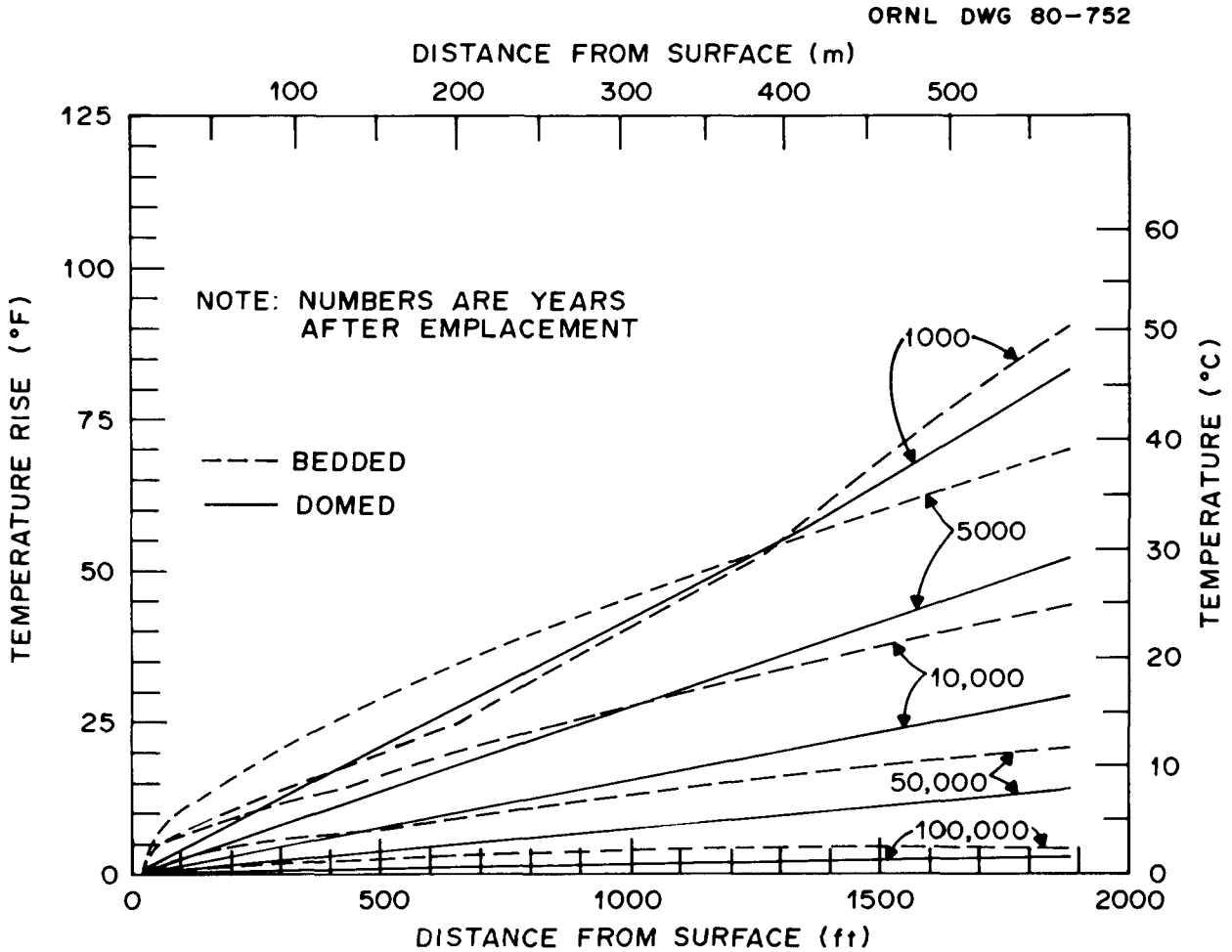

Fig. 34. Temperature rise vs the distance from the surface of the earth for spent fuel for an areal heat load of 60 kW/acre (14.8 W/m^2).

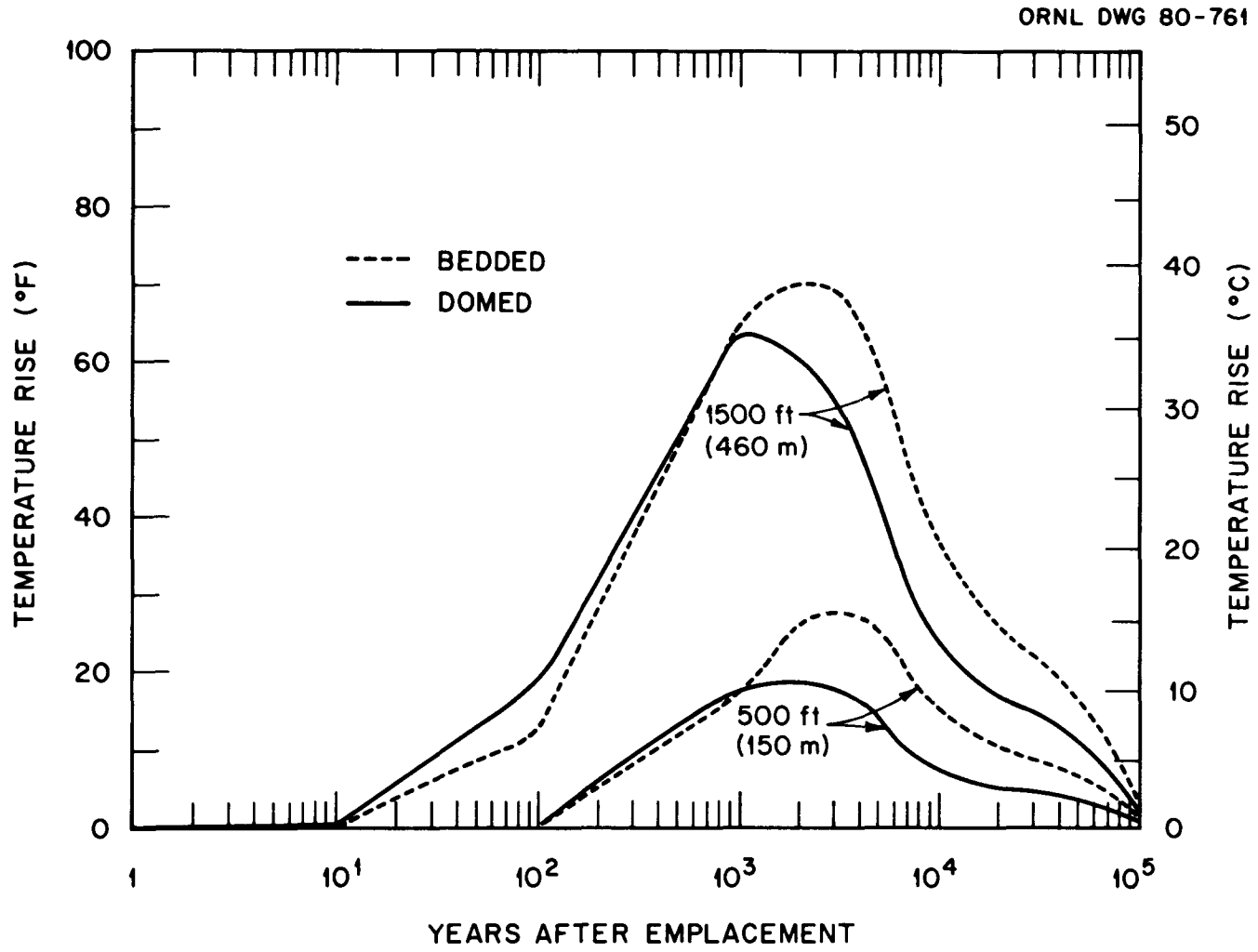

Fig. 35. Temperature histories for 60-kW/acre (14.8-W/m^2) spent fuel at 500 and 1500 ft (150 and 460 m) below the surface of the earth.

3. BRINE MIGRATION

Bedded salt (halite) contains a small amount of water (usually <1 wt %) in the form of saturated brine or water of crystallization. The relatively pure salt formations considered as potential repository sites for radioactive waste—SF in the United States contain, among others, trace amounts of the minerals polyhydrate, carnallite, and bloedite which contain water of crystallization.

The rock temperature in a repository will be well below the decomposition temperatures of these hydrates, as well as below the temperatures required for exerting a sufficient vapor pressure to produce slow dehydration at crystal interfaces and other potential cracks.

The saturated brine will occur mostly as small inclusions ($\leq$ 1-mm diam) in the halite, with much smaller amounts at crystal interfaces. These inclusions can migrate through the salt under conditions where a sufficiently large gradient exists in the chemical potential in the salt surrounding the inclusions, and, until recently, this has been thought to be a major problem.[8]

3.1 The Brine Migration Model

When the chemical potential is changed by imposing a temperature gradient, the brine inclusions will either move up or down the gradient. An inclusion containing only a brine liquid phase will move up the gradient in the direction of the heat source, while an inclusion containing some gas phase will move down the gradient away from the heat source. It is unlikely that a gas phase will be present in the brine inclusions at a repository site, but a sufficient gas phase could develop as a result of radiolysis of the brine. The subsequent refluxing action — condensation of water with dissolution on the cold side and evaporation of water with precipitation of salt on the hot side — causes the movement away from the heat source, which could prevent the brine from reaching the waste canister. Another effect of high radiolytic gas pressure would be to increase the tendency of cracking and release of brine in the crystals near the edge of the hole in the solid state.

Brine migration toward the heat source is more likely since this process does not require a gas phase; it simply results from the fact that salt solubility increases with temperature, causing dissolution of salt on the hot side and precipitation on the cold side. This phenomenon has been observed in single crystals in laboratory studies and has been discussed in ref. 9, although other phenomena may also have been involved in the latter experiment.

A thorough evaluation of the available theoretical and experimental information has been made by Jenks.[10] He concluded that the effects of crystal stressing, high pressure, and energy storage from radiation damage would have little effect on brine migration in halite crystals and that the kinetic potential was largely responsible for most of the scatter in experimental results. The kinetic potential acts as a retardant to the speed of migration, so ignoring this phenomenon would produce conservative results. Consequently, Jenks drew a curve passing near the maximum values of brine migration and fitted the following equation to it:

$$\log V/G = 0.00656T - 0.6036 , \qquad (1)$$

where

V/G = velocity per unit temperature gradient, $cm^2/yr \cdot °C$;

T = temperature of salt, °C.

Jenks also showed that Eq. (1) was in agreement with the theory of brine migration as developed by Anthony and Cline.[11]

According to Jenks, the greatest uncertainty associated with prediction of rates of brine migration into a waste emplacement cavity in bedded salt involves questions regarding the effects of the grain boundaries in bedded salt deposits. It is likely that grain boundary trapping will have important retarding effects on brine migration under the conditions which are expected to prevail within probable repository designs, such as maximum temperature gradients $\leq 2°C/cm$, impurities present on grain boundaries, and boundaries compressed by thermal expansion of the salt. However, this trapped brine could be released when salt that has been heated is allowed to cool. He also concluded,

on the basis of theoretical considerations, that the kinetic potential was insufficient in practical repository designs to cause an inclusion to cross a grain boundary. In Project Salt Vault,[9] it was observed that water was collected only during or immediately after a failure of electrical power, at which time the salt adjacent to a canister cooled to some extent. The amount of water collected during the first 2 d after shutdown of the heaters at the end of the experiment was about ten times greater than that collected during the entire 580-d period of operation. The explanation offered was that the tangential stresses created by thermal expansion of the salt during heating were released upon cooling, thus allowing the trapped water in the salt to break free. Jenks has further suggested that the brine was trapped on grain boundaries during heating and that release of tangential stresses allowed the grain boundaries to open sufficiently for the brine to escape to the air gap space.

Recent experiments at the Sandia Laboratories have produced results that apparently could not be explained by the previously described migration model. This led to the postulation of a different model. The salt is treated as a continuous porous medium, and the liquid-vapor flow is computed using Darcy's Law together with a simple two-phase water model. To account for the sudden increase in water release when the heat is turned off, it was assumed that thermal cracking occurred due to the thermal gradient reversal. A one-dimensional spherical model was developed that employed a finite-element method similar to that used in other finite-element computer codes, such as ADINA (ref. 12), to determine when tension cracking occurred because of the change in the thermal gradient. When the stress calculation is combined with the porous-flow calculation, a test is made to determine whether radial cracks develop at any time. If they do, the permeability is increased by a large factor (40 was used) in those regions. Test calculations indicated that cracking takes place when the temperature gradient is reversed, which could explain the sudden brine flow. In three experiments on a 1-kg salt block, the data could not be reproduced in detail, but the general features of a peaked profile after each heater power increase and a brine flow spike following turn-off of the heater were consistent.

This model is undergoing further investigation using a right circular cylinder of bedded salt measuring 1 m in diameter and 1 m in height. Comparison of calculations and the experiment for this model are not yet available.

3.1.1 Calculational model

Equation (1), as recommended by Jenks, was used in calculating the velocity of migration through the rock mass. Inasmuch as the evidence indicates that the brine inclusions will remain trapped at the grain boundaries since the heat source cannot be turned off in a repository, this assumption of single crystal behavior should be conservative with respect to the amount of brine entering the emplacement hole.

In implementing the calculations, it was noted that the brine inclusions could be considered in terms of a density of particles that obeyed the time-dependent continuity equation, namely,

$$\frac{\partial \rho}{\partial \tau} + \nabla(v\rho) = 0 \quad , \tag{2}$$

where

ρ = inclusion density, vol %;

τ = time;

v = velocity of migration;

∇ = gradient operator.

A computer code (MIGRAIN) was developed for both Cartesian coordinates and two-dimensional cylindrical coordinates (R-Z with azimuthal angle symmetry). The required input of temperatures and temperature gradients as a function of time and space is supplied by separate heat-transfer calculations. The computer code greatly facilitates brine migration calculations and properly accounts for brine volume densities along flow paths.

Any equation representing the velocity of brine migration as a function of temperature and temperature gradient can be used in the MIGRAIN code.

3.1.2 Waste Isolation Pilot Plant Salt Block II experiment

In an effort to compare the calculational technique with experiment calculations using the MIGRAIN code were made for the Salt Block II experiments conducted at the Sandia Laboratories. Appendix F presents a discussion of the model and the calculation of the temperature fields and the brine migration. The comparison of the calculated values and the experimental data as given in Appendix F shows reasonably good agreement.

3.2 Expected Brine Migration

The prediction for the brine flow into the emplacement hole, using the method discussed in Sect. 3.1, is presented for the baseline repository and the two special studies described in Sect. 2.3 as the ventilated repository and the two-row configuration repository. The brine flow is presented as the total inflow per canister hole over a period of 1500 yr after canister emplacement.

3.2.1 The baseline repository

The predictions for the brine flow into the emplacement hole for the baseline repository are shown in Fig. 36. For the 150-kW/acre (37-W/m^2) HLW case, the total flow is <10 ℓ in the first 100 yr (0.1 ℓ/yr) and ∿12 ℓ after 1500 yr (note the logarithmic scale for time). This water essentially comes from the salt within 2 ft (60 cm) of the emplacement hole. The total flow for the 60-kW/acre (14.8-W/m^2) SF case in 1500 yr is ∿6 ℓ. The dependence on areal loading shows a decrease in flow that is roughly proportional to the decrease in area loading.

3.2.2 The ventilated repository

Although it is not likely that the repository would be ventilated for very long, the effect of continuous ventilation of the storage room above the canisters is shown in Fig. 37. Although the effect of ventilation is minimal during the first few years after emplacement, it has a marked effect later on. As before, the ventilation air is assumed to be 100°F (38°C). A further reduction in the brine flow would result

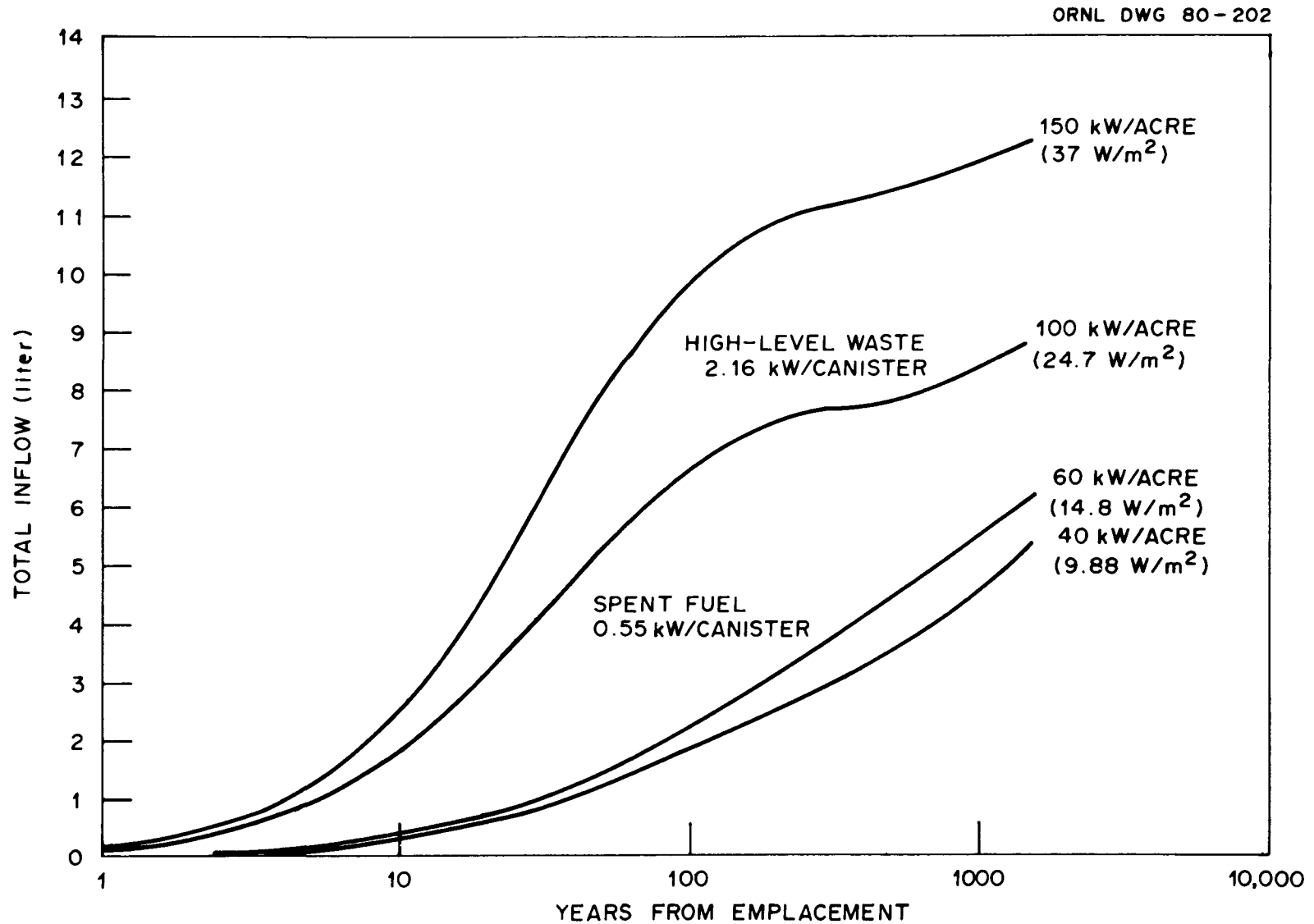

Fig. 36. Brine migration histories for the baseline repository.

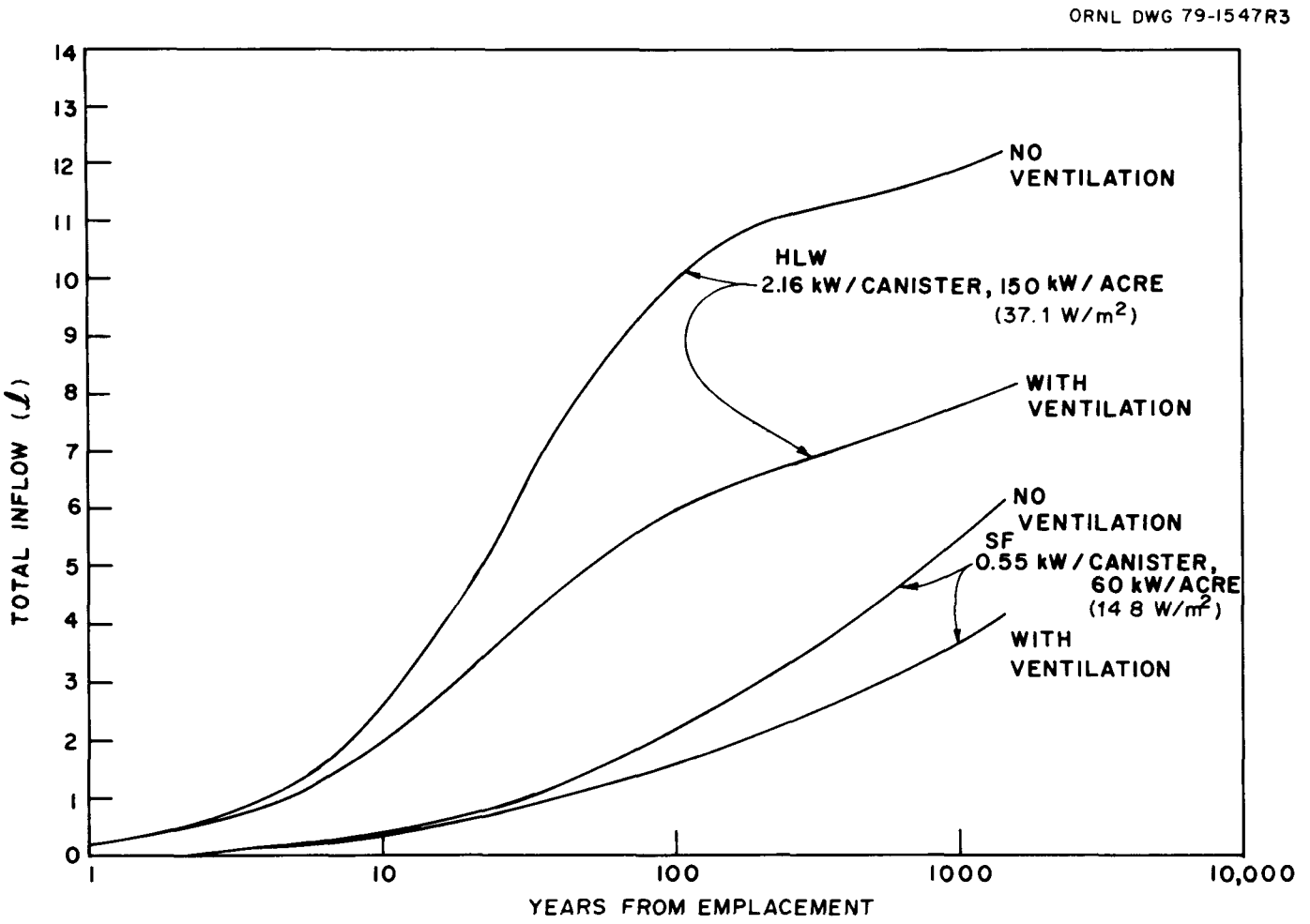

Fig. 37. Brine migration histories — ventilation vs no ventilation.

from cooler ventilation air. These results suggest that any efforts to reduce the heat in the formation or to reduce temperature gradients could have dramatic effects on the brine flow in the long term.

3.2.3 The two-row configuration repository

The two-row repository design for SF would incorporate both PWR and BWR canisters in the array of emplacement holes. The predicted brine flow for the SF two-row configuration repository are shown in terms of BWR and PWR repositories (all emplacement holes in the array are filled with either BWR or PWR canisters) for various areal heat loads. In Fig. 38, the predicted brine flow is shown for thermal loads of 83 kW/acre (20.5 kW/m^2) for the BWR case and 130 kW/acre (32.2 kW/m^2) for the PWR case.

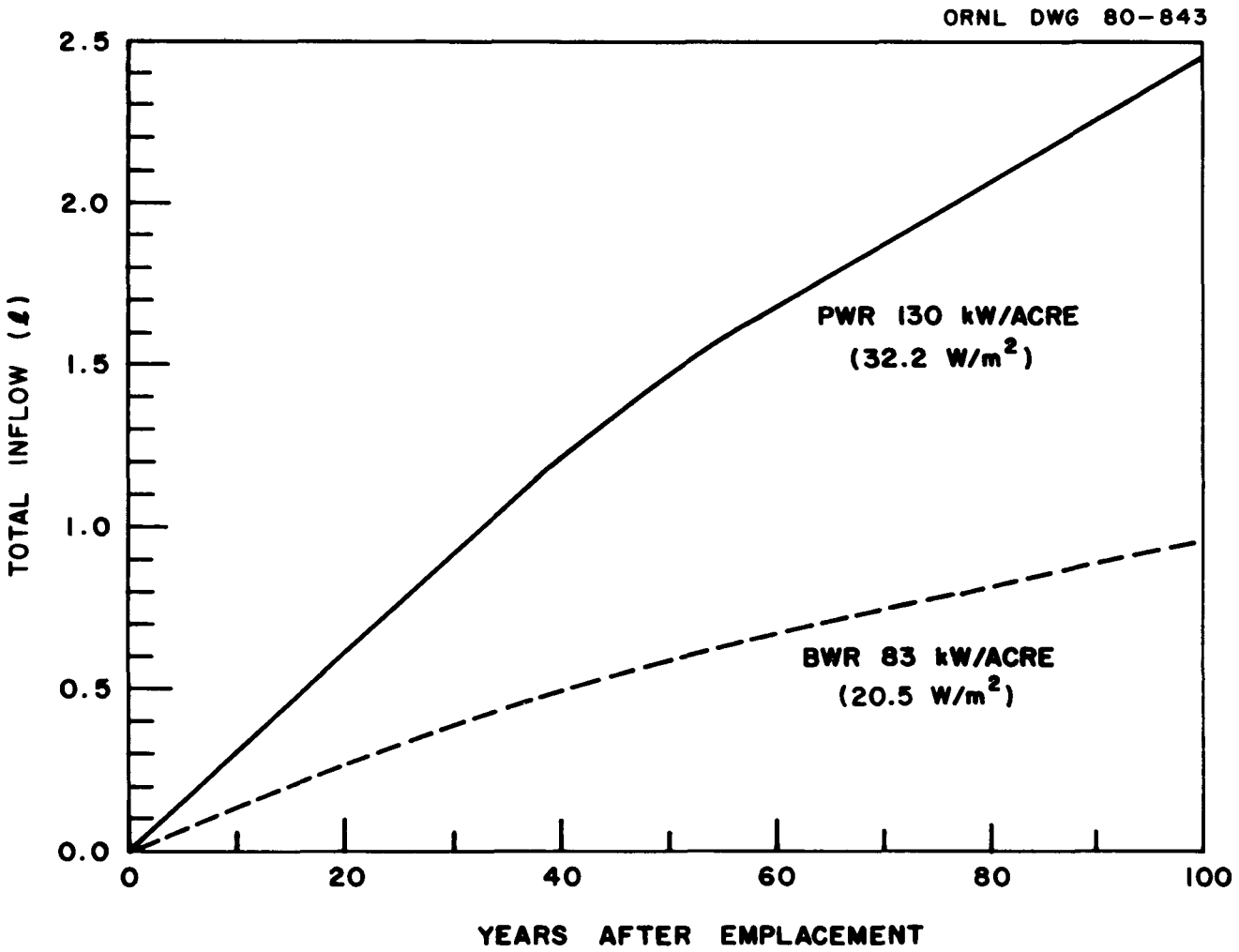

Fig. 38. Brine migration histories for a spent-fuel two-row repository.

4. VAPOR SPACE PRESSURE ENVIRONMENT

Within the heated environment of the emplacement hole, the pressure would be expected to increase. The predicted pressure rise depends on the scenario which is assumed to take place, the volume available for gas expansion, whether or not the emplacement hole is sealed, and the amount of water present. In the simplest case, the repository is completely dry and the gas in the emplacement hole is allowed to escape into the storage room, producing pressure increases <1 atm in the vicinity of the canister. To provide more conservative estimates, it may be assumed that the emplacement hole is sealed, thus preventing escape of the gas. Water may collect in the emplacement hole due to the migration of natural brine in the salt. Furthermore, the available volume in the emplacement hole may diminish due to the creep flow of the salt in this vicinity. In this case, once complete closure of the hole takes place, the pressure will be limited by the lithostatic pressure of the formation.

4.1 The Vapor Space Pressure Model

A model has been developed to predict the emplacement hole pressure over time from temperature and volume data, brine inflow rates, and the gas inventory. It is assumed that the gas in the system consists of air (N_2, O_2) and water vapor. The model can be modified in a straightforward manner to accommodate radiolysis and corrosion products such as hydrogen gas, but this application is not made here. Vapor-liquid equilibrium are evaluated to identify the limiting conditions on cavity pressure. Changes in temperature, volume, and brine inflow are assumed to occur so slowly that the system pressure is always at its equilibrium value.

A computer code (REPRESS) was developed in order to obtain the saturation pressures and water inventories for a given temperature and volume in a waste cavity. The methodology used to predict the vapor space pressures presented herein is presented in Appendix G.

4.2 Expected Vapor Space Pressures

Four scenarios have been assumed in order to estimate pressures. In the first scenario, the emplacement hole is sealed and not backfilled, and the volume is constant (i.e., no closure of the hole takes place). In the second scenario, it is assumed that the hole is backfilled after the waste emplacement and is sealed by some mechanism, but, again, the volume of the cavity does not change. The hole is sealed but not backfilled in the third scenario. In this case, however, the hole is assumed to close due to thermal expansion of the salt. The hole is not sealed in the fourth scenario. The data for the closure rates are taken from the RE/SPEC study[13] for the effect of emplacement of 5-kW canisters at an areal loading of ∿46 kW/acre (11.5 W/m^2). Based on this study, closure of the hole is estimated to take place 250 yr after emplacement. These results should not be strongly dependent on areal loading, but it is conservatively assumed that closure occurs 100 yr after emplacement to account for the higher loadings in this case.

It should be noted that the temperatures used here were calculated for the dry repository. The small amounts of water present may increase the conductivity of the backfill and decrease the average temperature in the cavity. Therefore, these results may be somewhat more conservative than anticipated. Furthermore, any connection permitting leakage from the hole cavity to the room would permit the pressure to decrease.

Other possible scenarios, including reconsolidation of the crushed salt backfill or thermal expansion of the canister, would not be expected to provide pressures that are very different from the above pressures.

Pressure histories for HLW (150 kW/acre or 37.1 W/m^2) and SF (60 kW/acre or 14.8 W/m^2) are shown in Figs. 39 and 40, respectively, for each of the four scenarios previously mentioned. In the case of no hole closure and no backfill for HLW, Fig. 39 shows a peak pressure of 700 psia (4.0 MPa) occurring ∿20 yr after emplacement. If the hole is assumed to be backfilled, the pressure is increased to ∿950 psia (6.6 MPa) and the peak now occurs ∿10 yr after emplacement. If the hole is assumed to close due to thermal expansion of the salt, the peak pressure occurs at 750 psia (5.2 MPa) ∿20 yr after emplacement. Finally,

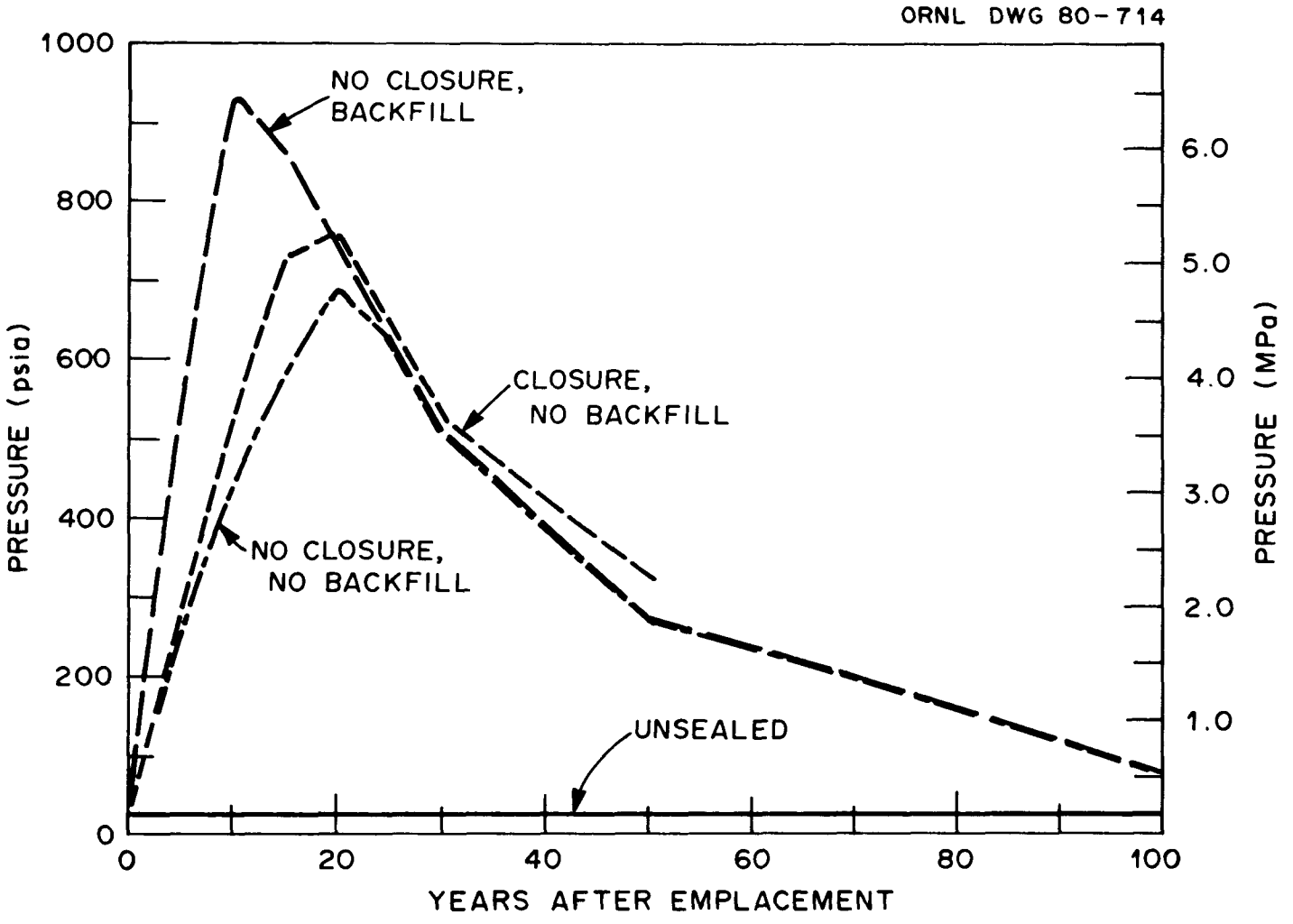

Fig. 39. Pressure histories for high-level waste for an areal thermal load of 150 kW/acre (37.1 W/m^2).

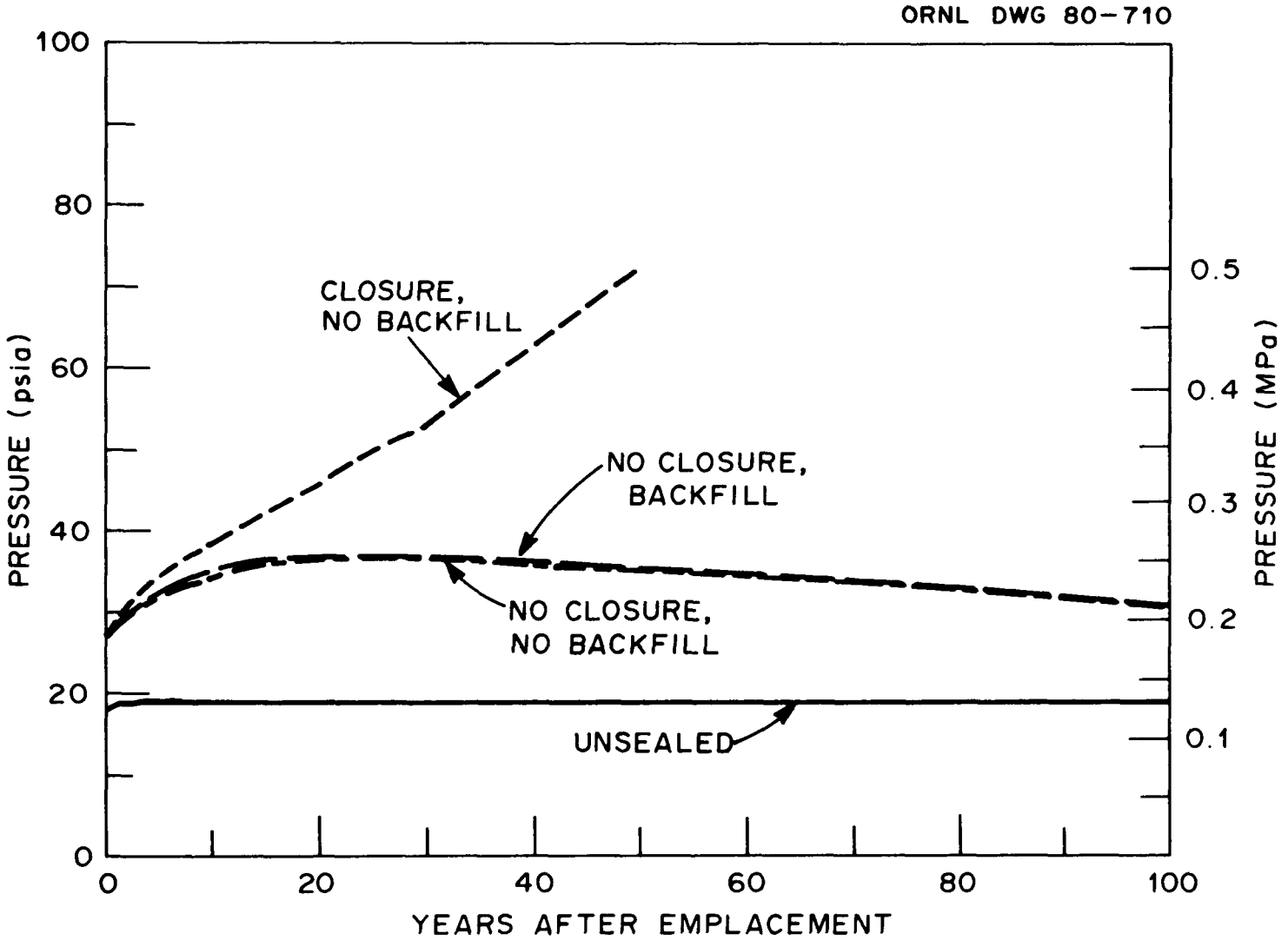

Fig. 40. Pressure histories for spent fuel for an areal thermal load of 60 kW/acre (14.8 W/m^2).

the unsealed hole shows virtually no rise in pressure. In this case, any changes in the pressures are due to an increase in air temperature since the vapor is essentially at infinite dilution.

The SF case at an areal heat load of 60 kW/acre (14.8 W/m^2) is shown in Fig. 40. The no-closure scenarios with and without backfill have nearly identical pressure histories, with a broad peak occurring at 35 psia (0.24 MPa) ~20 yr after emplacement. The hole-closure scenario shows a steadily increasing pressure up to 70 psia (0.48 MPa) at 50 yr after emplacement. Since complete closure of the hole was assumed to occur 150 yr after emplacement, the pressure would be expected to approach the lithostatic pressure of the salt formation. Again, the unsealed hole scenario shows essentially no pressure rise over the period of interest.

Also shown in Figs. 41 and 42 are the two-row configuration pressure histories for 130 and 83 kW/acre (37.1 and 20.5 W/m^2), respectively.

Additional results are shown for 100-kW/acre (24.8-W/m^2) HLW and 40-kW/acre (14.8-W/m^2) SF in Appendix G.

4.3 Expected Quantity of Residual Brine in the Emplacement Hole

The quantity of brine and the available water present in the emplacement hole will help determine the environments encountered by the waste package. For example, temperatures within the waste package could be modified since the heat conductance through the brine is substantially higher than in void space in the hole. In addition, the corrosion rate of the waste package materials exposed to the brine would be expected to be different from those in a liquid-free environment. However, the amount and composition of the brine existing in the emplacement hole can be different from the incoming amount and composition since vaporization of water and water-depleting reactions can occur. If the water vapor is unable to escape, the pressure will increase within the emplacement hole. If this water vapor escapes, as is likely to be the case, pressures will not increase substantially, and the oxygen available for canister corrosion will be reduced, particularly after final sealing of the repository. Quantitative estimates of the amount of residual brine in

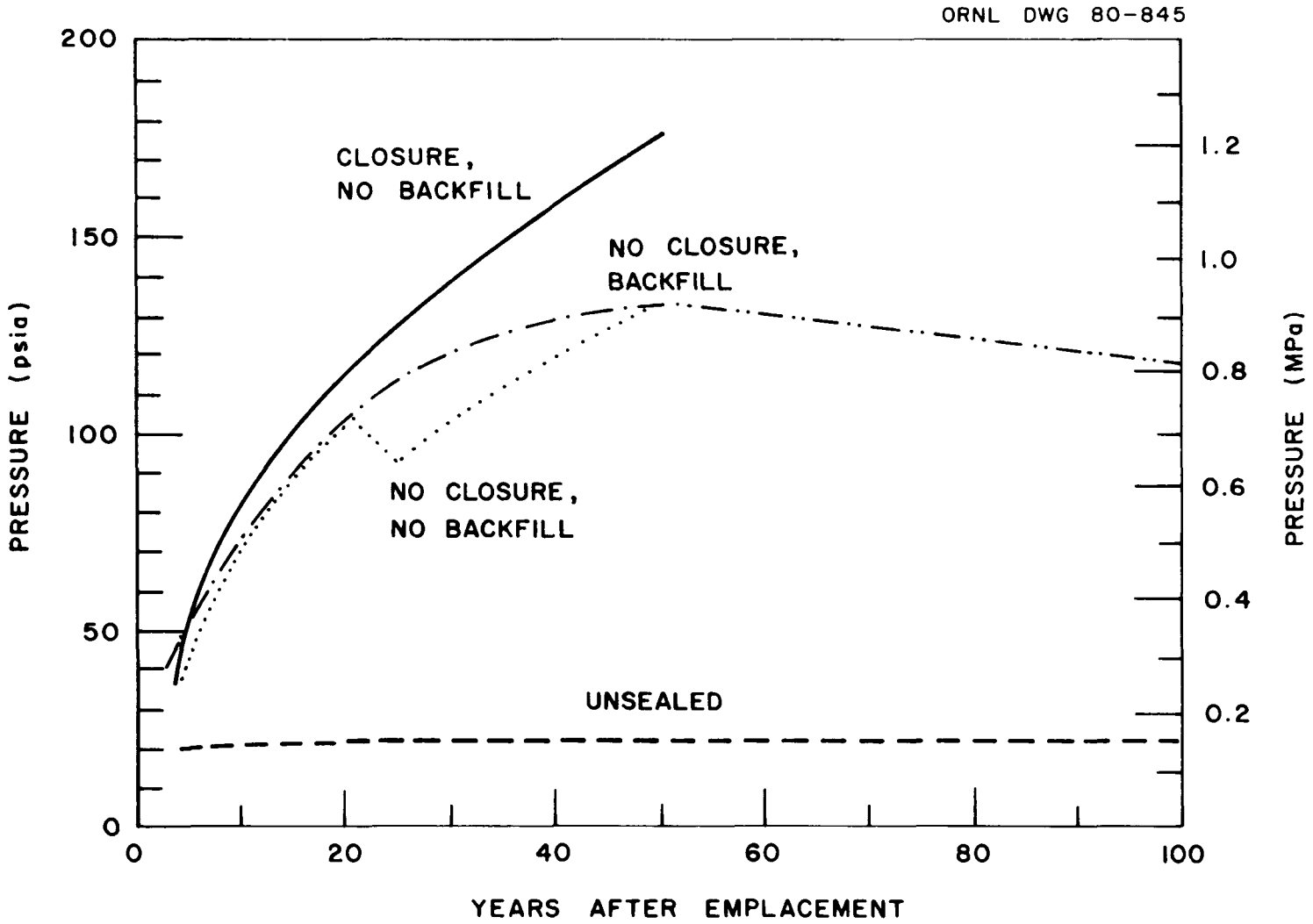

Fig. 41. Pressure histories for two-row configuration — PWR spent fuel at 130 kW/acre (37.1 W/m^2).

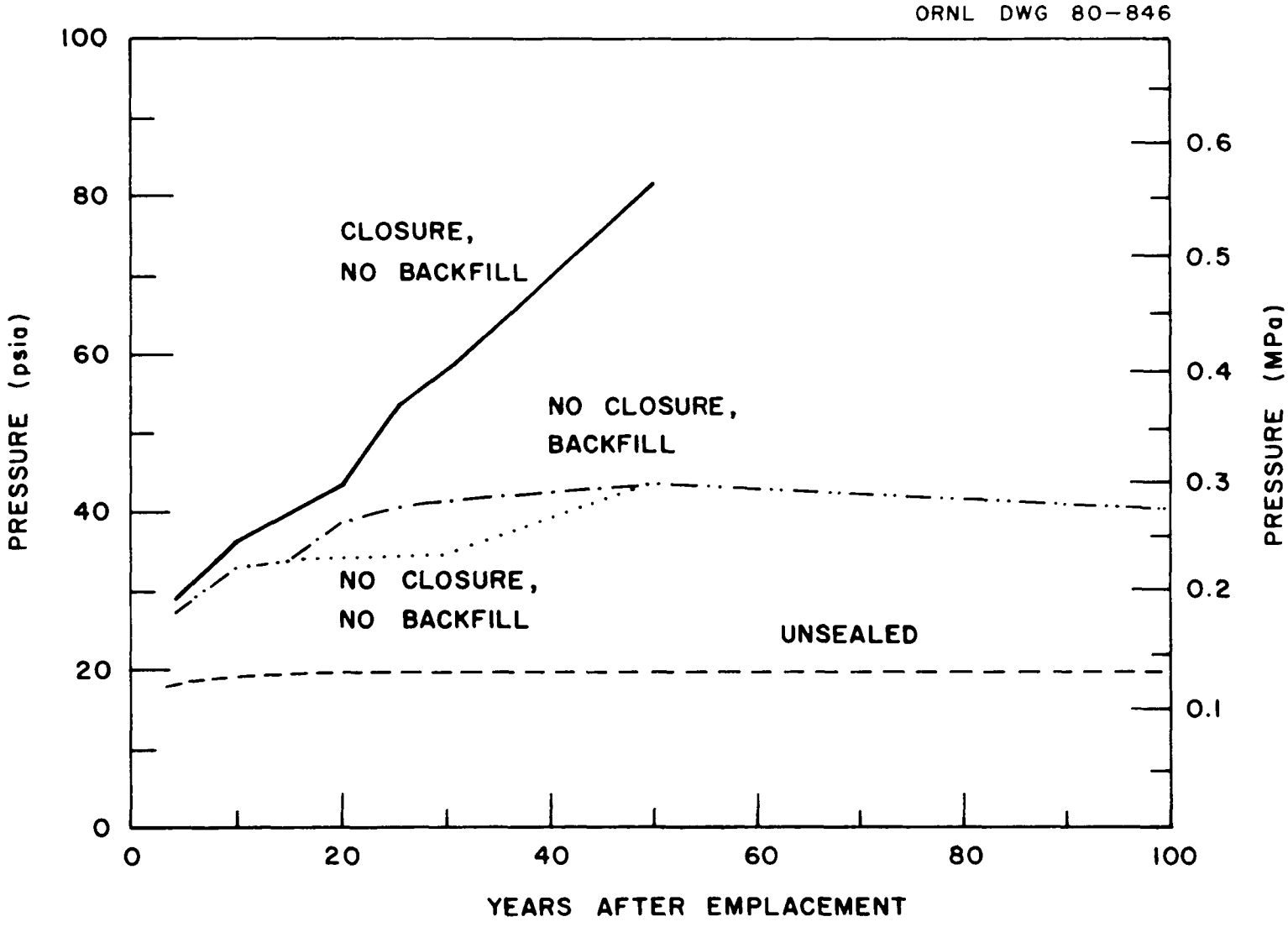

Fig. 42. Pressure histories for two-row configuration — BWR spent fuel at 83 kW/acre (20.5 W/m^2).

the emplacement hole have been made for the sealed-hole scenarios of Sect. 4.2. The results for the HLW and SF baseline cases are shown in Figs. 43 and 44, respectively. Additional results are given in Appendix G. The weight of residual brine in Figs. 43 and 44 includes the liquid water and the salt dissolved in the water. Since the water is in intimate contact with the solid salt, the concentration of salt in the brine is assumed to be the saturation value. The water vapor obviously does not contain salt, and the salt that was associated with this water prior to the phase change must precipitate out.

The amount of residual brine remaining in liquid form depends on the temperature and pressure encountered in the emplacement hole. The temperatures used in these calculations are those existing at the midplane of the emplacement hole wall. The equilibrium approximations previously discussed are applied based on the midplane temperature at the inner edge of the salt. Possible condensation of the fluid at cooler regions above the waste package with potential reflexing action and other dynamic effects were not taken into account. The model is obviously very crude because of these dynamic effects and the axial temperature variations were neglected. However, it was felt that the model would be useful in demonstrating possible brine water behavior and guiding future experiments and model development.

Figure 44 shows a sudden decrease in the brine quantity at $\sim$10 yr. At this point, the temperature exceeds the boiling point for the existing pressure, and water begins to vaporize to reduce the amount of brine. This dip is not seen for the HLW case in Fig. 41 since the temperatures are higher and the pressure is below the associated saturation pressure from the time that brine begins to flow into the emplacement hole.

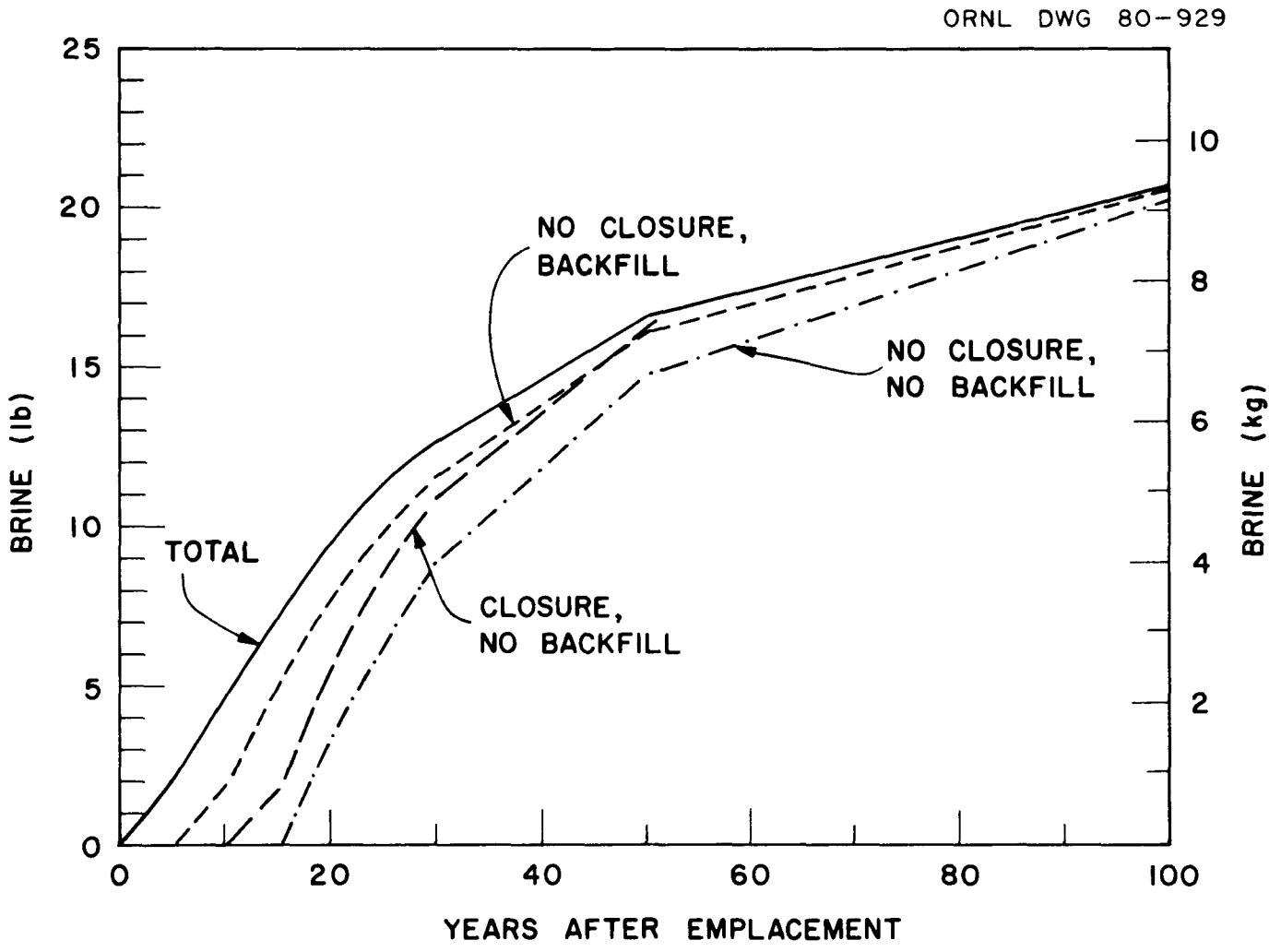

Fig. 43. Residual brine histories for high-level waste for an areal thermal load of 150 kW/acre (37.1 W/m^2).

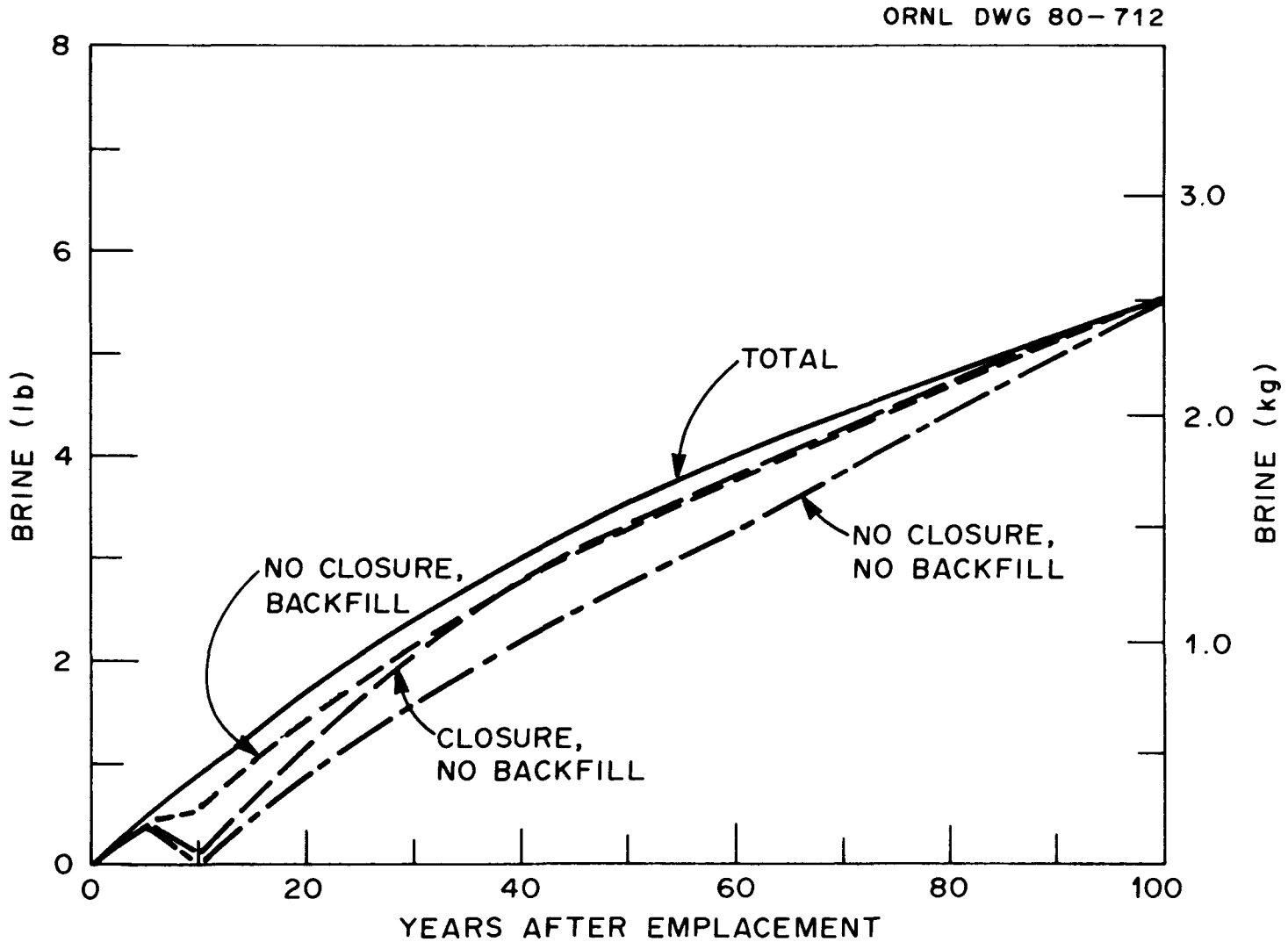

Fig. 44. Residual brine histories for spent fuel for an areal thermal load of 60 kW/acre (14.8 W/m^2).

5. CHEMICAL ENVIRONMENT

The postulated inflow of brine to the emplacement hole leads to complex chemical reactions that involve radiolysis and hydrolysis of the brine and reactions with the canister and backfill material. The actual radiation chemistry depends on the compositions of the liquids and solids around a waste-SF package and the characteristics and dimensions of the waste package. The effects of these chemical reactions do not seem to pose a threat to the long-term integrity of the geologic formation but could cause deterioration of the waste package. Generation of hydrogen gas by the corrosion of steel can cause a problem in the operational phase, but the hazard can be minimized by proper design and safety procedures.

With the advent of the multiple-barrier concept, where the canister is considered to be a barrier, corrosion of the canister in the disposal phase becomes an important consideration. Prior concepts for salt disposal assumed that the canister could corrode away within a few months. The canister merely served as a handling medium prior to emplacement. The later ready-retrievability restriction added the requirement that the integrity of the canister in air be maintained for 5 to 25 yr when protected from any incoming brine by a steel sleeve or overpack. A specification for the lifetime of a canister in the disposal phase in salt has not yet been established. It could be months, 100 yr, or 1000 yr, depending on regulatory decisions. Estimated effects of brine chemistry and corrosion rates on the canisters would then become very important.

5.1 Brine Chemistry

Jenks has thoroughly examined the available theoretical and experimental information on brine chemistry in radiation fields in two reports (refs. 14-15). In a third report,[16] he estimated potential corrosion rates on waste-SF canisters. Considering the complexity of radiation chemistry and possibilities for widely varying corrosion rates which depend on assumed conditions, the results will be only briefly summarized here.

In the first report (ref. 14), he gave a detailed review and analysis of literature related to the radiation and thermal chemistries of the salt and brines within the vicinity of a buried HLW canister in a waste repository in salt. The objectives were to identify the final radiolysis and thermal reaction products and to estimate the amounts formed and released into the spaces around a can. It was determined that important radiolysis products include H_2, O_2, and possibly ClO_3^- and BrO_3^-. Most of the ClO_3^- and BrO_3^- will decompose to halides and O_2 at the high temperatures around a can; $Mg(BrO_3)_2$, if present, may give rise to some Br_2. Radiolytic H_2, and the accompanying oxidized species, is formed within the migrating brine inclusions by the radiation absorbed within the brine and by dissolution of the aggregates of trapped holes and trapped electrons within the irradiated salt. Any brine that enters the open spaces around a canister will lose water by several processes, including reaction with the iron canister, radiolytic decomposition, and evaporation. The loss of water from the $MgCl_2$-rich, NaCl-saturated solutions results in the precipitation of NaCl and an increase in the concentration of $MgCl_2$. With continued loss of water, the solutions become saturated in $MgCl_2$, and a solid hydrate precipitates. Either $MgCl_2 \cdot 6H_2O$ and/or $MgCl_2 \cdot 4H_2O$ may form, depending on the temperature of the system. Radiolysis will continue in the space around the canister at a higher rate of generation of radiolytic products per unit weight of water present in the space. However, the total amount generated within the space per unit weight of incoming brine will decrease because of the water-loss mechanisms described above (Jenks, Appendix A, ref. 15). The brine is rich in $MgCl_2$ (2.3 to 3 M), and hydrolysis of the $MgCl_2$ around a can at temperatures >180°C will produce HCl that could accelerate corrosion.

In the second report,[15] the state of the art was again reviewed. The principle objective was to assess the need for any additional work in radiation chemistry involving the brines and solids around the waste canisters. The reference waste and SF packages considered were essentially the same as those in this report. Jenks concluded that the following additional experimental information would be useful:

1. yield of radiolytic hydrogen in NaCl and $MgCl_2$ solutions at 25 to 200°C and vapor pressures $\leq$1 atm (0.10 MPa);
2. effects of gamma rays on $MgCl_2$ hydrates at 25 to 200°C;
3. effect of gamma rays on slushes of salt and salt-mine brine at temperatures up to 200°C and vapor pressures $\leq$1 atm (0.01 MPa);
4. chemistry and radiation chemistry of dessicant-containing backfills after they have been exposed to salt brines.

5.2 Corrosion of Steel and Zircaloy

In a specific application of the information on chemistry and radiation chemistry, Jenks estimated corrosion rates of carbon steel in the environments which might occur around a reference SF canister emplaced in a salt repository.[16] Slightly higher corrosion ratios could be expected for a HLW canister because of the higher temperatures involved. Stainless steel does not appear to be a good material for the canister and overpack designs because of possible stress-corrosion cracking due to the presence of chlorides.

The experimental indications were that in the absence of a liquid phase, corrosion rates of <1 mil per year would occur for the conditions around a SF canister. With the liquid phase present, corrosion rates could still be minimal under certain conditions. The final reaction products of the corrosion of steel in deaerated environments are Fe_3O_4 and H_2, with some ferrous ions remaining in solution. Under the conditions that would exist for a sealed repository, the required oxygen must come primarily from brine that migrates into the emplacement hole, since a liquid phase is necessary in the corrosion mechanism. The oxygen and brine in the backfill can be isolated from the waste package by engineering design. Jenks points out that 455 g water/yr when completely reacted with a steel canister SF will result in an average corrosion rate of 1 mil per year.[16] For the smaller HLW canister, the same quantity of water could produce an average corrosion rate of $\sim$2 mil per year. On this basis, lifetimes of 100 yr or more could be predicted for the case discussed in Sect. 3. However, Jenks concluded that rapid localized corrosion is the most likely avenue through which the wall of the

canister could be breached in a relatively short time (2 to 30 yr) after emplacement. The potential mechanisms for localized corrosion could occur as a result of the pressure-temperature-concentration properties of the brines and the formation of radiolytic O_2 in the liquid brine. He also concluded that rapid, localized corrosion is a strong possibility, unless special provisions are made to avoid it.

It appears that on the basis of this investigation into corrosion properties of carbon steel that a steel canister could remain essentially intact for hundreds of years in the estimated environment of an SF repository, although small holes seem probable in a shorter time.

As a precaution against a serious underestimation of the brine inflow or other mechanisms that could supply sufficient water to completely corrode the canister, water scavenging materials are being considered for use in the backfill. Jenks[16] suggested the use of quicklime (CaO)-sand mixtures or possibly quicklime-crushed salt mixtures.

Other types of desiccants for use around waste canisters in salt are under investigation by others (ref. 17). Chemical addition that would promote the formation of tachydrite ($2MgCl_2 \cdot CaCl_2 \cdot 12H_2O$) or a mixture of bentonite and quartz are other possibilities.

The Zircaloy or stainless steel used as fuel pin cladding could serve as an additional barrier in the case of SF disposal. Zircaloy is very resistant to general corrosion in salt brines at temperatures of interest in SF disposal in bedded salt. However, it is known to be subject to stress-corrosion cracking in brine solutions when anodically polarized by galvanic coupling with alloys such as a stainless steel which would be present as part of the fuel assembly. Austenitic stainless steel is also subject to stress-corrosion cracking in chloride solutions at elevated temperatures, especially when oxygen is present. Consequently, it must be assumed that both the stainless steel or Zircaloy cladding on fuel pins will be breached by cracking soon after the cladding is contacted by any brine solution that enters through a break in the canister.

5.3 Brine Compositions

Three types of brine compositions that need to be considered in determining the effects of interaction with a waste-SF canister include compositions of the brine inclusions, the reacted brine in the emplacement hole, and brine resulting from dissolution of the salt formation, such as what might occur from mine flooding or other water intrusion incidents. The following material on brine compositions is taken from reports by Jenks.[10,16]

5.3.1 Composition of brine inclusions and dissolution of the salt formation

The estimated concentrations of various elemental species that occur in the bedded salt (Hutchinson formation) near Lyons, Kansas, are shown in Table 9. These values are based on a combination of experimental determinations, available information on the solubility of NaCl in NaCl-saturated $MgCl_2$ solutions, and a reasonable assumption that small concentrations of the other constituents have a negligible effect on the NaCl solubility.

The brines included within bedded salt at potential repository sites have not been analyzed directly. The composition for the WIPP brine inclusions (Brine A in Table 10) was based on the analyses of several brines from the McNutt potash-bearing region of the Salado formation. Consequently, these brines were rich in potassium; the concentration in Brine A was 0.77 M at 25°C. The concentrations of sodium and calcium in Brine A are comparable to those found in the Kansas brines mentioned previously; the magnesium concentration is appreciably smaller.

Results of chemical analyses of core samples of salt obtained near the WIPP area have been reported by Beane and Popp[18] and by Molecke,[17] and information on brine composition can be inferred from their data.

The following is a summary of information given by Beane and Popp for samples of salt taken from AEC Core 8 between depths of 2615 and 2821 ft (797 and 860 m). The results showed that NaCl was the major constituent and anhydrite was a minor constituent with trace amounts of

Table 9. Summary of analytical and deduced values for concentrations of various species in Kansas salt brine inclusions

	Concentrations	
	Molar at 25°C (mol/ℓ)	Molal (mol/kg H_2O)
Mg	2.12	2.41
Na	1.91	2.16
K	0.28	0.32
Ca	0.03	0.034
Cl	6.29	7.15
Br	0.04	0.045
SO_4	0.078	0.089

Table 10. Compositions of Waste Isolation Pilot plant Brines A and B[a]

Ion	Concentration [(mg/ℓ) ± 3%]	
	Brine A	Brine B
Na^+	42,000	115,000
K^+	30,000	15
Mg^{2+}	35,000	10
Ca^{2+}	600	900
Fe^{3+}	2	2
Sr^{2+}	5	15
Li^+	20	
Rb^+	20	1
Cs^+	1	1
Cl^-	190,000	175,000
SO_4^{2-}	3,500	3,500
$B(BO_3^{3-})$	1,200	10
HCO_3^-	700	10
NO_3		
Br^-	400	400
I^-	10	10
pH (adjusted)	6.5	6.5
Specific gravity	1.2	1.2

[a]M. A. Molecke, Sandia Laboratories, personal communication to G. H. Jenks, ORNL.

one or more of the following: iron oxide, K-feldspar, talc, chlorite, polyhalite, carnallite, bloedite, and quartz. The results of analyses for K, Mg, and Ca were as follows: K, 0.03 wt % average, with maximum and minimum values of 0.09 and 0.01 wt %, respectively; Mg, 0.05 wt % average, with maximum values of 0.006 and 0.13 wt % in the soluble and insoluble portions of the samples, respectively; Ca, 0.62 wt % average, with maximum and minimum values of 1.3 and 0.14 wt %, respectively. The average weight losses on heating finely ground samples to 70, 200, and >400°C were 0.17, 0.18, and 0.47 wt %, respectively. The three largest weight losses among the samples that were heated to >400°C were 1.66, 0.77, and 0.48 wt %. Samples from the same locations as these three also had appreciable amounts of insoluble material — 1.25, 0.92, and 0.91%, respectively.

The results reported by Beane and Popp[18] for AEC Core 7 samples were in substantial agreement with those summarized above for Core 8 samples.

Pertinent inferences that can be drawn from the analytical results summarized previously and from those presented by Beane and Popp are as follows:

1. The samples contained very little potassium, 0.032 wt % average.
2. The magnesium content of the samples was very low, averaging 0.006 wt % in the soluble portions. If the brine inclusions within the crystal boundaries of the salt contained $MgCl_2$ at a concentration of 2 M, the average amount of water within the inclusions was 0.13 wt %.
3. All of the calcium (average, 0.62 wt %) was in the anhydrite form. No calcium was present as CaCl.

The WIPP Brine B, which represents the composition of brine occurring in a flooded mine condition (Table 10), was based on the analysis of a saturated brine solution obtained by dissolving a portion of AEC Core 8 taken at a depth of 2725 ft (830 m). The reported composition is in good agreement with expected results based on previously summarized data for Core 8. In particular, it can be noted that the molar concentration

of SO_4 exceeded that of calcium by ∿60%, indicating that all of the calcium was present as $CaSO_4$, which would preclude the presence of significant amounts of $CaCl_2$.

5.3.2 Possible brine composition in the emplacement hole

If the brine inclusions enter the open spaces around a canister, they will lose water by several processes, including reaction with the iron canister, radiolytic decomposition, and evaporation. The loss of water from the $MgCl_2$-rich, NaCl-saturated solutions results in the precipitation of NaCl and an increase in the concentration of $MgCl_2$ (Figs. 45 and 46). With continued loss of water, the solutions become saturated in $MgCl_2$, and a solid hydrate precipitates. This hydrate is either $MgCl_2 \cdot 6H_2O$ and/or $MgCl_2 \cdot 4H_2O$, depending upon the temperature of the system (Fig. 45). These hydrates exert vapor pressures of water, and they can be converted to lower hydrates at suitably low partial pressures of water vapor (Fig. 46). The hydrates can also undergo hydrolysis to form solid hydroxy chloride, MgOHCl, and HCl gas. However, this hydrolysis reaction is likely to be very slow at the relatively low temperatures around SF canisters in salt and not much greater for the HLW case.

The $MgCl_2$-rich solutions will undergo hydrolyses to some extent at temperatures which are present around reference canisters (<150°C) and will be accompanied by the formation of soluble hydroxy complexes and hydrogen ions.

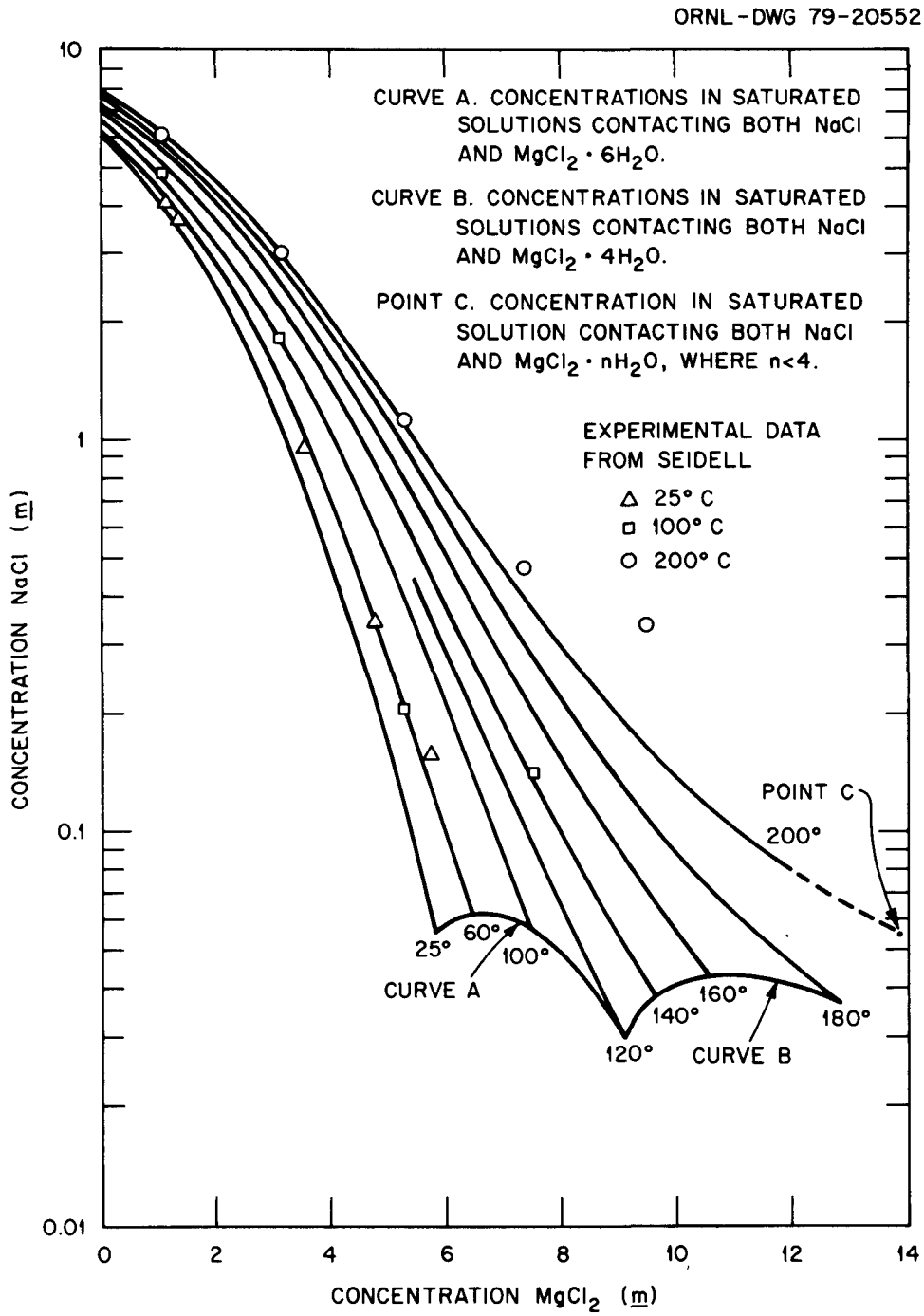

Fig. 45. Calculated concentration of NaCl vs concentration of $MgCl_2$ in NaCl-saturated solutions at 25 to 200°C compared with experimental values (taken from Jenks[15]).

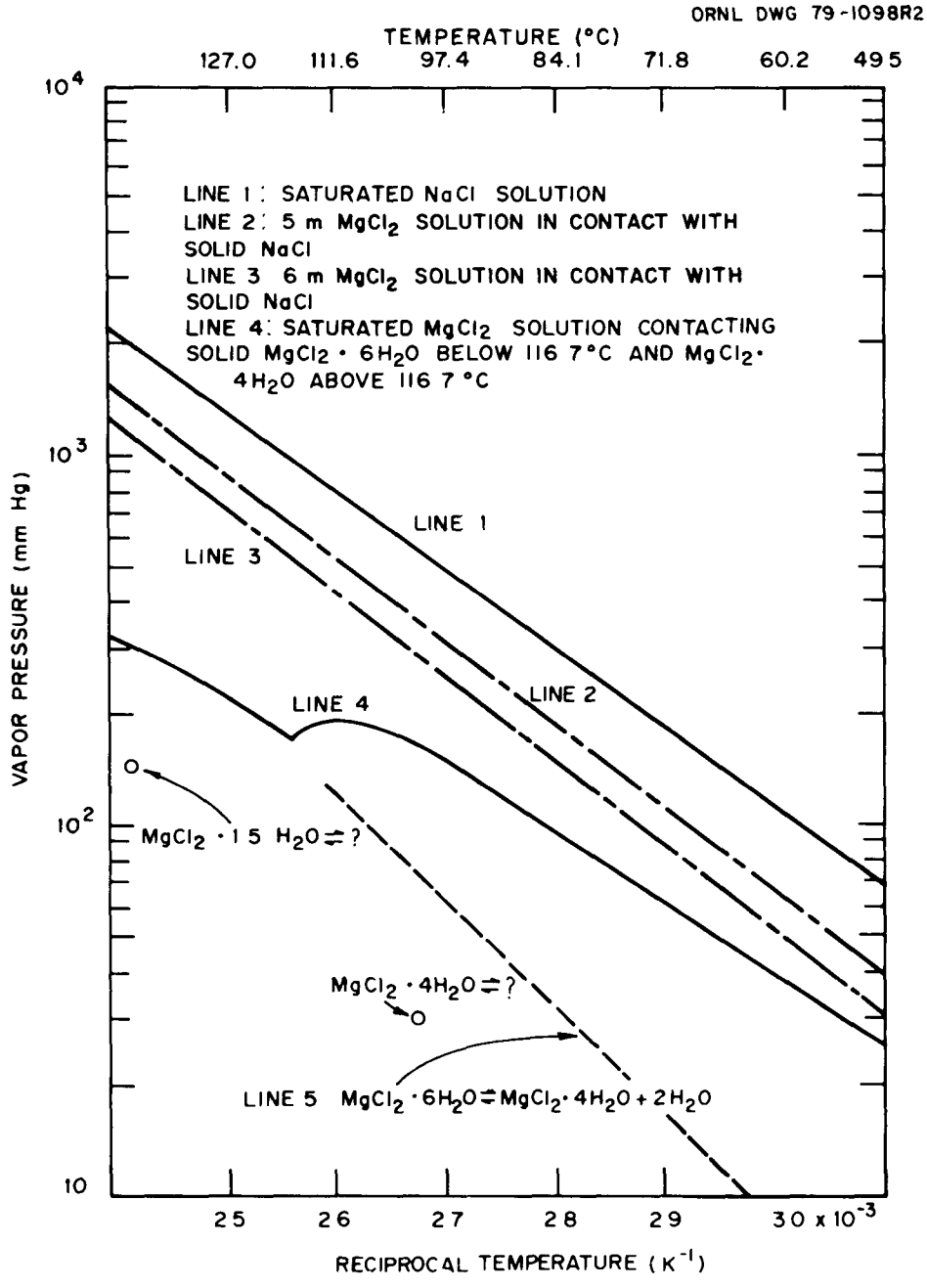

Fig. 46. Vapor pressure of water over NaCl and $MgCl_2$ solutions and over $MgCl_2$ solid hydrates vs temperature.

6. NUCLEAR RADIATION ENVIRONMENT

The neutron and gamma-ray radiation fields arising from the waste-SF canisters can be divided into three categories of effects: (1) exposure to operating personnel, (2) radiation chemistry, and (3) stored energy in the waste forms and rock salt. The first category is dependent on a specific design and operating procedure and, consequently, is beyond the scope of this report. The effects of radiation on brine chemistry was briefly discussed in the previous section based on the work by Jenks.[16] He estimated the radiation effects on brine using absorbed radiation doses to the brine based on the calculations of others, which are approximately applicable to the reference repository environments.

Energy can be stored in solids as a result of radiation damage or crystal dislocations within crystal lattices. Theoretically, this energy can be released when annealed at higher temperatures. This phenomenon has been under investigation for many years. In an analysis of the effects of energy storage in a salt repository, Blomeke et al.[19] concluded that the release of stored energy (if at all possible for a repository) would produce no serious consequences even for the most pessimistic assumptions.

Jenks and Bopp[20] later conducted extensive experimental studies of the gamma-ray energy that is stored in salt under a variety of exposure conditions, the thermal annealing characteristics of the stored energy, the chemical reactions that radiation defects in the salt undergo upon aqueous dissolution of the salt, and the retention of the radiation defects within the salt crystals. The objective was to obtain additional information for predicting the amounts and release characteristics of stored gamma-ray energy in the salt of a waste repository.

The results of this work confirmed that appreciable amounts of gamma-radiation energy can be stored under certain exposure conditions and that thermally activated annealing takes place at elevated temperatures. The rates of this annealing at temperatures above $\sim$150°C are such that negligible amounts of energy will be stored in salt in a repository where the salt is at temperatures above $\sim$150°C.

Jenks and Bopp were unable to show that thermally activated annealing takes place in rock salt at temperatures below ∿150°C, although it is possible, as well as some radiation-induced annealing. The results of the measurements of energy stored at irradiation temperatures between 30 and 150°C, together with the results of theoretical considerations, showed that the maximum stored energy that would be formed in salt in a repository with no annealing whatsoever would be ∿50 cal/g (209 J/g). They could not conceive of a means by which the stored energy could be released abruptly, nor was any significant hazard believed to be possible from the release if it should occur abruptly by some unforeseen mechanism.

Radiation damage in salt results in the formation of F-centers, which are formed by the displacement of the chlorine atom from a lattice position and the trapping of an electron at that position. Aggregates of these defects lead to the formation of collodial sodium and chlorine that remains trapped in the crystal structure. Jenks and Bopp report that the available evidence from thermal annealing observations and from calorimetric and dissolution measurements indicated that there were no significant losses of either chlorine or sodium during or after irradiation.

Another effect of the stored energy is the generation of H_2, which takes place upon aqueous dissolution of radiation-damaged salt; ∿0.1 cm^3 of H_2 at STP is generated per calorie (4.2 J) of stored energy. However, fresh water is required for the dissolution, which normally will not be present. In any event, there appears to be no problems arising from this effect that cannot be counteracted by appropriate design and operation of a repository.

The energy absorbed in the salt for the reference cases of this report was calculated using the one-dimensional ANISN shielding code.[21] Actually, kerma (kinetic energy released in materials) factors were used to convert gamma fluxes to absorbed dose rates (the neutron contribution will be negligible), but for all practical purposes kerma and absorbed dose are equal for the configurations considered here. The calculated dose rates (beginning at the inner edge of the crushed salt zone) are shown in Figs. 47 and 48 for HLW and SF, respectively, at emplacement

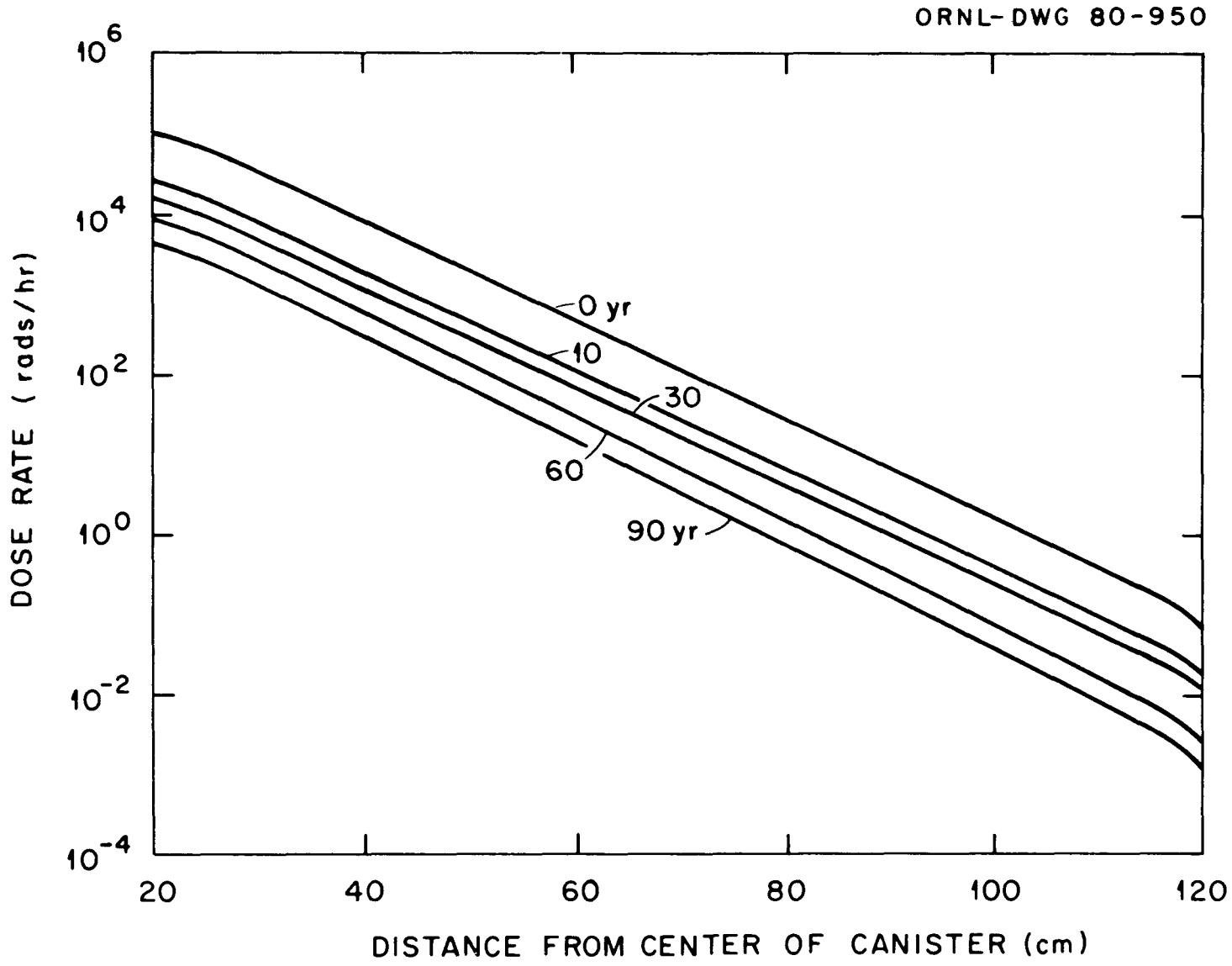

Fig. 47. Dose rates to the salt from an emplaced high-level-waste canister (2.16 kW/canister) for 0 to 90 yr after emplacement.

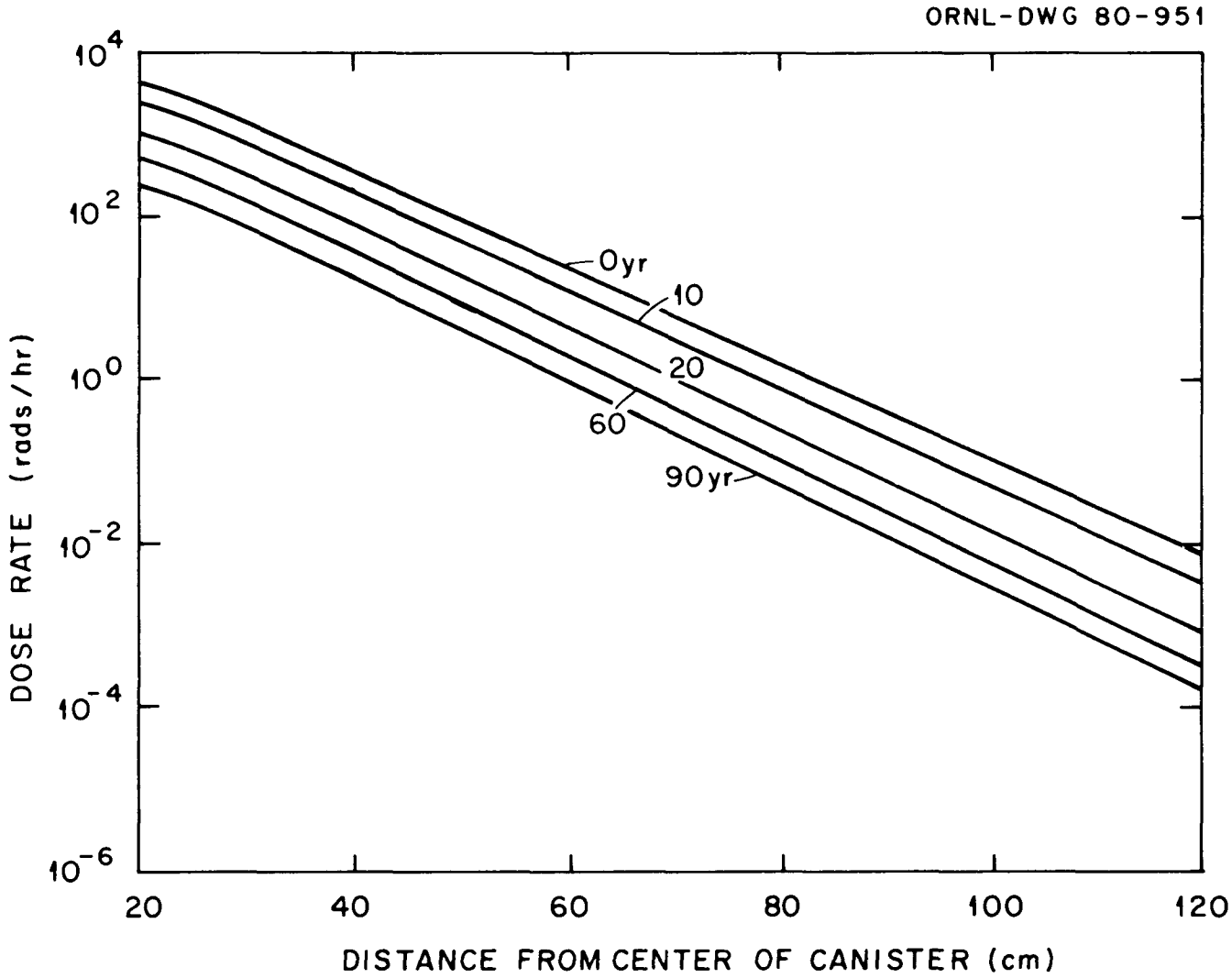

Fig. 48. Dose rates to the salt from an emplaced SF canister (0.55 kW/canister) for 0 to 90 yr after emplacement.

and 10, 30, 60, and 90 yr after emplacement. The maximum absorbed dose rate at the inner edge of the crushed salt backfill at emplacement is 10×10^5 and 4.1×10^3 rads/h for HLW and SF, respectively. These results will closely approximate the mid-plane dose rates that would be obtained with a 2-D calculation using a finite canister height that would tend toward a slight overestimation with increasing distance from the canister. The dose rates at the ends of the canisters would be approximately one-half of the mid-plane values.

The integrated dose at the inner edge of the crushed salt as a function of time is shown in Fig. 49 for both HLW and SF. Dose rates beyond 90 yr were estimated by assuming that the shape of the gamma spectrum remains constant and that the dose rates would be proportional to the total gamma-energy release rate. The absorbed dose integrated over 10,000 yr is 1.6×10^{10} and 9.6×10^8 rads for HLW and SF, respectively.

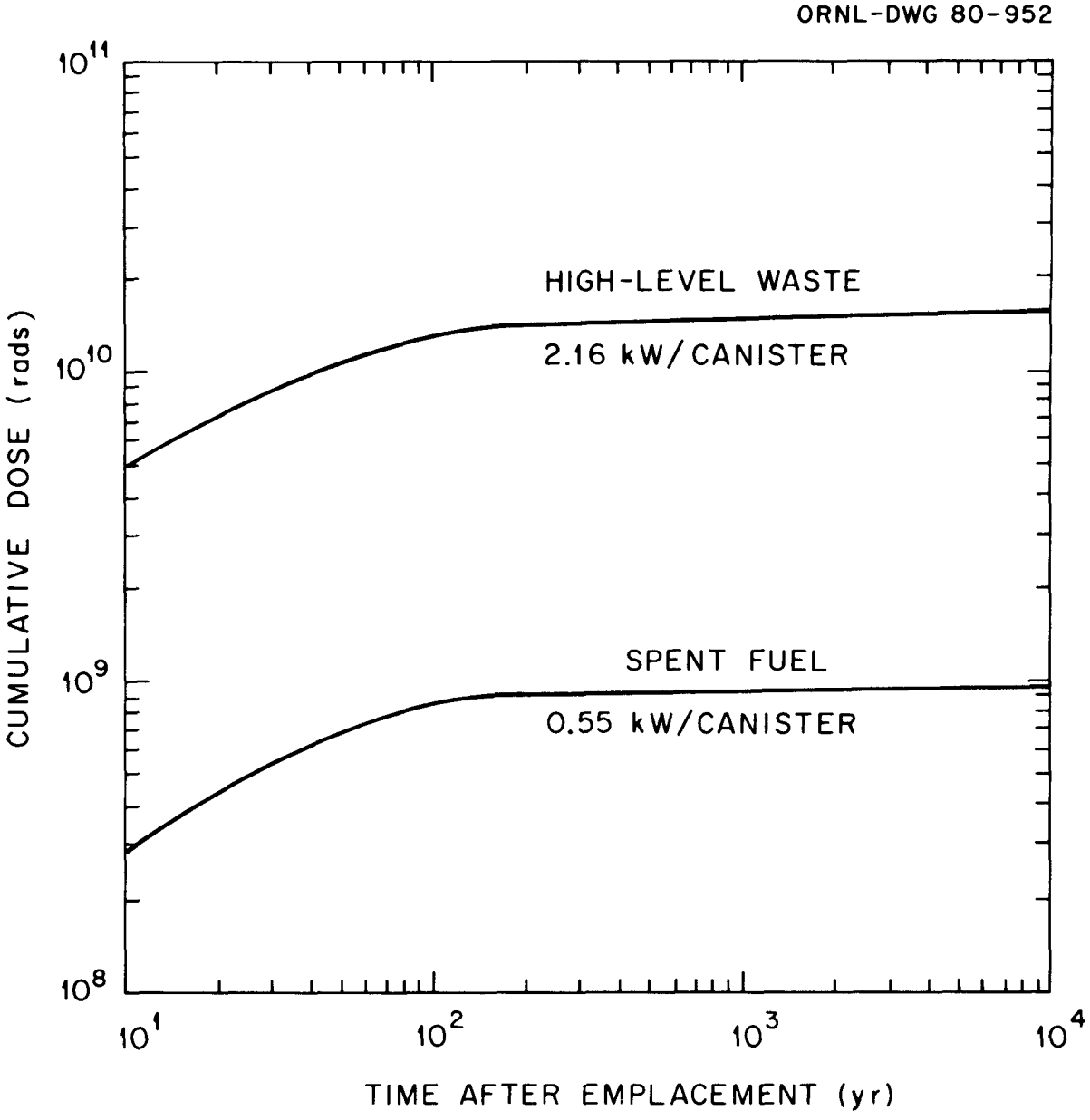

Fig. 49. Cumulative doses to the salt as a function of time for high-level-waste and spent-fuel canisters.

7. REFERENCES

1. U.S. Department of Energy, Management of Commercially Generated Radioactive Waste, DOE/EIS-0046-D, vol. 2 (April 1979).

2. Conceptual Design Report—National Waste Terminal Storage Repository for Storing Reprocessing Waste in a Dome Salt Formation—Conceptual Design Study No. 6—Thermal Analysis, DOE Contract No. EY-77-C-05-5367 (September 1977).

3. National Waste Terminal Storage (NWTS) Conceptual Reference Repository Description (CRRD), Office of Nuclear Waste Isolation, ONWI/SUB/79/E512-01600.16, vol. 3 (September 1979).

4. W. D. Turner, D. C. Elrod, and I. I. Siman-Tov, HEATING5—An IBM 360 Heat Conduction Program, ORNL/CSD/TM-15 (March 1977).

5. Office of Waste Isolation, Thermal Analysis of a Ventilated High-Level Waste Repository, Y/OWI/SUB-76/16527 (April 1977).

6. Office of Waste Isolation, Technical Support for GEIS: Radioactive Waste Isolation in Geologic Formations, vol. 19, Thermal Analysis, Y/OWI/TM-36/19 (April 1978).

7. G. H. Llewellyn, Prediction of Temperature Increases in a Salt Repository Expected from the Storage of Spent Fuel or High Level Waste, ORNL/ENG/TM-7 (April 1978).

8. J. O. Bredehoeft, Geologic Disposal of High-Level Radioactive Wastes — Earth Sciences Perspectives, USGS Circular 779, 1978.

9. N. L. Bradshaw and W. C. McClain, Project Salt Vault: A Demonstration of the Disposal of High-Activity Solidified Waste in Underground Salt Mines, ORNL-4555 (1971).

10. G. H. Jenks, Effects of Temperature, Temperature Gradients, Stress, and Irradiations of Brine Inclusions in a Salt Repository, ORNL-5526 (July 1979).

11. T. R. Anthony and H. E. Cline, "Thermal Migration of Liquid Droplets through Solids," J. Appl. Phys. 42, 3380 (1971).

12. K. J. Bathe, ADINAT—A Finite Element Program for Automatic Dynamics Incremental Nonlinear Analysis of Temperature, Massachusetts Institute of Technology Report 82448-5 (May 1977).

13. RE/SPEC, Inc., Heat Transfer Analysis of the Waste-Container Sleeve/Salt Configuration, ORNL/SUB-4269/7 (March 1976).

14. G. H. Jenks, Radiolysis and Hydrolysis in Salt-Mine Brines, ORNL/TM-3717 (March 1972).

15. G. H. Jenks, Radiolysis in Salt Brines and Effects on Repositories in Rock Salt, ORNL-5607 (March 1980).

16. G. H. Jenks, Effects of Gaseous Radioactive Nuclides on the Design and Operation of Repositories for Spent LWR Fuels in Rock Salt, ORNL-5578 (December 1979).

17. M. A. Molecke, Sandia Laboratories, personal communication to G. H. Jenks, ORNL (Nov. 15, 1978).

18. R. E. Beane and C. J. Popp, Chemical, Mineralogical, and Thermogravimetric Analysis of Selected Core Samples from Carlsbad, New Mexico, ORNL/SUB-3673/3 (June 1975).

19. J. O. Blomeke et al., An Analysis of Energy Storage and Its Effects in the Proposed National Radioactive Waste Repository, ORNL/TM-3403 (June 1971).

20. G. H. Jenks and C. D. Bopp, Storage and Release of Radiation Energy in Salt in Radioactive Waste Repositories, ORNL-5058 (October 1972).

21. W. W. Engle, Jr., A User's Manual for ANISN—A One Dimensional Discrete Ordinates Transport Code with Anisotropic Scattering, UCND-K-1693 (1967).

APPENDIX A: DETAILS OF THE NEAR-FIELD MODELS

The detailed listings of the model coordinates used to define the mesh spacing for the unit-cell models described in Sect. 2.1.1 are given here.

The 3-D unit-cell model (Fig. 1) has the mesh spacing indicated by Table A-1. The waste (or fuel assembly) is assumed to be uniformly distributed in a right parallelepiped with a cross-section equal to that of a canister. For HLW, the cross section is a square that is 0.886 ft (0.264 m) on a side and for SF, 0.974 ft (0.297 m) on a side. The calculational model comprises only one-quarter of the unit cell because of symmetry with respect to the x and y axes. The model width is equal to one-half the room and pillar width [39 ft (11.9 m)], and the dimension (half-pitch) of the unit cell between the plane normal to the pillar that intersects the canister centerline and the one that forms the adiabatic boundary between successive canisters is obtained from the following equation:

$$Y = \frac{\text{canister heat load}}{2 \times \text{areal heat load} \times (\text{room width} + \text{pillar width})} \quad . \qquad \text{(A-1)}$$

The near-field axisymmetric unit-cell model as discussed in Sect. 2.1.1 and shown pictorially in Fig. 2 has the mesh spacing indicated by Table A-1. The model is cylindrical, with the HLW located between 1996 and 2004 ft (608.4 and 610.8 m) and the SF located between 1994 and 2006 ft (607.8 and 611.4 m). The HLW canister has a 6-in. (15.2-cm) radius (Fig. 3). An air gap is between the canister and the overpack and is 1.5 in. (9.8 cm) thick for the HLW and 0.875 in. (2.22 cm) thick for SF. The emplacement hole radius is 10 in. (25.4 cm), making the backfill thickness 2 in. (5.08 cm) for both the HLW and SF.

The model radius has been given in Sect. 2.1.1 for all the HLW and SF cases, and Table A-2 shows the 150-kW/acre (37.1 W/m^2) case for HLW and the 60-kW/acre (14.8-W/m^2) case for SF. The model radius depends on the canister load and the areal load as given by the following equation:

$$\text{model area} = \frac{\text{canister heat load}}{\text{areal heat load}} \quad . \qquad \text{(A-2)}$$

Table A-1. Nodal coordinates for near-field 3-D unit-cell studies

z (depth below surface, ft)		x (distance from centerline normal pillar, ft)		y (distance from waste centerline along storage room, ft)	
HLW	SF	HLW	SF	HLW	SF
0	0	0	0	0	0
1000	1000	0.443	0.487	0.443	0.487
1600	1600	1.0	0.8	1.0	0.8
1850	1850	1.75	1.75	1.75	1.3
1928	1928	3.5	3.5	2.6	2.56
1961	1961	7.0	7.0	4.2	
1986	1986	10.0	10.0		
1991	1994	15.0	17.2		
1995	1995	25.0	29.0		
1996	1996	39.0	39.0		
1997	1997				
2000	2000				
2003	2003				
2004	2004				
2005	2006				
2009	2009				
2018	2018				
2035	2035				
2072	2072				
2150	2150				
2400	2400				
3000	3000				
4000	4000				
8000	8000				

Table A-2. Nodal coordinates used for near-field axisymmetric unit-cell studies

z (depth below surface, ft)		r (radial distance from centerline, ft)	
HLW	SF	HLW	SF
1000	1000	0.0	0.0
1600	1600	0.5	0.55
1850	1850	0.53	0.56
1928	1928	0.63	0.63
1961	1968	0.66	0.67
1986	1981	0.833	0.833
1991	1991	1.0	1.0
1994	1994	1.33	1.33
1994.5	1995	1.75	1.75
1995	1996	3.0	3.0
1996	1997	6.0	6.0
1997	2000	9.0	9.0
2000	2003	14.13	11.27
2003	2004		
2004	2005		
2005	2006		
2009	2009		
2018	2018		
2035	2035		
2072	2072		
2150	2150		
2400	2400		
3000	3000		

The iteration scheme used for both models was the implicit finite-difference Crank-Nicolson technique, with an initial time step of 0.01 h and an initial successive overrelaxation acceleration parameter of 1.1, which was optimized every time step by no more than a 10% change.

APPENDIX B: TEMPERATURES OF SPENT FUEL ELEMENTS

Heat transfer from SF assemblies in canisters involves radiative heat transfer among the rods in the SF bundle, convective processes involving any gas filler in the canister, and heat conduction processes. Because of the nature of the configuration of SF rods in the canister, the time-dependent heat-generation rates, and the nonuniform material and heat transfer properties, the problem presents severe calculational difficulties. However, because temperature criteria will be placed on the SF rods stored in a repository for SF canisters, it is crucial that these temperatures be predicted accurately.

Recently, some fairly reliable techniques have been developed to treat these processes. The radiative heat transfer can be calculated using the geometrical techniques developed by Watson,[1] Klepper,[2] or Cox.[3] In the last reference, theoretical expressions are given for a variety of configurations. These equations have been programmed and can be evaluated numerically for both steady-state and transient conditions once the canister or boundary temperature is specified. R. A. McCann has recently developed a comprehensive computer model, HYDRA-1, which simultaneously treats convection, conduction, and radiative heat transfer and is described in reference 4. However, the application of the model to a specific problem requires considerable effort, experience, and cost. Nevertheless, calculations of the convection contribution to the heat transfer show contributions which justify the explicit treatment of this process along with radiation. A simplified procedure that is suitable for SF canisters placed in a geologic repository is proposed and applied here.

Theory predicts and calculations have shown that temperatures outside the canister are relatively independent of the configuration within the canister, depending almost entirely on the time-dependent heat flux across the canister walls. In this case, it is possible to calculate canister wall temperatures in a near-field model knowing only the total heat-generation rate in the canister. These calculations have been described elsewhere in this report. Calculations using HYDRA-1 for

selected canister wall temperatures and SF rod heat-generation rates show two interesting features:

1. For specified canister-wall temperatures, steady-state conditions are achieved fairly quickly (within 24 h).
2. In the range of canister temperatures expected for a repository, convective heat-transfer rates show a linear relationship to the heat generation rate, and canister wall temperatures.

These results are achieved for a variety of gas and solid fillers in the canister. The first result suggests that since changes in the heat generation rate and repository temperatures are known to be quite slow (peaks being achieved in the order of years), a quasi-static approximation may be used for the calculations. The second result suggests that it is possible to use interpolation or tabular information approaches to estimate convection effects on the maximum SF rod temperatures. These approximations have been tested and satisfactorily reproduce the results of the full calculation for SF element temperatures using HYDRA-1.

The procedure is illustrated for the case of canisters containing a single PWR SF element emplaced in a salt repository. The steady-state expression for the center pin temperature based on radiative heat transfer only is:

$$T_{pin} = [(T_{wall} + 460)^4 + (1.74 \times 10^6)QY]^{1/4} - 460 , \qquad (B\text{-}1)$$

where

T_{wall} = the canister wall temperature, °F;
Q = the assembly heat-generation rate, Btu/h; and
Y = a factor characteristic of the geometry and radiosity of the fuel rods.

Using the Cox program, Klepper's coefficients for nonuniform radiosity, and dimensions typical of a PWR spent fuel bundle, Y is calculated to be 93.6°F^4·h/Btu (30.4 K^4/W). Table B-1 shows the results of calculations for maximum SF temperatures based on the above equation. The values of Q chosen reflect those for 10- and 25-yr-old SF elements. The canister wall temperatures chosen are typical of those achieved in a repository. The results for other values of these parameters may be approximated by double interpolation of the results shown in Table B-1.

Table B-1. Calculated spent fuel temperatures

	Q(W)	T_{wall}		$\Delta T = T_{pin} - T_{wall}$				$\frac{\Delta T_{COX} - \Delta T_{HYDRA}}{\Delta T_{COX}}$
		°F	°C	COX, radiation only (°F)	COX, radiation only (°C)	HYDRA-1, full calculation (°F)	HYDRA-1, full calculation (°C)	
Nitrogen	0.554	212	100	175	97.2	106	58.9	0.39
	0.332	212	100	119	66.1	72	40.0	0.39
	0.554	356	180	115	63.9	92	51.1	0.20
	0.332	356	180	74	41.1	61	33.9	0.17
Helium	0.554	212	100	178	98.9	70	38.9	0.60
	0.332	212	100	119	66.1	45	25.0	0.62
	0.554	356	180	115	63.9	54	30.0	0.53
	0.332	356	180	74	41.1	32	17.8	0.57
Mullite and nitrogen	0.554	212	100			45	25.0	
	0.332	212	100			27	15.0	
	0.554	356	180			45	25.0	
	0.332	356	180			27	15.0	
Mullite and helium	0.554	212	100			29	16.1	
	0.332	212	100			18	10.0	
	0.554	356	180			29	16.1	
	0.332	356	180			18	10.0	

Also shown in Table B-1 are the results for the full calculation using HYDRA-1, including convection and conduction. From this table, it can be seen that the temperature rise is decreased ∿39% by convection for a canister wall temperature of 212°F (100°C). For a canister wall temperature of 356°F (180°C), the temperature rise is decreased ∿20% by convection. Similar behavior is observed in other situations, as illustrated in Table B-1 for fillers of helium gas, nitrogen gas, and mullite with the void spaces filled by helium or nitrogen. In the last two cases, only conduction is considered; there is no calculated radiative heat transfer. The conductivity of the mullite is taken to be 0.19 Btu/h·ft·°F (0.34 W/m·K).

A procedure that takes advantage of the uniform behavior of the convective and conductive processes involves the calculation of canister wall temperatures in a near-field model, ignoring details of the canister interior. The temperature rise is then calculated assuming radiative heat transfer only using a model such as that of Cox. Finally, a linear correction is applied to take into account possible convection and conduction processes.

REFERENCES FOR APPENDIX B

1. J. S. Watson, Heat Transfer from Spent Reactor Fuels during Shipping: A Proposed Method for Predicting Temperature Distribution in Fuel Bundles and Comparison with Experimental Data, ORNL-3439 (May 1963).

2. O. H. Klepper, Radiant Interchange Factors for Heat Transfer in Parallel Rod Arrays, ORNL/TM-583 (December 1963).

3. R. L. Cox, Radiative Heat Transfer in Arrays of Parallel Cylinders, ORNL-5239 (June 1977).

4. R. E. Westerman, Preliminary Conceptual Designs for Advanced Packages for the Geologic Disposal of Spent Fuel, PNL-2990 (April 1979).

APPENDIX C: ADDITIONAL DATA RELATIVE TO THE SENSITIVITY STUDIES

As noted in Sects. 2.2.2 and 2.2.3, additional data have been generated for the backfill thermal conductivity and barrier thickness and the delay of canister backfill studies. These data can be divided into four parts:

1. effect of temperature gradient and air gap,
2. effect of backfill thermal conductivity,
3. effect of barrier thickness,
4. effect of delay of canister backfill.

The effect of the temperature gradient is shown in Fig. C-1. If the initial temperature at the waste midplane of a SF canister is increased by 32°F (18°C), the peak temperature at the waste midplane is increased by nearly 40°F (22°C). The effect of air gap is shown in Figs. C-2 and C-3 for HLW and SF, respectively. The effect of the air gap decreases as the years from emplacement increase. This effect is especially evident in the HLW case (Fig. C-2). At the peak temperature, the air gap increases the temperature by nearly 50°F (28°C) for HLW (Fig. C-2) and ∿15°F (8.3°C) for SF (Fig. C-3). In the case of SF, the air gap also causes the peak to occur ∿10 yr earlier.

The effect of backfill thermal conductivity is shown by the temperature histories of Figs. C-4 through C-10. Figures C-4 to C-7 show canister surface temperature histories for 150- and 100-kW/acre (37.1- and 24.7-W/m^2) HLW and areal heat loads of 60 and 40 kW/acre (14.8 and 9.88 W/m^2). All HLW curves are for backfill thermal conductivities of 0.05, 0.075, and 0.1 Btu/h·°F·ft (0.90, 0.13, and 0.17 W/m^2·K), and all SF curves are for backfill thermal conductivities of 0.025, 0.05, and 0.1 Btu/h·°F·ft (0.043, 0.090, and 0.17 W/m·K). For HLW canister surface temperature, the effect of decreasing the backfill thermal conductivity by one-half increases the temperature at the waste midplane by nearly 300°F (167°C). For SF canister surface temperatures, the effect of decreasing the backfill thermal conductivity by one-half increases the temperature at the waste midplane by nearly 40°F (22°C). These results are not linear and cannot be extrapolated except as shown in Sect. 2.2.

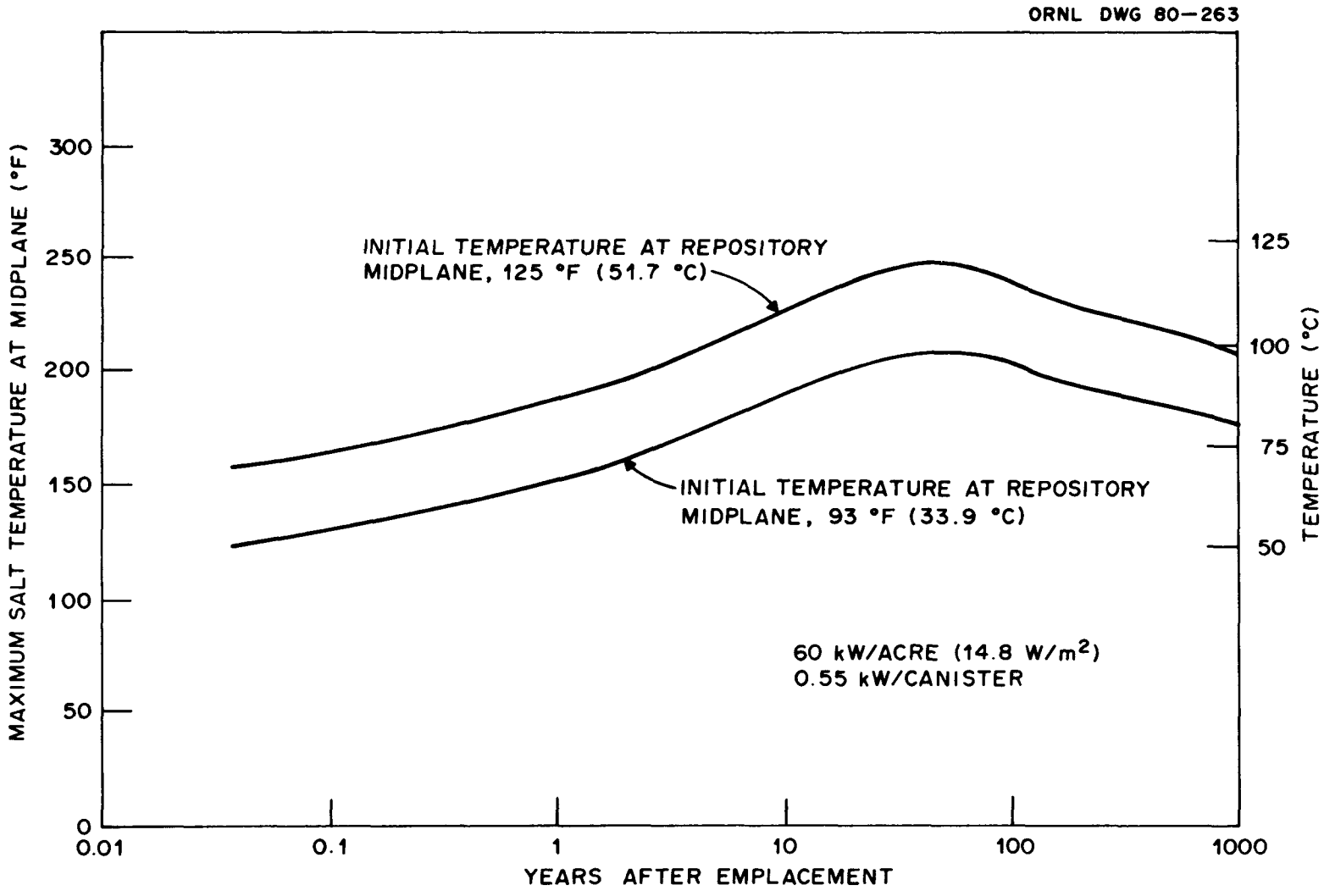

Fig. C-1. Effect of initial temperature gradient on maximum salt temperature histories for spent fuel.

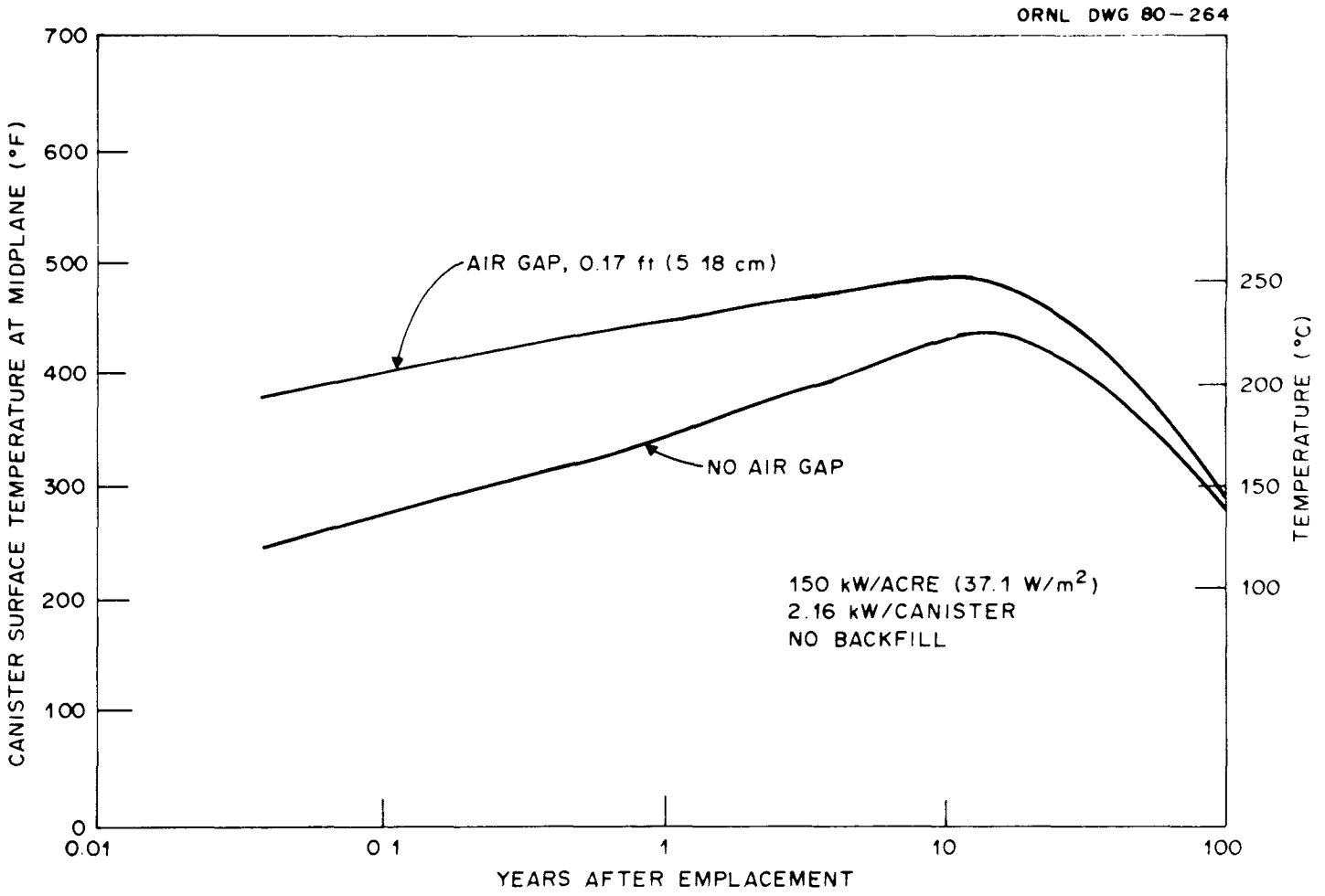

Fig. C-2. Effect of an air gap on the maximum canister surface temperature for high-level waste.

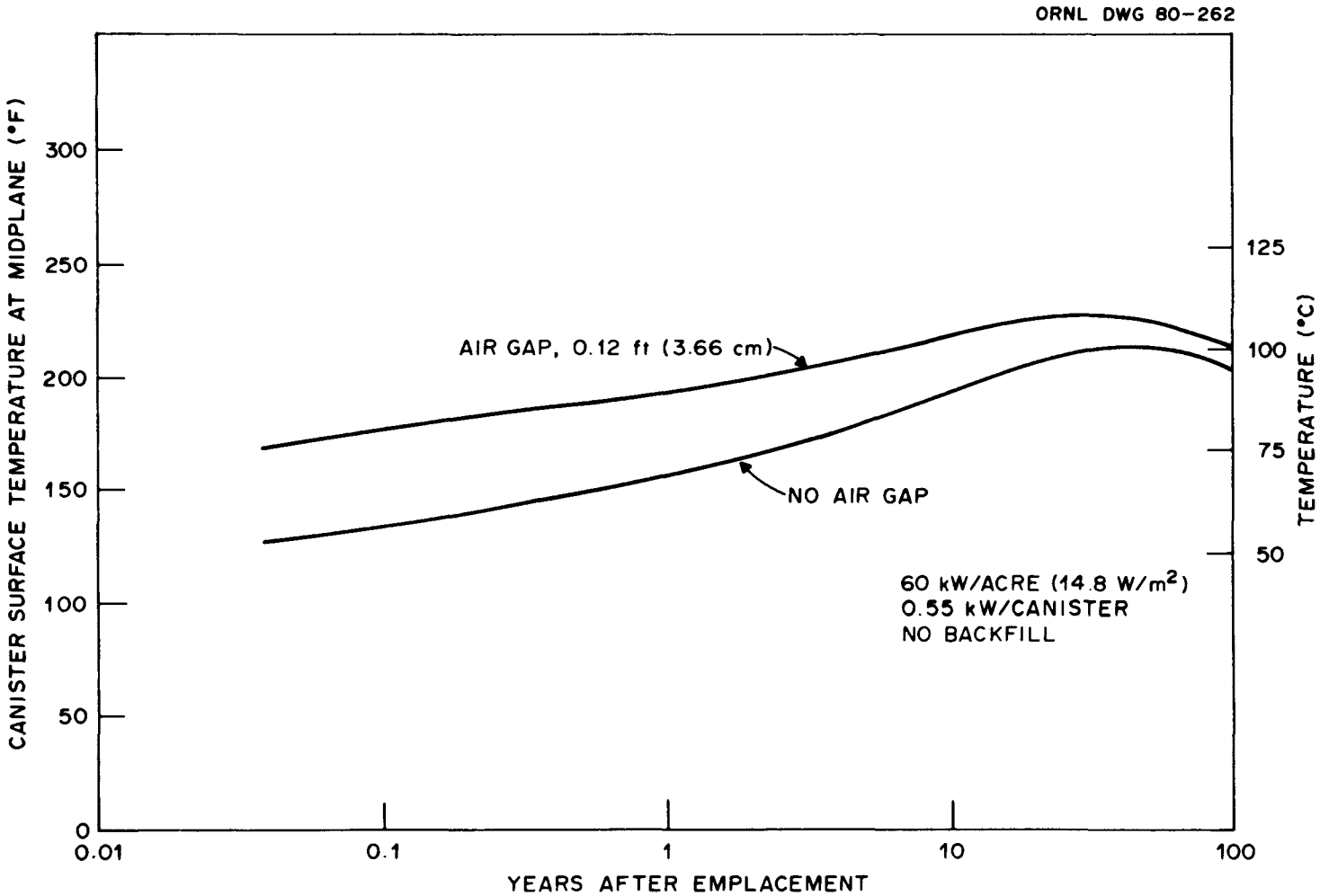

Fig. C-3. Effect of an air gap on the maximum canister surface temperature for spent fuel.

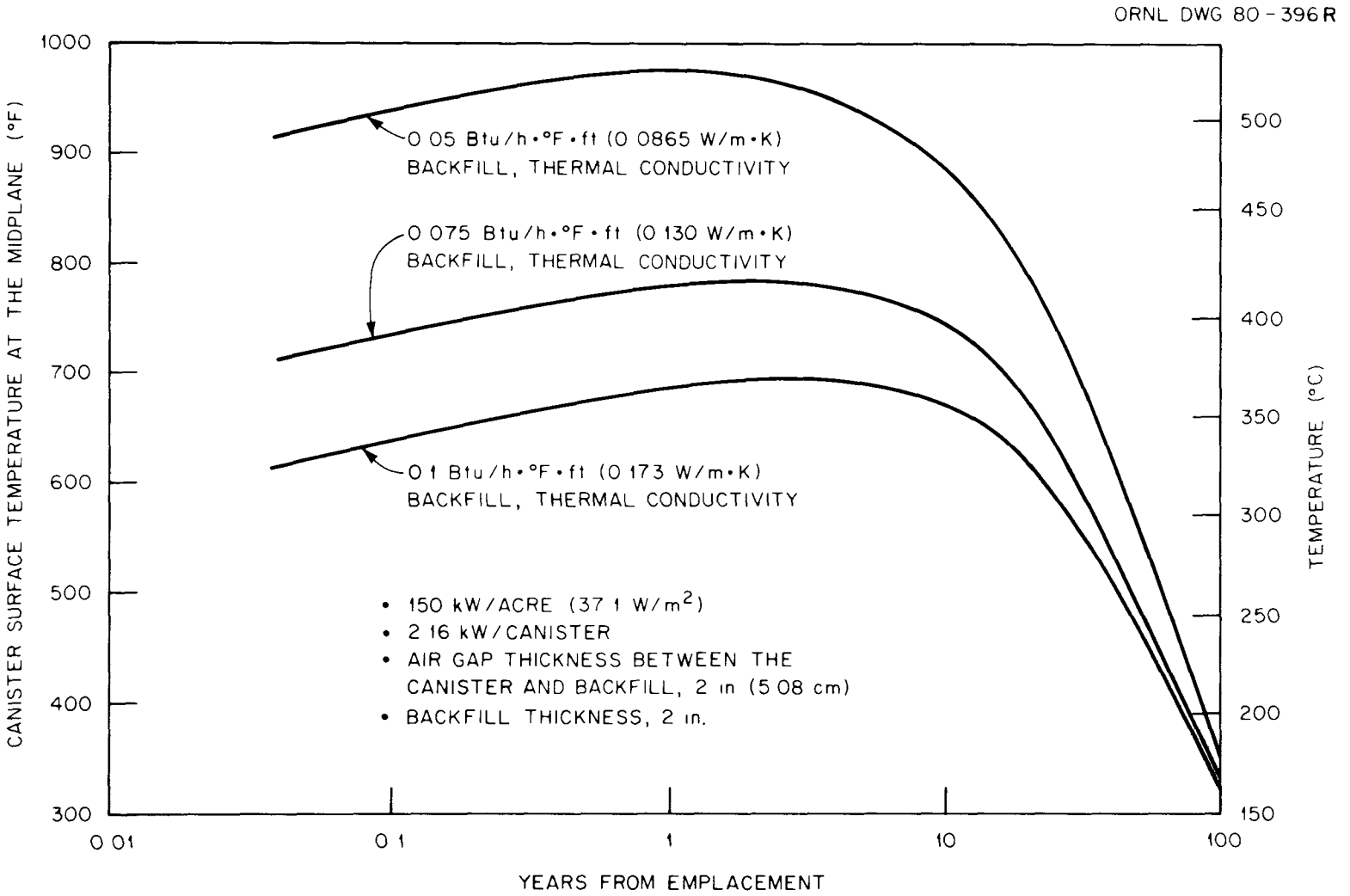

Fig. C-4. Effect of backfill thermal conductivity on maximum temperature histories of canister surface for high-level waste [150 kW/acre (37.1 W/m^2)].

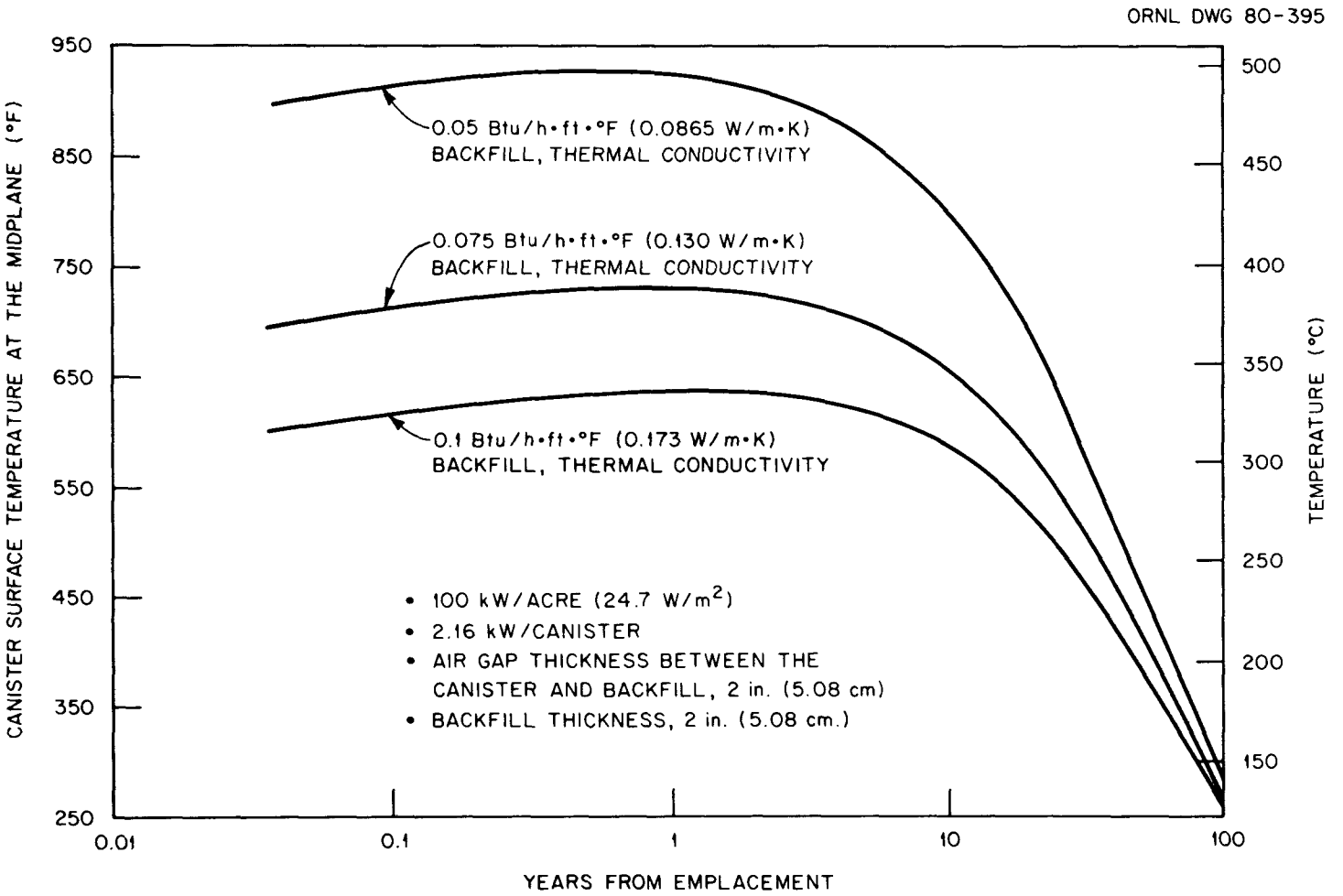

Fig. C-5. Effect of backfill thermal conductivity on maximum temperature histories of canister surface for high-level waste [100 kW/acre (24.7 W/m^2)].

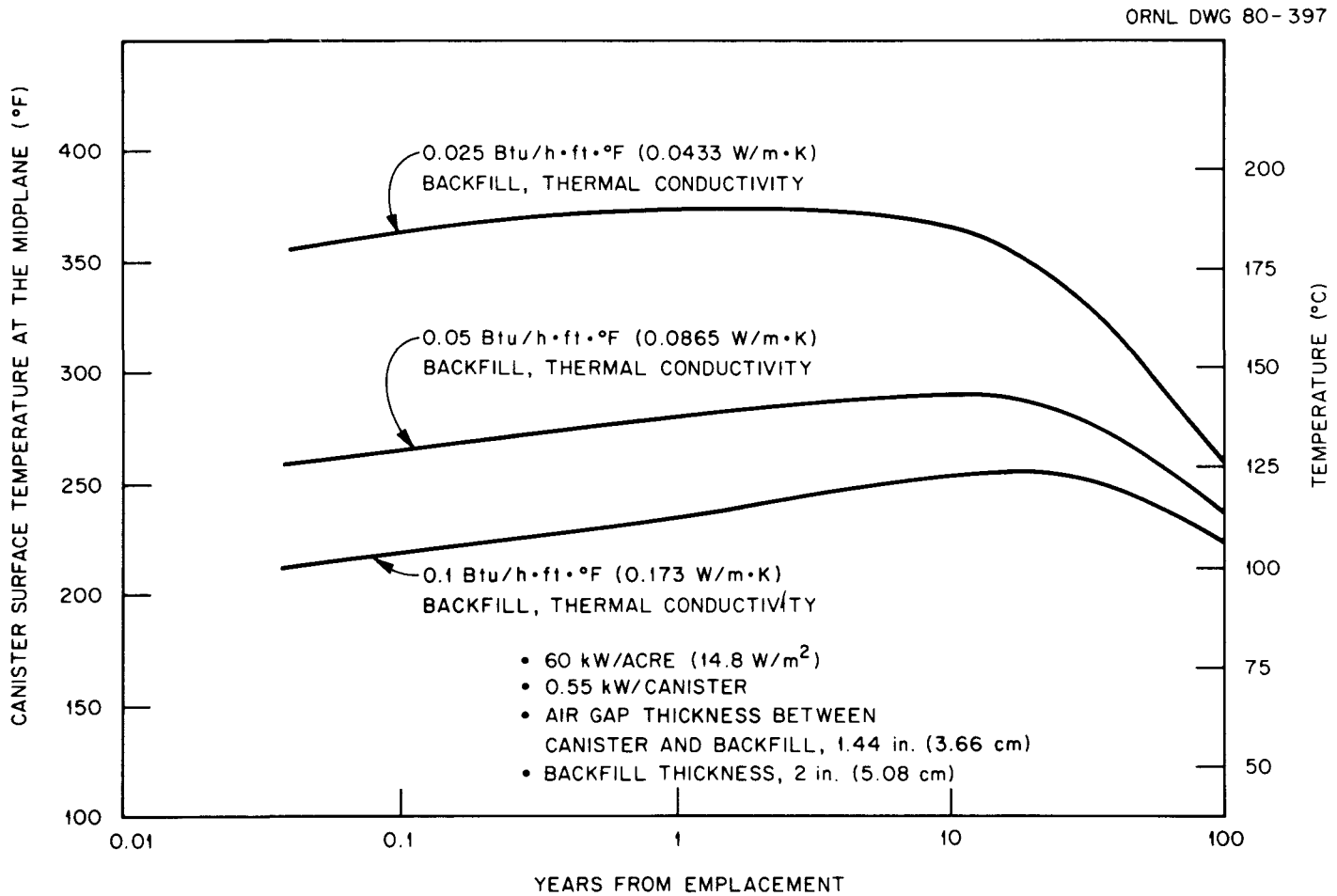

Fig. C-6. Effect of backfill thermal conductivity on maximum temperature histories of canister surface for spent fuel [60 kW/acre (14.8 W/m^2)].

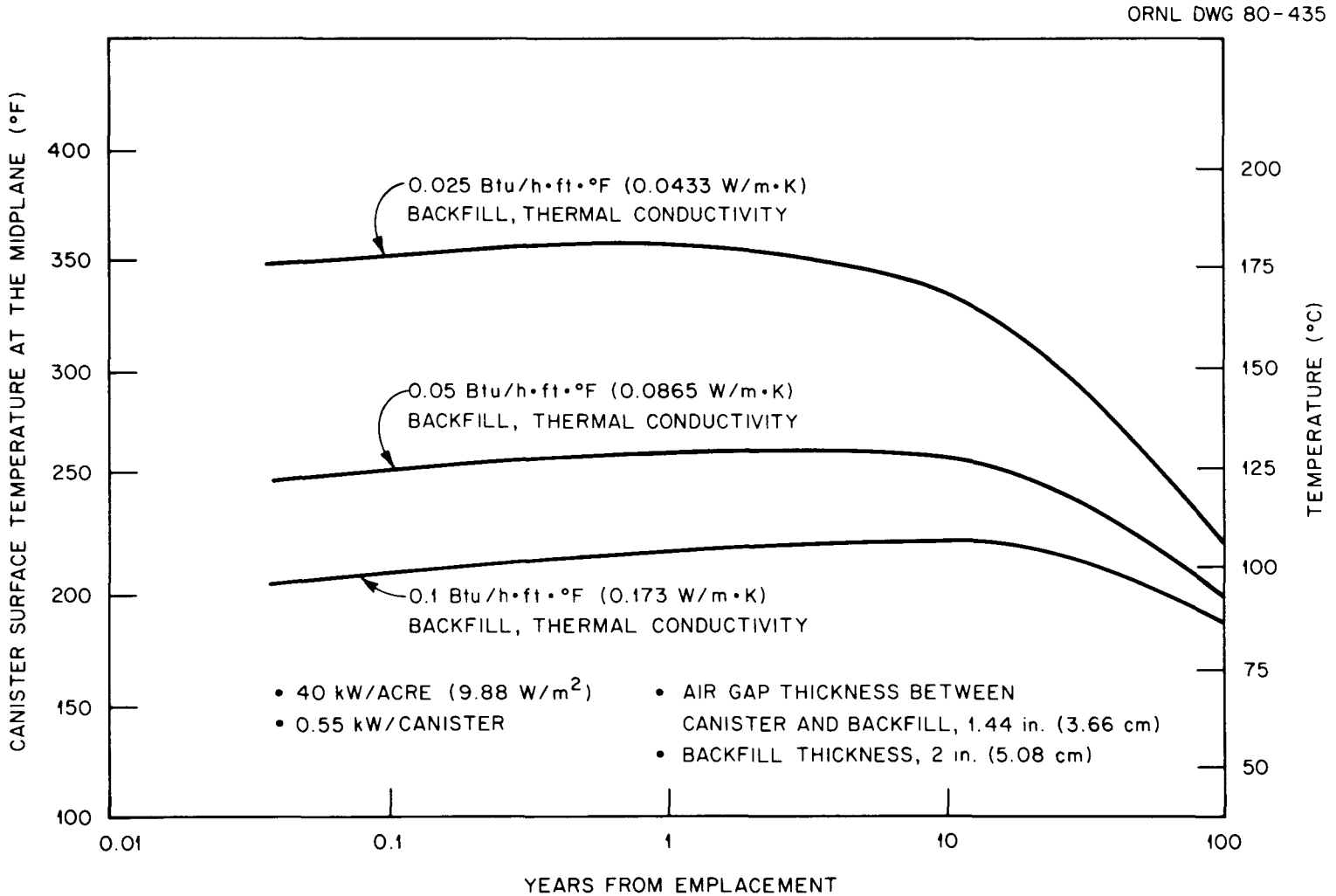

Fig. C-7. Effect of thermal conductivity on maximum temperature histories of canister surface for spent fuel [40 kW/acre (9.88 W/m^2)].

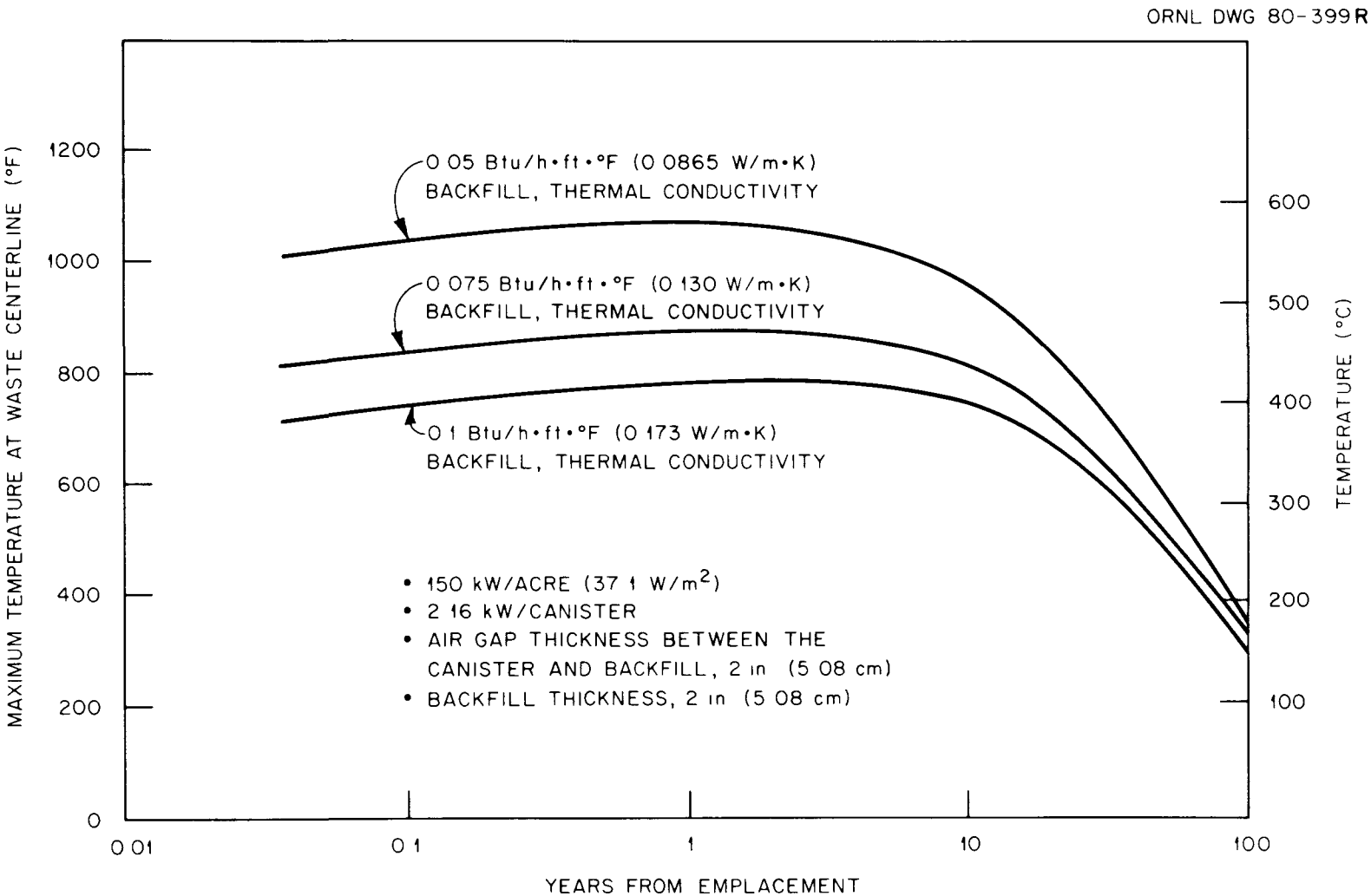

Fig. C-8. Effect of backfill thermal conductivity on maximum waste temperature histories at the waste centerline for high-level waste [150 kW/acre (37.1 W/m^2)].

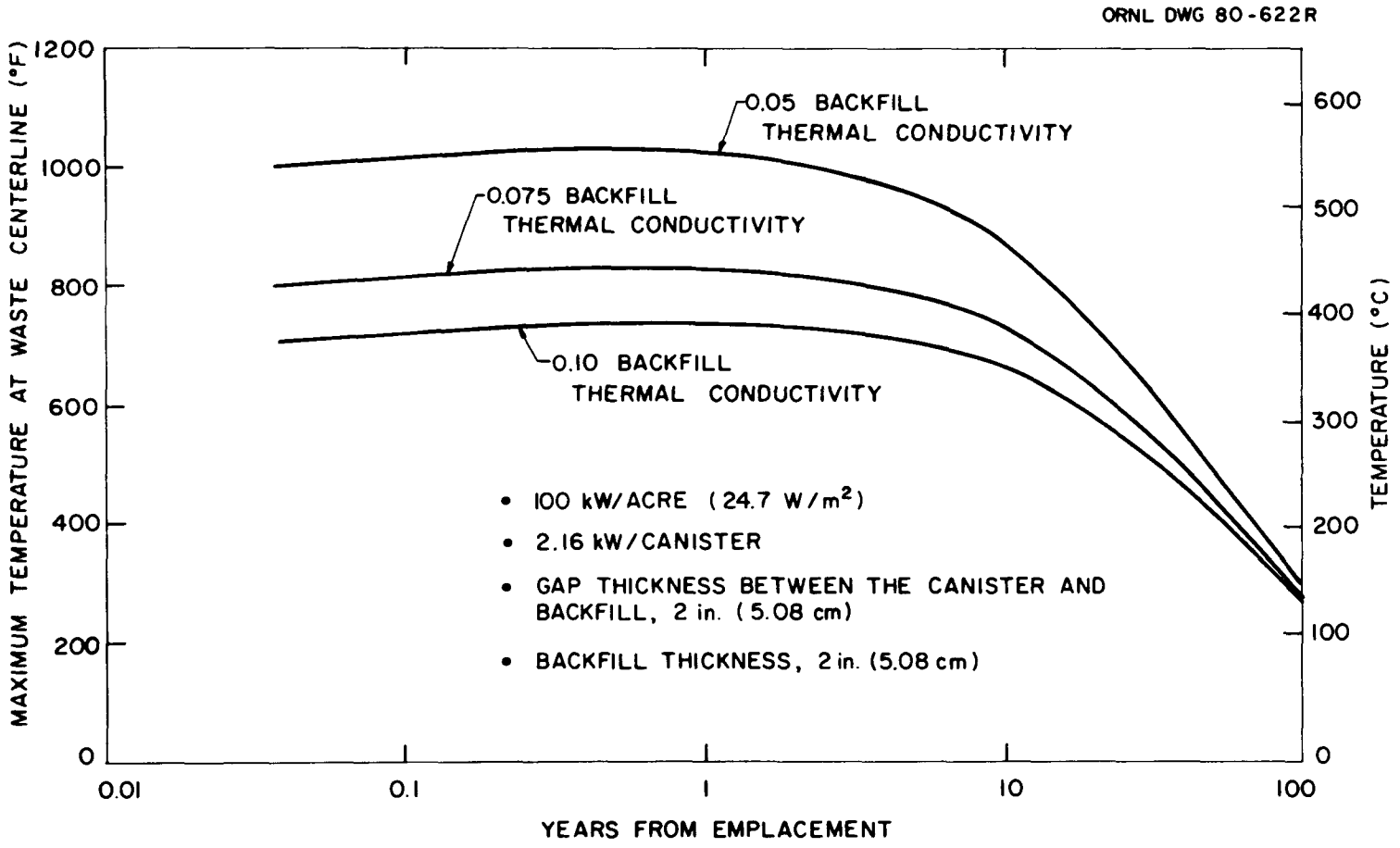

Fig. C-9. Effect of thermal conductivity on maximum temperature histories for high-level waste at the waste centerline [100 kW/acre (24.7 W/m^2)].

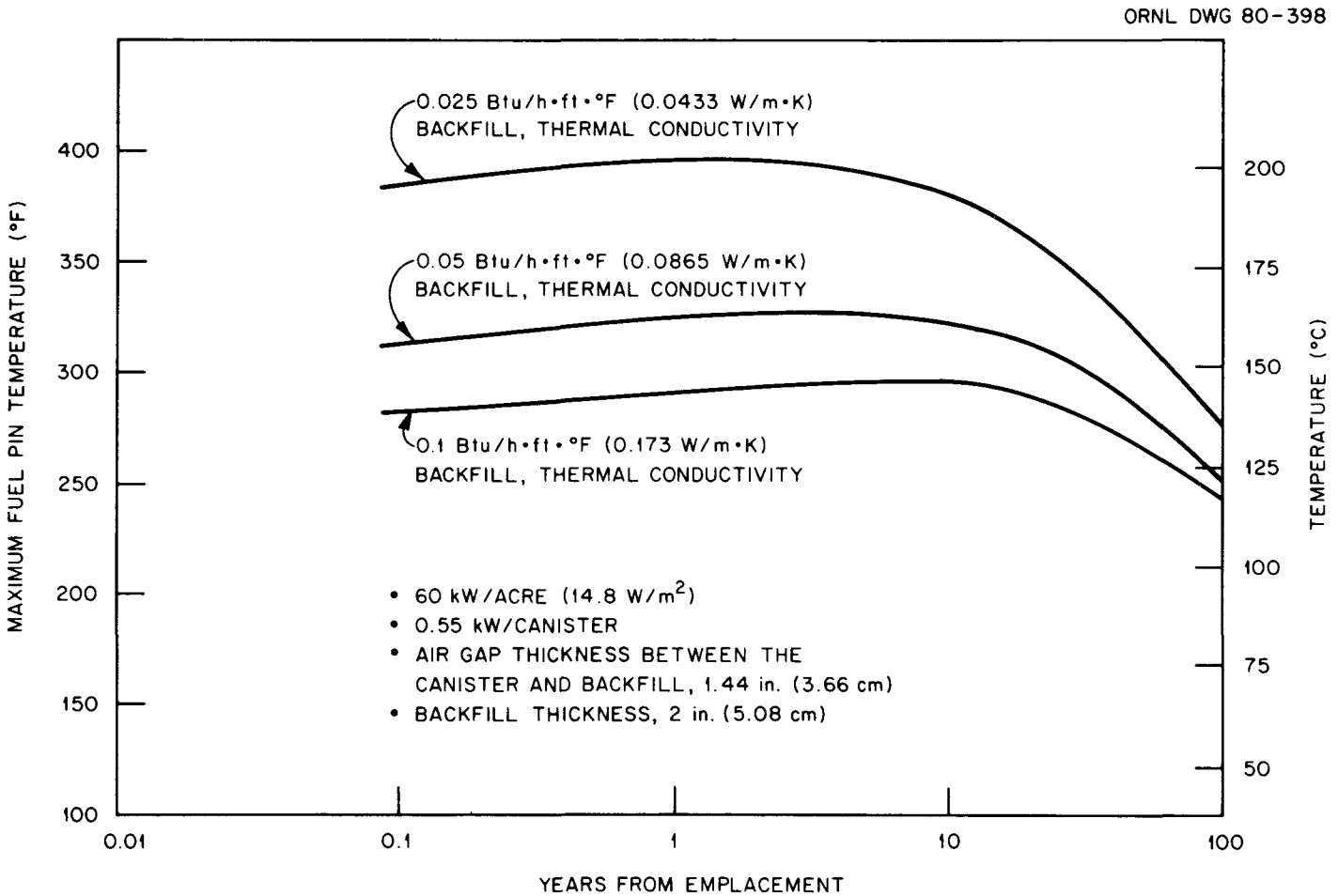

Fig. C-10. Effect of backfill thermal conductivity on maximum temperature histories for spent fuel assembly [60 kW/acre (14.8 W/m^2)].

The effect of barrier thickness is shown in Figs. C-11 through C-18 as temperature histories at the waste midplane. Figures C-11 to C-14 show canister surface temperature histories for 150- and 100-kW/acre (37.1- and 24.7-W/m^2) HLW and 60- and 40-kW/acre (14.8- and 9.88-W/m^2) SF. Figures C-15 to C-18 show HLW centerline and SF assembly temperature histories for 150, 100, 60, and 40 kW/acre (37.1, 24.7, 14.8, and 9.88 W/m^2), respectively. The barrier thickness is varied from 4 to 8.4 in. (10 to 21.3 cm) for HLW and from 7.8 to 3.4 in. (19.8 to 8.64 cm) for SF. Increasing the barrier thickness by a factor of 2.1 increases the canister surface temperature at the waste midplane by nearly 500°F (278°C) for HLW. Increasing the barrier thickness for SF by a factor of 2.3 increases the canister surface temperature at the waste midplane by ∿70°F (39°C).

The effect of the delay of canister backfilling on temperature histories is shown in Figs. C-19 to C-23. Figures C-19 to C-22 show canister surface temperature histories for 5- and 25-yr closure at areal heat loads of 150 and 100 kW/acre (37.1 and 24.7 W/m^2) for HLW and 60 and 40 kW/acre (14.8 and 9.88 W/m^2) for SF. Figure C-23 shows HLW centerline temperature for 5- and 25-yr closure for 100 kW/acre (24.7 W/m^2).

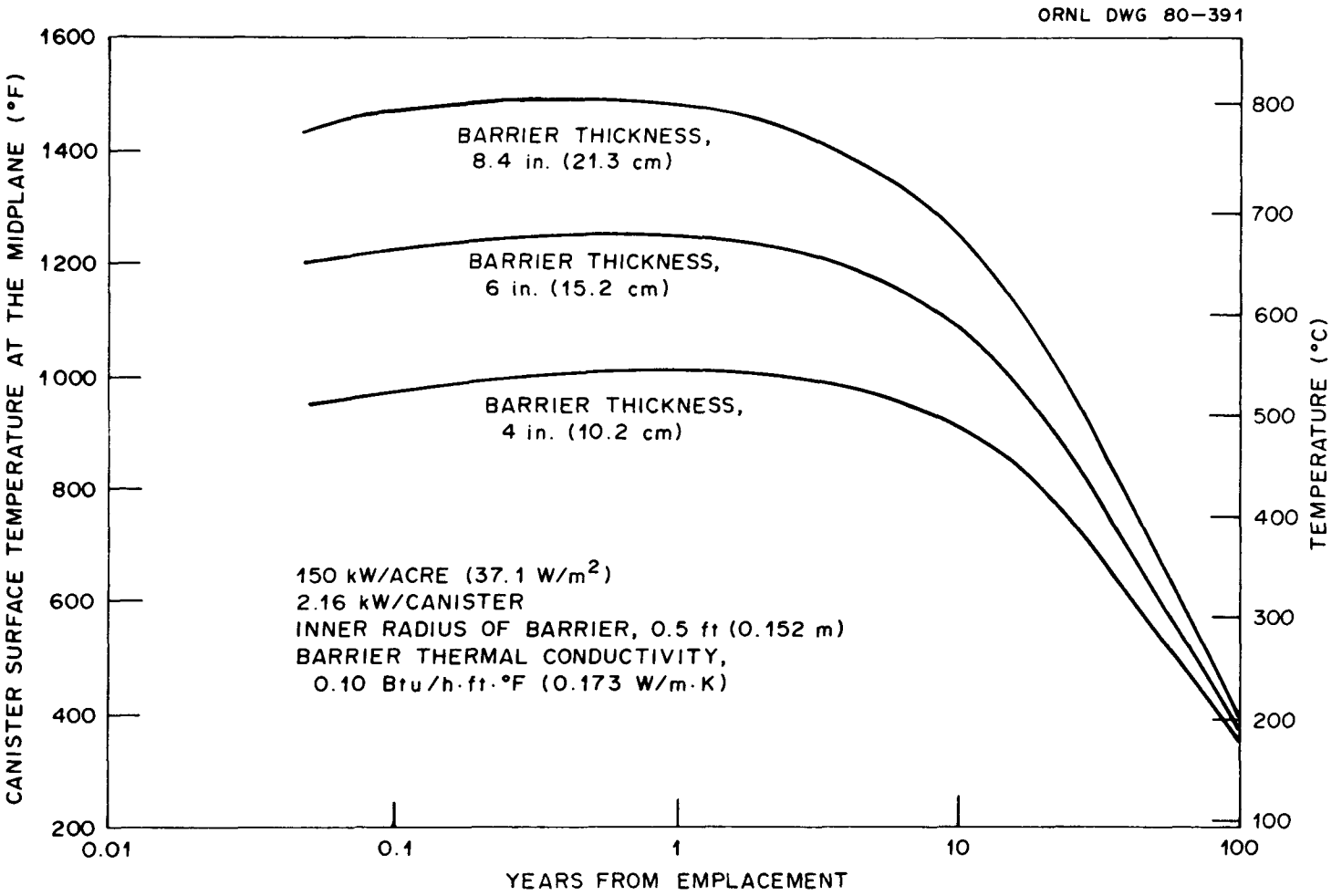

Fig. C-11. Effect of barrier thermal thickness on temperature histories of canister surface for high-level waste [150 kW/acre (37.1 W/m^2)].

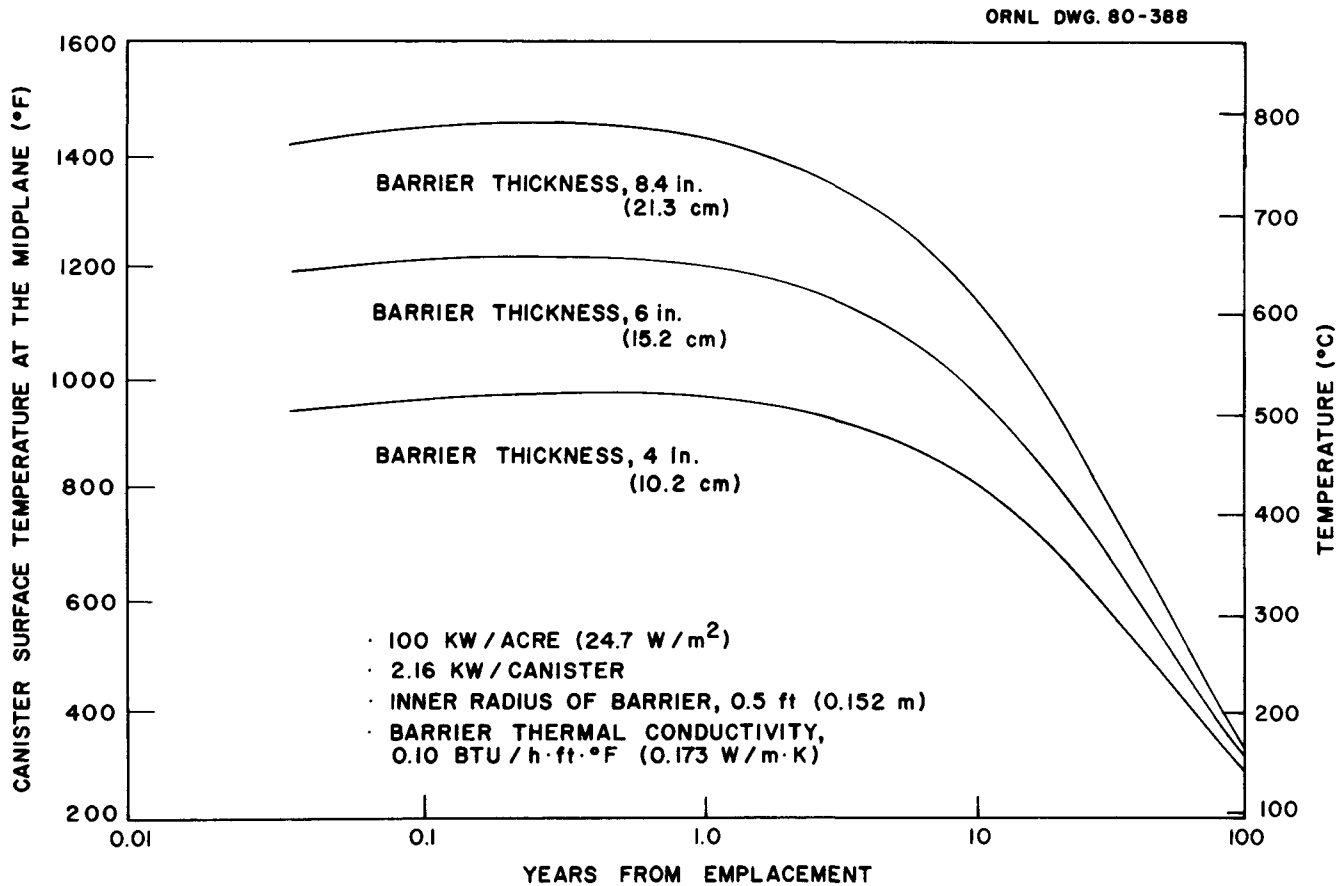

Fig. C-12. Effect of barrier thickness on maximum temperature histories of canister surface for high-level waste [100 kW/acre (24.7 W/m^2)].

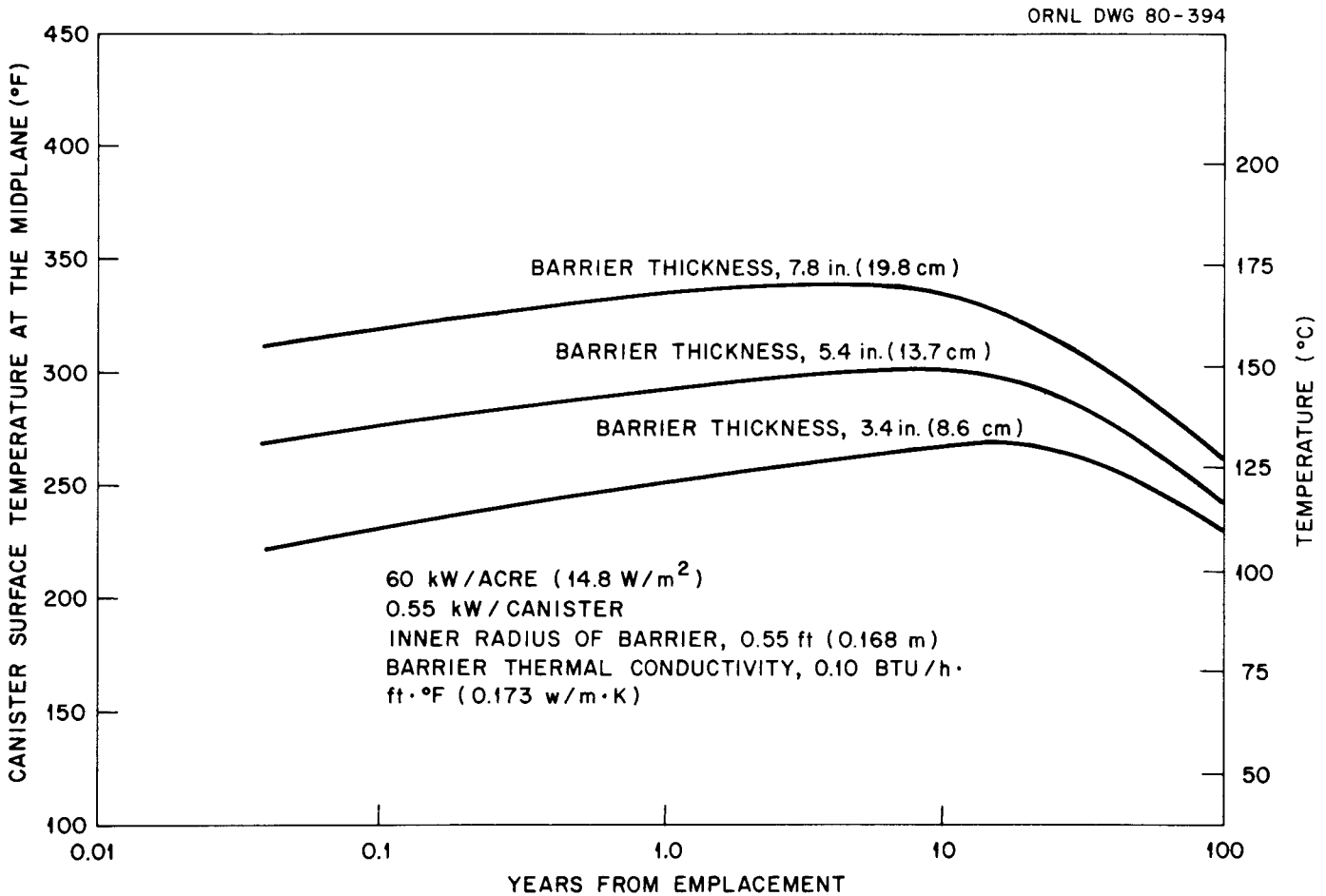

Fig. C-13. Effect of barrier thickness on temperature histories of canister surface [60 kW/acre (14.8 W/m^2)].

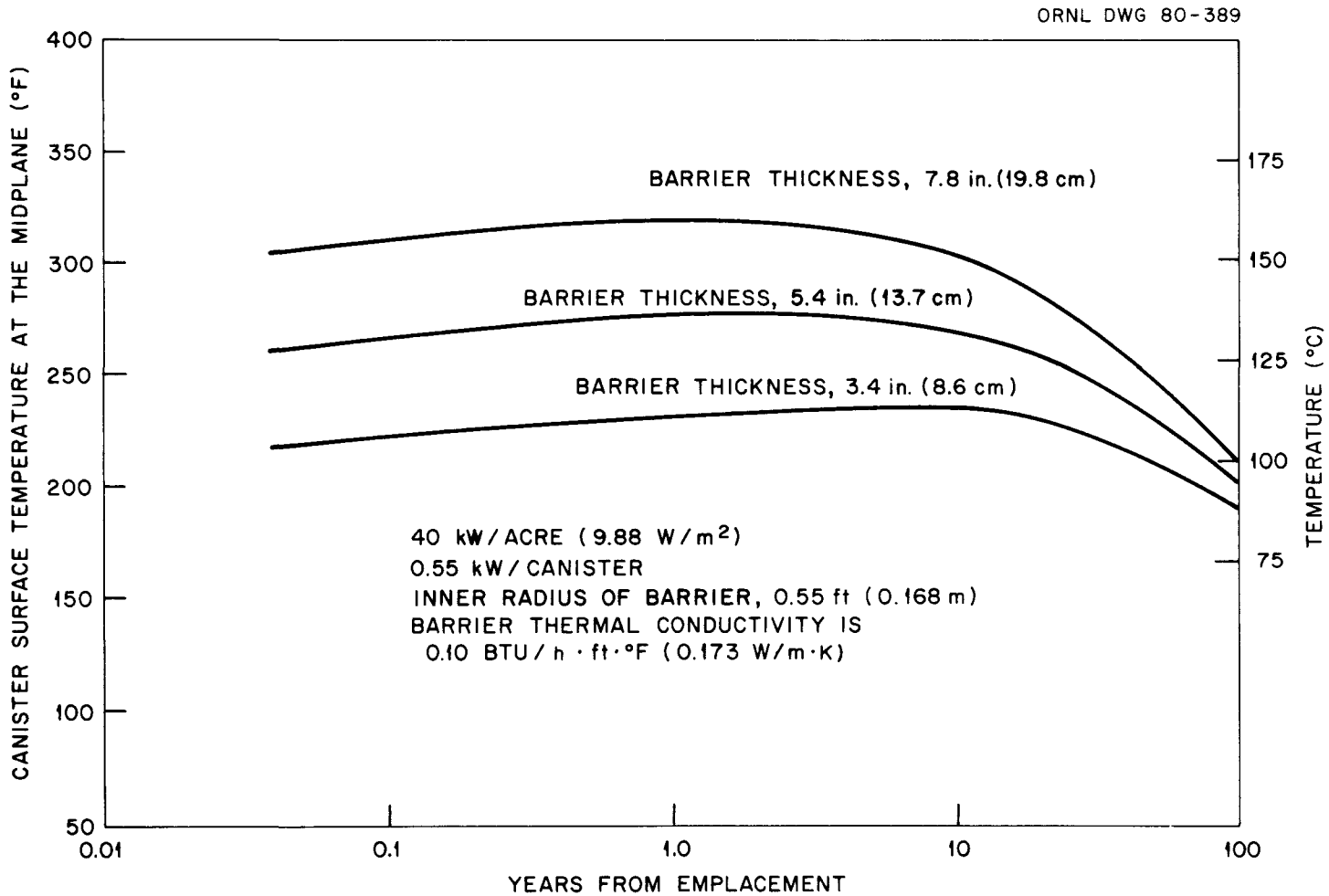

Fig. C-14. Effect of barrier thickness on maximum temperature histories of canister surface for spent fuel [40 kW/acre (9.88 W/m^2)].

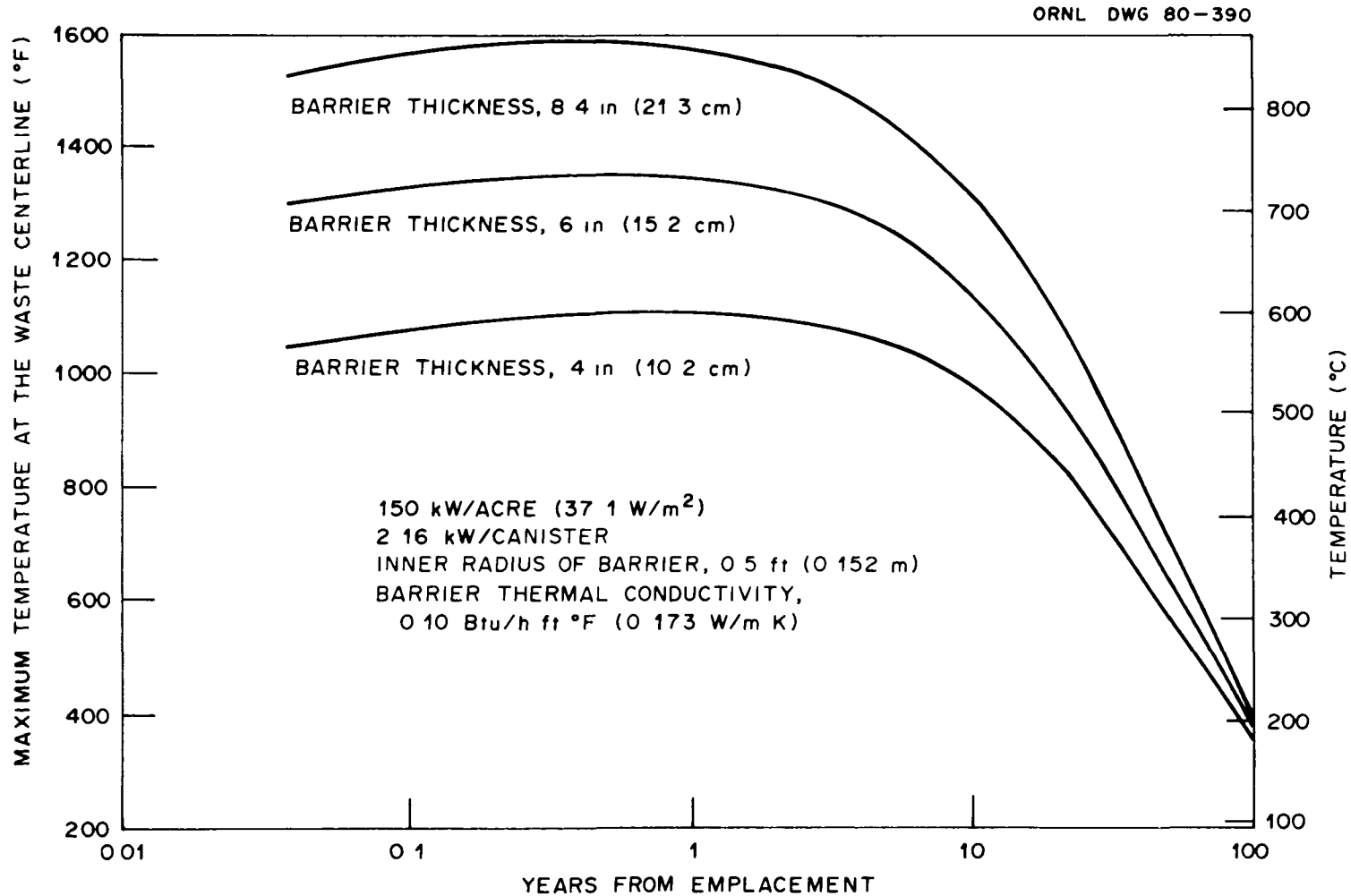

Fig. C-15. Effect of barrier thickness on maximum temperature histories of waste centerline for high-level waste [150 kW/acre (37.1 W/m^2)].

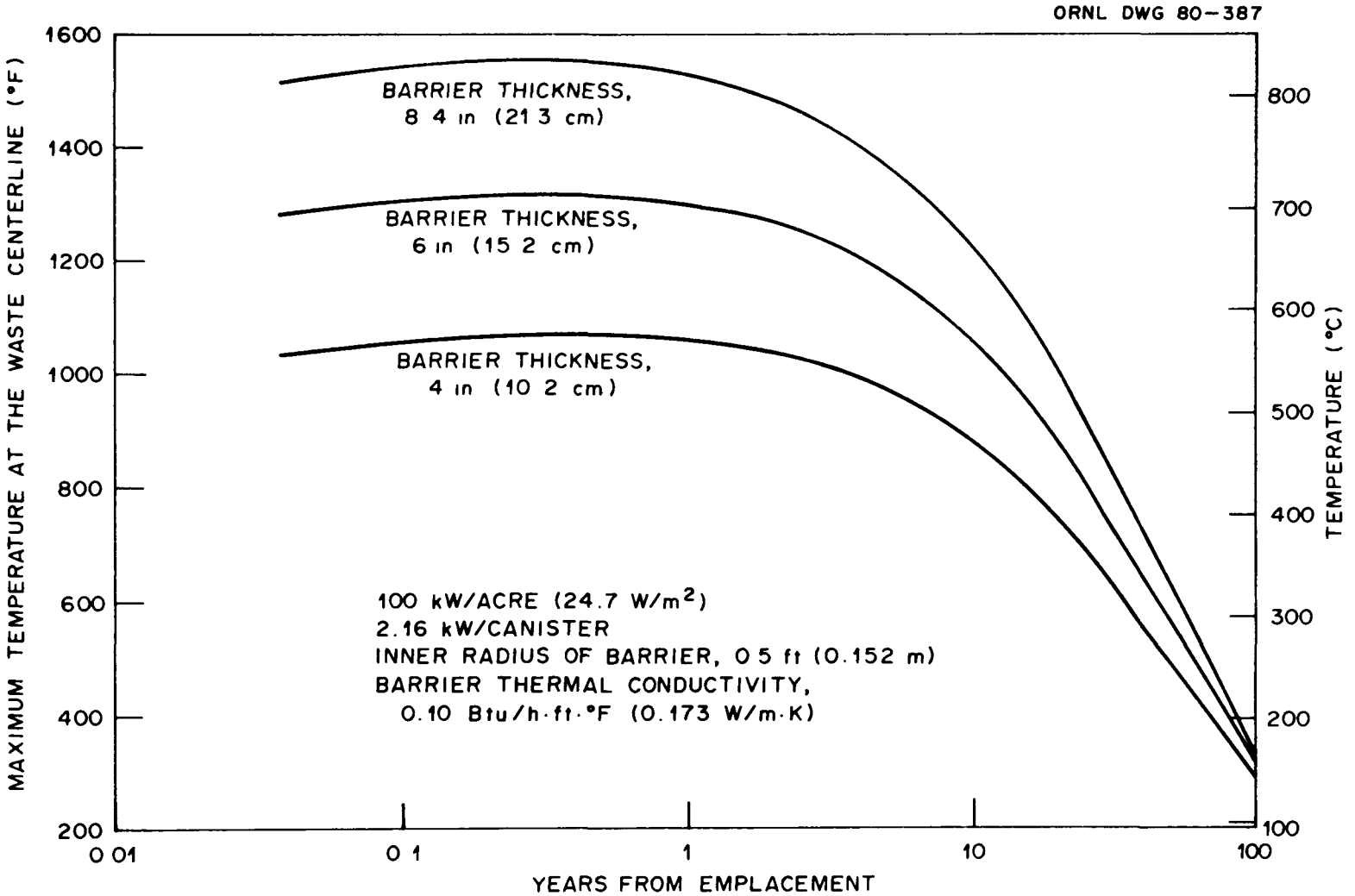

Fig. C-16. Effect of barrier thickness on maximum waste centerline temperature histories for high-level waste [100 kW/acre (24.7 W/m^2)].

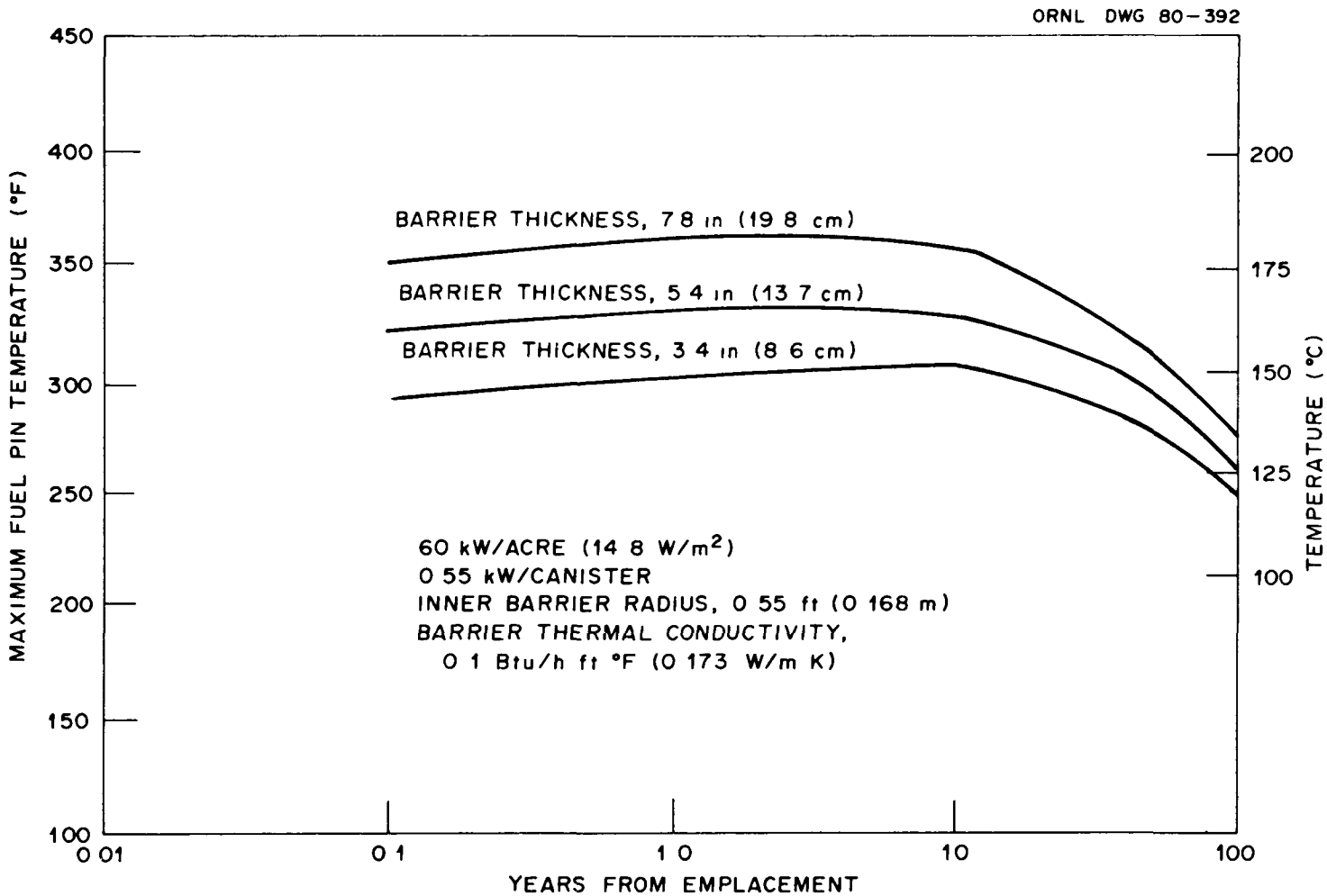

Fig. C-17. Effect of barrier thickness on maximum temperature histories of spent fuel [60 kW/acre (14.8 W/m^2)].

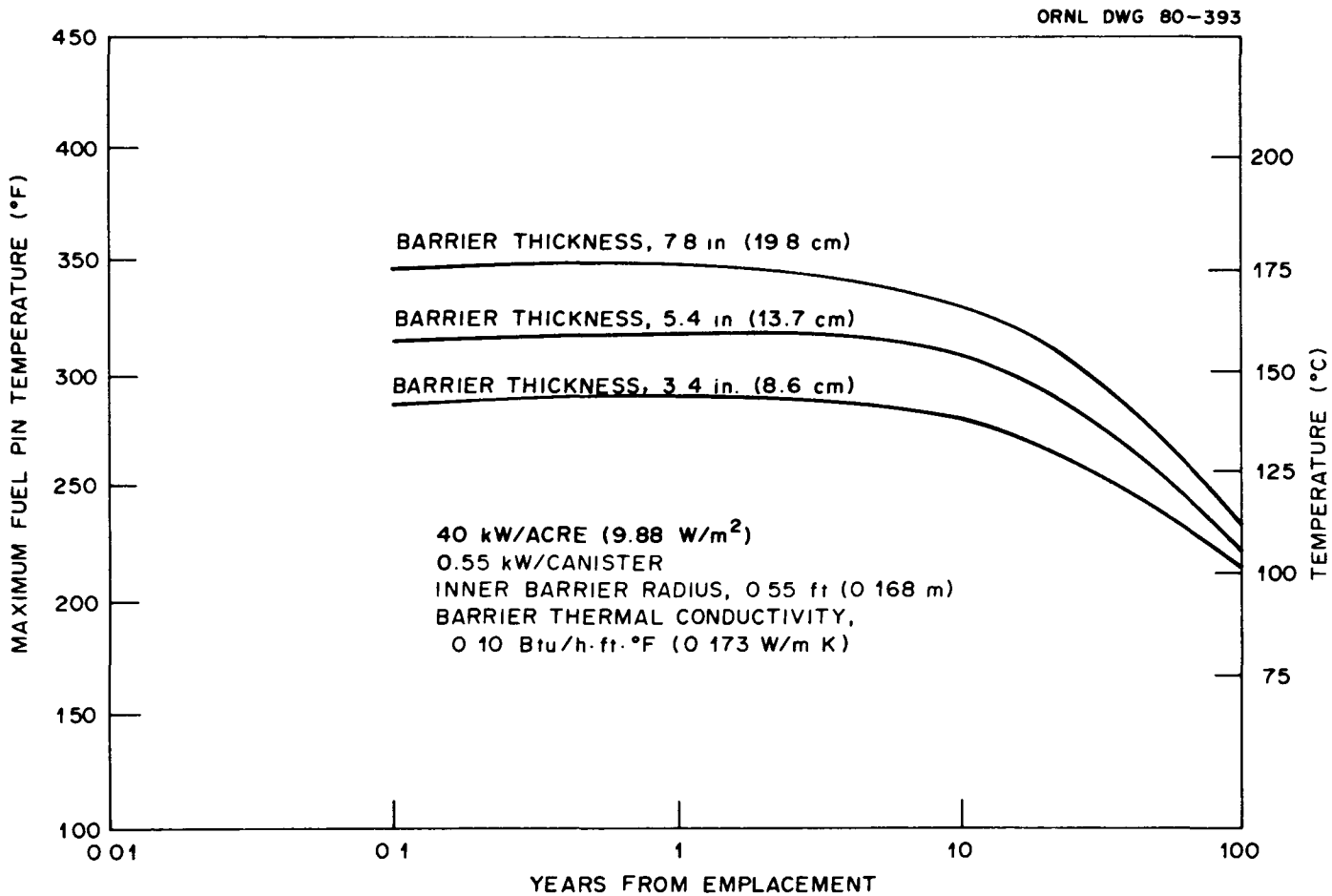

Fig. C-18. Effect of barrier thickness on maximum temperature histories of spent fuel [40 kW/acre (9.88 W/m^2)].

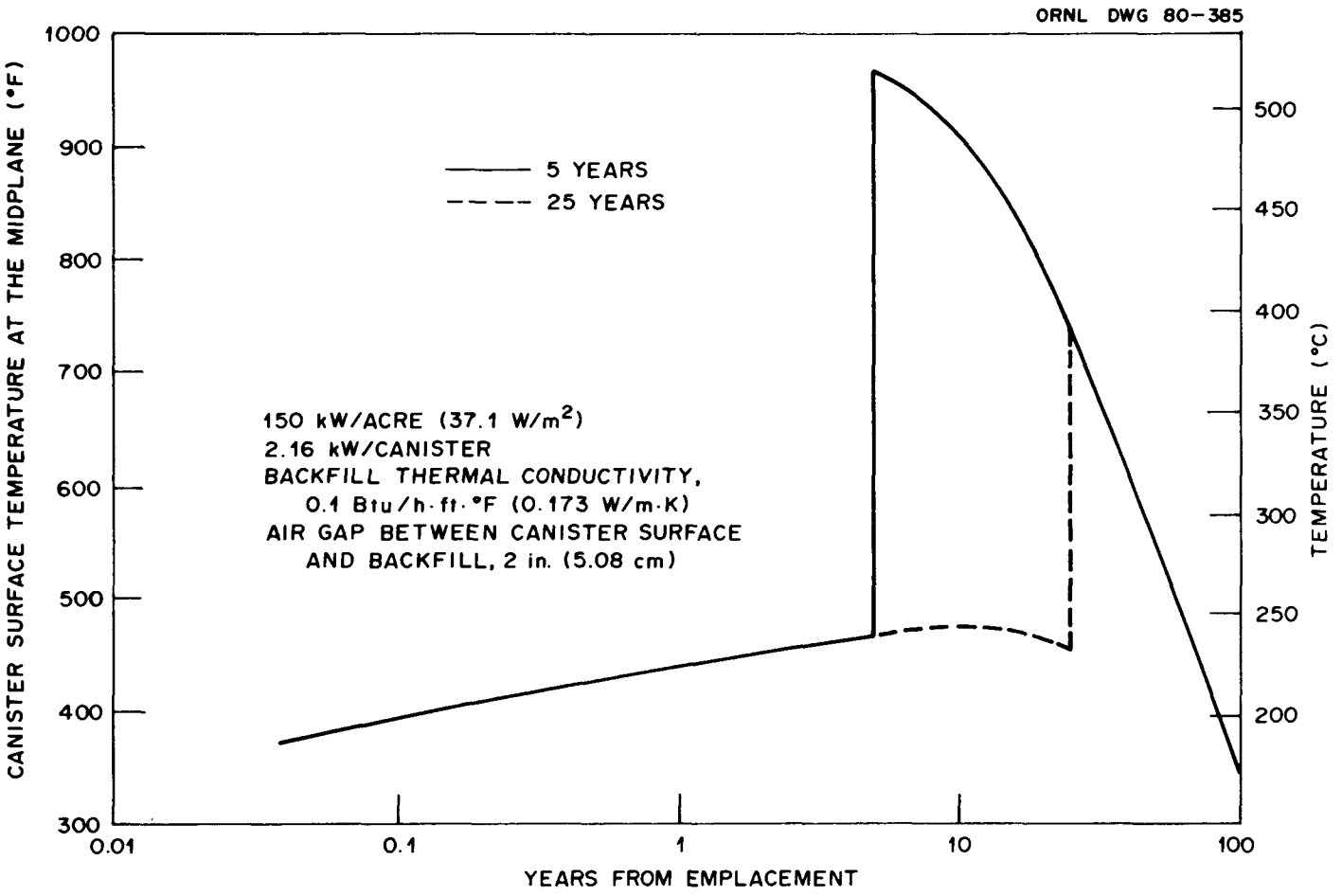

Fig. C-19. Maximum temperature histories of the canister surface for 5- and 25-yr retrievability of high-level waste [150 kW/acre (37.1 W/m^2)].

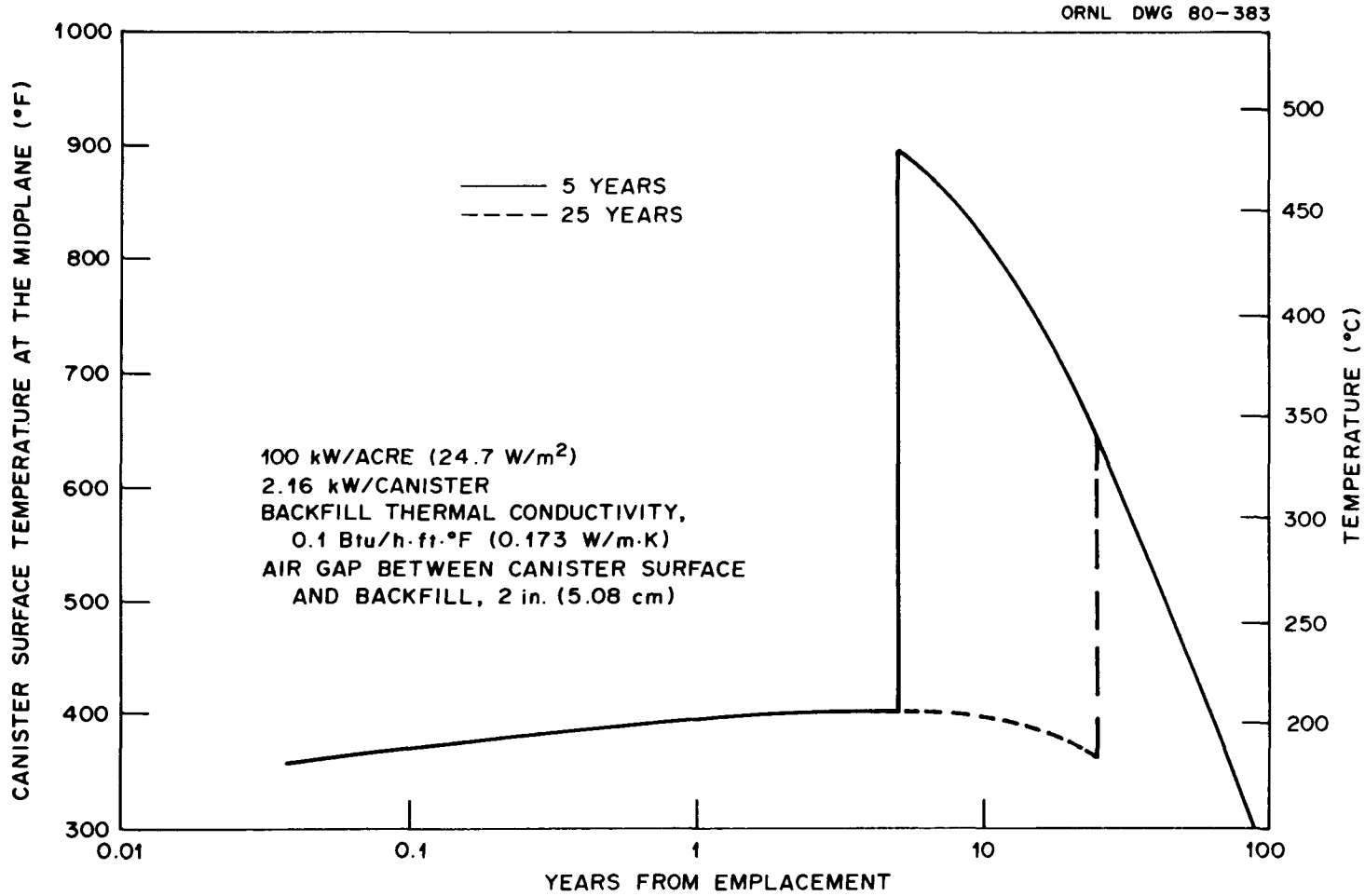

Fig. C-20. Maximum temperature histories of canister surface for 5- and 25-yr retrievability of high-level waste [100 kW/acre (24.7 W/m^2)].

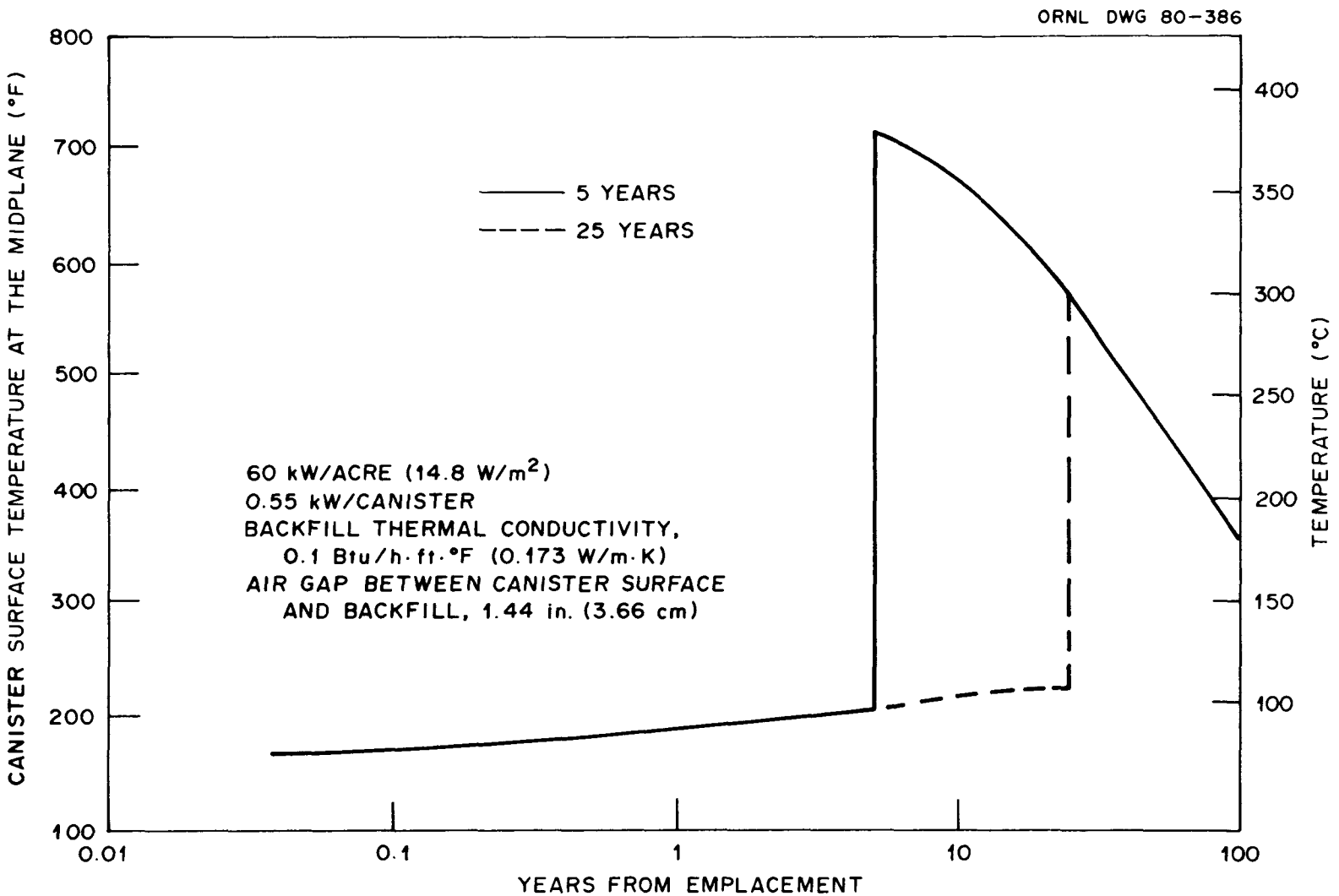

Fig. C-21. Maximum temperature histories of canister surface for 5- and 25-yr retrievability of spent fuel [60 kW/acre (14.8 W/m^2)].

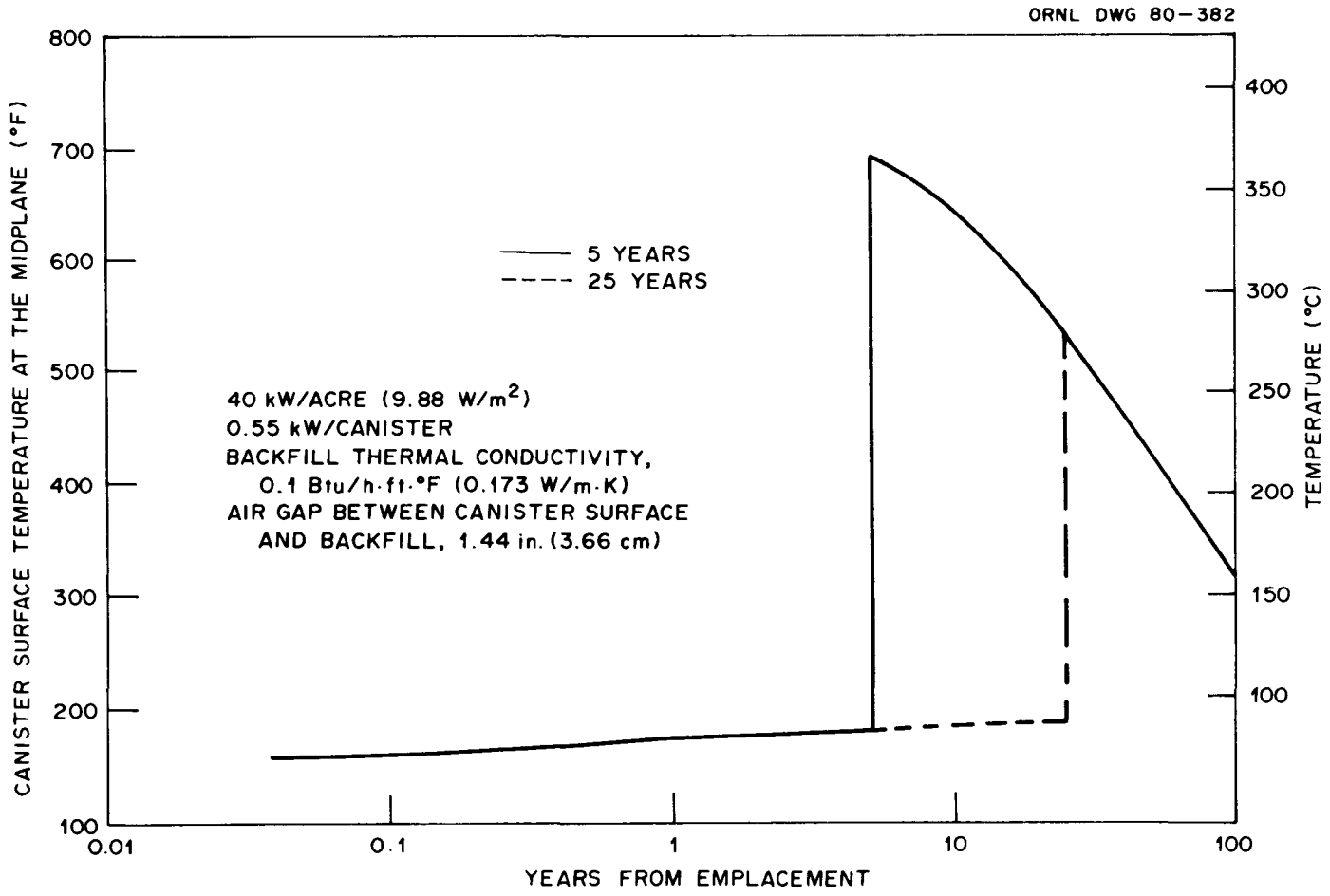

Fig. C-22. Maximum temperature histories of canister surface for 5- and 25-yr retrievability of spent fuel (40 kW/acre (9.88 W/m^2)].

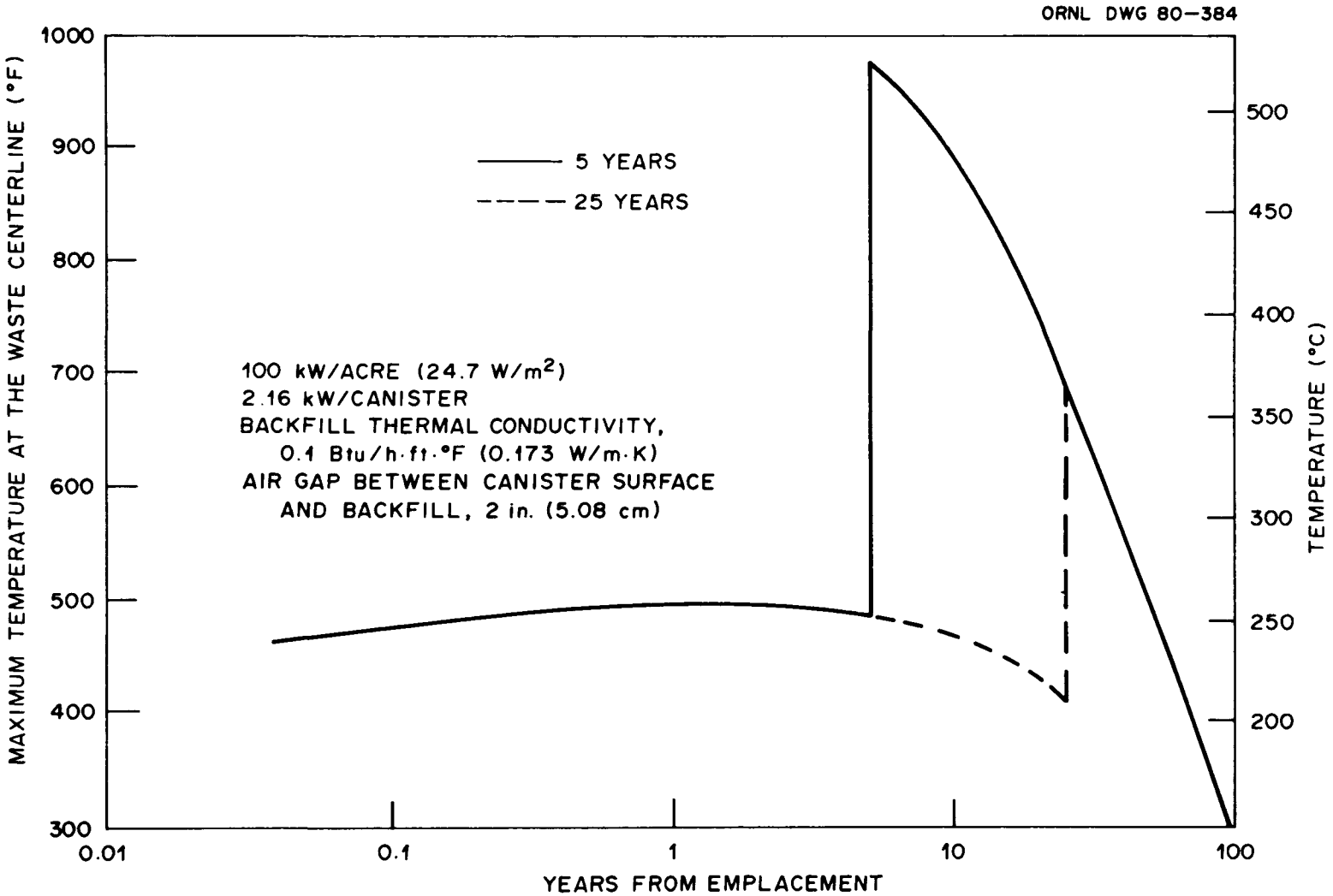

Fig. C-23. Maximum temperature histories of waste centerline for 5- and 25-yr retrievability of high-level waste [100 kW/acre (24.7 W/m^2)].

APPENDIX D: SPECIAL SENSITIVITY STUDIES — DETAILS OF THE MODELS AND ADDITIONAL DATA

Two special sensitivity studies were completed — the ventilation of storage rooms and the two-row configuration.

The details of the model for the ventilation study are the same as for the baseline repository (see Figs. 3 and 4) discussed in Sect. 2.1. The coordinates for the mesh spacing for the ventilation model are the same for the near-field axisymmetric unit-cell model in Table A-1 and the near-field 3-D unit-cell model in Table A-2.

The two-row configuration geometry is shown in Fig. D-1, with the details of the canister region shown in Fig. D-2. It should be noted that the storage room shown in Fig. D-1 was assumed to be filled with salt. The nodal coordinates that define the mesh spacing for the two-row configuration are shown in Tables D-1 and D-2 for the near-field axisymmetric and near-field 3-D unit-cell models, respectively.

Additional data have been generated for the two-row configuration and are shown as maximum temperature histories for the salt and canister surface, and centerline (central fuel pin) for BWRs and PWRs in Figs. D-3 to D-6. The different areal heat loads are obtained by varying the pitch along the room. Figures D-3 and D-4 are for areal heat loads of 60 kW/acre (14.8 W/m^2) for BWR and PWR spent fuel elements, respectively. The corresponding results for areal heat loads of 98 kW/acre (24.3 W/m^2) for BWR and PWR spent fuel elements are shown in Figs. D-5 and D-6, respectively. This latter loading was initially designated as a maximum local thermal loading for the two-row design. However, no particular mixing arrangement of the PWR and BWR canisters was specified. Actually, in all these cases, the difference in the maximum temperatures for BWRs and PWRs is small.

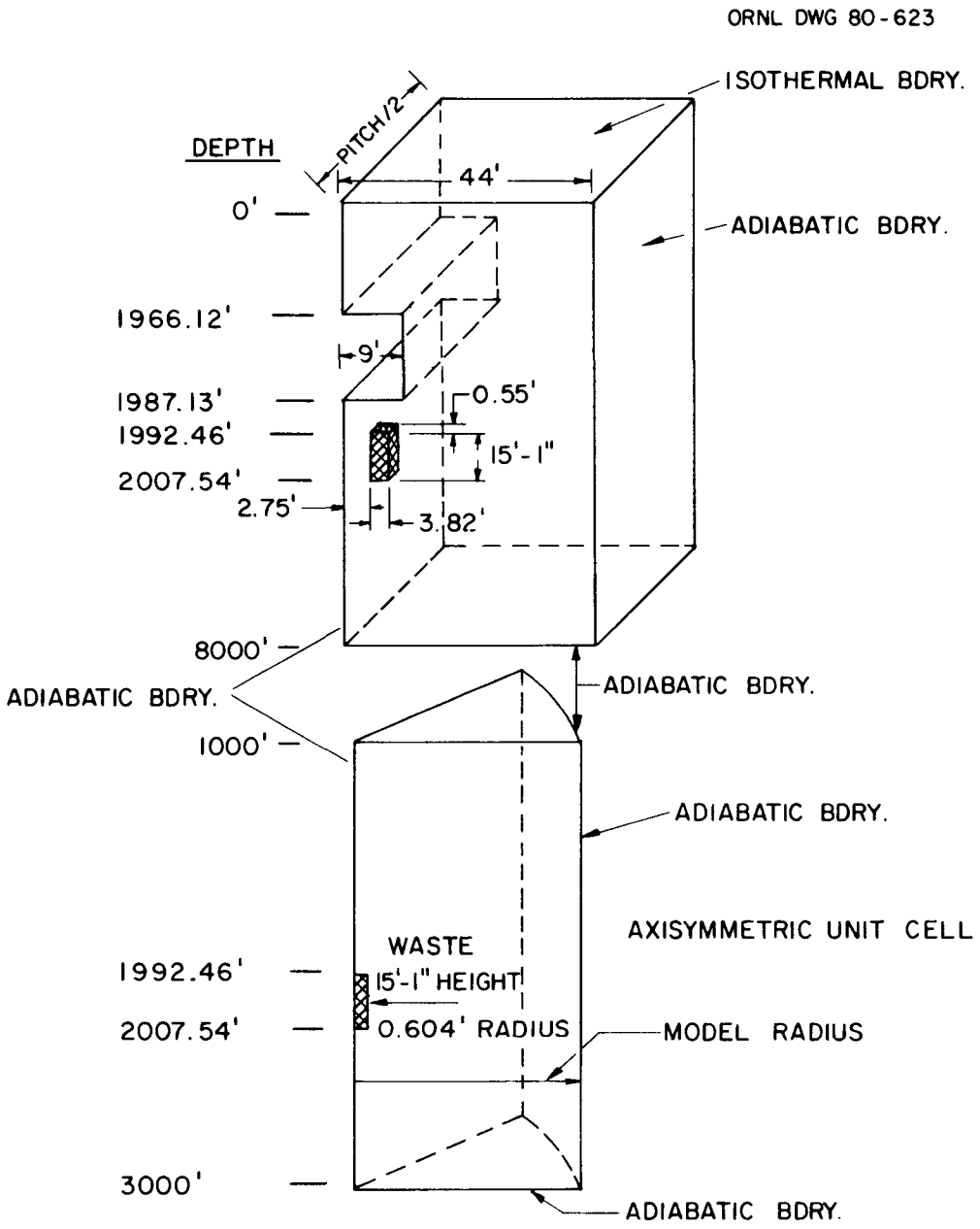

Fig. D-1. Axisymmetric and 3-D unit cells for the two-row configuration.

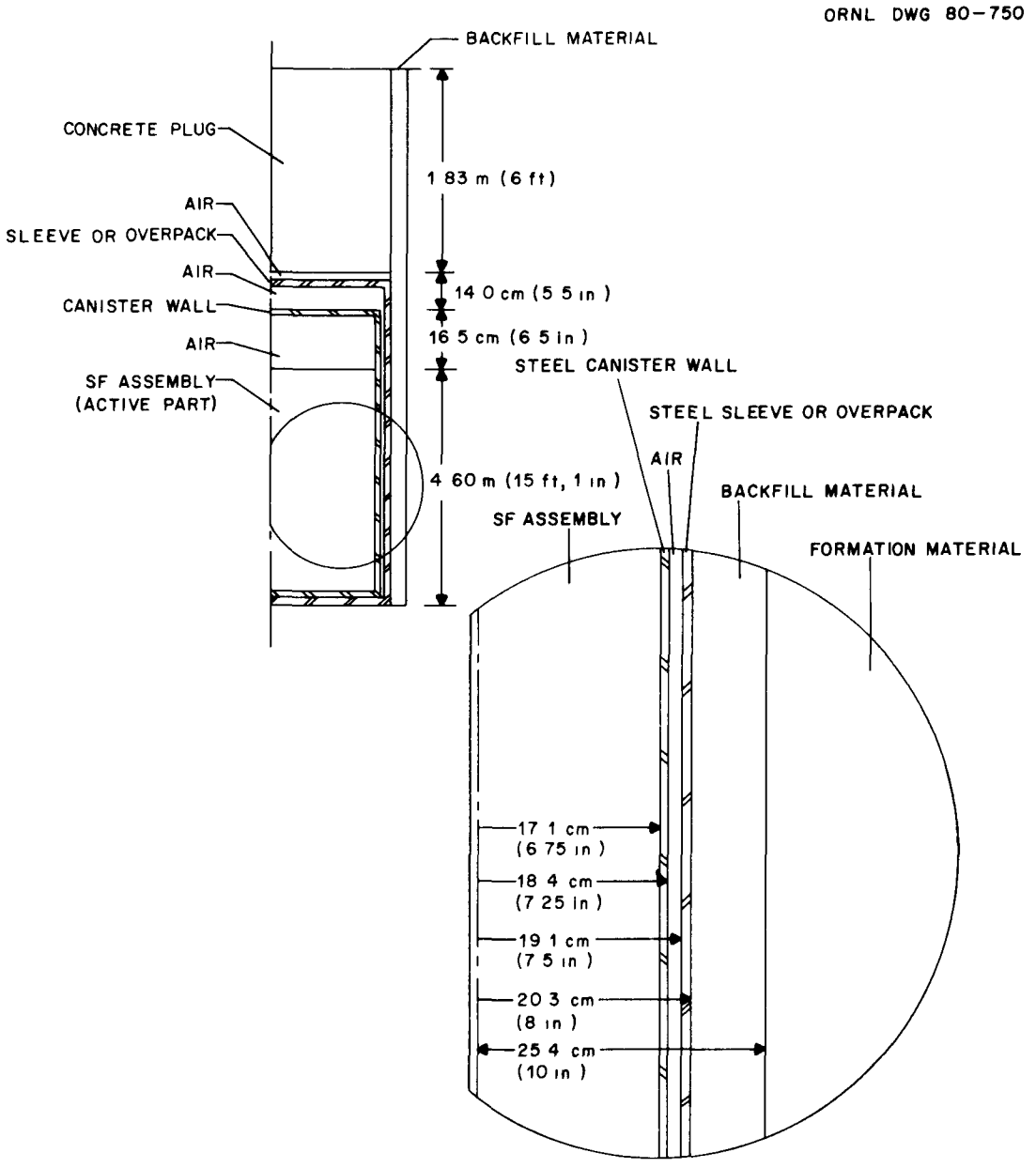

Fig. D-2. Details of waste receptacle and canister for the two-row configuration.

Table D-1. Nodal coordinates for near-field axisymmetric unit-cell studies for the two-row spent fuel configuration

Depth below surface (ft), z	Radial distance from waste centerline (ft), r
1000	0
1600	0.607
1850	0.63
1928	0.727
1981	0.9
1991	1.0
1992.46	1.33
1995	1.75
1996	3.0
1997	6.0
2000	7.48
2003	
2004	
2005	
2007.54	
2009	
2018	
2035	
2072	
2150	
2400	
3000	

Table D-2. Nodal coordinates for near-field 3-D unit-cell studies for the two-row spent fuel configuration

Depth below surface (f), z	Distance from waste centerline normal to storage room (ft), x	Distance from waste centerline along the storage room (ft), y
0	0	0
1000	0.7	0.535
1600	1.5	0.9
1850	2.75	1.5
1928	3.82	2.0
1966.13	6	
1987.13	9	
1990	17.2	
1992.46	29	
1995	44	
1997		
2000		
2003		
2006		
2007.54		
2009		
2018		
2035		
2072		
2150		

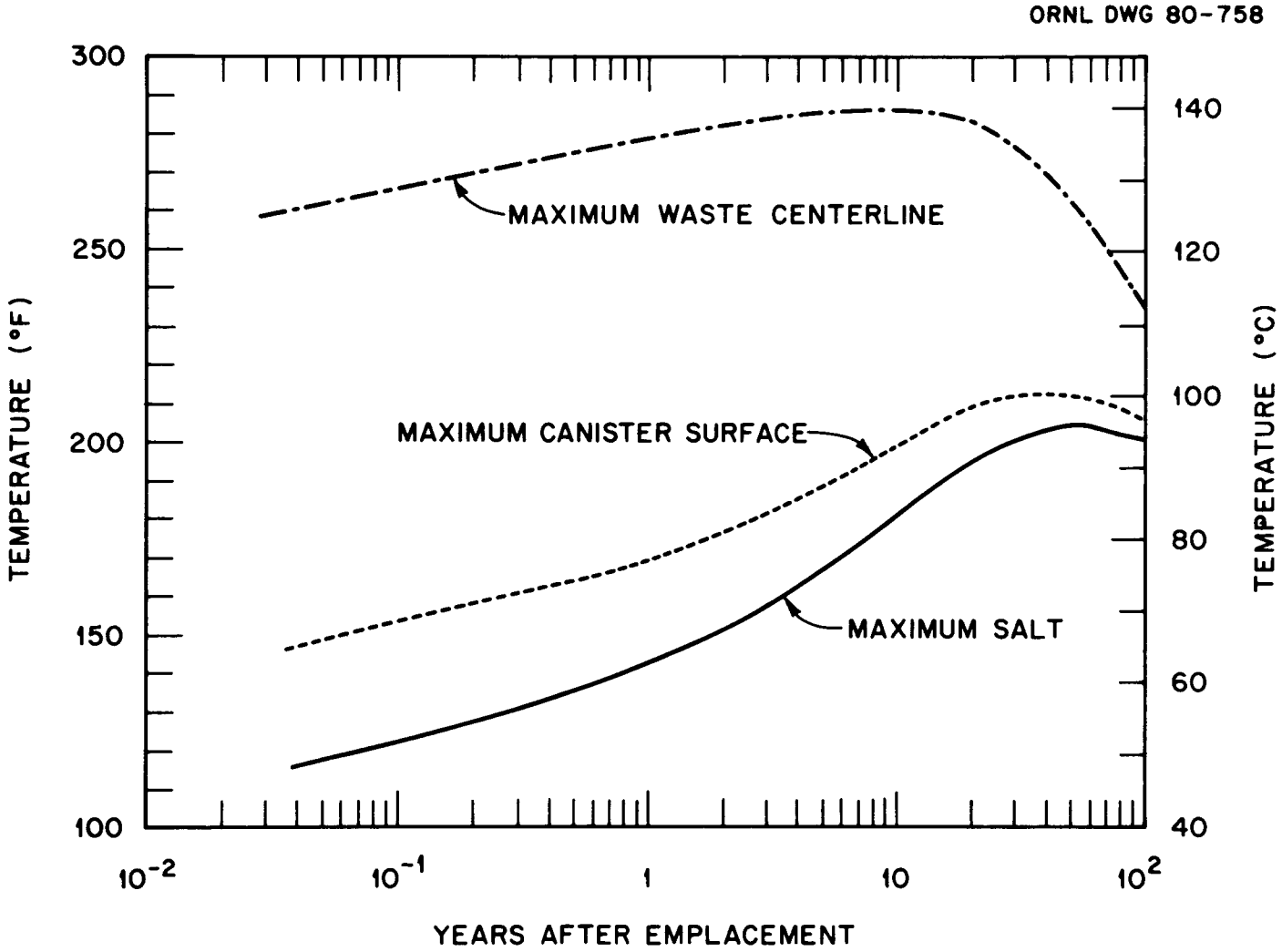

Fig. D-3. Maximum salt, canister surface, and centerline temperature histories for BWR spent fuel elements for an areal heat load of 60 kW/acre (14.8 W/m^2) in the two-row configuration.

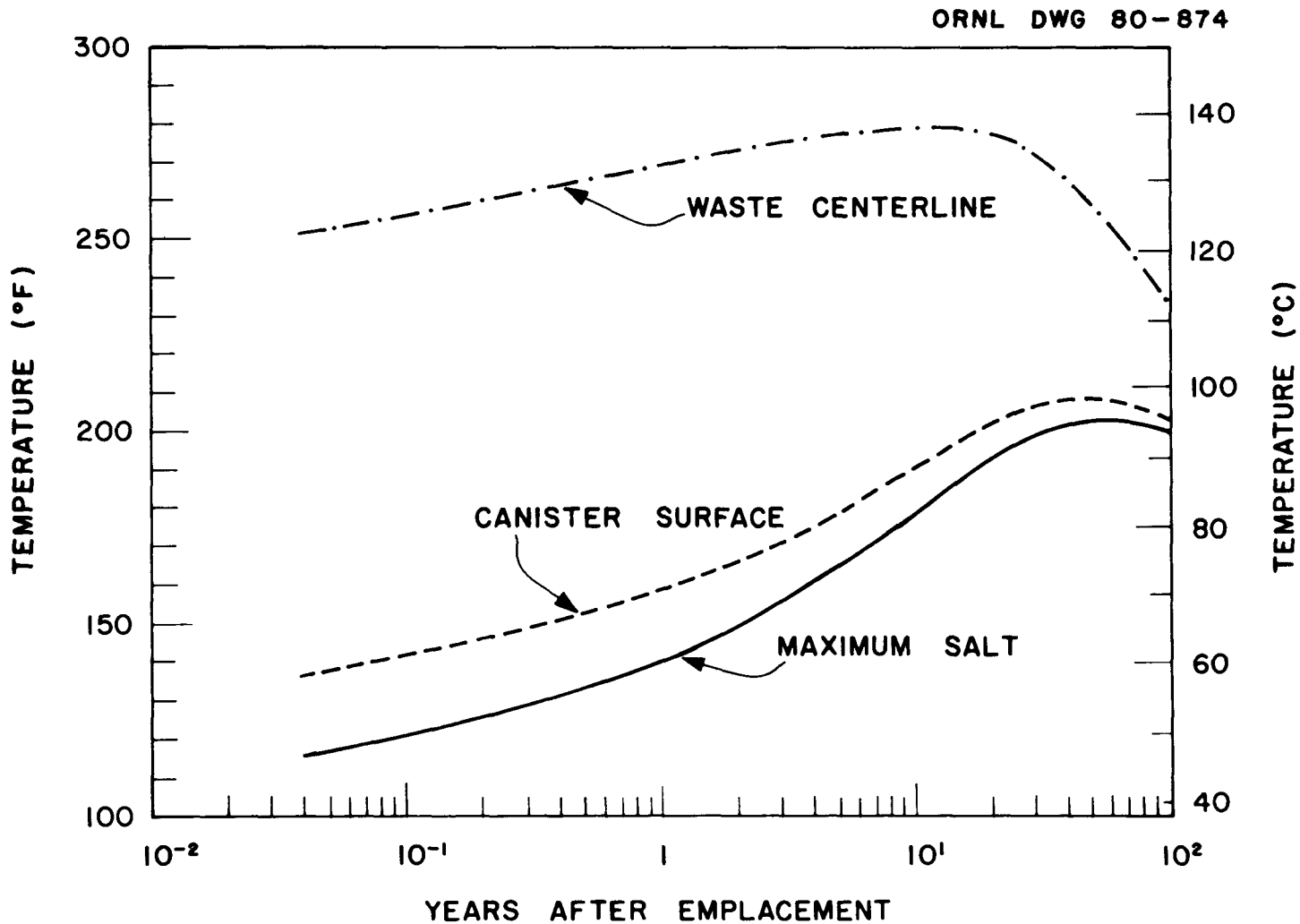

Fig. D-4. Maximum salt, canister surface, and centerline temperature histories for PWR spent fuel elements for an areal heat load of 60 kW/acre (14.8 W/m^2) in the two-row configuration.

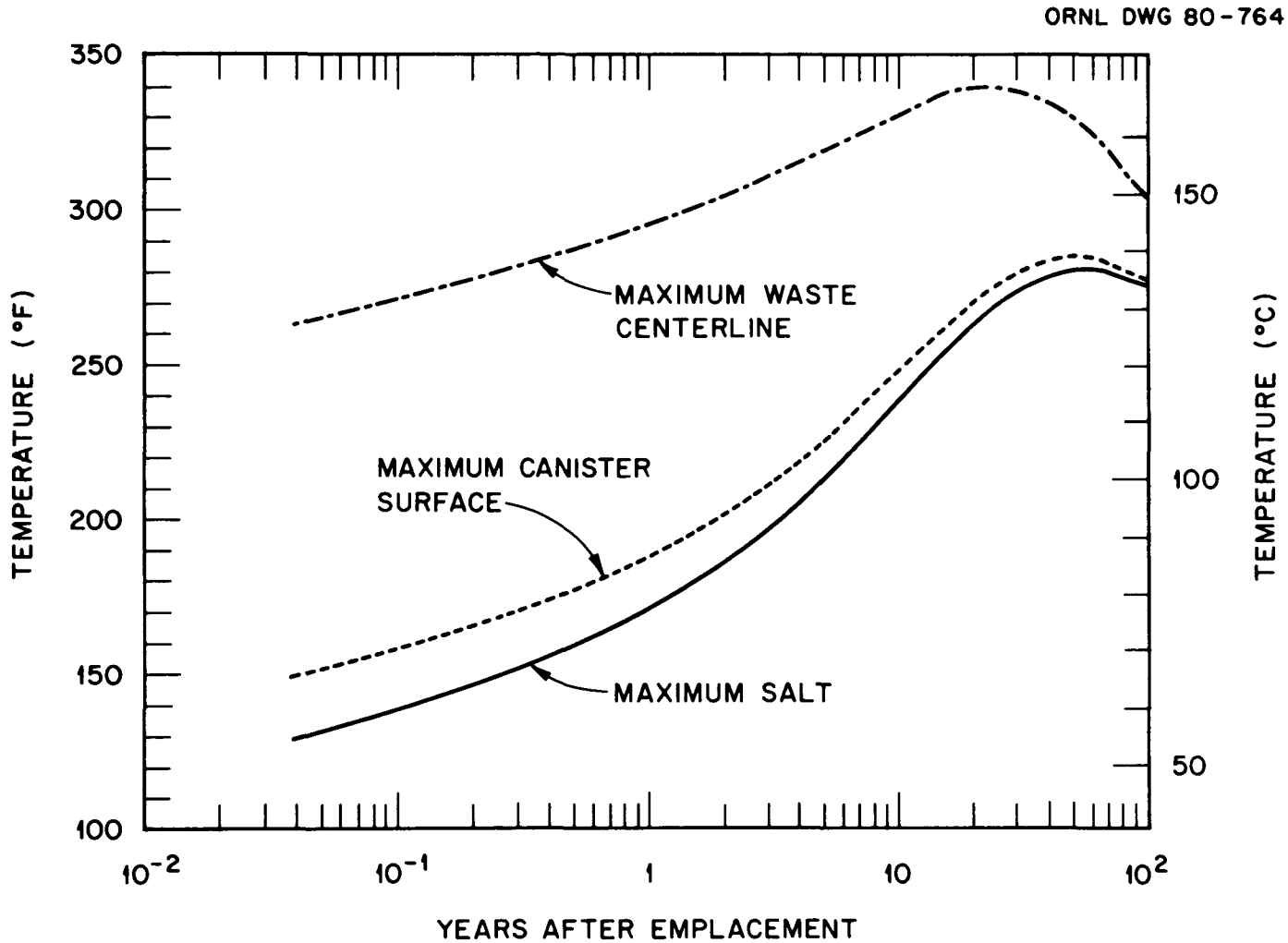

Fig. D-5. Maximum salt, canister surface, and centerline temperatures for BWR spent fuel elements for an areal heat load of 98 kW/acre (24.3 W/m^2) in the two-row configuration.

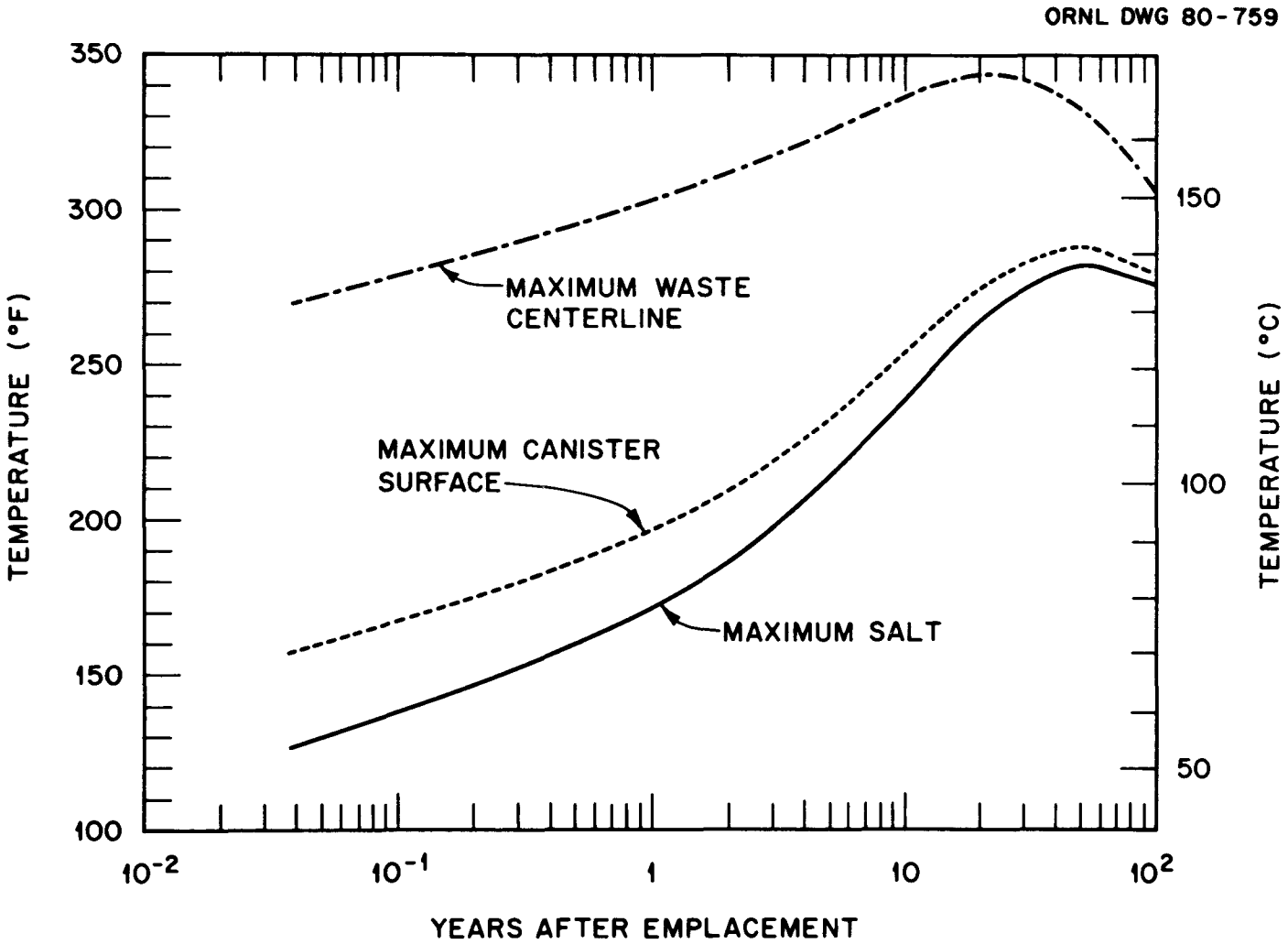

Fig. D-6. Maximum salt, canister, surface, and salt temperature histories for PWR spent fuel elements for an areal heat load of 98 kW/acre (24.3 W/m^2) in the two-row configuration.

APPENDIX E: DETAILS OF THE FAR-FIELD MODEL

The far-field analysis is described in Sect. 2.4, and a cylindrical model is used as shown in Fig. 31. The coordinates used for the far-field mesh spacing is shown in Table E-1 for both the domed and the bedded salt models. The volumetric heat-generation rate required for input in the numerical model, for example, is obtained for the far-field analysis as follows:

$$\text{volumetric heat-generation rate} = \frac{\text{areal heat load}}{\text{waste (or SF assembly) heat load x height}} \qquad \text{(E-1)}$$

Note that the waste (or SF assembly) is assumed to be smeared over a 1-mile (0.631-km)-radius, 50-ft (15-m)-thick region. Therefore, only the results at a distance from this region are valid.

Results were presented in Sect. 2.4 for HLW at 150 kW/acre (37.1 W/m^2) and SF at 60 kW/acre (14.8 W/m^2) and SF at 40 kW/acre (9.88 W/m^2). Figures E-1 and E-2 show the temperature rise vs the distance from the surface of the earth for the 100- and 40-kW/acre (24.7- and 9.88-W/m^2) cases, respectively. Figures E-3 and E-4 present temperature rise histories at 0, 500, and 1500 ft (0, 150, and 460 m) below the the surface of the earth for the 100- and 40-kW/acre (24.7- and 9.88-W/m^2) cases, respectively. The maximum use at the surface of the earth >1°F (0.8°C) and cannot be seen on the scale of the figure.

Table E-1. Nodal coordinates used for mesh spacing in far-field studies

z (depth below surface, ft)		r (distance from waste centerline normal to storage room, ft)	
Dome salt	Bedded salt	Dome salt	Bedded salt
0	0	0.0	0
10	50	10	10
20	100	35	35
100	250	50	50
500	300	75	75
1000	500	100	100
1500	800	150	150
1900	1050	225	225
1950	1200	350	350
2000	1400	600	600
2050	1500	1000	1000
2100	1700	1700	1700
2500	1900	2700	2700
4000	1950	3900	3900
6000	2000	5832	5282
10000	2050	6764	6764
15000	2100	8000	8000
	2200	10000	10000
	2250	12000	12000
	2550	15000	15000
	3200		
	3500		
	3750		
	3900		
	4000		
	6000		
	10000		
	15000		

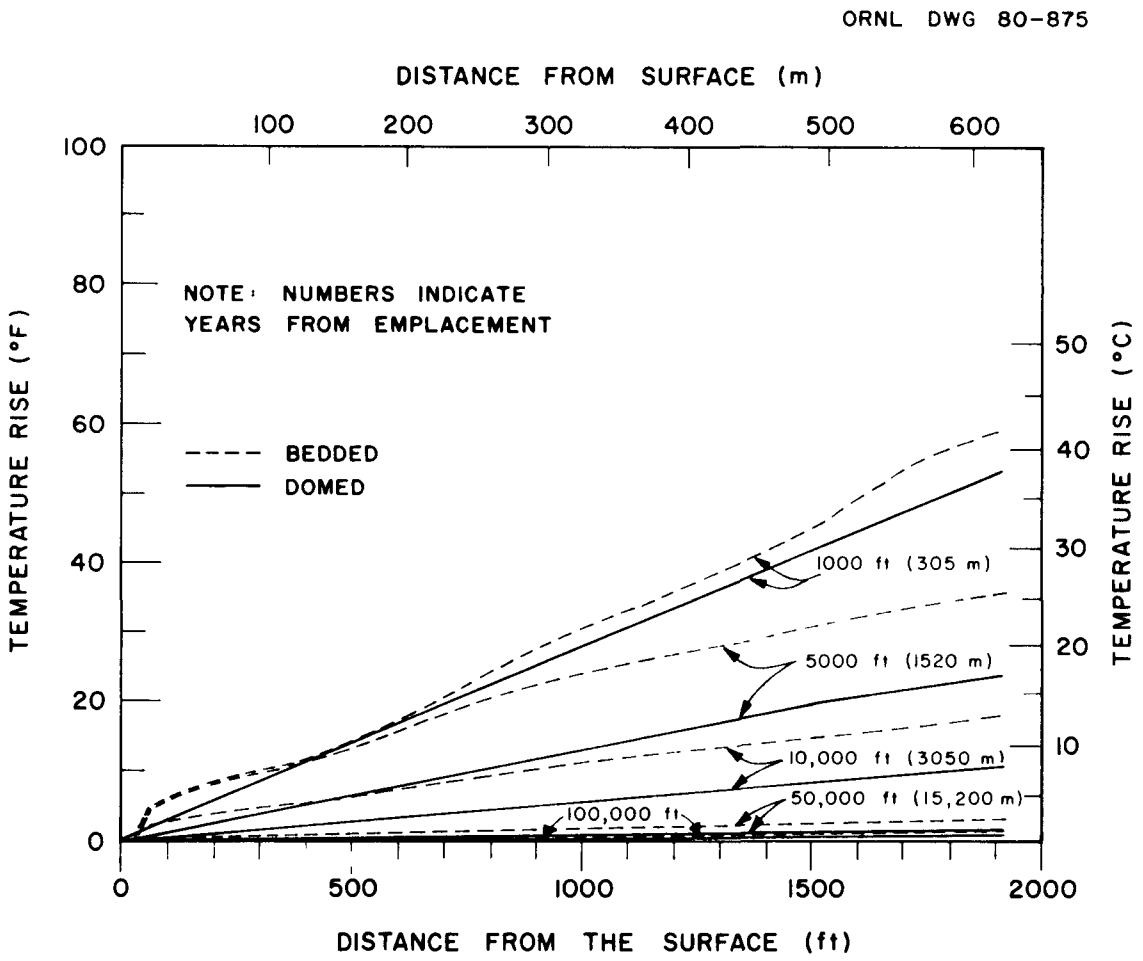

Fig. E-1. Temperature rise vs the distance from the surface of the earth for 100-kW/acre (24.7-W/m^2) high-level waste.

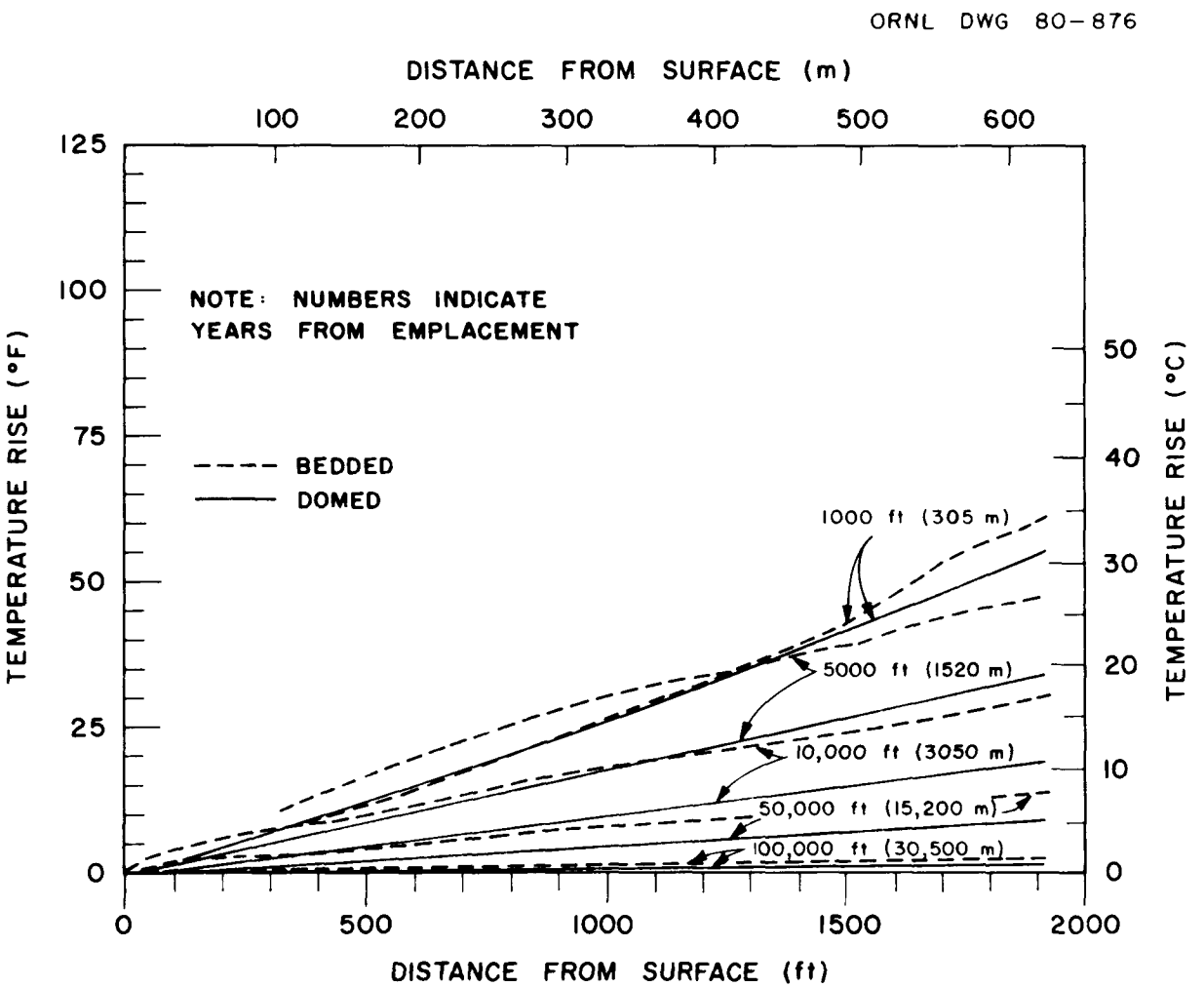

Fig. E-2. Temperature use vs the distance from the surface of the earth for 40-kW/acre (9.88-W/m^2) spent fuel.

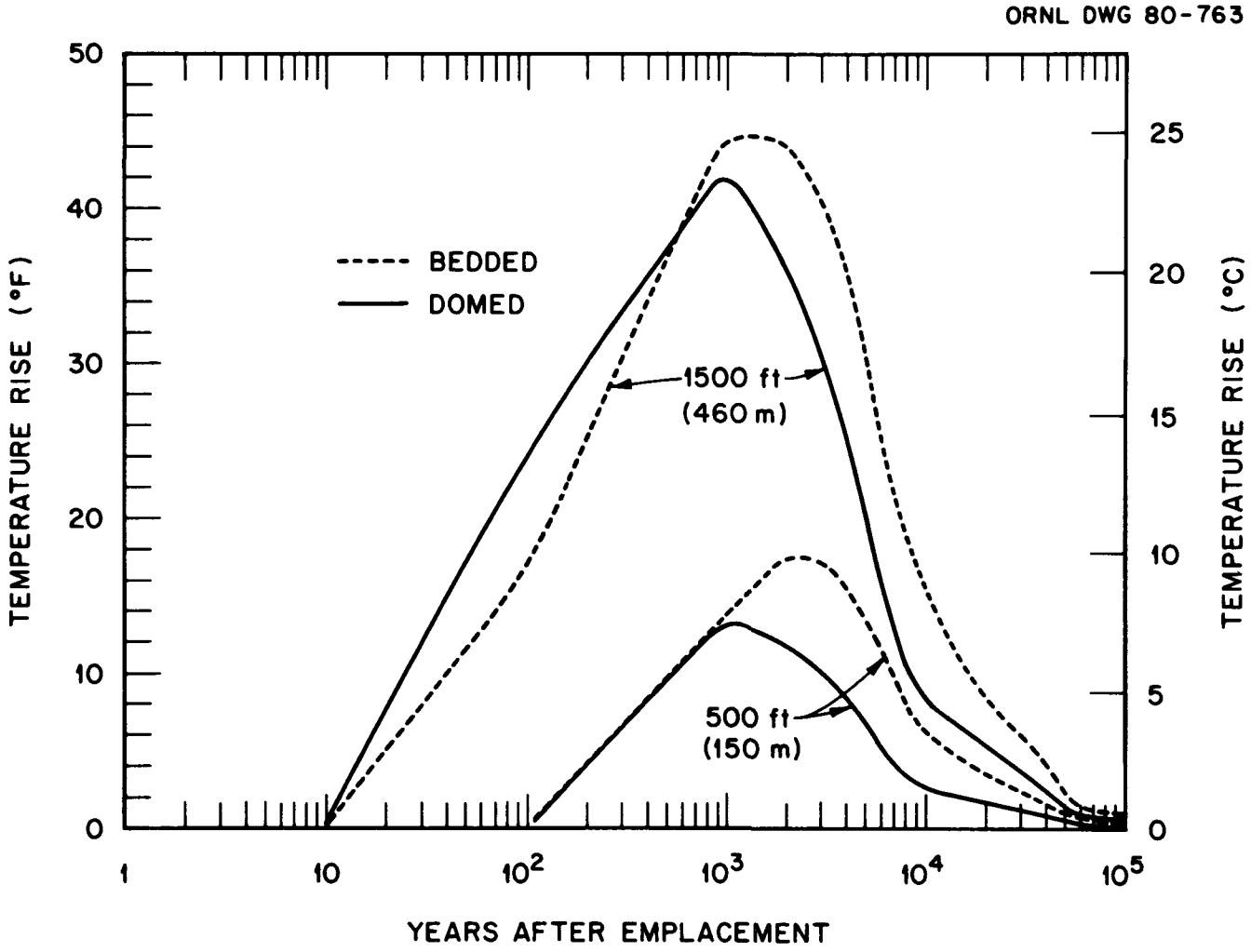

Fig. E-3. Temperature histories for 100 kW/acre (24.7 W/m^2) high-level waste at 500 and 1500 ft (150 and 460 m) below the surface of the earth.

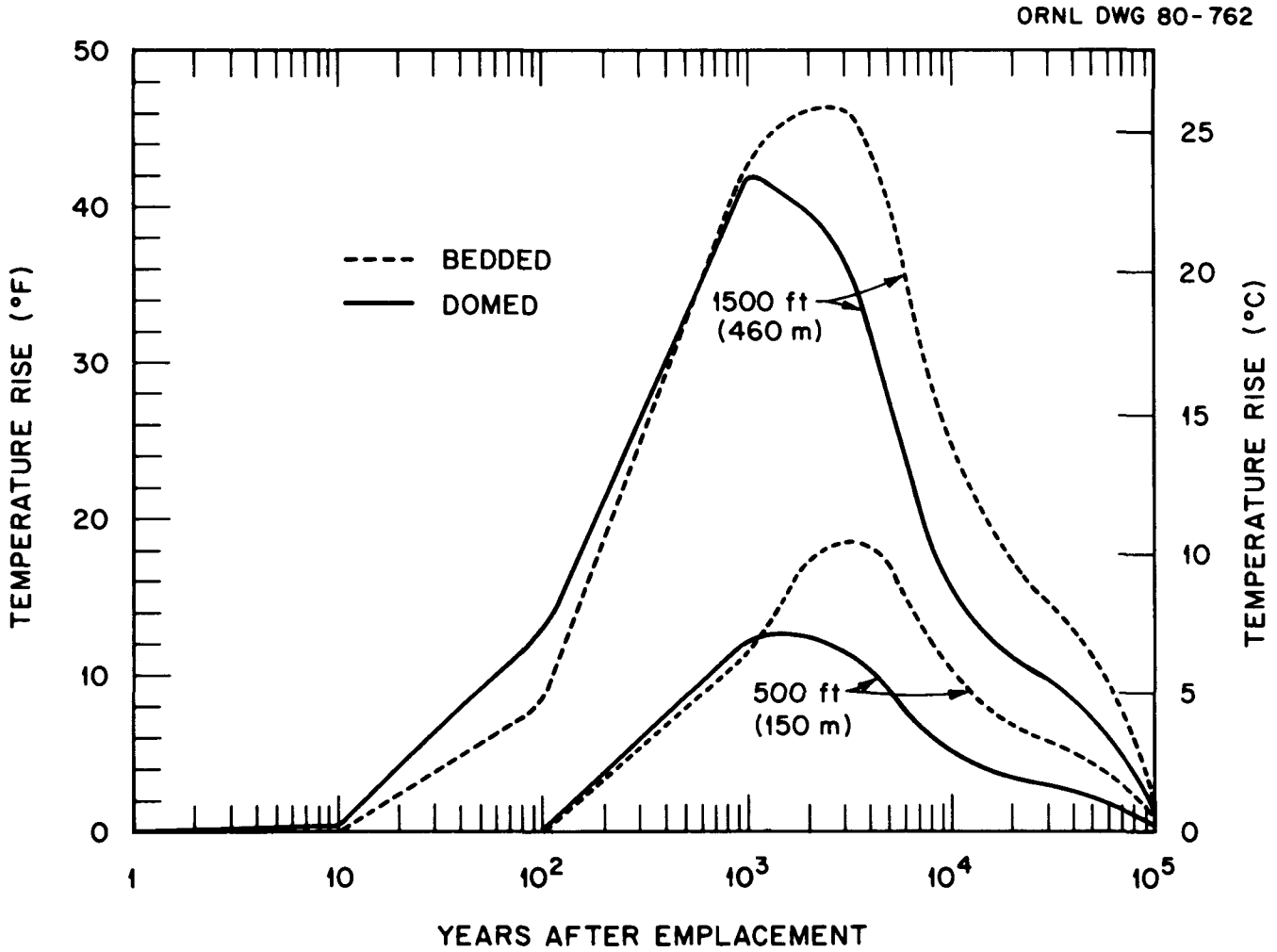

Fig. E-4. Temperature histories for 40 kW/acre (9.88 W/m^2) spent fuel at 500 and 1500 ft (150 and 460 m) below the surface of the earth.

APPENDIX F: THE MIGRAIN CODE

In this Appendix, the theory and description of the MIGRAIN code are given and a comparison of calculation using Eq. (1) of Sect. 3.1 is made with the available results of the Salt Block II experiments at Sandia Laboratories.

F.1 Comparison of Calculations and Experiment

The configuration modeled is shown in Fig. F-1. The top and bottom surfaces of a salt cylinder measuring 1 m in diameter and 1 m high were insulated. The outer surface was fixed at a temperature of 70°F (21°C). A heater 0.6 m in length was placed into a 10-cm hole centered along the axis of the block. The heater power as a function of time is given in Table F-1.

The temperature field was computed using the heat conduction code HEATING5.[1] Since the thermal properties of the salt sample were not known, the temperature-dependent conductivity of Birch and Clark[2] was used.

The brine migration into the heater hole was computed for the model, and the results are given in Fig. F-1. The prediction for the net collection of water into the heater hole is shown as the lowest curve in Fig. F-2 and is based on an initial brine inclusion density of 0.5 vol. %, which was determined from the analysis of core samples from the WIPP site. The points in this figure give the experimental data. For comparison, the results due to a constant heat source of 1.5 kW are also shown, and the shape of the curve is qualitatively different. The comparison of these curves suggests that the model predicts the shape of the curve reasonably well, although the results are lower than the data by $\sim$30% or less.

Aside from the possibility that other phenomena may exist (such as Darcy flow through cracks or opened grain boundaries), a possible explanation for the high brine inflow is that the actual temperature distribution may have been different than that computed. The thermal conductivity used in the calculation was that for pure salt, and since the salt block was taken from a salt bed, the actual conductivity may have been lower,

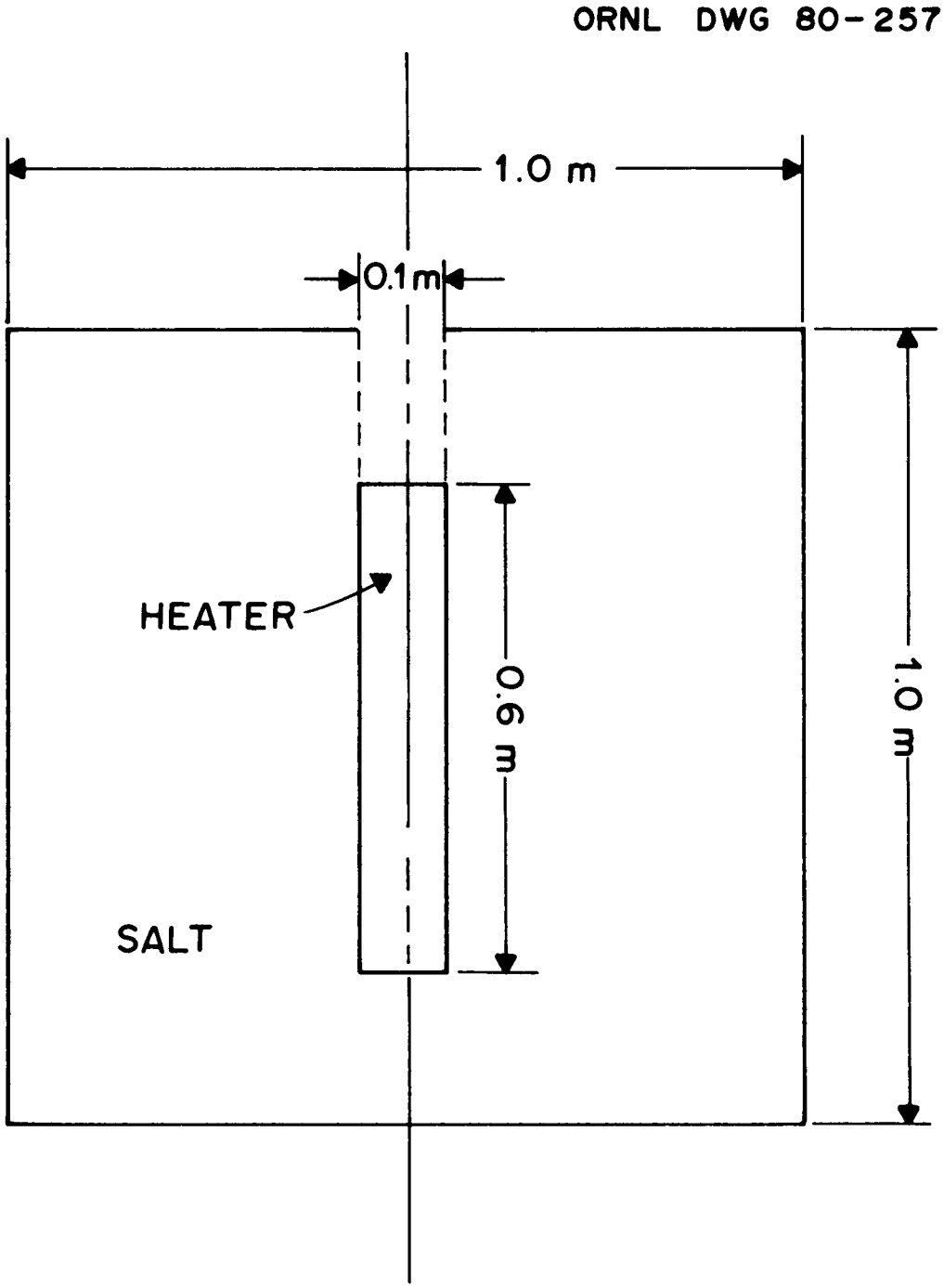

Fig. F-1. Schematic diagram of Salt Block II model.

Table F-1. Heater output for the Sandia Salt Block II experiment

Time interval (d)	Output (W)
0–6	0
6–12	200
12–12	400
20–35	600
35–50	1000[a]
50–118	1500
118–125	1000
125–132	600
132–140	0

[a]Power outage for 30 min on day 42 was not taken into account.

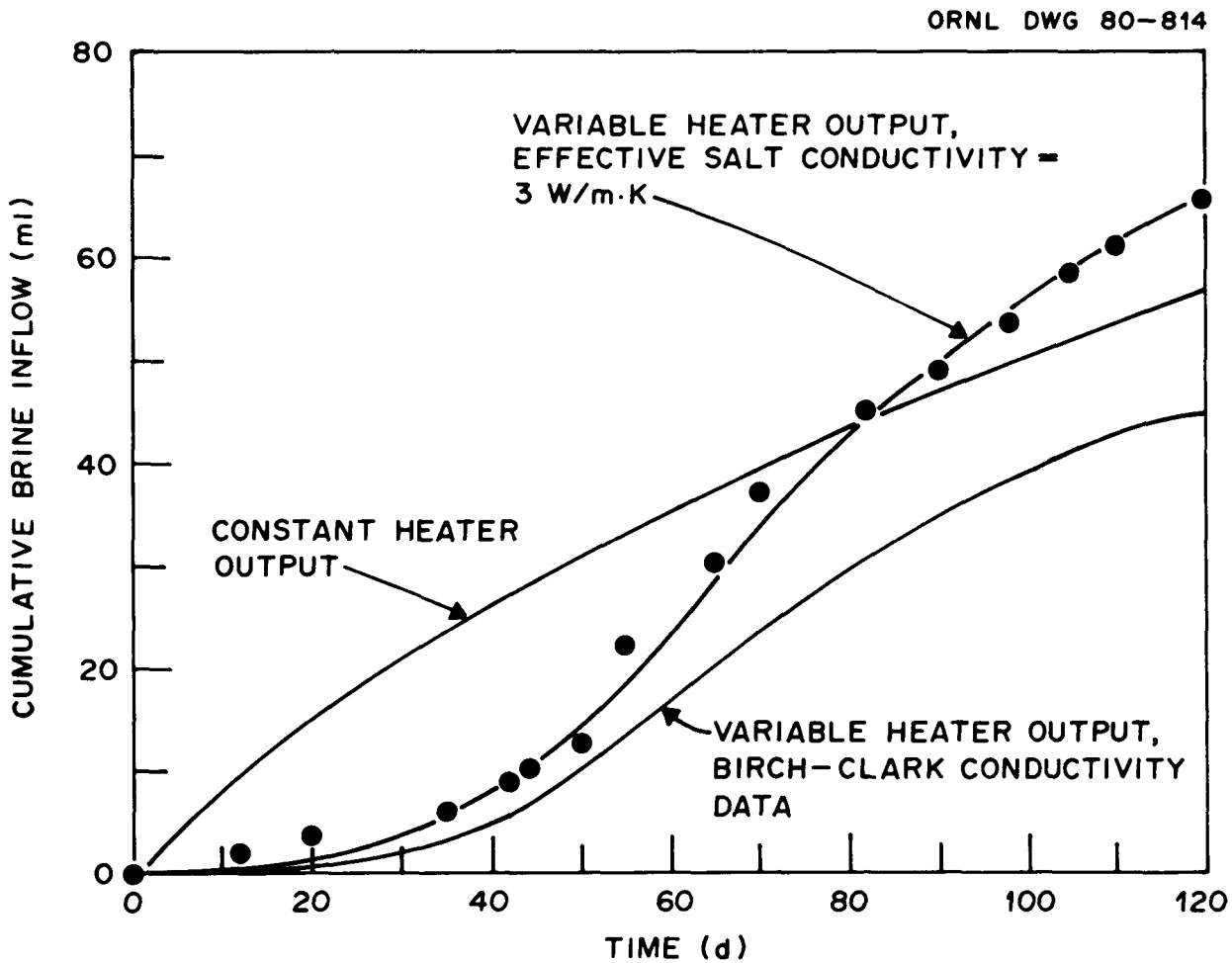

Fig. F-2. Comparison of calculated brine inflow with results for the Salt Block II experiment.

resulting in a steeper temperature gradient and therefore higher migration rates. If a constant salt thermal conductivity of 3 W/mK is used, calculated results (bottom curve) agree quite well with the prior experiment when the heater was turned off, assuming a brine content of 0.7 vol % will also produce good agreement (not shown in Fig. F-1). The calculational model cannot be used to predict the brine spike that occurred after the heater was turned off; consequently, no comparison was made after that time.

F.2 Theory and Description of the MIGRAIN Code

The MIGRAIN (MIGRAtion of INclusions) treats the distribution of brine inclusions as a compressible fluid obeying the time-dependent continuity equation. The momentum and energy equations are not explicitly solved, but the velocity field is evaluated from a phenomenological expression that relates the velocity to the temperature and gradient. The expression used in this report was the Jenks equation [Eq. (1), Sect. 3.1], which correlates the inclusion velocities in salt crystals; however, any similar expression could be used. The assumption is made that the temperature field can be supplied by an independent calculation. In addition multiphase effects are not currently treated.

The flow is calculated from the mass conservation equation. Upwind differences are used to approximate the continuity equation,[3] and Levy's modification[4] is used to ensure stability for the explicit scheme. The inflow to any specified volume is then calculated by both mass balance and density variation techniques in order to check the procedure.

The present version of the code is written for an IBM-360 computer, although only minor modifications would be needed to convert to other systems. The input required for this version is listed in Table F-2. The input must specify the boundaries of the cavity where the brine accumulates. Other input variables describe the data pointed out and the initial density of the brine in the salt. Both cartesian coordinates (1-D, 2-D, or 3-D) or cylindrical coordinates (r-z) may be specified. The code is presently designed to interface with the HEATING5 heat conduction code, but the modification to accept temperature files generated by other codes is straightforward.

Table F-2. Input for the MIGRAIN code

Record	Format	Variables	Description
1	3I5	IR, IW, IT	Input, output, and temperature input units
2	4F8.3	XB1, XB2, XP1, XP2	X or R cavity boundaries, X or R printout limits
3	4F8.3	YB1, YB2, YP1, YP2	Y cavity boundaries, Y printout limits (leave card blank if cylindrical)
4	4F8.3	ZB1, ZB2, ZP1, ZP2	Z cavity boundaries, Z printout limits
5	F8.3	Density	% density (by volume) Time conversion factor[a]
6	3F8.3	YEAR, TIME IN, TIME OUT	Time limits of problem

[a]The time conversion is used for convenience to convert from the time units used in the temperature calculation to any other units. The time limits refer to starting and ending model time.

REFERENCES FOR APPENDIX F

1. W. D. Turner, D. C. Elrod, and I. I. Siman-Tov, HEATING5-An IBM 360 Heat Conduction Program, ORNL/CSD/TM-15 (March 1977).

2. F. Birch and H. Clark, The Thermal Conductivity of Rocks and its Dependence upon Temperature and Composition, Part II, Am. J. Sci. 238, 613–35 (1940).

3. P. J. Roache, Computational Fluid Dynamics, pp. 237–242, Hermosa Publishers, Albuquerque, New Mexico, 1972.

4. S. Levy, Use of Explicit Methods in Heat Transfer Calculations with an Arbitrary Time Step, General Electric Company Report No. 68-C-282 (1968).

APPENDIX G: VAPOR SPACE PRESSURE METHODOLOGY — THE REPRESS CODE

The pressure exerted by a gas is a function of gas quantity and composition, temperature, and volume. The functional relationship between these variables is referred to as an equation of state. The simplest and most widely known equation of state is the ideal gas law,

$$PV = nRT \ , \qquad \text{(G-1)}$$

where

P = pressure,
V = volume,
n = number of moles of gas, and
T = absolute temperature.

The ideal gas law is most accurate in the region of high temperatures, low pressure, and no molecular interaction. However, departures from ideal gas behavior cause considerable error near the critical point, the dewpoint, and at very high pressures or low temperatures. Empirical corrections to the ideal gas law are usually expressed as charts or tables of the compressibility factor Z. The compressibility factor of a real gas is obtained from the relation

$$Z = \frac{PV}{nRT} \ , \qquad \text{(G-2)}$$

with Z being a dimensionless parameter and the other variables defined above. The Nelson and Obert general compressibility charts[1] give compressibilities as a function of reduced pressures and temperatures. For nonpolar and slightly polar gases, the charts are accurate to within 1%.

The equation of state along with the compressibility correction discussed above is adequate for describing the PVT relationships of nonpolar gases (N_2, O_2, H_2) which may be encountered in the waste repository. However, the equations fail to describe the behavior of steam. For this industrially important substance, tables of experimentally

measured thermodynamic data are available. The PVT data from these tables may be interpolated so that pressure can be predicted from any specified condition of temperature and volume. Therefore, the pressure prediction model utilizes the Combustion Engineering steam tables[2] and the U.S. Geological Survey tables of the thermodynamic properties of brine[3] to provide the data used in the modeling of air-steam mixtures.

The above discussion of thermodynamic state applies to pure substances. Since mixtures of air and water vapor are expected in the repository, a methodology for modeling mixtures is necessary. The most common procedures include parameter modification in analytic equations of state and application of compressibility data to simple mixing rules. Such modified equations still bear the inability to account for polar interactions and are therefore unsuitable for steam-air mixtures. Compressibility data may be applied to simple mixture values such as those given by Dalton's Law. Dalton's Law is most suitable since it can predict nonideal behavior and does not require the exclusive use of the generalized compressibility chart. Dalton's Law is given as follows:

$$P = \sum_{i=1}^{n} P_i \ , \qquad \text{(G-3)}$$

where

P = total pressure, and

P_i = pressure of component i.

Using this equation requires a knowledge of the P_i values. These can generally be found by applying Eq. (G-2) to Dalton's Law:

$$P_i = \frac{RT}{V} (n_i Z_i) \ . \qquad \text{(G-4)}$$

Since the compressibility factor for each component is a function of P_i and T, an iterative procedure would be required to determine the total pressure.

Examination of expected repository conditions allows the above equations to be simplified. Assuming that the cavity temperatures lie in the range of 100 to 700°F (38 to 371°C), the major components of air

(N_2, O_2) behave as ideal gases, which have a constant compressibility factor of 1.0. This simplifies Eq. (G-4) to the ideal gas law — Eq. (G-1).

For steam, the thermodynamic data tabulated in the steam tables[2] may be used to interpolate to P_i. A complicating factor is that the ratio of the vapor pressure of water vapor to the brine is less than that of the water vapor to pure water. Superheating the system (no liquid present) has no effect. The superheated steam tables may be used directly to find P_i for the steam. This value is then added to the P_i for air to calculate the total pressure.

The saturated steam tables may not be used when the system is saturated (liquid present). Instead, a U.S. Geological Survey publication[2] containing the thermodynamic properties of saturated brine was used to find the vapor pressure.

A region of uncertainty exists where, according to the steam tables, the system would be superheated, and according to the brine table, the system would be saturated. When this situation occurs, it was decided to assume the system is saturated (according to the brine table).

These considerations serve as the basis for the saturation pressure and water inventory calculation in the REPRESS code. If the amount of brine inflow meets or exceeds the amount required to saturate the vapor space, the phase equilibrium relations will apply. If the available water is less than the saturation value, only the water vapor phase will exist in the cavity and the phase equilibrium relations will not apply. In this event, the specific volume of the vapor is calculated and the pressure is obtained by interpolation from the steam tables. Results illustrating this methodology using the REPRESS code are shown in Figs. G-1 through G-4. Figures G-1 and G-2 show the predicted pressure histories for the HLW [100 kW/acre (24.8 W/m^2)] and SF [40 kW/acre (14.8 W/m^2)] emplacement holes, respectively. Figure G-3 shows the liquid brine history for high-level waste for an areal loading of 100 kW/acre (24.8 W/m^2).

The REPRESS code, which was developed for these calculations, is described briefly below. The inputs to the REPRESS program are the original volume, and temperature, brine inflow, and closure as a function

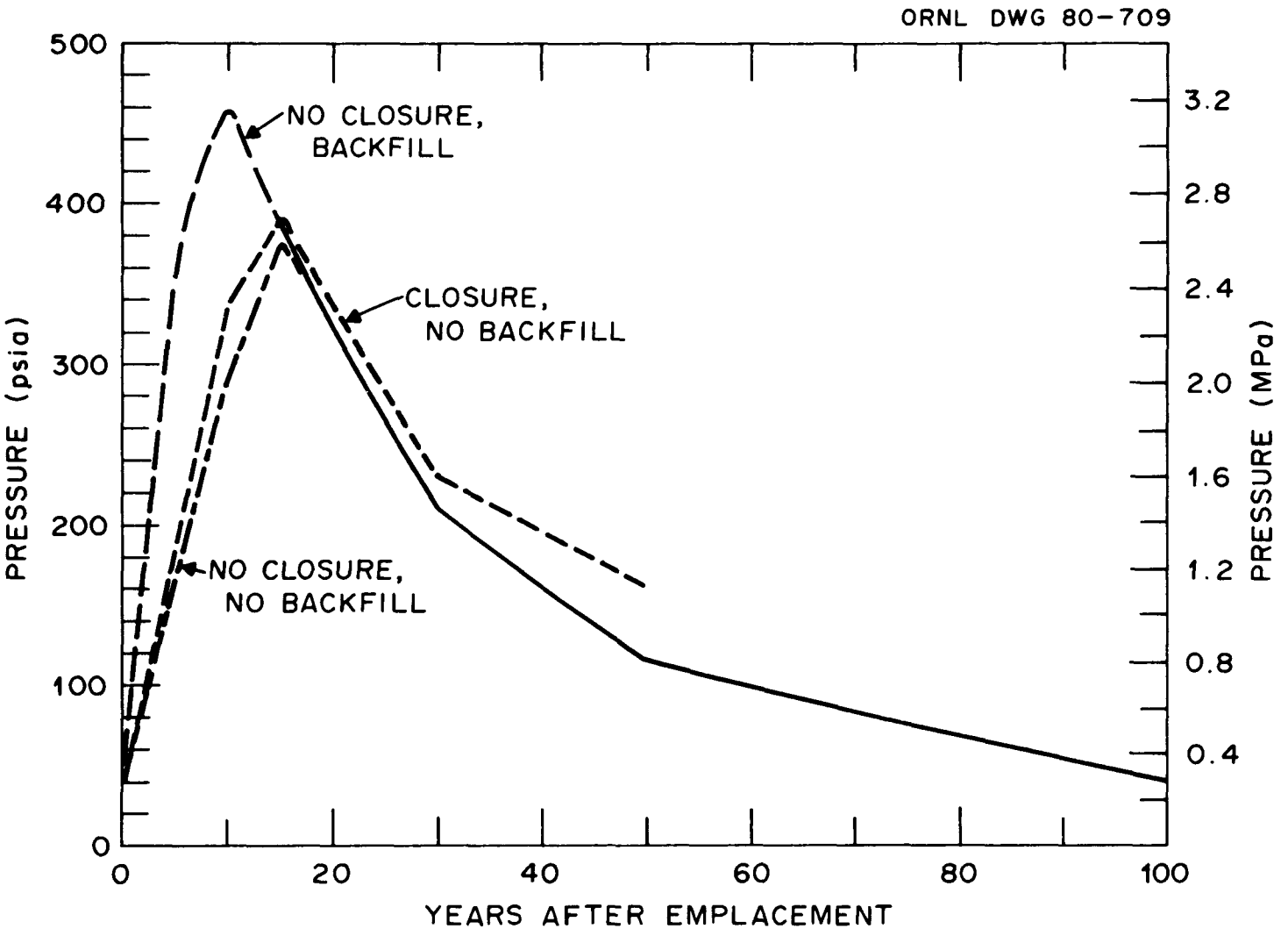

Fig. G-1. Pressure histories for 100-kW/acre (24.7-W/m^2) high-level waste.

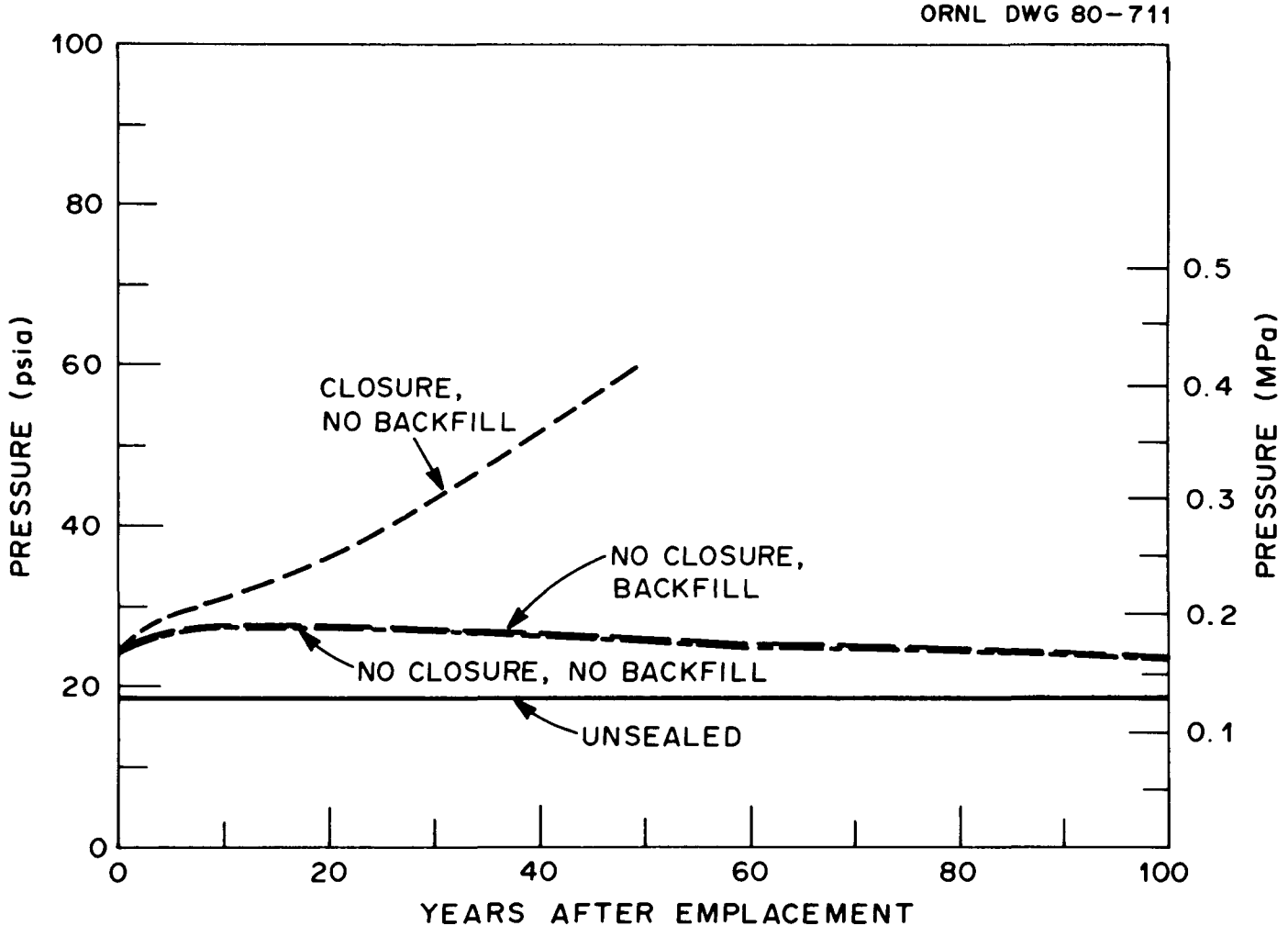

Fig. G-2. Pressure histories for 40-kW/acre (9.88-W/m^2) spent fuel.

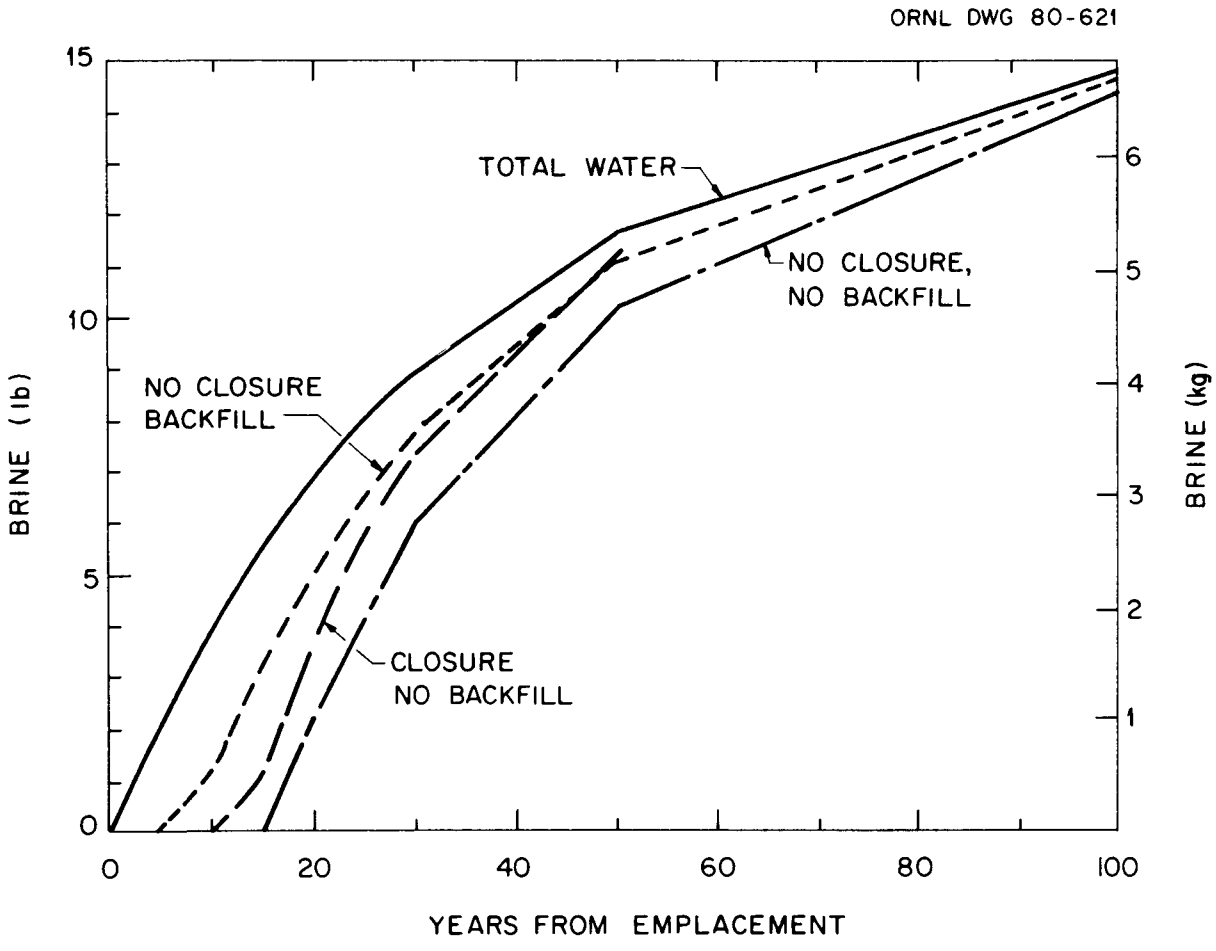

Fig. G-3. Liquid brine histories for 100-kW/acre (24.7-W/m^2) spent fuel.

of time. The output in its present form is total pressure, weight of brine as liquid, and weight of water vapor. The code can be easily modified to provide the amount of salt precipitated.

When run, the name of the input data file will be requested. This should be a file that contains first, the title of the data; second, the original volume; third, the column headings Time, Temperature, Inflow, Closure; and fourth, the data itself. In its present form, the code will process data as a function of time. The initial volume is to be specified in liters. Time can be in any units, temperature is in degrees Fahrenheit, °F, brine inflow is in liters, and closure is the fraction of original volume.

The code processes these data using the superheated steam tables and the saturated brine tables. One note of confusion occurs near the dew point where the first drop of vapor condenses, or equivalently in most systems, where the last drop of liquid vaporizes. In a salt-water system, however, the last drop of liquid to vaporize is a saturated brine, but the first drop of liquid to condense is pure water. This, in theory, would cause a hysteresis effect upon cyclically vaporizing and condensing the solution. Since this would not be acceptable in the model (to achieve continuity), it was assumed that the pressure was determined by vaporization of the liquid (i.e., it was assumed there was always at least a very small amount of brine, which could be rationalized by the fact that some brine is always flowing into the system).

Finally, the output is in five columns. The first two are time and temperature repeated from the input. The next three are total pressure (psia), weight of brine (lb), and weight of vapor (lb). The present version of REPRESS is written for use on a DEC FORTRAN Processor, although only minor modifications would be needed for use on other systems. The input required is shown in Table G-1, the output in Table G-2. A sample input file is shown in Table G-3. The results from this file are shown as the curves for the no-closure, no-backfill scenarios in Figs. G-1 and G-3.

Table G-1. Input for REPRESS

Variables	Format	Description
ITITLE	80A1	Name of the data
VOLSP	F10.5	Original volume of cavity, in liters
ITITL1	80A1	Column headings
TIME	Unformatted	Time at each point, years; 21 points
TEMP	Unformatted	Temperature at each point, °F; 21 points
FLOW	Unformatted	Total brine into the system at each point, liters; 21 points
CLOS	Unformatted	Fraction of the original volume left at each point, 21 points

Table G-2. Output from REPRESS

Variables	Format	Description
TIME		Time at each point, from input
TEMP		Temperature at each point, °F, from input
PTOT	(F10.3, 2F10.1, 2F10.3)	Total pressure at each point, psia
WLIQ		Weight of brine in the system at each point, lb
WVAP		Weight of water vapor in the system at each point, lb

Table G-3. Sample input file[a] for REPRESS

Years	Temperature (°F)	Flow	Closure
0.003	418.91	0.000157	1.0
0.038	455.64	0.005	1.0
0.08	468.33	0.011	1.0
0.17	479.82	0.024	1.0
0.25	486.11	0.038	1.0
0.5	495.57	0.081	1.0
0.67	498.15	0.103	1.0
0.83	501.07	0.141	1.0
1.0	502.52	0.171	1.0
1.25	504.53	0.217	1.0
1.5	505.89	0.264	1.0
2	507.10	0.357	1.0
3	508.20	0.544	1.0
5	505.57	0.916	1.0
10	490.48	1.772	1.0
15	469.32	2.504	1.0
20	448.22	3.120	1.0
25	427.10	3.640	1.0
30	403.12	4.072	1.0
50	344.12	5.304	1.0
100	243.65	6.732	1.0

[a]For high-level waste, 2.16 kW per canister [100 kW/acre (24.8 W/m^2)], no closure.

REFERENCES FOR APPENDIX G

1. R. H. Perry and C. H. Chilton, Chemical Engineers Handbook, pp. 3–232, 5th ed., McGraw-Hill, New York, 1973.

2. American Society of Mechanical Engineers, 1967 ASME Steam Tables, New York, 1967.

3. U.S. Geological Survey, Thermodynamic Properties of the Coexisting Phases and Thermochemical Properties of the NaCl Component in Boiling NaCl Solutions, Bulletin 1421-B, 1966.

APPENDIX H: NUMERICAL MODEL SENSITIVITIES

The thermal environments described in this report for HLW and SF repositories were obtained through the use of numerical models of the repository design. The choice of numerical models can sometimes affect the results due to the assumptions of the model or the inaccuracy of the computational technique. The HEATING5 finite-difference analysis[1] was used in obtaining all the thermal environments presented in this report. HEATING5 has been used in previous repository studies[2,3] with good success and has been found to be in excellent agreement with other methods.[4] In addition to these HEATING5 checks, an extensive series of model tests has been carried out. These include the sensitivity of the model to mesh spacing, model boundary contribution, and the sensitivity of numerical parameters such as initial time step, time-step iteration limits, and the differencing technique.

It must be emphasized that the particular results presented here basically represent scouting calculations that were used to establish reasonable limits on the numerical models. These scouting calculations were actually made before the baseline repository characteristics were established; consequently, they should not be related to the results in the body of the report because of the different parameters involved.

H.1 The Test Case Model

A cylindrical model (R-Z geometry) which assumed that the waste canister was directly embedded in solid salt with an upper adiabatic boundary at 1600 ft (488 m) and a lower adiabatic boundary at 2400 ft (732 m) was the base model. The areal heat load was 150 kW/acre (37.1 W/m^2), but a canister heat load of 3.2 kW was assumed. The heat-source decay history was somewhat different than described in Table 2. These differences, however, are unimportant with regard to the purpose of this sensitivity study.

H.2 The Effect of Mesh Spacing

A series of calculations was made to determine the effect of mesh spacing on the maximum salt temperature. In addition to the base case of 152 nodes (8 grid lines in the R direction and 19 in the Z direction), three additional cases were run — with 405 nodes (15 R and 27 Z grid lines), 481 nodes (13 R and 37 Z grid lines), and 1022 nodes (14 R and 73 Z grid lines). The results of these calculations are shown in Fig. H-1, where the temperature of the salt at the waste midplane (2000 ft (610 m) below the surface of the earth) is plotted vs the years after emplacement. Increasing the number of nodes by nearly a factor of 7 causes an increase in the maximum salt temperature (at Z = 2000 ft (610 m) and R = 0.05) of ∿27°F (15°C). This is less than a 7% increase over the test case. Doubling the grid spacing in the R and Z direction increases the maximum salt temperature by nearly 8°F (4.4°C), but increasing the Z grid spacing, particularly in the vicinity of the waste, will produce an increase of nearly 14°F (7.8°C) in the maximum salt temperature. Doubling the Z grid spacing from the above value shows an additional increase of 5°F (2.8°C).

H.3 The Effect of Model Boundary Location

In addition to the base case, four different thicknesses or separation distances between the upper and lower adiabatic boundaries were made to determine the effect of model thickness in the vertical direction. These different thicknesses were 144 ft (44 m), 300 ft (91 m), 2000 ft (610 m), and 4000 ft (1220 m). The waste horizon was located at the midplane of the model in all cases. The results plotted in Fig. H-2 show that the change in salt temperature at the midplane was insignificant for thicknesses beyond 2000 ft (610 m) up to at least 100 years.

H.4 The Effect of Numerical Parameters

The implicit finite-difference Crank-Nicholson iteration scheme was used in the test case calculation, and the classical implicit finite-difference scheme was computed for comparison. The results show slight

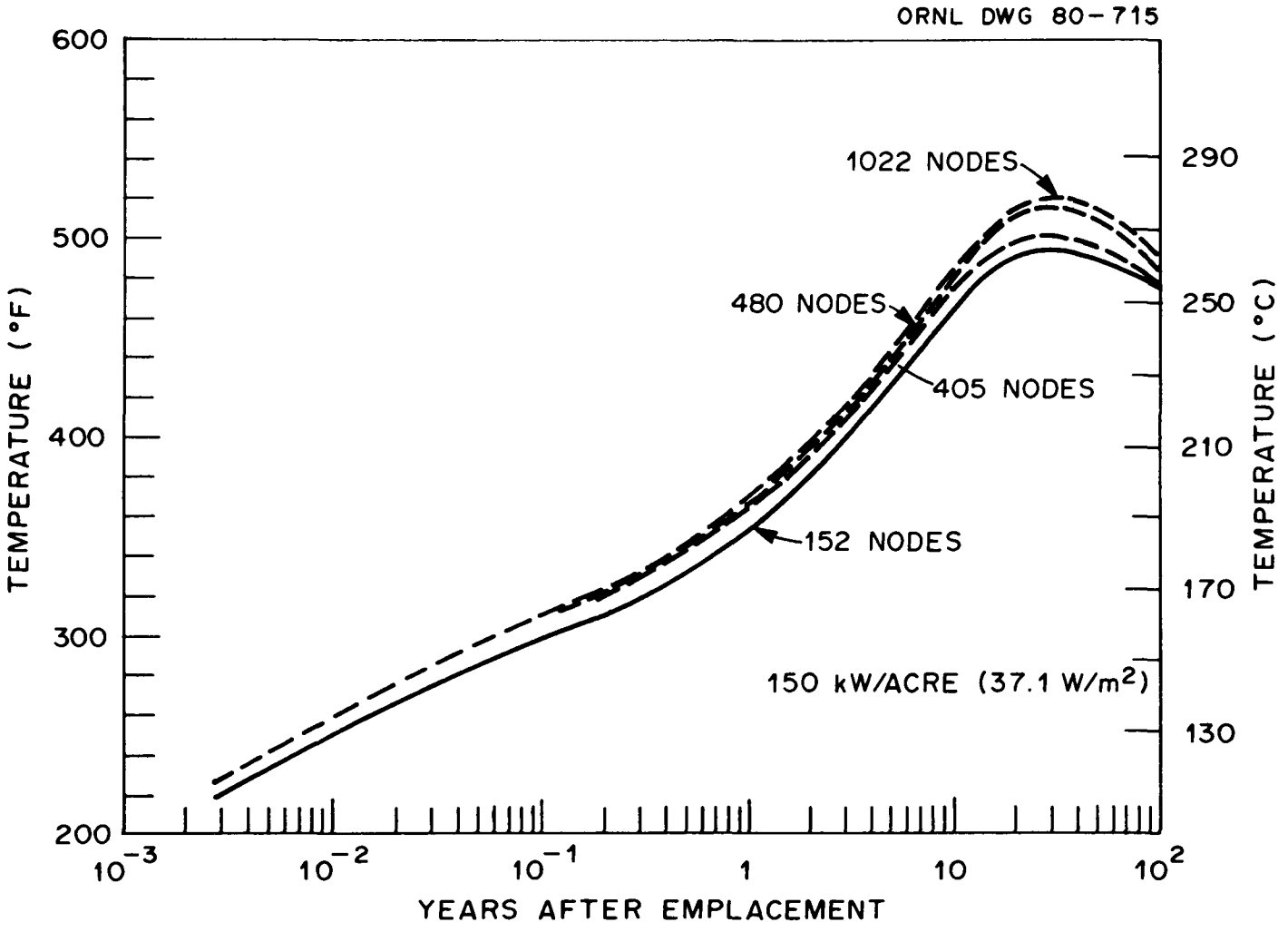

Fig. H-1. Effect of the variation in the number of nodes on the maximum salt temperatures.

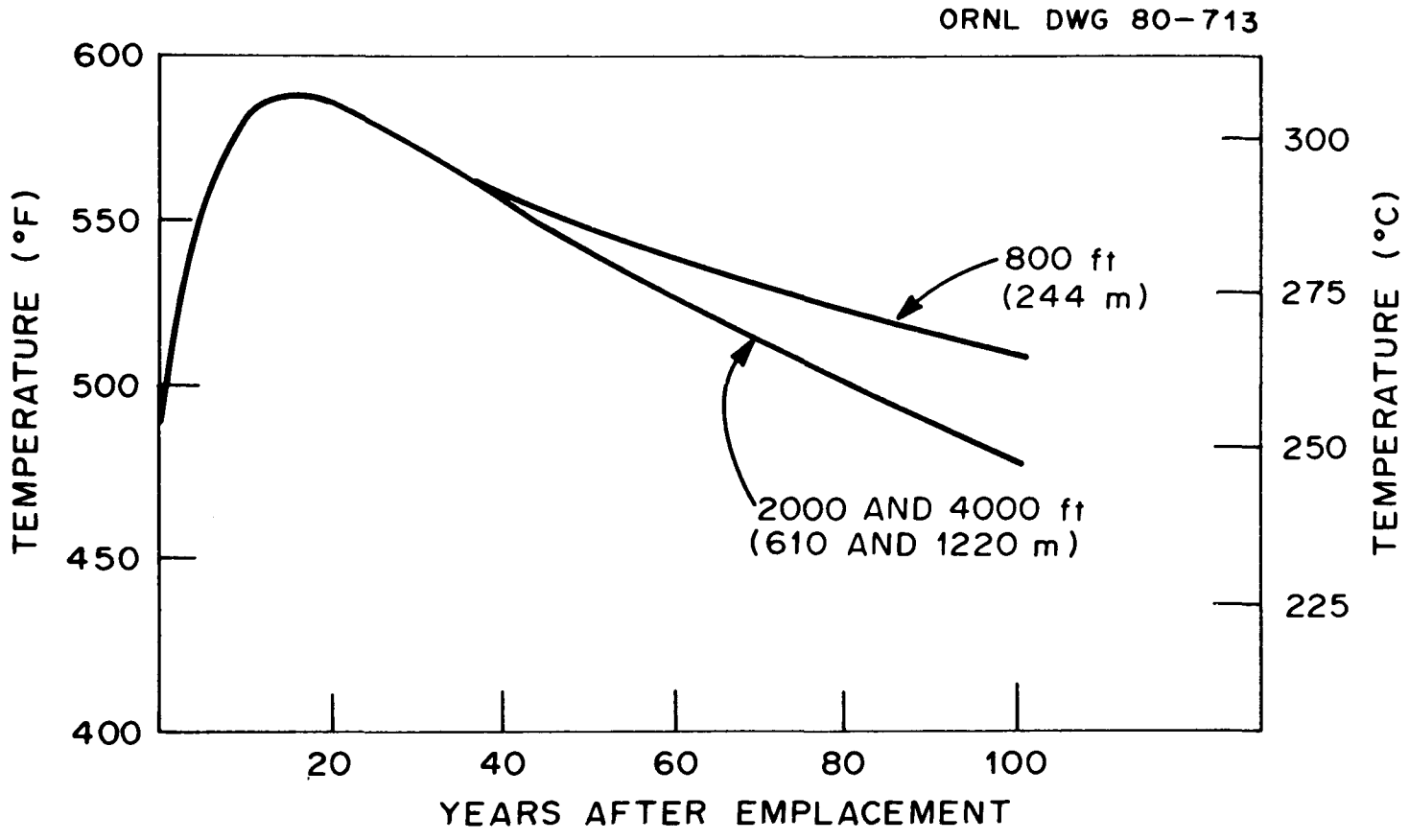

Fig. H-2. Effect of model boundary location on the maximum salt temperature histories.

differences (<0.2%) for the temperature at the waste midplane up to 5 yr after emplacement. This difference increases to nearly 1% by 100 yr after emplacement.

ORNL/TM-7201
Dist. Category UC-70

INTERNAL DISTRIBUTION

1. C. W. Alexander
2. C. F. Baes
3. J. O. Blomeke
4-23. H. C. Claiborne
24. A. G. Croff
25. L. R. Dole
26. R. W. Glass
27. G. H. Jenks
28. R. A. Just
29. T. F. Lomenick
30. A. L. Lotts
31. R. S. Lowrie
32. B. F. Maskewitz
33. J. G. Moore
34. S. Stow
35. D. K. Trubey
36-37. Central Research Library
38-41. Laboratory Records
42. Laboratory Records, RC
43. ORNL-Y-12 Technical Library
Document Reference Section
44. ORNL Patent Office

EXTERNAL DISTRIBUTION

Battelle Memorial Institute, Office of Nuclear Waste Isolation, 505 King Avenue, Columbus, OH 43201
45. W. A. Carbiener
46-50. N. E. Carter
51. N. Hubbard
52-56. G. E. Raines
57. ONWI Library

NUKEM GmbH, Postfach 110080, D-6450 Hanau 11, Federal Republic of Germany
58. R. Schönfeld

Physikalisch-Technische Bundesanstalt, D3300 Braunschweig, Bundesalle 100, Federal Republic of Germany
59. F. Oesterle

RE/SPEC, Inc., P. O. Box 725, Rapid City, SD 57709
60. J. D. Osnes
61. J. L. Ratigan

Sandia Laboratories, P. O. Box 5800, Albuquerque, NM 87185
62. T. O. Hunter
63. J. R. Wayland

Science Applications, Inc., P.O. Box 843, Oak Ridge, TN 37830
64. R. F. Graham
65-69. L. D. Rickertsen

70. Assistant Manager for Energy Research and Development, DOE-ORO, Oak Ridge, TN 37830

71. W. R. Wunderlich, U.S. Department of Energy, Richland Operations Office-Columbus, 505 King Avenue, Columbus, OH 43201

72. J. L. McElroy, Battelle Pacific Northwest Labortories, P.O. Box 999, Richland, WA 99352

73. K. R. Hoopingarner, Rockwell Hanford Operations, Columbia Bank Building, P.O. Box 800, Richland, WA 99352

74. J. R. Wiley, Savannah River Laboratories, E. I. DuPont DeNemours & Company, Aiken, SC 29801

75-388. Given distribution as shown in TID-4500 under Nuclear Waste Management Category (UC-70)

Special ONWI Distribution

389. Joan C. Abena, Administrative Assistant, Mintsubishi Metal Corporation, New York Office, 277 Park Avenue, New York, NY 10017

390. David Alaniz, U.S. Department of Energy Region IV, 1655 Peachtree Street, NE, Atlanta, GA 30309

391. John A. Apps, University of California, Lawrence Berkeley Laboratory, East End of Hearst Avenue, Berkeley, CA 94720

392. Dede Armentrout, National Audubon Society, P.O. Box 416, Brownwood, TX 76801

393. Alvin Askew, Governor's Energy Advisory Council, 7703 North Lamar, Austin, TX 78752

394. Lindsay Audin, One Everett Avenue, Ossining, NY 10562

395. Beverly S. Ausmus, Battelle Columbus Laboratory, Room 6146, 505 King Avenue, Columbus, OH 43201

396. H. Babad, Research Department, Rockwell Hanford Operations, Energy Systems Group, P.O. Box 800, Richland, WA 99352

397. Jack Badman, Gibbs & Hill, 393 7th Avenue, New York, NY 10001

398. Yossef Balas, Commonwealth Associates, Inc., 209 Washington Avenue, Jackson, MS 39201

399. W. W. Ballard, Department of Energy, Division of Waste Isolation, Washington, DC 20545

400. Dr. P. T. Bankston, Assistant Director, Mississippi Fuel and Energy Management Commission, 1307 Woolfolk State Office Building, Jackson, MS 39202

401. R. W. Barnes, Nuclear Materials Management Department, Ontario Hydro, 700 University Avenue, Toronto, Ontario, Canada M5G 1X6

402. G. S. Barney, Rockwell International, Atomic International Division, Rockwell Hanford Operations, P.O. Box 800, Richland, WA 99352

403. Lou Battams, Foundation Sciences, Inc., 1630 Southwest Morrison Street, Portland, OR 97205

404. T. A. Bauman, U.S. Department of Energy, Richland Operations Office, P. O. Box 550, Richland, WA 99352

405. W. G. Belter, Environmental Systems Group, NUS Corporation, 4 Research Place, Rockville, MD 20850

406. Mr. Gene Blanc, Assistant to the President, Pacific Gas and Electric Company, 1050 17th Street, NW, Suite 1180, Washington, DC 20036

407. Robert R. Blickwedehl, Dames & Moore, 2996 Belgium Road, Baldwinsville, NY 13027

408. Dr. R. J. Borg, L-233, Lawrence Livermore Laboratory, University of California, P. O. Box 808, Livermore, CA 94550

409. James Boyd, 282 Del Mesa Carmel, Carmel, CA 93921

410. Regis R. Boyle, Mail Station 68655, Nuclear Regulatory Commission, Washington, DC 20555

411. Don J. Bradley, Senior Scientist, Battelle Pacific Northwest Laboratory, P. O. Box 999, Richland, WA 99352

412. Larry Bradley, 2726 Country Club Road, Olympia, WA 98502

413. A. Brandstetter, Battelle Pacific Northwest Laboratories, P. O. Box 999, Richland, WA 99352

414. Randy Brewer, 21 Evergreen Street, Cortland, NY 13045

415. L. L. Burger, Chemistry Technology Department, Battelle Pacific Northwest Laboratories, Battelle Boulevard, Richland, WA 99352

416. A. S. Burgess, Acres American, Inc., The Liberty Bank Building, Main at Court, Buffalo, NY 14202

417. J. B. Burnham, Battelle Pacific Northwest Laboratories, P. O. Box 999, Richland, WA 99352

418. J. D. Byerlee, U.S. Geological Survey, 345 Middlefield Road, Menlo Park, CA 94025

419. Jerry Callen, 59 Livingston Street, 2A3, Brooklyn, NY 11201

420. Darrell H. Card, Ford, Bacon and Davis Engineers, Constructors, 375 Chipeta Way, Salt Lake City, UT 84108

421. Sophie Carman, Librarian, Science Applications, Inc., 2450 Washington Avenue, Suite 120, San Leandro, CA 94577

422. Valerie Cassaday, James F. MacLaren, Ltd., 735 McNicall Avenue, Willowdale, Ontario, Canada L5N 2E5

423. Tommy Chesser, 1300 Castlegate Drive, Gastonia, NC 28052

424. E. R. Christie, TRW Systems and Energy, 7600 Colshire Drive, McLean, VA 22101

425. R. N. Christensen, Nuclear Engineering Department, 2133 Robinson Lab., Ohio State University, 206 West 18th, Columbus, OH 43210

426. Wilson Clark, Assistant to the Governor for Issues and Planning, State Capitol Building, Sacramento, CA 95814

427. Jeffe Cleveland, U.S. Geological Survey, Water Resources Division, Denver Federal Center, Denver, CO 80225

428. John Cogan, Principal Geotechnical Engineer, International Engineering Company, Inc., 220 Montgomery Street, San Francisco, CA 94104

429. B. L. Cohen, University of Pittsburgh, Pittsburgh, PA 15260

430. Lewis Cohen, 94-1140, Lawrence Berkeley Laboratory, Berkeley, CA 94720

431. James L. Cohon, Department of Geography and Environmental Engineering, The Johns Hopkins University, Baltimore, MD 21218

432. David G. Coles, University of California, Lawrence Livermore Laboratory, Mail Code L-233, P. O. Box 808, Livermore, CA 94550

433. Horace R. Collins, Division of Geological Survey, The Ohio Department of Natural Resources, Fountain Square Building 6, Columbus, OH 43225

434. Community Development Planner, South Plains Association of Governments, 1709 26th Street, Lubbock, TX 79411

435. C. R. Cooley, Department of Energy, Division of Waste Isolation, Washington, DC 20545

436. Dr. R. G. Corbett, Professor of Geology and Coordinator of Research, University of Akron, Akron, OH 44325

437. Ernest Coriz, Administrative Assistant, Department of Energy and Minerals, P. O. Box 2770, Santa Fe, NM 87503

438. Rex Couture, CEN, Argonne National Laboratory, Argonne, IL 60439

439. C. W. Craven, Science Applications, Inc., P. O. Box 843, Oak Ridge, TN 37830

440. Jaak Daemen, Assistant Professor, Mining and Geological Engineering, College of Mines, University of Arizona, Tucson, AZ 85721

441. Dames & Moore Library, Suite 1000, 1100 Glendon Avenue, Los Angeles, CA 90024

442. Edward M. Davis, Vice President, American Nuclear Energy Council, 1750 K Street Northwest, Washington, DC 20006

443. H. G. Davis, 2500 Colorado, Santa Monica, CA 90404

444. R. J. Davis, NUS Corporation, 4 Research Place, Rockville, MD 20850

445. Richard E. Davis, Building 705, Brookhaven National Laboratory, Upton, NY 11973

446. Duane Day, Department of Energy Region I, 150 Causeway Street, Room 700, Boston, MA 02114

447. "Hap" Day, Illinois Atomic Energy Commission, Lincoln Tower Plaza, 524 South Second Street, Room 415, Springfield, IL 62706

448. T. K. DeBoer, Director, Technical Development Programs, New York State Energy Office, Agency Building #2, Empire State Plaza, Albany, NY 12223

449. R. A. Deju, Rockwell International, Atomics International Division, Rockwell Hanford Operations, P. O. Box 800, Richland, WA 99352

450. Louis F. Dellwig, Department of Geology, University of Kansas, Lawrence, KS 66045

451. Department of Energy, Region VIII Library, Attention J. L. C. Gosney, P. O. Box 26247, Belmar Branch, Lakewood, CO 80226

452. Department of Energy Library, 1902 Federal Building, 915 Second Avenue, Seattle, WA 98174

453. J. Di Nunno, NUS Corporation, 4 Research Place, Rockville, MD 20850

454. Brian Dombrowski, Sanitarian, Seneca County Department of Health, Waterloo, NY 13165

455. F. S. Doolittle, Community Relations Consultant, New York State Electric and Gas Corporation, 4500 Vestal Parkway East, Binghamton, NY 13902

456. John Roger Drake, 952 Azelea Street, Lafayette, LA 70506

457. A. Duba, Lawrence Livermore Laboratory, P. O. Box 808, Livermore, CA 94550

458. Bill Duesing, 153 Bowers Hill, Oxford, CT 06483

459. Dr. A. G. Duncan, UK Department of Environment, Route 427, Becket House, 1 Lambeth Palace Road, London, England

460. Mary A. Eadden, Technical Information Specialist, Nuclear Regulatory Commission, Division of Safeguards, Mail Stop 881 SS, 7915 Eastern Avenue, Silver Spring, MD 20910

461. Earth Science Laboratory, 920 Chipeta Way, Suite 120, Salt Lake City, UT 84108, ATTN: Librarian

462. Geoffrey Eichholz, Regent's Professor of Nuclear Engineering, School of Nuclear Engineering, Georgia Institute of Technology, Atlanta, GA 30332

463. Warren Eister, Department of Energy, Division of Waste Isolation, Washington, DC 20545

464. Bud Ellis, Addison High School, Addison, MI 49220

465. J. Ellis, Department of Energy, Grand Junction Operations Office, P. O. Box 2567, Grand Junction, CO 81501

466. Paul A. Ellis, Kaman Sciences Corporation, 1500 Garden of the Gods Road, P. O. Box 7463, Colorado Springs, CO 80933

467. Energy System Group, 8900 DeSoto Avenue, Canoga Park, CA 91304, ATTN: Library

468. Envirosphere Company, 10800 NE 8th Street, Bellevue, WA 98004

469. Bruce R. Erdal, University of California, Los Alamos Scientific Laboratory, P. O. Box 1663, Los Alamos, NM 87545

470. Arthur R. Eschner, Professor of Forest Influences, State University, College of Environmental Sciences and Forestry, Syracuse, NY 13210

471. George C. Evans, Columbia Bank Building, Basalt Waste Isolation Program, Rockwell Hanford Operations, P. O. Box 800, Richland, WA 99352

472. Dr. Robert H. Fakundiny, Geological Survey, State Geologist, New York Education Building, Room 973, Albany, NY 12224

473. J. V. Feuss, PE, Director of Public Health, Cortland County Health Department, Courthouse, Cortland, NY 13045

474. Robert H. Fickies, New York State Geological Survey, Education Building Annex, Albany, NY 12234

475. Sue Fingerman, Dames and Moore, 44 Mall Road, Burlington, MA 01803

476. Tom Fitzpatrick, Energy Division, Office of Policy and Management, 80 Washington Street, Hartford, CT 06115

477. Kevin Flinn, Argonne National Laboratory, 9700 South Cass Avenue, Argonne, IL 60430

478. Patrick Forrester, Assistant Director for Nuclear, Office of Energy Resources, 73 Tremont Street, Boston, MS 02108

479. A. J. Francis, Department of Nuclear Engineering, B830, Brookhaven National Laboratory, Upton, NY 11973

480. Jules Friedman, U.S. Geological Survey, Denver Federal Center, Denver, CO 80225

481. Fugro Incorporated, Consulting Engineers and Geologists, P. O. Box 7765, Long Beach, CA 90807

482. Bob Funderburg, Radiation Control Officer, Idaho Department of Health and Welfare, Statehouse, Boise, ID 83720

483. P. C. Fung, Atomic Energy of Canada, Ltd., Whiteshell Nuclear Research Establishment, Pinawa, Manitoba, Canada ROE 1LO

484. William J. Galyean, Falcon Research and Development, 2350 Alamo Avenue SE, Albuquerque, NM 87106

485. Howard F. Gandt, 15 Houghton Boulevard, Stony Brook, NY 11790

486. M. E. Gates, Manager, U.S. Department of Energy, Nevada Operations Office, P. O. Box 14100, Las Vegas, NV 89114

487. Dr. Todd M. Gates, Dames and Moore, 1150 West Eighth Street, Cincinnati, OH 43203

488. Geological Survey Section, North Carolina Department of Natural Resources and Community Development, P. O. Box 27687, Raleigh, NC 27611

489. C. H. George, Department of Energy, Division of Waste Isolation, Washington, DC 20545

490. L. H. Gevantman, U.S. Department of Commerce, National Bureau of Standards, Office of Standard Reference Data, Washington, DC 20234

491. Shirley M. Gifford, 97 Spring Street, Amherst, MA 01002

492. K. V. Gilbert, Monsanto Research Corporation, Mound Laboratory, P. O. Box 32, Miamisburg, OH 45342

493. Paul F. Gnirk, RE/SPEC, Inc., P. O. Box 724, Rapid City, SD 57701

494. A. S. Goldin, U.S. Environmental Protection Agency, Mail Stop ANR-461, Washington, DC 20460

495. Marc W. Goldsmith, Energy Research Group, Inc., 400-1 Trotter Pond Road, Waltham, MA 02154

496. R. B. Goranson, U.S. Department of Energy, Richland Operations Office, P. O. Box 550, Richland, WA 99352

497. Jane L. C. Gosney, U.S. Department of Energy, Region B Library, P. O. Box 26247, Belmar Branch, Lakewood, CO 80226

498. Governor's Office of Planning Coordination, 1050 East Williams Street, Suite 402, Carson City, NV 89710

499. W. Grams, South Dakota School of Mines and Technology, Rapid City, SD 57701

500. David A. Gray, Assistant Director, Special Services Division, Institute of Geophysical Sciences, Exhibition Road, London SW7, England

501. John W. Green, Mississippi Department of Natural Resources, Bureau of Geology and Energy Resources, P. O. Box 4915, Jackson, MS 39216

502. Craig F. Grochmal, Technical Liaison Engineer, Stone and Webster Engineering Corporation, 7315 Wisconsin Avenue, Room 332W, Bethesda, MD 20014

503. Bruce D. Guilbeault, NUS Corporation, 4 Research Place, Rockville, MD 20850

504. Dr. Charles R. Hadlock, Arthur D. Little, Inc., Acorn Park, Cambridge, MA 02140

505. A. R. Hakl, Westinghouse Electric Corporation, Six Gateway Center, Room 1559, Pittsburgh, PA 15222

506. J. Haley, Executive Assistant to the General Manager, Westinghouse Electric Corporation, Advanced Energy Systems Division, Box 10864, Pittsburgh, PA 15236

507. G. W. Hannaman, General Atomic Company, Room TOE-293, P. O. Box 81608, San Diego, CA 92138

508. Wayne Harl, Director, Energy Resource Programs, Idaho Office of Energy, State House, Boise, ID 83720

509. Edward F. Hawkins, Leader, Safety Analysis Section, High-Level Waste Licensing Management Branch, Division of Waste Management, U.S. Nuclear Regulatory Commission, Mail Stop 905SS, Washington, DC 20555

510. C. A. Heath, Department of Energy, Division of Waste Isolation, Washington, DC 20545

511. John B. Heil, University of Wisconsin Center, University Drive, Fan du Lac, WI 54935

512. E. E. Held, Nuclear Regulatory Commission, Division of Fuel Cycle and Environmental Research, Washington, DC 20555

513. Dr. Michael R. Helfert, Department of Ocean Sciences/DS, U.S. Coast Guard Academy, New London, CT 06320

514. Ed Helminski, Hall of the States, 444 North Capitol Avenue, Washington, DC 20001

515. John B. Henderson, International Energy Associates, Ltd., 600 New Hampshire Avenue NW, Washington, DC 20037

516. Sigrid Higdon, U.S. Department of Energy Region VIII, 1075 South Yukon Street, Lakewood, CO 80226

517. A. O. Hobbs, Box 887, Raleigh, NC 27602

518. G. L. Hohmann, Manager, Safety and Environmental Assessment, Westinghouse WIPP Project, P. O. Box 40039, Albuquerque, NM 87196

519. Norman Hubbard, SN7, NASA-Johnson Space Center, Houston, TX 77058

520. Keel Hunt, Office of the Governor, State Capitol Building, Nashville, TN 37219

521. Tom Hunt, Public Affairs Manager, AIF, Inc., 7101 Wisconsin Avenue, Washington, DC 20014

522. International Engineering Company, Inc., Headquarters Office, 220 Montgomery Street, San Francisco, CA 94104

523. Dr. R. Danford Ip, Director, International Research and Evaluations, 21098 IRE Control Center, Eagan, MN 55121

524. Taro Ito, Japan Atomic Energy Research Institute Tokai-Mura Nakagun Ibaraki, Japan

525. O. E. Jones, Sandia Laboratories, P. O. Box 5800, Albuquerque, NM 87185

526. Clyde Jupiter, Program Manager, Waste Management Research, Office of Nuclear Regulatory Research, U.S. Nuclear Regulatory Commission, Mail Stop 1130SS, Washington, DC 20555

527. Dr. K. F. Kahle, Professor of Geology, Bowling Green State University, Bowling Green, OH 43403

528. Barry Kaplovitz, Office of the Governor, State House, Boston, MS 02133

529. Dr. S. K. Kao, The University of Utah, Department of Meteorology, Room 819, William C. Browning Building, Salt Lake City, UT 84112

530. Lawrence Kehoe, Secretary, Energy and Minerals Department, 113 Washington Street, P. O. Box 2770, Santa Fe, NM 87501

531. J. B. Kemp, Bechtel Corporation, 50 Beale Street, P. O. Box 3965, San Francisco, CA 94119

532. Francis J. Keneshea, Nuclear Services Corporation, 1700 Dell Avenue, Campbell, CA 95008

533. James T. King, NEFCO, 137 South Main Street, Delaware Building, Suite 300, Akron, OH 44308

534. J. H. Kittel, Manager, Office of Waste Management Programs, Argonne National Laboratory, 9700 South Cass Avenue, Argonne, IL 60439

535. Keith Klein, U.S. Department of Energy, Division of Waste Isolation, Washington, DC 20545

536. Cyrus Klingsberg, Department of Energy, Division of Waste Isolation, Washington, DC 20545

537. R. L. Knecht, Manager, Structural Engineering, Hanford Engineering Development Laboratory, P. O. Box 1970, Richland, WA 99352

538. James A. Koster, 609 North Broadway, Watertown, SD 57201

539. Scott Kramer, 770 Parkmoor Drive, Brookfield, WI 53005

540. William H. Kramer III, 78 May Drive, Chatham, NJ 07928

541. P. Kruger, Department of Civil Engineering, Terman Engineering Center, Stanford University, Stanford, CA 94305

542. Dr. F. A. Kulacki, Department of Mechanical Engineering, The Ohio State University, 206 West 18th Avenue, Columbus, OH 43210

543. W. J. Kurzeka, Manager, Commercial Waste Technology Unit, Rockwell Hanford Operations, P. O. Box 800, Richland, WA 99352

544. Peter Lagus, Systems Science and Software, 3398 Carmel Mountain Road, San Diego, CA 92121

545. Dr. Edward P. Laine, Graduate School of Oceanography, University of Rhode Island, Narragansett, RI 02882

546. R. A. Langley, Jr., Bechtel National, Inc., P. O. Box 3965, San Francisco, CA 94119

547. T. R. Lash, National Resources Defense Council, 25 Kearny Street, San Francisco, CA 94108

548. J. A. Laswick, Department of Chemistry, Clarion State College, Clarion, PA 16214

549. Dr. Joe D. Ledbetter, Civil Engineering Department, ECJ 8.6, University of Texas, Austin, TX 78712

550. Lenore Ledman, U.S. Department of Energy Region II, 26 Federal Plaza, Room 3206, New York, NY 10007

551. Dr. C. F. Lee, Geotechnical Engineering Department (H16 g 26), Ontario Hydro, 700 University Avenue, Toronto Ontario M6G 1X6, Canada

552. Larry Lefebvre, Director of Policy Analysis and Planning, Office of Energy Resources, Edgar A. Brown Building, Columbia, SC 29201

553. H. E. Lefoure, U.S. Nuclear Regulatory Commission, Division of Site Safety, Geosciences Branch, Washington, DC 20555

554. Roger LeGassie, U.S. Department of Energy, Office of Energy Research, Washington, DC 20545

555. J. W. Lentsch, Portland General Electric, 121 SW Salmon Street, Portland, OR 97204

556. David H. Lester, Science Applications, Inc., 1200 Prospect Street, P. O. Box 2351 La Jolla, CA 92038

557. G. B. Levin, EG&G Idaho, Inc., P. O. Box 1625, Idaho Falls, ID 83401

558. Dr. John Lewis, Geosciences Department, Northeast Louisiana University, Monroe, LA 71209

559. Anthony Liberatore, Director of Policy Services, Institute of Natural Resources, 222 South College Street, Springfield, IL 62706

560. J. A. Lieberman, Nuclear Safety Associates, 5101 River Road, Bethesda, MD 20016

561. R. Lincoln, Sandia Laboratories, P. O. Box 5800, Albuquerque, NM 87185

562. E. N. Lindmer, University of Minnesota, Department of Civil and Mineral Engineering, 221 Church Street Southeast, Minneapolis, MN 55455

563. S. E. Logan, Los Alamos Technical Associates, Inc., P. O. Box 410, Los Alamos, NM 87544

564. Louisiana Office of Commerce and Industry, P. O. Box 44185, Baton Rouge, LA 70804

565. R. W. Lynch, Sandia Laboratories, P. O. Box 5800, Albuquerque, NM 87185

566. Charles Lyon, Electrical Engineering Department, University of Arizona, Tucson, AZ 85721

567. J. B. Lyons, Department of Earth Sciences, 402 Fairchild, Dartmouth College, Hanover, NH 03755

568. Pat Machledt, NUS Corporation, West Central Environmental Center, 720 South Colorado Boulevard, Denver, CO 80222

569. Dr. D. Majumdar, Building 130, Brookhaven National Laboratory, Upton, NY 11973

570. Murli H. Manghnani, University of Hawaii at Manoa, Hawaii Institute of Geophysics, 2525 Correa Road, Honolulu, HI 96822

571. C. W. Manry, Rockwell Hanford Operations, P. O. Box 800, Richland, WA 99352

572. David Marks, Director, Governors Office of Energy Resources, Suite 502, 7703 North Lamar Street, Austin, TX 78752

573. Maria Marks, U.S. Department of Energy Region III, 1421 Cherry Street, Philadelphia, PA 19102

574. Amy Martin, Armadillo Coalition of Texas, 4227 Herschel, Suite 306, P. O. Box 26390, Dallas, TX 75226

575. J. D. Martinez, Institute for Environmental Studies, Louisiana State University, Baton Rouge, LA 70803

576. Dr. Walter Mason, Environmental Health Department, Tulane University, New Orleans, LA 70118

577. E. F. Mastal, Office of Nuclear Waste Management, U.S. Department of Energy, Washington, DC 20545

578. W. C. McClain, RE/SPEC, Inc., One Concourse Drive, P.O. Box 725, Rapid City, SD 57709

579. James G. McCray, Nuclear Engineering Department, University of Arizona, Tucson, AZ 85721

580. Max McDowell, Emporia Gazette, Box 1, Elmdale, KS 66850

581. J. M. McGough, WIPP Project, Albuquerque Operations Office, P.O. Box 5900, Albuquerque, NM 87115

582. Ed Meek, Director of Public Relations, University of Mississippi, Oxford, MS 38677

583. Neil Meldgin, 13020 Choctaw Road, Palos Heights, IL 60463

584. Gail Melson, Legislative Office of Science Advisor, Box 30036, Lansing, MI 48909

585. Harvey W. Merrell, Consulting Geologist, 125 East Center, Moah, UT 84532

586. Fred Millar, Potomac Alliance, 1743 Q Street Northwest, Washington, DC 20009

587. Camille Minichino, L-390, Lawrence Livermore Laboratory, P.O. Box 808, Livermore, CA 94550

588. Louis Miron, 1100 South 28th Avenue, Hattiesburg, MS 39401

589. John E. Mosier, Science Applications, Inc., P.O. Box 29497, Columbus, OH 43229

590. J. B. Muckerheide, 755 Boyleston Street, Suite 306, Boston, MA 02116

591. John Muhlestein, U.S. Department of Energy, San Francisco Operations Office, 1333 Broadway, Oakland, CA 94612

592. Malcolm Murray, Office of the Governor, Room 127 State Capitol Building, Denver, CO 80203

593. Susan A. Murtha, NUS Corporation, 4 Research Place, Rockville, MD 20850

594. Zoran Musicki, 454 West Dayton Street #307, Madison, WI 53703

595. Steve Nacht, Dalton-Dalton-Little-Newport, Architects, Engineers, Planners, 3605 Warrensville Center Road, Cleveland, OH 44122

596. Barry N. Naft, Manager Licensing, Consulting Division, NUS Corporation, 4 Research Place, Rockville, MD 20850

597. Joe Nanus, Texas Department of Health 1100 West 49th Street, Austin, TX 78756

598. National Bureau of Standards, Office of Measurements for Nuclear Technology, Physics Building B-318, Washington, DC 20234

599. Lamar Priester, Executive Director, South Carolina Office of Energy Resources, Edgar A. Brown Building, 1205 Pendleton Street, Columbia, SC 29201

600. Public Reading/Document Rooms, Chicago Operations Office, 9800 South Cass Avenue, Argonne, IL 60439

601. Public Reading/Document Rooms, DOE Headquarters, Room GA-152 Forrestal Building, 100 Independence Avenue, SW, Washington, DC 20001

602. Public Reading/Document Rooms, Idaho Operations Office, 550 Second Street, Idaho Falls, ID 83401

603. Public Reading/Document Rooms, Nevada Operations Office, 2753 South Highland Drive, Las Vegas, NV 89109

604. Public Reading/Document Rooms, Oak Ridge Operations Office, Federal Building, Oak Ridge, TN 37830

605. Public Reading/Document Rooms, Richland Operations Office, Federal Building, Richland, WA 99352

606. Public Reading/Document Rooms, San Francisco Operations Office, 1333 Broadway, Oakland, CA 94612

607. Public Reading/Document Rooms, Savannah River Operations Office, Savannah River Plant, Aiken, SC 29801

608. John Rae, Theoretical Physics Division, Atomic Energy Research Establishment, B 424.4 AERE Harwell, Didcot, Oxon, England OX11 ORA

609. Charles A. Ratte, State Geologist, Office of the Secretary, Agency of Environmental Conservation, Montpellier, VT 05602

610. J. R. Raymond, Battelle Pacific Northwest Laboratory, PSL-1259, P.O. Box 999, Richland, WA 99352

611. Reddy Communications, Inc., 537 Steamboat Road, Greenwich, CT 06830, Attn: Library

612. RE/SPEC, Inc., P.O. Box 725, Rapid City, SD 57709

613. William R. Rhyne, Manager, Licensing and Risk Analysis Division, Science Applications, Inc., Building C, Suite 100, 800 Oak Ridge Turnpike, Oak Ridge, TN 37830

614. Gary Robbins, Office of Standards Development, Nuclear Regulatory Commission, Washington, DC 20555

615. T. M. Robertson, Automation Industries, Inc., Vitro Laboratories Division, 1400 Georgia Avenue, Silver Spring, MD 20910

616. Sally Rodgers, Friends of the Earth, New Mexico Ranch, Box 131, Santa Fe, NM 87501

617. D M. Rohrer, Division of Waste Management, Nuclear Regulatory Commission, MS-687-SS, Washington, DC 02555

618. Eugene H. Rosenboom, Jr., U.S. Geological Survey, Mail Stop 959, Reston, VA 22092

619. Herbert N. Rosenberg, Energy Systems Group of TRW, Inc., 800 Oak Ridge Turnpike, Suite B-202, Oak Ridge, TN 37830

620. Eva Rosinger, Atomic Energy of Canada, Ltd., Pinawa, Manitoba ROE ILO, Canada

621. Jacob Rubin, U.S. Geological Survey/WRD, 345 Middlefield Road, Menlo Park, CA 94025

622. David E. Ruiter, NUS Corporation, 720 South Colorado Boulevard, Suite 900, Denver, CO 80222

623. James E. Russell, Texas A&M University, College Station, TX 77843

624. John Russell, Georgia Tech., Atlanta, GA 30332

625. John L. Russell, U.S. Environmental Protection Agency, AW-45, Washington, DC 20460

626. Kari Saari, University of California, 440 Davis Hall, Berkeley, CA 94720

627. Dr. George P. Sabol, Westinghouse Electric Corporation, Research and Development Center, Pittsburgh, PA 15235

628. Dr. B. Sagar, Dames & Moore, 1100 Glendon Avenue, Suite 1000, Los Angeles, CA 90024

629. San Juan County Commission, Box 338, Monticello, UT 84535

630. Sandia Laboratories, Department 4510, Albuquerque, NM 87185

631. F. P. Sargent, Storage & Disposal Branch, Atomic Energy of Canada, Ltd., Pinawa, Manitoba, Canada ROE 1LO

632. Muriel Scarborough, U.S. Department of Energy, WIPP Project Office, Mail Sta B-107, Washington, DC 20545

633. Mark Schleifstein, Jackson Clarion-Ledger, P.O. Box 40, Jackson, MS 39205

634. Dornest Schueler, Albuquerque Operations Office, U.S. Department of Energy, P. O. Box 5400, Albuquerque, NM 87185

635. Sheldon Schwartz, Assistant Director for Program Development, Office of State Programs, Nuclear Regulatory Commission, Washington, DC 20555

636. Dr. Donald Schweitzer, Building 703, Brookhaven National Laboratory, Upton, NY 11973

637. W. E. Selph, Manager Program Development, IRT Corporation, P.O. Box 80817, San Diego, CA 92138

638. R. A. Sexton, Rockwell Hanford Operations, P. O. Box 800, 2704-E/200-E, Richland, WA 99352

639. Dr. Heyward Shealy, Conference of Radiation Control Program Directors, 1600 Bull Street, Columbia, SC 29201

640. G. W. Shurr, U.S. Geological Survey, Denver Federal Center, Denver, CO 80225

641. Sierra Club, Mississippi Chapter, P.O. Box 4335, Jackson, MS 39216

642. James N. Siltanen, Manager, Project Development, Advanced Projects Division, General Atomic Company, P. O. Box 81608, San Diego, CA 92138

643. Authur E. Slaughter, State Geologist, Michigan Department of Conservation, Geological Survey Division, Stevens T. Mason Building, Lansing, MI 48926

644. Alvin E. Smith, Manager of Nuclear Processing, The Ralph M. Parsons Company, 100 West Walnut Street, Pasadena, CA 91124

645. Lawrence J. Smith, TRU Waste Systems Office, Building T-796, Rockwell International, P.O. Box 464, Golden, CO 80401

646. Dr. Michael J. Smith, Manager Engineered Barriers, Basalt Waste Isolation Program, Rockwell Hanford Operations, Richland, WA 99352

647. T. H. Smith, EG&G Idaho, Inc., P.O. Box 1625, Idaho Falls, ID 83401

648. A. J. Soinski, California Energy Commission, 1111 Howe Avenue, MS-18,Sacramento, CA 95825

649. David L. South, Mining Department, University of Arizona, Tucson, AZ 85721

650. J. D. Spaulding, Center for Applied Isotope Studies, 110 Riverbend Road, University of Georgia, Athens, GA 30602

651. Ed Spitzer, Executive Director, Tennessee Energy Authority, Suite 707, Capitol Boulevard Building, Nashville, TN 37219

652. Lewis L. Staley, Supervisor of Energy Information, New York State Electric and Gas Corporation, 4500 Vestal Parkway East, Binghamton, NY 13902

653. F. R. Standerfer, U.S. Department of Energy, Richland Operations Office, P.O. Box 550, Richland, WA 99352

654. Richard W. Starostecki, Science Applications, Inc., 1764 Old Meadow Lane, McLean, VA 22102

655. State Planning Office, Library, 4528 Bennington Avenue, Baton Rouge, LA 70808

656. Ralph Stein, D/WM, U.S. Department of Energy/Headquarters, WIPP Project Office, Mail Sta B-107, Washington, DC 20545

657. M. Steindler, Argonne National Laboratory, 9700 South Cass Avenue, Argonne, IL 60439

658. J. Carl Stepp, Director of Geosciences, Furgo, Inc., 3777 Long Beach Boulevard, Long Beach, CA 90807

659. Peter R. Stevens, Resident Geologist, U.S. Geological Survey, National Center (410), 12201 Sunrise Valley Drive, Reston, VA 22092

660. David B. Stewart, U.S. Geological Survey, 959 National Center, Reston, VA 22092

661. L. A. Stinnett, NUS Corporation, 720 South Colorado Boulevard, Suite 900, Denver, CO 80222

662. Ken Stefflet, 1706 Cameron Drive, Madison, WI 53711

663. Sheldon D. Strauss, Senior Editor, Power, 1221 Avenue of the Americas, New York, NY 10020

664. Arthur Sutherland, Ford, Bacon & Davis, Utah, P.O. Box 8009, Salt Lake City, UT 84108

665. R. T. Sutton, Commissioner, Louisiana Department of Conservation, P.O. Box 44275, Baton Rouge, LA 70808

666. M. J. Szulinski, Science Applications, Inc., 292 Torbett, Richland, WA 99352

667. Daniel M. Talbert, Sandia Laboratories, SEABED Programs Division 4536, P.O. Box 5800, Albuquerque, NM 87185

668. Charles L. Taylor, Woodward-Clyde Consultants, 3 Embarcadero Center, Suite 700, San Francisco, CA 94111

669. Dr. Irving H. Tesmer, Department of Geosciences NS270, State University College, 1300 Elmwood Avenue, Buffalo, NY

670. Burton J. Thamer, Ford, Bacon, and Davis Engineers Constructors, 375 Chipeta Way, P.O. Box 8009, Salt Lake City, UT 84108

671. John H. Thoman, Wisconsin State Energy Office, 1 West Wilson Street, Room 201, Madison, WI 53702

672. Dr. Jack Thomas, Tennessee Energy Authority, Suite 707, Capitol Boulevard Building, Nashville, TN 37219

673. L. S. Tobias, 662 Lincoln Avenue, Manville, NJ 08835

674. James R. Tomonto, Nuclear Analysis Department, Florida Power and Light Company, P.O. Box 529100, Miami, FL 33152

675. Charles Trautmann, 235 Forrest Home Drive, Ithaca, NY 14850

676. A. N. Turcan, Capitol Area Groundwater Conservation Commission, P.O. Box 64526, Baton Rouge, LA 70896

677. Richard W. Turnbull, Geotechnical Engineers, Inc., 1017 Main Street, Winchester, MA 01890

678. R. F. Turner, General Atomic Company, Box 81608, San Diego, CA 92138

679. U.S. Department of Energy, Library Room 1223, 20 Massachusetts Avenue NW, Washington, DC 20001

680. U.S. Department of Energy, Region IX Office, Attention: Public Reading Room, 111 Pine Street, San Francisco, CA 94111

681. Maurice A. Van Nostrand, Chairman, Iowa State Commerce Commission, Statehouse, Des Moines, IA 50319

682. D. L. Vieth, U.S. Department of Energy, Division of Waste Isolation, Washington, DC 02545

683. Charles J. Vitaliano, Department of Geology, University of Indiana, Bloomington, IN 47401

684. Richard Waddell, U.S. Geological Survey WRD MS-416, Box 25046 DFC, Lakewood, CO 80225

685. J. L. Wallace, Atomic Energy Control Board, P.O. Box 1046, Ottawa, Canada K1P 559

686. Peter J. Walley, Mississippi Fuel and Energy Management Commission, Suite 228 Barefield Complex, 455 North Lamar Street, Jackson, MS 39201

687. Dr. Jack L. Walper, Professor of Geology, Texas Christian University, Department of Geology, Fort Worth, TX 76129

688. Gary Waymire, Manager, Safety Analysis, Reprocessing and Field Services Department, Exxon Nuclear Company, Inc., 777 106th Avenue NE C-00777, Bellevue, WA 98009

689. David A. Webster, DAWCON, Management Consulting Service, 310 Tara Trail NW, Atlanta, GA 30327

690. George Wehman, 3955 Georgia Lane, Ammon, ID 83401

691. R. K. White, 205 Program Manager Cress, SRI International, 333 Ravenswood Avenue, Menlo Park, CA 94025

692. Dr. Robert E. Wilems, Science Applications, Inc., 800 Oak Ridge Turnpike, Oak Ridge, TN 37830

693. W. A. Williams, Environmental Protection Agency (ANP-459), Washington, DC 20460

694. Richard M. Winar, Dames & Moore, 1550 Northwest Highway, Park Ridge, IL 60068

695. Rick Windholz, 1803 Laramie, Manhattan, KS 66502

696. Robert H. Wolle, Deputy Commissioner for the Environment, Tennessee Department of Public Health, 349 Cordell Hull Building, Nashville, TN 37219

697. D. E. Wood, Rockwell Hanford Operations, Energy Systems Group, P.O. Box 800, Richland, WA 99352

698. Warren W. Wood, U.S. Geological Survey, 12201 Sunrise Valley Drive, Reston, VA 22092

699. Woodward-Clyde Consultants, Library, Western Regin 3 Embarcadero Center, Suite 700, San Francisco, CA 94111

700. Kenneth S. WURM, Battelle's Columbus Laboratories, Room 11-3082, X-4322, Columbus, OH 43201

701. P. A. Ybarra, Rockwell Hanford Operations, Energy Systems Group, P.O. Box 800, Richland, WA 99352

702. W. J. Ziefenbach, Battelle Columbus Laboratory, Room 11-2089, Columbus, OH 43201

703. Michael Zolensky, Pennsylvania State University, 236 Deike Building, University Park, PA 16802

☆U S GOVERNMENT PRINTING OFFICE 1980 640 245/228